Chair of Petroleum Geology

Doctoral Thesis

Isotope, biomarker, and organic petrographic investigations of organic matter-rich rocks in the basement of the Alpine Foreland Basin: Implications for paleoenvironment and source rock potential

Dott.mag. Stephen Ajuaba

October 2023

MONTANUNIVERSITÄT LEOBEN
www.unileoben.ac.at

AFFIDAVIT

I declare on oath that I wrote this thesis independently, did not use other than the specified sources and aids, and did not otherwise use any unauthorized aids.

I declare that I have read, understood, and complied with the guidelines of the senate of the Montanuniversität Leoben for "Good Scientific Practice".

Furthermore, I declare that the electronic and printed version of the submitted thesis are identical, both, formally and with regard to content.

Date 09.10.2023

Signature Author
Stephen Ajuaba

Abstract

Organic matter-rich rocks are potential source rocks for oil and gas but are also valuable archives for past environmental conditions. In this thesis, Permo-Carboniferous and Lower Jurassic sediments from southern Germany and Switzerland were studied, addressing both aspects. To evaluate source potential and depositional environment, organic petrographic, palynofacies, Rock-Eval pyrolysis, and geochemical techniques (incl. biomarker analysis and compound-specific carbon isotopy) have been used.

Permo-Carboniferous sediments in the basement of the North Alpine Foreland Basin (NAFB) occur in post-Variscan graben structures. Upper Carboniferous coals probably charged Switzerland´s only gas deposit, while lower Permian lacustrine shales with high organic matter contents are potential source rocks for oil. The study of the Permo-Carboniferous sediments is based on 90 core samples from borehole Weiach-1 (northern Switzerland). Carboniferous coal seams, up to 10 m thick, were deposited in low-lying freshwater mires. In Weiach-1, they reached a maturity stage corresponding to the onset of gas generation. Organic matter-rich Permian (Autunian) shales were deposited in anoxic lakes with a stratified water column. The organic matter is of mixed aquatic and terrigenous origin. $\delta^{13}C$ values of pristane and phytane provide evidence for reworking of organic matter in the water column. Locally, the Autunian shales have a very good oil potential. The main shale interval in Weiach-1 is about 12 m thick. It reached early oil window maturity and will generate about 0.35 tHC/m² when mature.

Lower Jurassic rocks with high organic matter contents (Posidonia Shale) represent the Taorcian anoxic event (T-OAE). A prominent negative carbon isotope excursion (CIE; ~183 Myr) is present in the lower part of the T-OAE. Posidonia Shale from an active quarry (Dormettingen; Swabian Alb) and a borehole core, recovered from the basement of the NAFB (Salem; Germany), has been investigated.

The Posidonia Shale at Dormettingen is about 10 m thick and was investigated using a total of 56 samples. Geochemical redox indicators provide evidence for photic zone anoxia during the Toarcian CIE, which reached its maximum after deposition of the “Unterer Stein” marker horizon. Biomarker data suggest enhanced activity of diazotrophic cyanobacteria. Oxygen-depleted conditions, albeit with lower intensity continued after the CIE. All investigated organic compounds replicate the negative CIE. The shift for short-chain *n*-alkanes, pristane, and phytane, interpreted to reflect marine biomass, varies between 4.5 and 5.0 ‰. This is the highest value observed so far for any Toarcian section. $\delta^{13}C$ values of pristane and phytane reach a minimum near the base of the CIE interval and increase upsection. Thus, the maximum negative isotope shift predates the strongest basin restriction. In Dormettingen, the Posidonia Shale is immature to marginal mature.

In the Salem borehole, the Posidonia Shale is also about 10 m thick. The lower 7.5 m and the uppermost part of the underlying Amaltheenton Shale were studied using a total of 62 core samples. In contrast to other Toarcian sections, TOC contents are high in sediments deposited during the CIE, but even higher in post-CIE sediments. Biomarker ratios suggest that this reflects strong oxygen-depletion during the CIE (*elegantulum* to lower *elegans* subzones), but also during the *falciferum* Subzone. While the lower part of the Posidonia Shale (*tenuicostatum* Zone to *elegans* Subzone) is significantly thinner than in neighbouring

sections (e.g., Dormettingen), its middle part (*falciferum* Subzone) is unusually thick. This suggests that increased subsidence contributed to anoxia and indicates major variations in basin geometry. Although the CIE interval is very thin, $\delta^{13}C$ values of *n*-alkanes confirm the time lag between the maximum negative isotope shift (below "Unterer Stein") and the strongest basin restriction (above "Unterer Stein"). Moreover, the onset of the CIE is recorded earlier for aquatic than for terrigenous organisms. In Salem, the Posidonia Shale is thermally mature and highly oil-prone. The residual source petroleum potential is about 0.8 tHC/m².

Kurzfassung

Sedimente mit hohen Gehalten an organischem Material sind potentielle Kohlenwasserstoff-Muttergesteine, aber auch wertvolle Archive für Paläo-Umweltbedingungen. In dieser Dissertation wurden Sedimente des Permo-Karbons und des Unterjuras untersucht. Zur Bewertung des Muttergesteinspotentials und der Rekonstruktion der Ablagerungsbedingungen wurde die Rock-Eval-Pyrolyse eingesetzt und organische petrographische und geochemische Methoden (Biomarker-Analyse; komponenten-spezifische Kohlenstoff-Isotopie) angewandt.

Permokarbone Sedimente im Untergrund des Nordalpinen Vorlandbeckens (NAFB) treten in postvariszischen Grabenstrukturen auf. Kohlen des Oberkarbons sind das wahrscheinliche Muttergestein für das einzige Gasfeld in der Schweiz, während organisch-reiche Seesedimente des Unterperms potenzielle Öl-Muttergesteine darstellen. Die Untersuchung der permokarbonen Sedimente stützt sich auf 90 Kernproben aus der Bohrung Weiach-1 (Nordschweiz). Die bis zu 10 m mächtigen Kohleflöze aus dem Karbon wurden in Niedermooren abgelagert. In Weiach-1 erreichten sie ein Reifestadium, das dem Beginn der Gasbildung entspricht. Die an organischen Stoffen reichen permischen (autunischen) Tonsteine wurden in anoxischen Seen mit einer geschichteten Wassersäule abgelagert. Das organische Material ist aquatischen und terrigenen Ursprungs. Niedrige $\delta^{13}C$ Werte für Pristan und Phytan belegen die Wiederverwertung organischen Materials in der Wassersäule. Die permischen Sedimente weisen lokal ein sehr gutes Ölpotenzial auf. Das wichtigste Tonstein-Intervall in Weiach-1 ist etwa 12 m mächtig. Es hat die Ölfensterreife erreicht und wird bei fortgeschrittener Reife 0,35 t Kohlenwasserstoffe/m² generieren.

Der unterjurassische Posidonienschiefer repräsentiert das „Toarcische Anoxische Ereignis“ (T-OAE). Eine negative Kohlenstoff-Isotopenexkursion (CIE; ~183 Myr) tritt im unteren Teil des T-OAE auf. Untersucht wurde Posidonienschiefer in einem aktiven Steinbruch (Dormettingen; Schwäbische Alb) und in einem Bohrkern aus dem Grundgebirge des NAFB (Salem; Deutschland).

Der Posidonienschiefer in Dormettingen ist etwa 10 m mächtig und wurde anhand von 56 Proben untersucht. Geochemische Redox-Indikatoren belegen anoxische Verhältnisse innerhalb der photischen Zone. Das Maximum der Sauerstoff-Reduktion wurde während der CIE nach Ablagerung des "Unteren Steins" erreicht. Biomarkerdaten deuten auf eine erhöhte Aktivität diazotropher Cyanobakterien hin. Die sauerstoffarmen Bedingungen setzten sich, wenn auch in geringerer Intensität, nach der CIE fort. Alle untersuchten organischen Verbindungen spiegeln die negative CIE wider. Die negative Exkursion für organische Kommponenten, die von mariner Biomasse abstammt (kurzkettige *n*-Alkane, Pristan und Phytan), schwankt zwischen 4,5 und 5,0 ‰. Dies ist der höchste Wert, der bisher im Toarcium beobachtet wurde. Die $\delta^{13}C$ Werte von Pristan und Phytan erreichen ein Minimum nahe der Basis des CIE-Intervalls und steigen im oberen Bereich an. Die maximale negative Isotopenverschiebung erfolgte daher vor der stärksten Beckenabschnürung. In Dormettingen ist der Posidonienschiefer unreif bis marginal reif.

Im Salem ist der Posidonienschiefer ebenfalls etwa 10 m mächtig. Die unteren 7,5 m und der oberste Teil des darunter liegenden Amaltheentons wurden anhand von 62 Kernproben untersucht. Im Gegensatz zu anderen Toarc-Profilen sind die TOC-Gehalte in den Sedimenten der CIE hoch, in den darüberliegenden Sedimenten aber noch höher. Die Biomarkerdaten

deuten darauf hin, dass dies starke Sauerstoffverarmung während der CIE (*elegantulum* bis untere *elegans*-Subzone), aber auch während der *falciferum*-Subzone widerspiegelt. Während der untere Teil des Posidonienschiefers (*tenuicostatum* Zone bis *elegans* Subzone) deutlich geringmächtiger ist als in benachbarten Profilen (z. B. Dormettingen), ist sein mittlerer Teil (*falciferum* Subzone) ungewöhnlich mächtig. Dies deutet darauf hin, dass eine verstärkte Subsidenz zu den anoxischen Verhältnissen beigetragen hat, und deutet auf erhebliche Veränderungen der Beckengeometrie waährend des Toarciums hin. Obwohl das CIE-Intervall sehr dünn ist, bestätigen die $\delta^{13}C$-Werte der *n*-Alkane den zeitlichen Abstand zwischen der maximalen negativen Isotopenexkursion (unterhalb des "Unteren Steins") und der stärksten Beckenabschnürung (oberhalb des "Unteren Steins"). Darüber hinaus erfolgte der Beginn der CIE für aquatische Organismen früher als für terrigene. In Salem ist der Posidonienschiefer thermisch reif und ein ausgezeichnetes Öl-Muttergestein. Das residuale Ölpotential beträgt 0,8 t Kohlenwasserstoffe/m².

Acknowledgements

Firstly, I give thanks to God for the realisation of this academic milestone, having kept me physically and mentally sound and secured throughout his turbulent times.

This thesis would not have been successful without the invaluable support of my supervisor, Univ.-Prof. Dr. Reinhard F. Sachsenhofer, and for this reason, my foremost appreciation and gratitude goes to him. I equally want to sincerely thank my mentor Assoc. Prof. Dr. Doris Groß together with Dr. Achim Bechtel for their great assistance in the organic petrography, biomarker, and stable isotope laboratories. Prof. Dr. David Misch is also thanked for his constant academic and expert contributions throughout this thesis.

Special thanks to our laboratory technician Günter Nobis for analytical support which led to the reliable data set that this thesis is based on. In addition, I am immensely grateful to the following co-authors for their significant contribution into this thesis: Dr. Francesca Galasso (Senckenberg Forschungsinstitut und Naturmuseum Frankfurt), Dr. Elke Schneebeli-Hermann (Universität Zürich), Dr. Johann Schnyder (Sorbonne Université, Paris), Dr. Silvia Omodeo-Salé (University of Geneva), Prof. Dr. Andrea Moscariello (University of Geneva), Dipl. Ing. Verena Meier (Charles Univesity Prague) and Dipl. Ing. Jonathan Oriabure (Montanuniversitaet Leoben). Prof. François Baudin (Sorbonne Université, Paris) and Dipl. Ing. Boris Jammernegg (Montanuniversitaet Leoben) are also thanked for experimental and scientific contribution.

Journal reviewers such as W. Rübsam and an anonymous reviewer as well as editorial comments by U. Riller (International Journal of Earth Sciences), P. Hackley and B. Katz (Marine and Petroleum Geology) are greatly thanked for constructive reviews.

I say thank you to my close colleagues and friends of Montanuniversitaet Leoben including but not limited to our wonderful secretary Alexandra Schellich, as well as Vusala Aghayeva, Hafidz Noor Fikri, Xiangyun Shi (aka Mia), Lukas Skerbisch, Joel Bensin, Petra Sleziakova, for their moral and academic assistance to this thesis.

I further want to acknowledge the motivational encouragements from friends such as Esther Gichumbi, Elvis Ayaba, Gael N. Nkwain, Ayaba Abendong …, to whom I say thanks. To my lovely girlfriend (Temgoua N. Maelle Cindy), I say a big thank you for always being there and providing support in your prayers, showers of love, and finances especially during the final phase of this PhD study.

Lastly, I want to express my deep appreciation to my mother (Deborah Achitoh), my siblings (Helen A. Ajuaba, Cletus A. Ajuaba, Comfort Ajuaba, Andre A. Ajuaba, Napthali Ajuaba, and Gwendoline E. Ajuaba), to my lovely daughter (Sensteph J. Ajuaba) and the entirety of the extended AJUABA family for their ceaseless prayers, moral and financial support throughout my educational career and especially during these challenging periods of my doctoral studies that was partly marred by the Covid-19 pandemic.

This work is particularly dedicated to my late father Mr. Ajuaba Stephen who would have wanted nothing less than this type of milestone achievements for all his lovely children.

Inhaltsverzeichnis

General Part of thesis

1 Introduction

For centuries, humans have been applying their knowledge (of science) to understand and extract vital resources from the earth. However, organic geochemistry as we know today is said to have started in 1936 with Treibs' recognition of macro-molecules called petroporphyrins, derived by loss of phytol from chlorophyll and substitution of magnesium (Mg) with vanadium (V) and nickel (Ni) consequently forming indisputable biological signatures in ancient shales (Treibs, 1936). This was followed by series of research that culminated in the 1960s when it was understood that specific organic compounds when connected to specific biological source can tell us about the nature of primitive life irrespective of recognisable fossils and also the concept that petroleum is a product of thermally altered biological remains (Tissot and Welte, 1984; Brocks and Summons, 2003; Naeher et al., 2022; Volkman, 2022).

Organic geochemistry can therefore be defined as the study of the sources and fates of organic matter in geological materials such as sediments, coal, peat, oil, and gas (Volkman, 2022). The knowledge and techniques obtained in this discipline have a wide range of application including studies of aquatic environment, food web relationships by employing lipid "signatures" and stable isotopes, bioavailability, mobility, and distribution of pollutants in the environment, and even on extra-terrestrial studies (Volkman, 2022).

Organic matter-rich rocks also known as source rocks encountered in sedimentary successions have been widely studied for various reasons including their being good repository for ancient environments. However, the main reason has been due to their importance in hydrocarbon exploration as it is the key element in establishing the certainty of a petroleum system (conventional or unconventional) (Magoon and Dow, 1994). A source rock is defined as any fine-grained organic-rich rock capable of generating petroleum giving sufficient exposure to heat and pressure. Its generating potential is directly related to its volume, organic richness, and thermal maturity. The organic richness is determined by the amount and type of organic matter contained within the rock while thermal maturity refers to a source rock's exposure to heat over time (Tissot et al., 1987). The heat increases with burial depth (which is the main controller of source rock maturation). Maturation can also be influenced by local or regional heat flow from crustal tectonics, proximity to igneous bodies and natural radioactive decay in the crust. This thermal transformation causes the source rock to generate hydrocarbon. The generated hydrocarbon contained in the source rock gets expelled in a process called primary migration which depends on the following inter-related parameters: abundance and distribution of organic matter, kerogen maturity, and compaction of source rock (porosity reduction). The organic content in the source rock is a key factor and it is controlled largely by biologic productivity, sediment mineralogy and oxygenation of the water column and sediments (Tissot and Welte, 1984).

Many hydrocarbon source rocks are organic-rich argillaceous carbonates (typically marls) or shales. While black shales are the principal source-rock that this work is focused on, coal and coaly sediments constituted a subset of the studied samples.

1.1 Aims and structure of the thesis

Organic matter-rich rocks are excellent archives for ancient sedimentary systems because they provide a highly undisturbed geological repository. This has given scientists the opportunity over many years to investigate these sedimentary deposits for an understanding of the rock contents both for economic reasons (hydrocarbon source rock) and to know the state of the past environments and the different factors affecting their changes.

The main aim of the thesis is to reconstruct the depositional environment of Carboniferous coals, Permian lacustrine shales, and the Jurassic (Toarcian) Posidonia Shale. The data are also used to quantify the petroleum potential of these stratigraphic units, which are considered as potential hydrocarbon source rocks in the western (Swiss and German) part of the North Alpine Foreland Basin (NAFB).

The latter aspect is also important to properly evaluate the risk for geothermal exploration activities as well as for radioactive waste disposal (storage) at the designated location in the Swiss sector of the NAFB. In both cases, the presence of hydrocarbons would have a very harmful influence (Moscariello, 2019; Moscariello et al., 2020; Omodeo-Salé et al., 2020 and reference herein).

Apart from biomarker patterns and bulk carbon isotope data, compound-specific carbon isotope ratios are used as a novel, hitherto little-used approach to contribute to the understanding of depositional environments, and to form the base for future oil-to-source correlation.

The present thesis is a cumulative work consisting of three individual scientific publications (Publications I to III in sections 8 to 10), preceded by a general introduction into the topic (chapter 1) and an introduction to the geological setting of the Central European Epicontinental Basin and the North Alpine Foreland Basin.

Publication III (section 10) is based on a core from borehole Salem (Amaltheenton and Posidonia Shale). Core photographs and SEM pictures have been taken and CT scans were made from this core but could not be included in the journal article due to space limitations. For a complete documentation of the core, these data are included in Appendix I to III at the end of the thesis.

1.2 Depositional environment of black shales (silled basin, upwelling, marine-lacustrine)

Shale is a fine-grained sedimentary rock consisting of more than fifty percent silt and clay-size minerals also known as mud (Tissot et al., 1987). Black shales have been defined as any dark coloured mudrock with organic matter that is capable of generating hydrocarbons naturally or by pyrolysis. Their formation and deposition have a global expression and in every part of the earth's geologic history. Black shales tend to be significantly more enriched in metallic deposits compared to regular shales and sometimes play the role of a host rock for syngenetic metal deposits (Tourtelot, 1976). See section 2.1 for detailed explanation.

Black shale deposition is strongly controlled by basin evolution and paleogeography. Their spatial and temporal distribution is connected to their environment of accumulation and other environmental variables, such as redox conditions, salinity, climate, availability of nutrient, etc.

Though present in different stratigraphic levels, global black shale events, so-called Oceanic Anoxic Events (OAEs), are especially abundant in the Mesozoic record (Jenkyns 2010, 2018 and references therein; Nozaki et al., 2012, Phelps et al., 2015; Boulila and Hinnov 2017; Jenkyns et al., 2017; Joo et al., 2020; Kemp et al., 2020; Uveges et al., 2020; Bonacina et al., 2021 and references therein). Different models have been put forward to describe the basin evolution and black shale deposition especially in the Central European Epicontinental Basin Sytems (Röhl and Schmid-Roehl, 2005).

This concept of OAEs was first delineated by Schlanger and Jenkyns (1976) based on the results of a deep-sea drilling project in the Pacific Ocean. Since then, it has been widely studied. Researchers have recognized OAEs in the Paleozoic, Mesozoic and Cenozoic Era (Table 1; after Singh et al., 2022) and related them to ocean-wide depletion of oxygen contents (e.g., Schlanger and Jenkyns, 1976; Jenkyns, 1980, 1988, Jenkyns et al., 2004; Jenkyns, 2010). These OAEs gave rise to prolific petroleum source rocks (up to 30% organic carbon content) that were deposited in different transient episodes punctuating the Mesozoic Era and studies have shown that, more than 50% of known global hydrocarbon deposits have their source rocks deposited during anoxic events (e.g., Arthur and Schlanger 1979; Klemme and Ulmishek 1991; Sageman, 2006). Research work has shown that on a global scale, changes in the paleoclimate and ocean water chemistry as well as perturbation in the global carbon cycle are well recorded in the OAEs (Jenkyns 2010; Jenkyns et al., 2017; Ruebsam and Schwark 2021 and references therein). Many OAEs habe been associated with large igneous provinces (LIP, Fig. 1) leading to mass/marine extinction events, (e.g., Ernst and Youbi 2017; Harries and Little 1999; Pálfy and Smith 2000; Dera et al., 2010; Caruthers et al., 2013). OAEs can be characterised sedimentologically and geochemically.

Table 1 Examples of global studied locations of Oceanic Anoxic Events (OAEs) in the Mesozoic and including related studies in the Cenozoic and Paleozoic

Era	Geologic time (age in Ma)	Examples of Studies Performed
Cenozoic	Middle Miocene (15.6-16) Early Oligocene (29-31) Oligocene-Miocene (39-23)	Kidder and Worsley 2010 (Columbia River Basalt) Kidder and Worsley 2010 (Ethiopian Highlands) Kokh et al. 2021 (Kerch Peninsula, Ukraine)
Mesozoic	Toarcian OAE (183)	Suan et al. 2008 (Lusitanian basin, Portugal); Gröcke et al., 2011 (Toyora area, Japan); Izumi et al. 2012 (Yorkshire); French et al. 2014 (Yorkshire, Germany, Italy); Huang and Hesselbo 2014 (Andean Basin, Chile, South-America); Fantasia et al. 2018 (Sakuraguchi-dani section, Japan); Kemp et al. 2020 (Trans-danubian Range, Hungary); Főzy et al., 2010 (Vocontian Basin, France); Duchamp-Alphonse et al. 2011 (Italy); Arora et al. 2015 (Juran Formation, India)
	Late Valanginian OAE (136.4)	Najarro et al. 2011 (North Spain); Moiroud et al. 2012 (Baltic Cordillera, SE Spain); Bottini et al., 2012 (Southern Alps, New Zealand)
	The Hauterivian OAE (130)	Kuypers et al., 2002 (North Atlantic Ocean of the coast of Florida and the Ravel section of the Southeast France); Khan et al. 2021 (Mughal kot section, Pakistan); Coccioni et al. 2012 (Poggio le Guaine section Umbria-mache basin, Italy)
	Early Aptian OAE 1a (120)	Li et al. 2016 (Southern Tibet, China); Karakitsios et al. 2010 (Greece); Bastos et al. 2020 (N-E Brazilian basin, Brazil), Sanchez-Hernandez and Maurrasse 2016 (Organya basin spain); Li et al. 2008 (Cismon Apticore in Italy, Santa Rosa Canyon in north-eastern Mexico, and Deep Sea Drilling Project Site 398) Matsumoto et al. 2020 (Poggio le Guaine, PLG, record, central Italy and Spain)
	Early Albian OAE 1b (112)	Mort et al. 2007 (Italy and Spain); Kellar et al. 2008 (Tarfaya Basin of Morocco); Tsiko et al. 2004 (Eastbourne, England, Gubbio, Italy, Tarfaya, Morocco); Tiwari et al. 1996, Nagendra and Reddy 2017, Bansal et al. 2018 (Cauvery basin, India)
	Cenomanian-Turonian OAE (99.6–93.5)	Wang et al. 2001 (Southern Tibet); Kassem et al. 2020 (Central Gulf of Surez, Egypt); Bomou et al. 2013 (Tibet); Voigt et al. 2008 (Wunstorf section, North Germany); Duque-Botero et al. 2009 (Indidura Formation, Mexico, Furlo in the Marche–Umbrian Apennines of Italy); Owens et al. 2017, Lenniger et al. 2014 (Axel Heiberg Island, Canada); Al-Sagri, 2015 (Gulneri Formation, Northern Iraq); Jenkyns 2018 (Cismon, North Italy, South Provence Basin, Southeast France Iberian Margin, Site 39); Keller et al., 2021 (Western Narmada basin, India)
	Coniacian-Santonian (93.5)	Sachse et al. 2012 (Tarfaya Basin, Morocco); Andjic et al. 2018 (Loma Chumico Formation of N-Costa Rica); (Tunisia, Africa); Heath et al. 2021 (English river formation, Illinois, US)
Paleozoic	Devonian (419.2–358.9)	Buggisch, 1991b(France, Australia); Kabanov 2019 (Mackenzie platform, Canada); Langsford 2020 (South Australia)
	Carboniferous (358.9–323.2)	Cheng et al. 2020 (Nevada, USA)

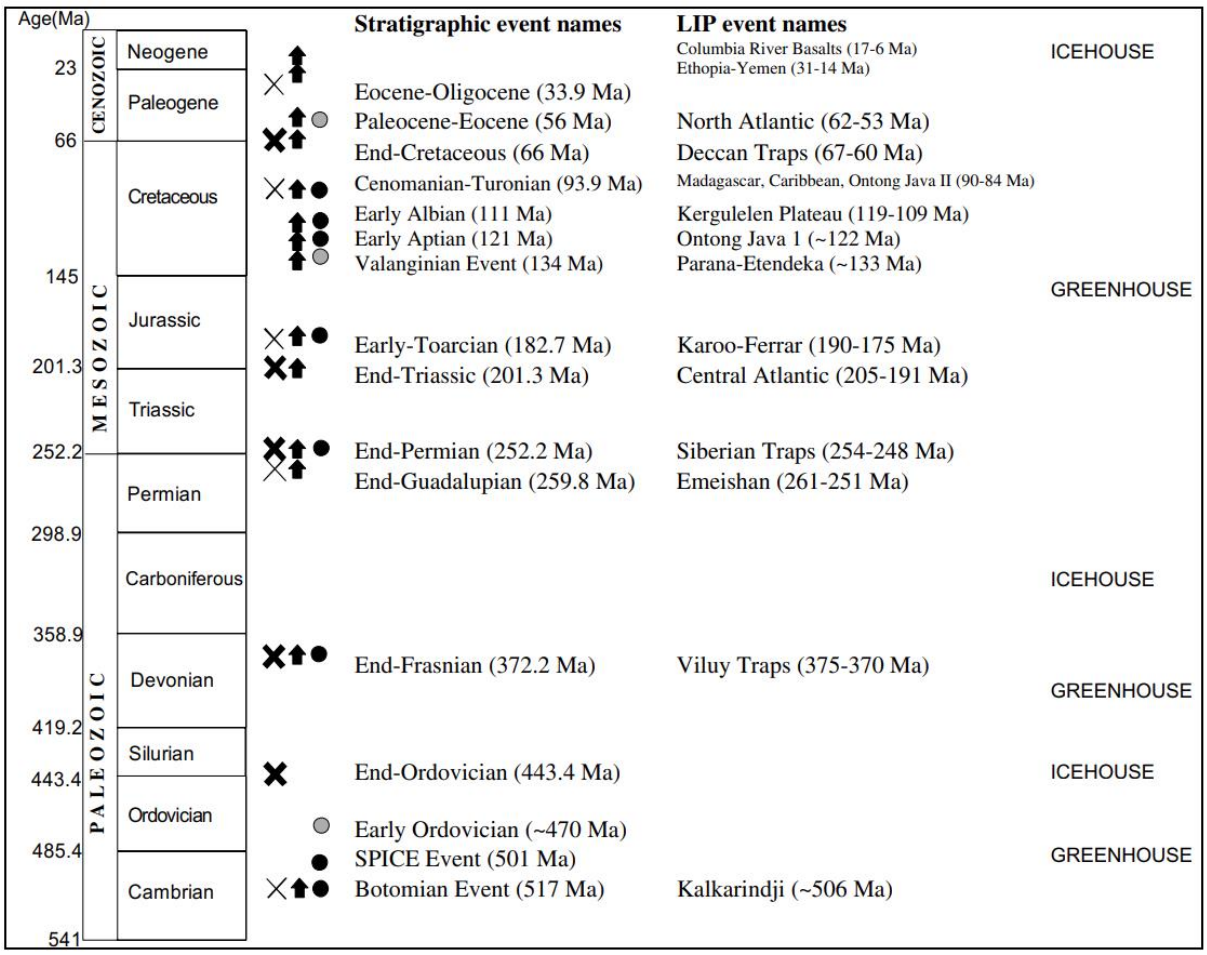

Fig. 1 Temporal correlation of LIPs with OAEs and/or extinction events. Symbols key: arrow represents LIP, filled circle represents OAE, bold cross represents major mass extinction and normal cross represents minor mass extinction (taken from Percival et al., 2015).

Sedimentary characteristics include the presence of grey, dark green to black coloured fine-grained shales comprising of alternative transgressive and regressive sedimentary facies that are laminated and with relatively high amount of total organic content (TOC) that is associated with the perturbation in the global carbon cycle. The trigger and forcing mechanism controlling this carbon perturbation during the OAEs remains highly debated. However, during this time, high temperatures and an enhancement of the hydrological cycle resulted in strong (six-fold) increased global weathering rates (Cohen et al., 2004; Kemp et al., 2020, Ajuaba et al., 2022). OAEs are suggested to have been caused by one or a combination of factors such as changes in the sea level (eustasy), tectonic and volcanic activities, dissociation of gas hydrates as well as asteroid impacts (Schlanger and Jenkyns 1976; Jenkyns et al., 2004; Jenkyns 2010; Pandey and Pathak 2016 and references therein; Jenkyns et al. 2017; Jenkyns 2018; Kemp et al. 2020; Bonacina et al. 2021) which could be responsible for the increased global temperature along with enhanced hydrological cycle, increased global weathering, enhanced nutrients supply and upwelling, and augmented organic productivity (Schlanger and Jenkyns 1976; Arthur and Sageman 1994; Larson and Erba 1999; Leckie et al. 2002; Weissert and Erba 2004; Jenkyns 2010; Jenkyns et al. 2017;

Kemp et al. 2020; Bonacina et al. 2021). Their lithology varies from shales to carbonates. Current ripples and hummocky cross stratification are also observed (Krencker et al., 2019). The main indicator for the occurrence of an OAE is the presence of high amounts of organic carbon (Tsikos et al., 2004). The Mesozoic is characterised by three major OAEs (Jenkyns 1999), globally comprising of similar pelagic black shales classified within a biostratigraphic interval of 1 Ma or less (e.g Schlanger and Jenkyns 1976; Weissert 1989; Jenkyns and Clayton 1997). On the contrary, at local scales, the sedimentary facies may strongly vary to an extent where sediments may be void of organic matter indicating the effect of organic productivity (Jenkyns 2010 and references therein). Still in the Mesozoic Era, while the Cretaceous have recorded several OAEs with a global outreach, only one has been reported for the Jurassic (Early Jurassic) called the Toarcian OAE (e.g, Schlanger and Jenkyns 1976; Coccioni et al. 1987; Jenkyns 1988, 2010; Hesselbo et al. 2000, 2007; Leckie et al. 2002; Baudin 2005; Cohen et al. 2007). In the early Jurassic sedimentary record of the T-OAE, the global characteristic distinction is that the black shales are rich in organic matter and display negative carbon isotope excursion ($\delta^{13}C$) (Jenkyns and Clayton 1997; Cohen et al. 2004; Hesselbo et al. 2007; Suan et al., 2008; Hermoso et al. 2009; Bodin et al. 2010).

Geochemically, total organic carbon (TOC), hydrogen index (HI), oxygen index (OI), molecular fossils (biomarkers), especially strains of green sulphur bacteria, and other major and trace elements (e.g., V, Ni, Mo, U) play a crucial role in characterising black shales as well as support the indication of OAEs. Isotope signature ratios of oxygen/nitrogen and magnesium/calcium show specific trends during OAE (Higgins et al., 2012). In marine sediments, high phosphorus concentrations are often indicative for OAEs (Ingall et al., 1993; Van Cappellen and Ingall 1994; Colman et al., 1997; Colman and Holland 2000).

1.3 Biomarkers and their applications in geosciences

Biological markers commonly referred to as biomarkers have been defined with slight nuances as follows: 1) Complex molecular fossils from biochemicals, particularly lipids, in once-living organisms. 2) Groups of compounds (primarily hydrocarbons) present in oils, and rock extracts, recent sediments, and soil. 3) Compounds with a distinctive chemical structure that can be related to specific organisms (e.g., Peters et al., 2005; Volkman, 2022).

Biomarkers from the geochemical viewpoint are products of diagenetic alterations of specific compounds produced by ancient living organisms. They commonly retain all or most of the original carbon skeleton of the original natural product giving them structural similarity that makes them to be termed molecular fossils (Peters et al., 2005).

Biomarker strains of the hydrocarbon compound class can be readily extracted and measured using gas chromatography mass spectrometer (GC-MS) techniques. Other important compound classes (alkenones, alkyl diols, and tetraether lipids) require different measuring techniques. In general, the scope of application is in-exhaustive considering more compound classes such as fatty acids, sterols, triterpenoids, carotenoids, porphyrins, amino acids, etc. While hydrocarbon compounds in their variety of structural forms make good proxies for organic matter sources, alkenones serves as good paleo-temperature and paleo pCO_2 proxies while alkyl diols as good paleo-temperature and salinity proxies. The isoprenoid glycerol

dialkyl glycerol tetraethers (commonly called GDGTs) are proven compounds and a new proxy used for paleo-temperature correlation studies however with a totally different technique developed to measure their biomarkers using a combination of normal-phase high performance liquid chromatography (HPLC) with positive ion atmospheric pressure chemical ionisation mass spectrometer (APCI-MS) (Hopmans et al., 2000). Work is still being done on the branched GDGTs compound class to establish the specific bacterial sources and other environmental variables (Volkman, 2022).

Biomarkers are of remarkable importance in the study of geological environments since specific biomarkers have been used as proxies to provide valuable information such as evidence of ancient microbial life in rocks formed hundreds of millions of years ago ("early life"), and records subsequent episodes of mass extinction within the geologic record (e.g., Whiteside and Grice 2016). However, the greatest application of biomarkers in the geosciences has been in the petroleum industry notably during the exploration phase. Examples of such applications include:

1) Oil-source rock (in case the oil and candidate source rock are available) or oil-oil correlations. To determine whether particular oil comes from a specific source rock or if two or more oils have the same source, designated maturity parameters and "fingerprinting" techniques are applied to establish their relation (Peters et al., 2004).
2) Biomarkers provide important information on the organic matter source such as if the source depositional environment is lacustrine or marine, of shale or carbonate lithology, fluvio-deltaic or hypersaline and, if the environmental condition during deposition is oxic or anoxic.
3) Biomarker parameters can be used to determine the thermal maturity experience range from immature to post-mature, generating the different hydrocarbon constituents and in the case of oil sample the relative amount of oil-prone versus gas-prone organic matter in the source kerogen (e.g., Peters and Moldowan, 1993).
4) Due to their general resistance to weathering, biodegradation and evaporation, biomarkers are used to determine hydrocarbon contamination in the environment.

All the above-mentioned applications serve as important input data for an effective user-friendly basin or field modeling that can influence the overall hydrocarbon production and also make the environment greener.

1.4 Bulk and compound-specific carbon isotopy (CSI) and their applications

Stable isotopes of elements such as carbon, hydrogen, nitrogen and to a lesser extent sulphur and oxygen play an important role in organic geochemistry especially with regards to the application of the isotopy of bulk organic matter and specific organic compounds in understanding biogeochemical processes. Geochemists have been the pioneers and at the forefront in using and developing measuring instruments such as gas chromatography isotope ratio mass spectrometer (GC-irMS) although continuous progress is still being made in this

field of stable isotope geochemistry. Of all the above-mentioned stable isotopes, carbon and hydrogen have been of particular interest especially carbon. This is simply due to the importance of this discipline in the petroleum industry where together with biomarkers and other geochemical methods, these stables isotopes play a crucial role in determining the genetic relationship among oils and bitumen (Pedentchouk and Turich 2017). Due to the dominant occurrence of carbon in the chemical and structural composition of petroleum, and since more is known about its bulk and compound-specific isotopy, stable carbon isotope is the most applied among the other stable isotopes in research works. Compound-specific isotope data of carbon and hydrogen have been a very useful tool in petroleum exploration (Pedentchouk and Turich 2017).

An isotope is defined as atoms of the same element with a nucleus consisting of the same number of protons but different numbers of neutrons (Fig. 2). Bulk organic matter isotope signature is the weighted mean of all its constituents as different compounds have been found to have different isotope signatures. On the other hand, compound-specific isotope refers to the isotopic signature of specific organic compounds (Volkman, 2022).

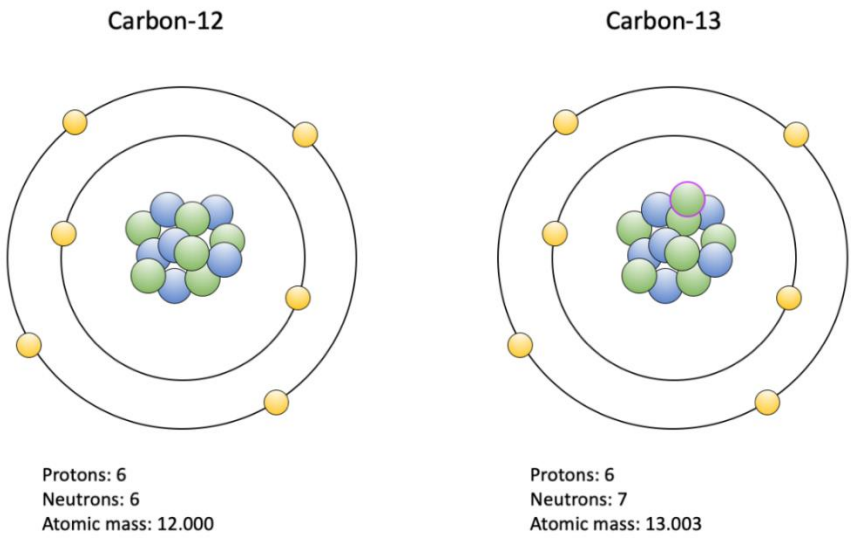

Fig. 2 Subatomic composition of two stable carbon isotopes

Stable Carbon-12 and Carbon-13 account for 98.89 and 1.11 wt.% of the entire natural carbon respectively with the remaining trace fraction belonging to the unstable (radioactive) Carbon-14. Due to its half-life of ~5730 years, ^{14}C is naturally absent in or less reliably measured in petroleum samples older than ~50000 years except in cases of contamination. This leaves us with ^{12}C and ^{13}C stable isotopes. In general, stable isotope data are expressed in delta notations (δ) representing deviations in parts per thousand (‰, per mil, or ppt) from an accepted standard (Hoefs, 2009 and references therein).

$$\delta\ (‰) = [(R_{sample} - R_{standard}) / R_{standard}] \times 1000$$

where R stands for isotope ratio abundance (e.g, $^{13}C/^{12}C$, $^{2}H/^{1}H$, $^{15}N/^{14}N$). In describing the carbon isotope composition in organic matter, the variation in relative abundance in ^{13}C is used. A negative (or comparatively more negative) δ values would indicate the organic matter

is depleted in ^{13}C isotope relative to the standard (commonly the Vienna Pee Dee Belemnite standard) while a positive (or comparatively less negative) values implies the organic matter is enriched in ^{13}C.

Stable carbon isotope ratios can help to understand and characterise source rocks, oils, and natural gas simply by looking at their isotope signatures which gives an idea of their biosynthesis and consequently the origin of the carbon in their structure and original habitat of the organism. For example, lipids that are highly depleted in ^{13}C isotope with isotope ratios in the range of -40 to -80‰ are normally associated with methane-oxidizing bacteria (methanotrophs) as opposed to ^{13}C enrichment values from -8 to -15‰ that is commonly associated with algae growing in carbondioxide restricted environment such as *Tasmanites* or diatoms in sea ice as well as organisms that can synthesise HCO_3^- such as *Botryococcus* (Hoefs, 2009 and references therein). C_3, C_4 or CAM (crassulacean acid metabolism) plants can be distinguished using the different carbon isotope composition of their lipids given their biosynthetic pathways is different (Volkman, 2022).

2 Geological Setting

The Lower Jurassic Posidonia Shale deposited in the epicontinental Central European Basin and Permo-Carboniferous coals and non-marine shales in the basement of the North Alpine Foreland Basin have been studied in the present thesis. Therefore, both the Central European Basin and the North Alpine Foreland Basin are briefly described in this section.

2.1 The Central European Epicontinental Basin (CEB)

During the Triassic and Jurassic, central and northern Europe was widely covered by the epicontinental Central European Basin (CEB) that widened towards the Tethys Ocean in the south and the proto-North Atlantic region to the north (Röhl and Schmid-Roehl, 2005). Geochemical evidence has been used to argue for the occurrence of widespread oceanic anoxic econditions during the Early Triassic using proxies such as carbon/sulphur ratios and anomalies in cerium (Hallam 1994).

The CEB is composed of several basins separated from each other by either submarine shoals and/or islands of different sizes (Fig.3) (Ziegler 1982, 1988, Röhl and Schmid-Roehl, 2005). Amongst others, these basins include the South West German Basin, North West German Basin, Yorkshire Basin and Paris Basin.

This study, however, focuses on the late Early Jurassic in the western part of the German Molasse Basin where two case studies were considered. The first being outcrop samples from the Dormettingen/Dotternhausen section which occupies the central position within the SWGB (e.g., Riegraf et al. 1985) and drill core samples from the Salem section. The investigated sediments from both sections are Posidonia Shale of Lower Jurassic age. However, the Dormettingen/Dotternhausen is the key section in the CEBS with stratigraphic succession constituted of lower Toarcian sediments overlain by bioturbated marls that belongs to the Pliensbachian Amaltheenton Formation which is intercalated with limestone beds of tens of cm thick. In both the Dormettingen and Salem sections, the Posidonia Shale follows above the Amaltheenton Formation without any evidence of a sedimentary gap (Galasso et al. 2021; Ajuaba et al (subm.). On the contrary, the Amaltheenton Formation in the Schesslitz section approximately 260 km NE of Dotternhausen was strongly affected by erosion and shows evidence of a large stratigraphic gap and thus a discontinuos transition between Pliensbachian–Toarcian boundary (Röhl and Schmid-Roehl, 2005). The Amaltheenton Formation is succeeded by light-gey bioturbated marls intercalated by three black shale layers (Tafelfleins, Seegrasschiefer, and Fleins) having thickness ranging in several cm. The Fleins is at the base of the massive black shales deposit that represents the T-OAE. The black shale deposit is also intercalated by prominent limestone beds of several cm thick. These Limestone beds are also referred to as “marker beds” due to their regional importance in lithostratigraphic correlation. In both the Dormettingen and Salem case studies undertaken in these thesis, prominent T-CIE were observed in both the bulk organic carbon and the specific molecular fossil of *n*-alkanes, pristane and phytane. However, the thickness interval of the excursion is almost twice in the Dormettingen compared to the Salem section. While the Dormettingen/Dotternhausen is at the center of the SWGB, the Salem drill site is located

close to the southeastern basin margin, where the SWGB was separated from the Tethys Ocean by a series of islands forming the continuation of the Vindelician High (Fig. 3).

The Posidonia Shale in the SWGB has been proven to be a hydrocarbon source rocks and especially the main source rock for hydrocarbon accumulation in the Bavaria.

In all these settings, fine-grained sedimentary rocks referred to as Toarcian black shales have been deposited. They are called “Posidonia Shale” in Germany and Switzerland, “Jet Rock” in England and Schistes Carton in France. The depositional environment of these basins has been described by various authors using different models (Röhl and Schmid-Roehl, 2005 and references therein) with the most prominent being,

1) The “silled basin” model which describes a condition of restriction in water circulation in a deep-water setting like the case of the modern Black See and having an oxygenated bottom water due to separation by shoal or island barriers. This separation of the water masses results to anoxic bottom waters.
2) The “irregular bottom topography” model was supported by the concept of pronounced relief on the seafloor creating isolated depocenters with stagnant water.
3) The “expanding puddle” model describes the progression of the “irregular bottom topography” model whereby the localised anoxic bottom waters due to transgression spreads across the entire basin as the topographic depression subsides.
4) The “upwelling” model describes a condition where upwelling enhances surface water productivity due to the distribution of the oxygen-minimum layer during transgression.

These models are limited to specific black shale depositional settings as other settings around the world have been described differently.

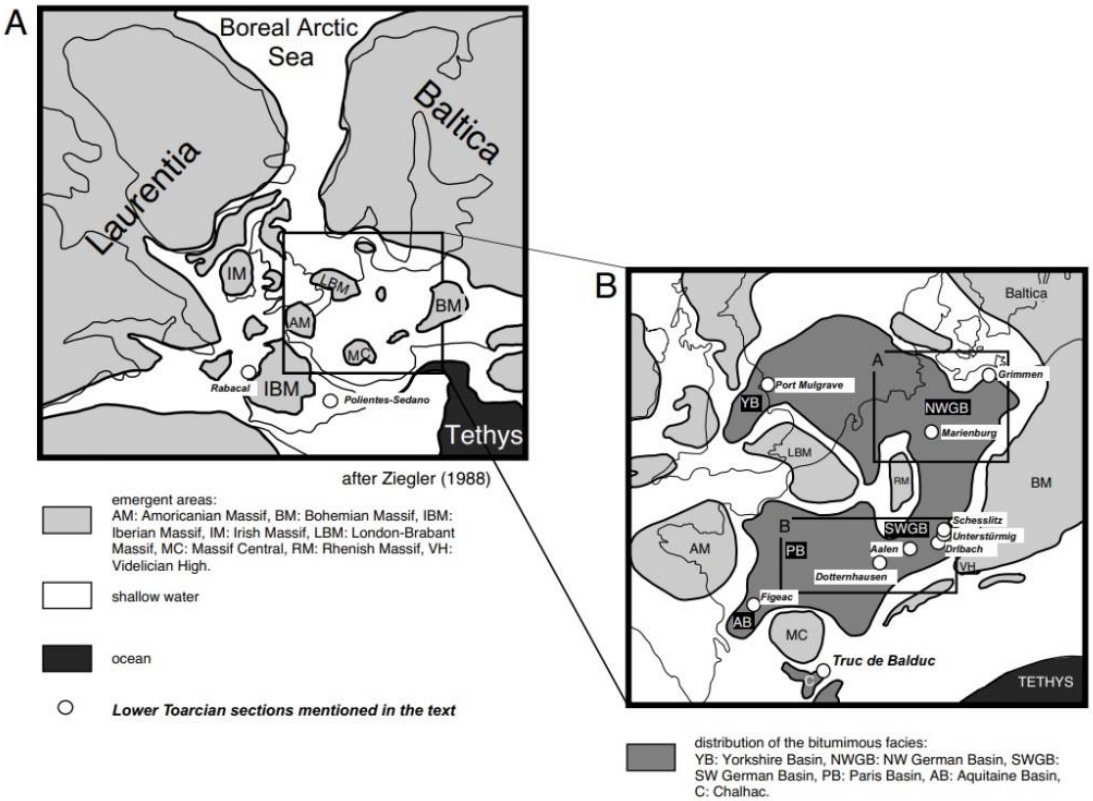

Fig. 3 Early Toarcian paleogeographic map showing distribution of black shales across Central and Western Europe (CEBs) (taken from Röhl and Schmid-Roehl, 2005).

Sedimentation rates play an important role in controlling the organic carbon content within the shale deposition. The rate and dilution effect of sedimentation can either lead to a high or low TOC values. High values would indicate moderate to high sedimentation rate and good preservation environment as opposed to low values indicating low sedimentation rate and/or organic matter dilution or degradation during sedimentation.

2.2 The North Alpine Foreland Basin (NAFB)

The North Alpine Foreland Basin (NAFB), commonly referred to as the Molasse Basin, is in Central Europe extending from Geneva (Switzerland) along the northern margin of the Alps to Vienna (Austria) with a general east-west trending orientation (Fig. 4). Cross-sections through the asymmetrical forland basin in the Austrian, German and Swiss sectors are provided in Fig. 5.

The NAFB is an economically important basin due to its oil and gas deposits and its geothermal potential (Véron, 2005; Boote et al., 2018, Misch et al., 2017). The Austrian and German sectors of the basin are minor oil and moderate gas provinces in Europe (Boote et al., 2018). Mesozoic (Posidonia Shale) and Oligocene rocks (Schöneck Fm.) are the main sources of hydrocarbon accumulations (Wehner and Kuckelkorn, 1995; Gratzer et al., 2011; Fig. 5). In contrast, a single semi-commercial gas field, probably charged by Permo-Carboniferous coals, was detected by well Entlebuch-1 in the Swiss sector (Leu, 2012; Misch et al., 2017).

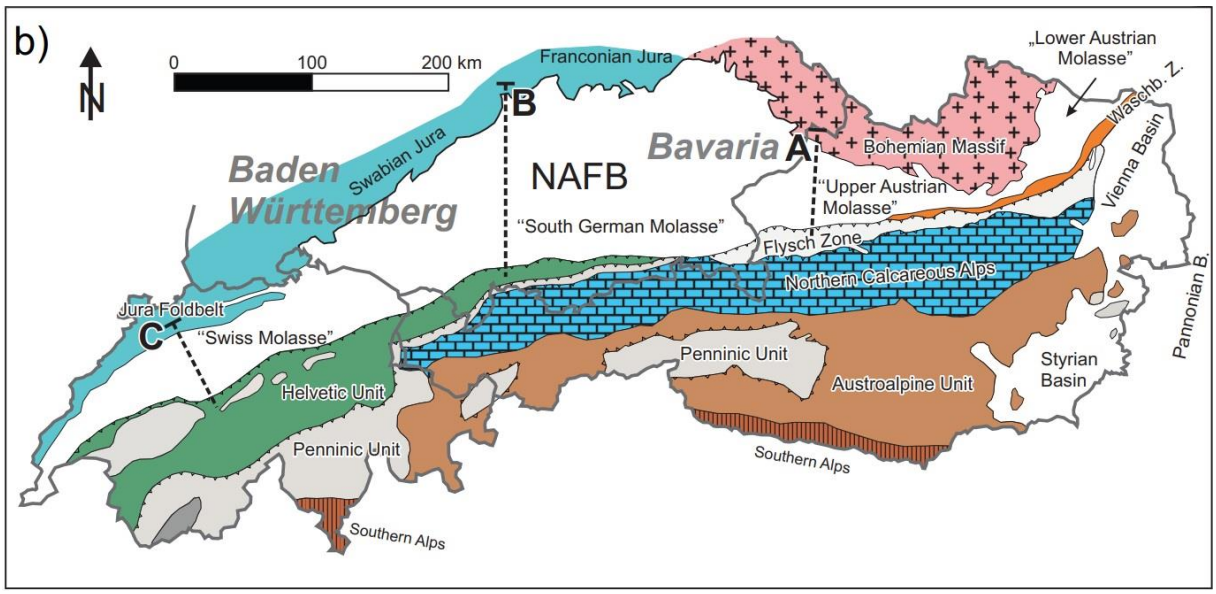

Fig. 4 The North Alpine Foreland Basin (NAFB) showing different regional settings a) Austrian sector, b) German sector and c) Swiss sector (Kuhlemann and Kempf, 2002).

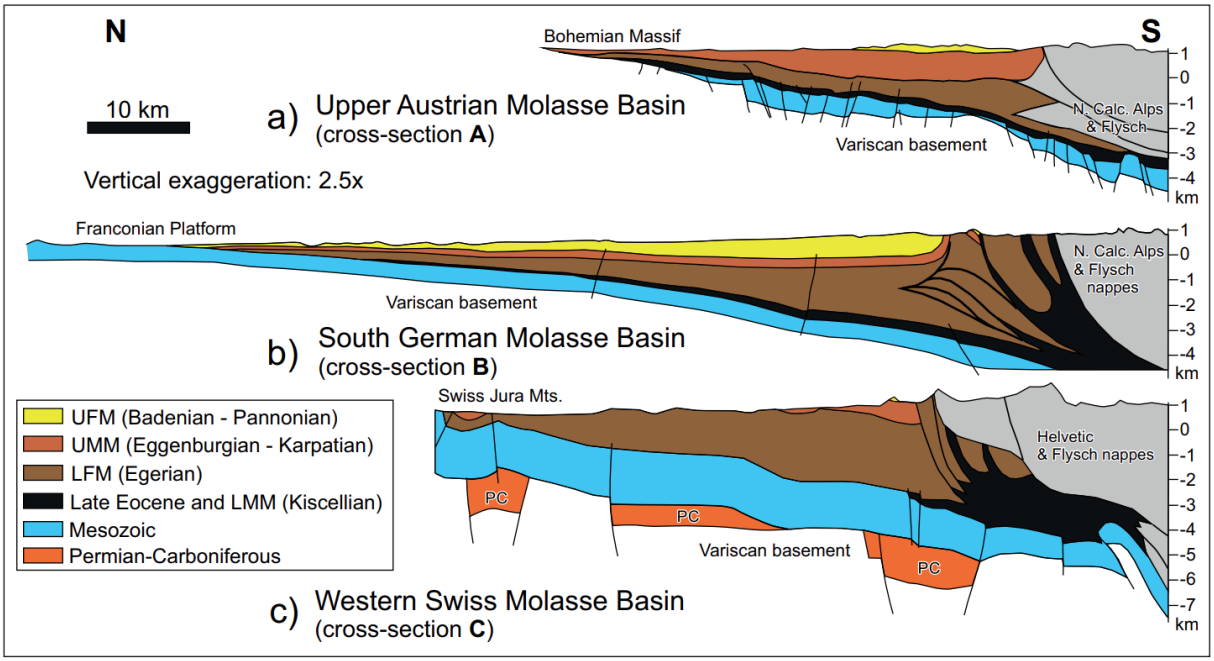

Fig. 5 North-south cross-sections through the North Alpine Foreland Basin (after Kuhlemann and Kempf, 2002). The location of profiles A, B and C is marked in Fig. 4. Note the significant north-south extent of molasse sediments in the South German Molasse Basin (section B).

2.2.1 Pre-Cenozoic Basement

Underlying the Cenozoic Molasse sediments of the NAFB is the Variscan crystalline basement (e.g., Bohemian massif) composed of metamorphic and magmatic rocks that crop out in Bavaria, SW Germany, and northern Austria (Figs. 4 & 5). Locally preserved Permo-Carboniferous sediments including disjointed coal seams filled graben structures formed at the final stages of the Variscan orogeny. The sedimentary succession overlying the crystalline basement and the Permo-Carboniferous graben sediments include mid-Triassic redbeds, carbonates, evaporites and Upper Triassic deltaic sandstones that are followed by fine-grained rocks (pelite) of Lower Jurassic age (including the Toarcian Posidonia Shale). The Middle Jurassic synrift sediments are overlain by postrift Upper Jurassic carbonates/Upper Cretaceous sediments. After a period of major erosion, Upper Cretaceous sandy and marly rocks were deposited (Fig. 5).

This thesis focuses on the elongated Permo-Carboniferous coal-baring basins that occupy the basement of the North Alpine Foreland Basin with specific case study location at Weiach in Northern Switzerland (e.g., Bachmann et al., 1987; Madritsch et al., 2018, Ajuaba et al., 2023). The Weiach-1 well is the only well that penetrated the Permian and Carbonifeous sediments that make the graben sedimentary infill in northern Switzerland with the Constance-Frick Trough (CFT) being the graben structure with the most in-depth studies (Diebold et al., 1991; Laubscher, 1987; Madritsch et al., 2018; Moscariello et al., 2021). Madritsch et al. (2018) provided a detail description of the basin architecture and evolution of the CFT where the authors explained that the 10-12 km wide CFT is made up of two segments likely with opposing half-graven geometries. The shallower segment is Weiach to the east while the deeper segment is Riniken to the west. The basin fill was also divided into three; the lower, middle, and upper trough fill corresponding to the Upper Carboniferous, Lower and Upper Permian clastic successions respectively (Matter, 1987; Madritsch et al., 2018). Permission to collect the samples used for this section of the thesis was granted by Swisstopo. The Carboniferous (Stephanian) is comprised of coal and shale series while the Permian ("Autunian") is characterised of lacustrine shale series. The Permian lacustrine shales (at the basement of the NAFB) together with the Toarcian Posidonia shales (in the NAFB) have been presented as potential source rocks for oil in the western part of the NAFB (Schegg and Leu, 1998; Veron, 2005; Leu, 2014; Misch et al., 2017; Moscariello, 2019; Do Couto et al., 2021).

Triassic and Jurassic sediments of the CEB continue southwards and are also found in the basement of the NAFB (see description above). Examples of black shales outside of the CEB include the black shales of the Lower Cretaceous Bazhenov Horizon in the Tutleim Formation, southwestern West Siberian Basin (Burnaz et., 2022). The organic matter-rich black shales were deposited during the Upper Jurassic - Lower Cretaceous period and in a marine deposional environment dominated by organic matter of aquatic and bacterial origin with minor contribution from higher land plants. In the sections where anoxia or euxenia was evident, there was the corresponding lowest amount of terrigenous input suggesting a relationship to the eustatic transgression-regression cycles (Burnaz et., 2022).

2.2.2 Cenozoic basin fill

This Cenozoic fill of the NAFB includes Upper Eocene to Upper Miocene sediment. In the Swiss and German sectors of the basin (west of Munich) the basin fill is traditionally subdivided into a Lower Marine Molasse (LMM; Eocene to Lower Oligocene), the Lower Freshwater Molasse (LFM; lower Oligocenen to lower Miocene), the Upper Marine Molasse (UMM; lower Miocene) and the Upper Freshwater Molasse (UFM; middle to upper Miocene). The Lower Freshwater Molasse is missing east of Munich (eastern part of the Basin), where marine conditions continued from late Eocene to early Miocene time.

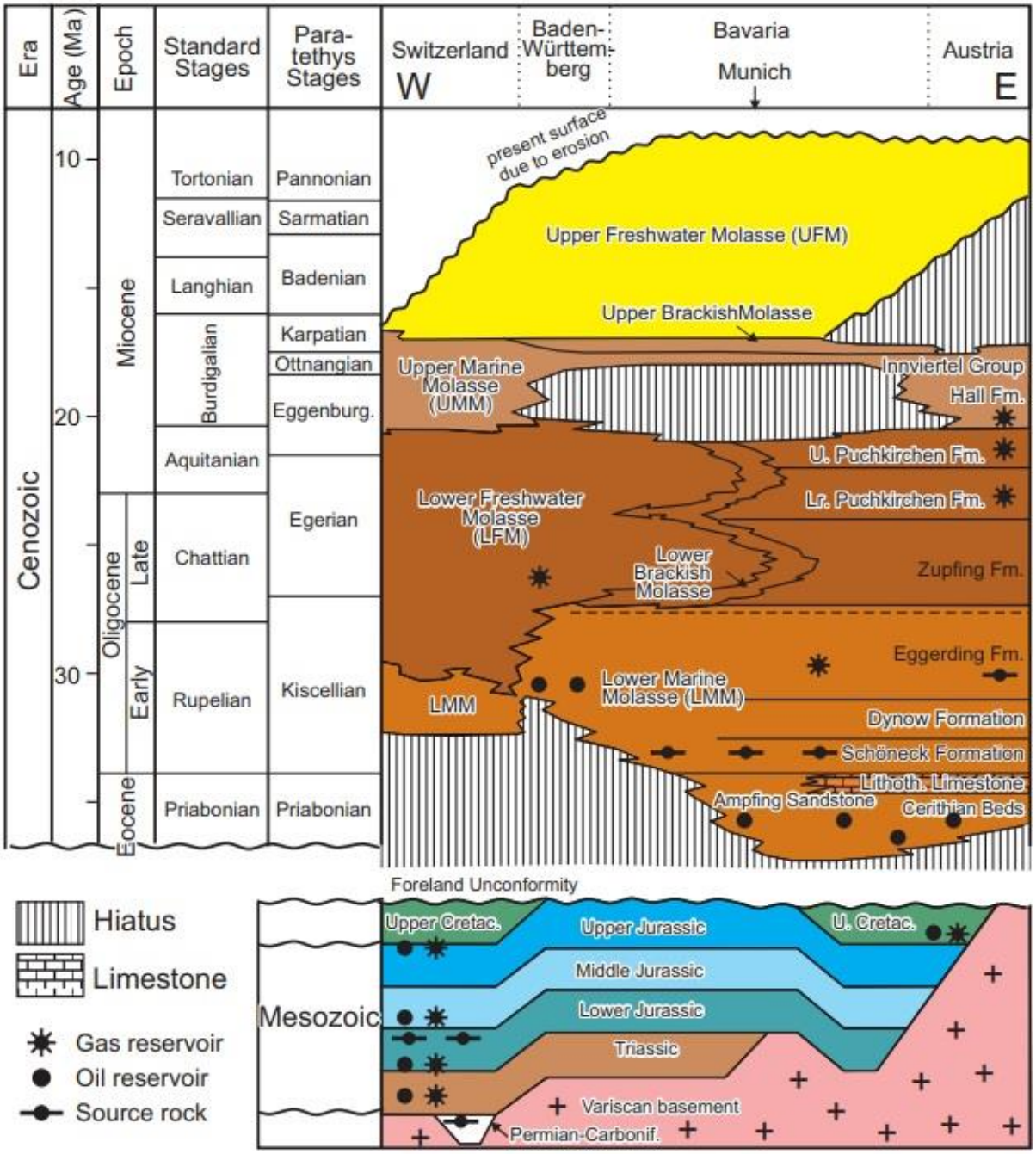

Fig. 5 Chrono- and lithostratigraphy of the North Alpine Foreland Basin (modified after GEOMOL TEAM, 2015). In the Swiss and German parts of the basin, molasse

sediments are divided into two marine members (Lower and Upper Marine Molasse) and two freshwater members (Lower and Upper Freshwater Molasse), separated by transitional brackish facies (Lower and Upper Brackish Molasse).

3 Analytical methods

A variety of analytical techniques has been applied to realise the objective of the present thesis. Table 2 provides an overview of the applied analytical techniques and the number of samples anaylzed. A detailed description of the applied techniques is provided below.

Table 2. Overview on the different analytical techniques and sample numbers.

Case Studies [Locations]	∑samples	Bulk para.	Rock Eval	Macerals	VR	Palyno-facies	Biomarkers	Isotopy	SEM	CT scans
Dormettingen	56	56	56	24	2	*	24	24	*	*
Salem	62	62	62	11	1	14	31	29	5	Yes
Weaich	90	90	90	18	7	12	28	20	*	*
Total	**208**	**208**	**208**	**53**	**10**	**26**	**83**	**73**	**5**	

*Bulk para. — bulk parameter, Rock eval — Rock Eval pyrolysis, VR — Vitrinite reflectance, SEM — Scanning electron microscope, CT — Computed Tomography, * — not performed*

3.1 Bulk geochemical analysis

Bulk geochemical parameters include total inorganic carbon, total organic carbon, and sulphur contents. Important because these parameters help us to determine if an organic matter-rich rock can be classified as a source rock.

An Eltra Helios CS elemental analyzer was used to analyse total carbon (TC; %), total sulphur (TS; %), total organic carbon (TOC; %) and total inorganic carbon (TIC) (Table 2). Broken pieces of the drill core and outcrop samples were powdered using a "FRITSCH pulverisette 2" mortar grinder and homogenized after which which 80-100 mg of powder sample was filled into crucibles. To determine the TOC, the powdered samples were later treated with concentrated phosphoric acid in a stepwise approach for approximately 10 hours and water (hot) added at each step to remove the acid. At 1350°C, the samples get incinerated in an inert condition and the resulting CO_2 and SO_2 is measured by an infrared detector. The results are given in weight percent (wt.%). Total inorganic carbon (TIC) content was derived from the difference between TC and TOC (TIC=TC-TOC) which is later applied to calculate calcite equivalent percentages.

$$Calcite\ Equivalent\ percent = TIC * 8.334\ [wt.\ \%]$$

The TOC/S ratio was also calculated. This is a widely applied ratio used to distimguish between marine and non-marine deposional environments. Below 2.8 indicates oxygen depleted conditions, while values above 2.8 are typically related to (sulphate-limited) freshwater environments (Berner and Raiswell, 1984).

3.2 Rock Eval Pyrolysis

Rock eval pyrolysis yields parameters such as S_1 and S_2 hydrocarbons and T_{max}. S_1 and S_2 parameters are used to indicate the quality of organic matter and to classify the kerogen type using the calculated hydrogen index (HI). T_{max} is also important because it indicates the maturity of the source rock. Also, S_1 and S_2 are used to calculate the genetic potential of the source rock.

For the Rock Eval analysis, a standard Rock-Eval Pyrolizer 6 instrument by Vinci Technologies was used for all samples analysed (Table 2). The free or adsorbed (volatized) hydrocarbons in mgHC/g rock already present before pyrolysis is recorded by the S_1 peak at 300°C. The residual hydrocarbon in the kerogen is produced during gradual heating from 300 to 650°C and recorded as the S_2 peak (mgHC/g rock). During this gradual temperature increase, heavy extractable compounds within the kerogen such as resins and asphaltenes are thermally broken down. The petroleum potential (PP) and production index (PI) are calculated from the S_1 and S_2 peaks. Hygrogen index (HI), bitumen index (BI) and quality index (QI) are also calculated using S_1, S_2 and TOC parameters. The temperature at which the maximum hydrocarbons are generated was measured and is referred to as T_{max} [°C], a widely accepted maturity indicator.

$$PP = S_1 + S_2 \; [mgHC/gRock]$$

$$\text{PI (Lafargue et al., 1998)} = \frac{S1}{S1+S2}$$

$$HI \text{ (Espitalie et al., 1977)} = \frac{S2}{TOC} * 100 \quad [mgHC/gTOC]$$

$$BI \text{ (Sykes and Snowdon, 2002)} = \frac{S1 * 100}{TOC}$$

$$QI \text{ (Sykes and Snowdon, 2002)} = \frac{(S1 + S2) * 100}{TOC}$$

The amount of hydrocarbons generated beneath 1 m² of surface area expressed in tHC/m^2 was also calculated after Demaison and Huizinga (1994) by applying the source potential index (SPI; m=thickness; δ=bulk density).

$$SPI \text{ (Demaison and Huizinga, 1994)} = \frac{m * (S1 + S2) * \delta}{1000} \quad [\text{tHC/m}^2]$$

3.3 Microscopy - Organic petrography, vitrinite reflectance and SEM

Maceral distribution is important because it indicates the relative amount of terrigenous and aquatic derived organic matter in the source rock. This also gives us an idea of the relative distribution of organic matter in the source rock, hence indicating the depositional environment. Vitrinite reflectance is very important as it indicates the maturity window of the source rock.

Macerals are microscopically visible organic particles. To determine maceral contents semi-quantitatively (Table 2), polished blocks were prepared, and the different macerals were

identified under a Leica DM 4P microscope using white and fluorescence light and a 50× oil immersion objective. The maceral analysis performed, and the terminology used, follow the ICCP sytem (ICCP 1998, 2001; Pickel et al. 2017). Depending on the TOC contents, up to 2000 points were counted in a single scan to distinguish, macerals, inorganic fossil remnants, mineral matrix, and pyrite. This allowed the calculation of the amount of total macerals, specific macerals, and total mineral matter. Macerals percentages are expressed in volume percent (vol.%) normalized to 100% organic matter. The three main maceral groups outlined by the International Comitee for Coal Petrology (ICCP) are vitrinite (remnants of higher land plants), liptinite (lipid/fatty remains of plants, algae, pollen, spores, resin…) and inertinite (oxidized and charred plant material, e.g., charcoal).

Kerogen type I and II are found to be dominated by liptinites, Kerogen type III is dominated by vitrinite, while kerogene type IV is dominated by inertinite ((ICCP system 1998, 2001).

The mean random vitrinite reflectance (Rr), a maturity indicator measurement was determined using the same microscope. Up to 100 vitrinite particles were measured and mean values calculated. The microscope was caliberated using either an yttrium–aluminum–garnet standard (Rr: 0.899%) or a synthetic reflectance standard (N-LASF46A; 1.311%).

For scanning electron microscope (SEM) analysis, a Tescan Clara field emmssion (FE)-SEM at the Chair of Physical Metallurgy and Metallic Materials, Montanuniversitaet Leoben (Austria) was employed on fresh broken limestone rock surfaces coated with few nm Au to prevent electron charging during high resolution imaging at 5 – 10 kV. The microscope was adapted with backscattered (BSE) and secondary electron detectors including an energy-dispersed X-ray (EDX) detector (Oxford Instrument). The objective was to determine any evidence of diagenetic activities in the limestone layers in the Salem core and to identify any micro-fossils of interest.

3.4 Particulate organic matter and palynology

Palynology is very important because it allows us to assess the origin and types of organic matter in the source rock in a more quantitative manner compared to maceral analysis.

Palynofacies and palynology investigations were performed at the iSTEP laboratory, Sorbonne Université, Paris, France and the palynological labotatory of the ETH Zürich by Francesca Galasso under the supervision of Elke Schneebeli-Hermann.

For each sample, 15 g of dry sediments was cleaned, crushed, and subsequently treated with concentrated HCl and HCF, followed by modified multi-step oxidation as described by Traverse (2007). In each step, the residues were sieved over a 11-µm mesh screen. For palynofacies analysis, organic matter particles were counted in unoxidised kerogen slides until a minimum of 400 counts per sample was reached. Particle counts include marine particles (i.e. acritarchs, prasinophytes, amorphous organic matter [AOM], foraminiferal test linings and dinoflagellate cysts) and terrestrial particles (i.e. translucent and opaque phytoclasts, cuticles, membranes, spores and bisaccate pollen grains) (Tyson 1995; Batten 1996). Subsequently, for a detailed palynological investigation, all the samples were further treated (with a stepped process of oxidation) using concentrated HNO_3, and ultrasonic

vibration. This treatment was done in order to increase the palynomorph concentration, remove the remaining inorganic residue (e.g. pyrite), and reduce the AOM density.

Qualitative sporomorphs fluorescence colour and spore colour (Thermal Alteration Index, [TAI]) were adopted to evaluate organic maturation levels. The analysis of qualitative spore fluorescence colour was performed using Zeiss Axiolab fluorescence microscope. Spore colour was investigated using kerogen slides under transmitted light using an Olympus BX51 light microscope.

Conventionally, fluorescence colour and TAI analysis should be assessed on smooth spores with medium to thick exines (e.g. Yule et al., 1998). However, in Salem core, the presence of thick and ornamented spores exine (e.g. *Kraeuselisporites* spp., *Leptolepidites* spp.), made this impossible at times. Therefore, the spore *Deltoidospora* sp. and the pollen grains *Classopollis* sp. and *Alisporites* sp. were adopted, as fulfilled the main prerequisites (i.e. medium-thick and smooth exines). The terminology used to describe fluorescence colour was blue (B), green (G), greenish-yellow, yellow (Y), golden yellow, orange (O) and red (R). The spore colour was defined (Fig. 7) using the Phillips Petroleum Colour Standard version no. 2 (1984), adapted from Staplin's Thermal Alteration Index (TAI) chart, which includes more shades for the same colour index (Fig. 7). For each interval the spore colour index was determined by observing the colour of the dominant sporomorph. Slides are stored in the repository of the Palaeontological Institute and Museum, University of Zurich, under PIMUZ XX (Ajuaba et al. Submitted).

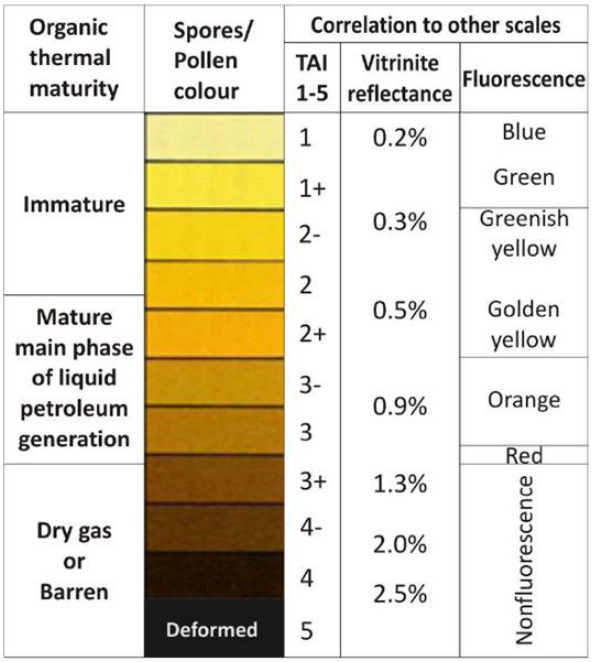

Fig. 7 Correlation chart showing the miospores colour, thermal alteration index (TAI) and fluorescence colour, used to evaluate organic maturation level (based and modified from the Phillips Petroleum Colour Standard, version no. 2, 1984 and Stach et al., 1982).

3.5 Geochemical analysis - Biomarker

Biomarker analysis is very important because the concentrations and concentration ratios of selected compounds of interest are used as proxies to reconstruct paleo environments and also to compare the origins of various lipid fragments. It also enables us to determine redox condition of the depositional environment, organic of organic matter type, source, and maturation.

In the frame of this thesis, 83 powdered sampes were extracted for biomarker analysis using dichloromethane in a Dionex ASE 350 intrument for ~ 1 h at 75°C and 100 bars. After that, a Zymark TurboVap 500 closed cell concentrator was used to concentrate the extract to ~ 0.5 ml. Afterwards, asphaltenes were separated using hexane:dichloromethane solution (80:1, according to volume) and separated using centrifugation. The hexane-soluble fracitons were separated into polar fractions (NSO compounds), saturated and aromatic hydrocarbons using a Köhnen-Willsch MPLC (medium pressure liquid chromatography) instrument (Radke et al., 1980). Prior to GC-MS measurements, equivalent amounts of internal standards (tetracosane or squalene for aliphatics; 1, 1´-binphthyl for aromatics) were added to each sample.

The saturated hydrocarbon fractions were analyzed for *n*-alkanes and isoprenoids by a gas chromatograph (Trace GC-Ultra) attached to a flame ionization detector (GC-FID), equipped with a 50 m HP-PONA capillary column (inner diameter [i.d.] 0.20 mm, 0.50 µm film thickness). After splitless sample injection (2 µl at 270 °C), the oven temperature was increased from 70 to 310 °C and held constant for 35 min (Ajuaba et al., 2022).

Specific biomarker molecules in the saturated and aromatic fractions were analyzed by gas chromatography-mass spectrometry (GC-MS) using a Thermo Scientific Trace GC-Ultra equipped with a Triplus 100 liquid auto-sampler and interfaced to a ThermoFisher ISQ mass spectrometer. The measurements were performed with a 60 m TG/DB-5MS fused silica capillary column (i.d. 0.25 mm; 0.25 µm film thickness). The GC oven temperature was initially programed from 40 °C/min, held for 2 minutes and ramped to 310°C with 4°C/min followed by an isothermal period of 40 min. Sample was injected in split mode with a split ratio of 20 at 260 °C using helium as carrier gas. The spectrometer was operated in the EI (electron ionization) mode with a mass-to-charge ratio (m/z) scan range from m/z 50 to m/z 650 (0.7 s total scan time) (Ajuaba et al., 2022).

For the determination of methylsterane concentrations, further investigating aliphatic fractions of selected samples using a Trace^{TM} 1300 GC (ThermoFisher) equipped with a 60 m TG-5MS fused silica capillary column (i.e., 0.25 mm; 0.25 µm film thickness) attached to a ThermoFisher TSQ9000 triple quadrupole GC-MS/MS. The oven was set to hold 40 °C for 2 minutes and then heated to 310 °C with 4 °C/min, followed by an isothermal period of 40 min. The sample was injected splitless with an injector temperature of 310 °C.

Methylsterane isomers were detected using selected reaction monitoring (SRM) through the application of different parent-to-daughter ion transitions (*m/z* 386–231, 400–231, 414–231, 414–98) to obtained C_{28} to C_{30} methylsteranes, methyldiasteranes, diamethylsteranes and dinosteranes (Ajuaba et al., 2022).

The raw data were processed using Xcalibur and Chromeleon data systems. The respective retention time for each compound within the mass spectra or total ion current (TIC) were used for their identification in addition to comparing the mass spectra with published data. Correction factors were appropriately applied for mass chromatograms to correct for fragment ions while for TIC chromatograms, absolute concentrations were determined from the peak areas of the saturated and aromatic fractions in relation to their internal standards per sample (Ajuaba et al., 2022).

A quantitative calculation of the target compounds was conducted based on results of total ion current (TIC) chromatograms. Absolute concentrations were determined for the methylsteranes using their TIC chromatograms (also detectable using *m/z* 231) set in relation to an internal standard (5β(H)-Cholane) per sample. Where no internal standard was available, areas of specifc compounds were taken then from the SRM mode and were set into relation to the TIC. With this relation, a proper estimation of the amount of methylsteranes was possible (Ajuaba et al., 2022).

3.6 Bulk and compound-specific carbon isotopy

Bulk and compound-specific carbon isotopes were determined for the bulk rock and *n*-alkanes, iso-alkanes (e.g., pristane, phytane, norpristane) respectively. These parameters are very important tools in establishing genetic relationship between organic carbon contents of different origins.

A total of 73 samples were investigated for their carbon isotope composition. For the bulk carbon isotope ($\delta^{13}C_{org}$) analysis, powdered samples were pre-treated stepwise with 6 N HCl for almost 12 hours to remove all carbonates. Distilled water was used at each step to remove the added acid. The samples were later oven dried for 24 hours at 40 °C. 6-8 mg per sample was weighed into tin foil boats and measured by combustion in excess of oxygen at 1020 °C using an elemental analyzer (Flash EA 1112). The CO_2 by-product is separated by column chromatography and analysed online by the DELTA V ir-MS, mentioned above. The carbon isotopic ratio ($^{13}C/^{12}C$) of the sample CO_2 are compared with that of the CO_2 reference gas and calibrated against PDB. Analytical reproducibility is in the range of 0.1 - 0.3‰ (Ajuaba et al., 2022).

To analyse the stable carbon isotope of *n*-alkanes and isoprenoids, the *n*-alkanes were separated from the *iso*-alkanes within the saturated hydrocarbon fraction using an improved 5 Å molecular sieve method (Grice et al. 2008). Measurement of the stable carbon isotope ratio was performed using a Trace GC-Ultra gas chromatograph attached to the ThermoFisher Delta-V isotope ratio mass spectrometer (IRMS) via a combustion and high temperature reduction interface (GC Isolink, ThermoFisher). The GC column has been described above; however, the oven temperature was set to 70 °C for 2 min followed by a ramp from 4 °C/min to 300 °C and isothermal period of 15 min. A CO_2 reference gas was used for calibration and injected before and after each analysis. Isotope composition per sample was measured at least twice and their mean values reported in the δ notation in permil (‰) relative to the V-PDB standard. The analytical reproducibility per sample is below 0.3‰ (Ajuaba et al., 2022).

4 Summary of publications

4.1 Publication I

Biomarker and compound-specific isotope records across the ToarcianCIEat the Dormettingen section in SW Germany

Ajuaba, S., Sachsenhofer, R.F., Galasso, F., Bechtel, A., Gross, D., Misch, D., SchneebeliHermann, E., 2022. Biomarker and compound-specific isotope records across the Toarcian CIE at the Dormettingen section in SW Germany. Int. J. Earth Sciences 111, 1631–1661. https://doi.org/10.1007/s00531-022-02196-z.

This article employs various geochemical and petrographic techniques to investigate the ~12 m long black shale (Posidonia Shale) deposit that outcrops in Dormettingen, in the Southwest German Basin. This basin is one of the various basins constituting the Central European epicontinental Basin System known to be a great repository to black shale deposition of Lower Toarcian age. This study applies bulk geochemical data, organic petrography, molecular fossils (biomarkers) and compound specific isotopes to reconstruct the depositional environment of Lower Toarcian rocks in the Southwest German Basin. The aim of the study is to understand the differences in carbon isotope trends of bulk organic matter and those of specific biomarkers and lastly, to combine both biomarkers and compound-specific isotope data to determine the factors influencing the SCI patterns and also to gain an understanding of the time relation between development of anoxia and processes that are influencing carbon isotopy (Ajuaba et al., 2022).

It was confirmed that the Posidonia Shale in Dormettingen, SW Germany is immature to marginal mature (vitrinite reflectance: 0.55 %Rr, average Tmax of 427 °C.) TOC contents and HI are high with values of up to 10 wt.% and 700 mgHC/gTOC, respectively. In support of previous studies in this area, biomarker parameters showed that anoxic conditions were due to basin restriction and stratification of the water masses. The chemical boundary (chemocline) within the water was at its lowest above the "Unterer Stein" marker horizon. 2α-Methylhopane was present in high concnetrations indicating the activities of diazotrophic cyanobacteria. This study also shows that there is a time shift (delay) between the isotopic minimum (Pr, Ph) and peak anoxia. At the bottom of the T-OAE interval, a prominent T-CIE was observed with the most prominent excursion captured by *n*-C_{27} *n*-alkanes (9 ‰). This study also showed that, the *n*-C_{27} pre- and post-CIE have different sources with the pre-CIE of terrogenous origin and the post-CIE of marine organic matter. This is inferred to their distinctive carbon isotope compositon with separate CO_2 reservoir. This article also submits that, the short-chain *n*-alkanes and isoprenoids at Dormettingen exhibit the highest CIE magnitude compared to other sub-basins within the Central European Epicontinental Basin (Ajuaba et al., 2022).

4.2 Publication II

Coaly and lacustrine hydrocarbon source rocks in Permo-Carboniferous graben deposits (Weiach well, Northern Switzerland)

Stephen Ajuaba, Reinhard F. Sachsenhofer, Verena Meier, Doris Gross, Johann Schnyder, Silvia Omodeo-Salé, Andrea Moscariello, David Misch, Coaly and lacustrine hydrocarbon source rocks in Permo-Carboniferous graben deposits (Weiach well, Northern Switzerland), Marine and Petroleum Geology, Volume 150, 2023, 106147, ISSN 0264-8172, https://doi.org/10.1016/j.marpetgeo.2023.106147.

In this study, coaly and shaly rocks deposited in the half graben structures in the Constance-Frick Trough (CFT) of Permo-Carboniferous age were investigated using the techniques of bulk geochemistry (Eltra and Rock Eval), organic petrology (maceral and palynology), biomarker, and compound-specific isotope data to enable us characterize the coals, shaly coals and shales by assessing the type and the amount of hydrocarbons present at various depth. These also helps us to valuate the risk associated with hydrocarbon production during the drilling of geothermal wells as this is the designated site for a geothermal well project in Switzerland. Within the carboniferous, coaly shales do not hold a significant hydrocarbon potential. Coals are potential source rocks for natural gas. The maturity reached the onset of gas generation. The coal would have generated only very limited amounts of oil, which could be identified easily based on biomarker ratios. Seam (#6), was the main studied seam and was deposited in low-lying, freshwater mire. Upward increasing mineral matter contents are probably due to delta channel(s) avulsion in a floodplain setting. For the Permian, the petroleum potential of the Lacustrine Series varies considerably. Bituminous shales in the "main shale interval" (1339.20-1326.95 m) contain very high amounts of organic matter (max. 10.3 wt.% TOC) with a high HI (max. 488 mgHC/gTOC). These sediments display "good" to "very good" oil potential (SPI: ~0.35 tHC/m²). The lacustrine series is probably not a main source rock interval in the NAFB, but it may have contributed to HC accumulations. It was possible to distinguish oil generated from Permian, Jurassic and Oligocene rocks based on their different biomarker ratios and CSI data. The OM is mainly of aquatic (algal) origin, but with a significant terrigenous input. Bacterial activity was high. Biomarker and palynofacies data show a strongly oxygen-depleted depositional environment (photic zone anoxia), controlled by water column stratification. δ13C values of pristane and phytane in the main shale interval reflect anoxic conditions and remineralization of organic matter.

4.3 Publication III

The Toarcian Posidonia Shale at Salem (North Alpine Foreland Basin; South Germany): Hydrocarbon potential and paleogeography

Ajuaba, S., Sachsenhofer, R.F., Galasso, F., Garlichs, T.U., Gross, D., SchneebeliHermann, E., Misch, D., Oriabure, J.E., submitted. Biomarker and compound-specific isotope records across the Toarcian CIE at the Dormettingen section in SW Germany. Int. J. Earth Sciences

In this last article, a detail examination of the Salem drill core was undertaken by applying the techniques of bulk geochemistry (Eltra and Rock Eval), organic petrography (maceral and palynology), biomarkers, bulk and compound-specific carbon isotopy, and computed tomography (CT) scans. This core was drilled near Salem (SW Germany), located in the central sector of the North Alpine Forlenad Basin (NAFB). Considering Salem is paleogeographically more distal compared to Dormettingen/Dotternhausen, the study delves into investigating the variations in sedimentary facies in these two paleogeographic locations and also looks into the impact of increasing thermal maturity on organic facies proxies which is a very important aspect when correlating oil and its source. Of the ~10 m thick Posidonial Shale interval encountered in the Salem borehole, only the lower 7.5 m (1763.5-1756.0 m) was cored together with the uppermost part of the underlying Amaltheenton Shale. 62 samples were used for the study. Difference in the thickess in the lower part of the Posidonia Shale in the Dormettingen and Salem sections suggests significant changes in basin geometry at the *elegans/falciferum* boundary. The TOC content is significantly higher in sediments deposited during the T-CIE compared to other Toarcian sections such as in Dormettingen. Compound-specific isotope performed on the *n*-alkanes, pristine and phytane replicate the negative carbon isotope excursion with a gentle expression. However, at the T-CIE interval, the *n*-alkanes follow a depth trend while surprisingly, pristane and phytane do not. Furthermore, the $\delta^{13}C$ for the pristane and phytane are very strange showing a very small negative isotope excursion of 2‰. The no correlation between the $\delta^{13}C$ of isoprenoids and *n*-alkanes or bulk organic matter suggest unrelated, yet unidentified carbondioxide (CO_2) reservoir. In terms of the interval thickness, the T-CIE for the Salem section is very thin (0.75 m) compared to the very prominent (~2 m) Dormettingen section. The calculated source potential index for an interval of the cored section yielded ~0.5 tHC/m² estimated to be higher (0.8 tHC/m²) if the entire Posidonia Shale is considered.

5 List of conference contributions related to this thesis

Ajuaba, S., Sachsenhofer, R.F., Galasso, F., Bechtel, A., Gross, D., Misch, D., Schneebeli-Hermann, E. (2022). Controls on biomarker and carbon isotope patterns during the Toarcian anoxic event (Dormettingen section; Swabian Alb). Pangeo 2022, Leoben, Austria, 10/09/2022 – 13/09/2022. *Oral presentation*.

Ajuaba, S., Sachsenhofer, R.F., Galasso, F., Bechtel, A., Gross, D., Misch, D., Schneebeli-Hermann, E. (2022). Controls on biomarker and carbon isotope patterns during the Toarcian anoxic event (Dormettingen section; Swabian Alb). Global Summit on Advances in Earth Science and Climate Change. Virtual Event, Paris, France 15/09/2022 – 16/09/2022. *Oral presentation*.

Ajuaba, S.; Sachsenhofer, R. F.; Meier, V.; Gross, D.; Omodeo Sale, S.; Schnyder, J. (2022). Hydrocarbon potential of Permo-Carboniferous rocks (Weiach, Switzerland). Pangeo 2022, Leoben, Austria, 10/09/2022 – 13/09/2022. *Poster presentation*.

6 Concluding remarks

The study yielded the following important new results;

- Improved our knowledge on the depositional environment of Permo-Carboniferous coals and non-marine shales and the Posidonia Shale deposited during the Toarcian Anoxic Event. The Carboniferous coals consisted of different seams and the main seam (#6) was deposited in a low-lying, freshwater environment. The mineral matter content in the coal increase upward suggesting a change in course of the river channel (avulsion effect) along the floodplain. The presence of freshwater algae *Botryococcus* as well as a high TOC/S ratio across the main shale interval indicates a non-marine environment of the lacustrine series. Evidence fom biomarker and palynofacies indicates the depostional environement of the non marine shales is strongly depleted of oxygen due to stratification of the water column in combination with a low energy environement. The Posidonia Shale deposited during the Toarcian Anoxic Event in Dormettingen and Salem sections show carbon isotope excursion (T-CIE) but of significantly different thickness with Salem T-CIE interval being thinner.
- Helped to quantifiy the petroleum potential of potential source rocks in the western and central part of the NAFB. Overall, Permian lacustrine shale in the western part suggested to be a main source rock in the NAFB shows “good” to “very good” oil potential with calculated source potential index of 0.35 tHC/m². In the central (German) part, the residual petroleum potential calculated from a section of the Salem drill core yielded 0.5 tHC/m², which could even be higher (0.8 tHC/m²) taken the entire Posidonia Shale secton into account.
- Showed the importance of CSI data for the reconstruction of the depositional environment and for oil-to-source correlation. In the main shale interval of the Permian shale, the $\delta^{13}C$ values of pristane and phytane reflects oxygen-reducing conditions and organic matter remineralization. Moreover, the CSI data was able to indicate that there is a time shift between the maximum negative carbon isotope excursion and the peak anoxic conditions in the T-CIE intervals of the posidonia shales of Dormettingen and Salem.
- Study of immature/marginal and mature Posidonia Shale shows significant differences in some molecular ratios (Pr/n-C17; Ph/n-C18 [which is expected], but also sterane/hopane ratios and Pr/Ph ratios.
- Temporal decoupling of strongest depletion of ^{13}C (maximum isotope excursion) and maximum anoxia (strongest basin restriction) based on pristane and phytane isotopes.

7 References (General Section)

Ajuaba, S., Sachsenhofer, R.F., Meier V., Gross, D., Schnyder J., Omodeo-Salé S., Moscariello A., Misch, D., 2023. Coaly and lacustrine hydrocarbon source rocks in Permo-Carboniferous graben deposits (Weiach well, Northern Switzerland). Marine and Petroleum Geology, 150, 106-147.

Ajuaba, S., Sachsenhofer, R.F., Galasso, F., Bechtel, A., Gross, D., Misch, D., Schneebeli-Hermann, E., 2022. Biomarker and compound-specific isotope records across the Toarcian CIE at the Dormettingen section in SW Germany. Int. J. Earth Sciences, 111:1631–1661. https://doi.org/10.1007/s00531-022-02196-z.

Ajuaba, S., Sachsenhofer, R.F., Galasso, F., Garlichs T.U., Gross, D., Schneebeli-Hermann, E., Misch, D., Oriabure, J.E., (submitted). The Toarcian Posidonia Shale at Salem (North Alpine Foreland Basin; South Germany): Hydrocarbon potential and paleogeography. Int. J. Earth Sciences.

Al-Sagri, K.E.A., 2015. Linking the timing of deposition and organic matter richness of the Gulneri formation of Northern Iraq to the global oceanic anoxic event 2 (OAE 2): implications to better constrain the depositional models of Iraqi's oil source beds and their timing of deposition. Iraq J Sci 56(3A):2007–2023

Andjić, G., Baumgartner, P.O., Baumgartner-Mora, C., 2018. Rapid vertical motions and formation of volcanic arc gaps: plateau collision recorded in the forearc geological evolution (Costa Rica margin). Basin Res 30(5):863–894

Arora, A., Banerjee, S., Dutta, S., 2015. Black shale in late Jurassic Jhuran formation of Kutch: possible indicator of oceanic anoxic event. J Geol Soc India 85(3):265–278

Bachmann, G.H., Müller, M., Weggen, K., 1987. Evolution of the Molasse basin (Germany. Switzerland). Tectonophysics, 137. 77 92.

Bansal, U., Banerjee, S., Ruidas, D.K., Pande, K., 2018. Origin and geochemical characterization of Maastrichtian glauconites in the, Central India. J Palaeogeogr 7:99–116

Bastos, L.P.H., Pereira, E., da Costa Cavalcante, D., Alferes, C.L.F., de Menezes, C.J., Rodrigues R., 2020. Expression of Early Cretaceous global anoxic events in Northeastern Brazilian basins. Cretac Res 110:104390

Batten, D.J., 1996. Palynofacies. In J. Jansonius and D.C. McGregor (Eds), Palynology: Principles and applications (Vol. 3, pp. 1011–1064). Park Ridge; American Association of Stratigraphy Palynologists Foundation.

Berner, R.A., Raiswell, R., 1984. C/S method for distinguishing freshwater from marine sedimentary rocks. Geology, 12, 365-368.

Bomou, B., Adatte, T., Tantawy, A.A., Mort, H., Fleitmann, D., Huang, Y., Föllmi, K.B., 2013. The expression of the Cenomanian–Turonian oceanic anoxic event in Tibet. Palaeogeogr Palaeoclimatol Palaeoecol 369:466–48.

Bottini, C., Mutterlose, J., 2012. Integrated stratigraphy of Early Aptian black shales in the Boreal Realm: calcareous nannofossil and stable isotope evidence for global and regional processes. Newsl Stratigr 45(2):115–137.

Brocks, J.J., Summons, R.E., 2003. Sedimentary hydrocarbons, biomarkers for early life. In: Holland HD, Turekian KK (eds) Treatise on Geochemistry, Volume 8. Pergamon Press, Oxford, pp 63-115. doi: 10.1016/ B0-08-043751-6/08127-

Buggisch, W., 1991a. The global Frasnian-FamennianKellwasser Event. Geol Rundsch 80(1):49–72

Burnaz, L., Kalmykov, A., Grohmann, S., Kalmykov, G., & Littke, R., 2022. Geochemistry and organic petrology of organic-rich shales of the Upper Jurassic-Lower Cretaceous Bazhenov Horizon in the Frolov Region, West Siberian Basin: Implications for the reconstruction of the organic matter origin and paleoredox conditions. Marine and Petroleum Geology, 143. https://doi.org/10.1016/j.marpetgeo.2022.105809

Cheng, K., Elrick, M., Romaniello, S.J., 2020. Early Mississippian Ocean anoxia triggered organic carbon burial and late Paleozoic cooling: evidence from uranium isotopes recorded in marine limestone. Geology 48(4):363–367.

Coccioni, R., Bancalà, G., Catanzarit, R., Fornaciari, E., Frontalini, F., Gius-berti, L., Jovane L., Luciani, V., Savian, J., Sprovieri, M., 2012. An integrated stratigraphic record of the Palaeocene–lower Eocene at Gubbio (Italy): new insights into the early Palaeogene hyperthermals and carbon isotope excursions. Terra Nova 24(5):380–386.

Demaison, G., Huizinga, B.J., 1994. Genetic classification of petroleum systems using three factors: charge, migration, and entrapment. In: Magoon, L.B., Dow, W.G. (Eds.): The Petroleum System, from Source to Trap. AAPG Memoir, 60, 73-89.

Diebold, P., Naef, H., Ammann, M., 1991. Zur Tektonik der zentralen Nordschweiz: Interpretation aufgrund regionaler Seismik, Oberflächengeologie und Tiefbohrungen. Nagra Tech. Ber. NTB 90-04, Nagra, Wettingen, 277.

Do Couto, D., Garel, S., Moscariello, A., Bou Daher, S., Littke, R., Weniger, P., 2021. Origins of hydrocarbons in the Geneva Basin: insights from oil, gas and source rock organic geochemistry. Swiss Journal of Geosciences, 114(1), 1-28.

Duchamp-Alphonse, S., Fiet, N., Adatte, T., Pagel, M., 2011. Climate and sea-level variations along the northwestern Tethyan margin uring the Valanginian C-isotope excursion: mineralogical evidence from the Vocontian Basin (SE France). Palaeogeogr Palaeoclimatol Palaeoecol 302(3-4):243–254.

Duque-Botero F, Maurrasse FJR, Hickey-Vargas R, Melinte MC, Jafe R, López-Oliva JG (2009) Microspheroid accumulations and geochemical characteristics of a Cenomanian–Turonian anoxic basin: the record of the Indidura formation, NE México: geologic problem solving with microfossils: a volume in honor of Garry D. Jones, Society of Economic Paleontologists and Mineralogists. Special Publ 93:171–186

Fantasia, A., Föllmi, K.B., Adatte, T., Bernárdez, E., Spangenberg, J.E., Mattioli, E., 2018. The Toarcian oceanic anoxic event in southwestern Gondwana: an example from the Andean basin, northern Chile. J Geol Soc 175(6):883–902.

Főzy, I., Janssen, N.M., Price, G.D., Knauer, J., Pálfy, J., 2010. Integrated isotope and biostratigraphy of a lower Cretaceous section from the Bakony Mountains (Transdanubian Range, Hungary): a new Tethyan record of the Weissert event. Cretac Res 31(6):525–545.

French, K.L., Sepulveda, J., Trabucho-Alexandre, J., Gröcke, D.R., Summons, R.E., 2014. Organic geochemistry of the early Toarcian oceanic anoxic event in Hawsker Bottoms, Yorkshire, England. Earth and Planetary Science Letters 390: 116-127. https://doi.org/10.1016/j.epsl.2013.12.033Galasso et al. 2021

Gratzer, R., Bechtel, A., Sachsenhofer, R.F., Linzer H.-G., Reischenbacher, D., Schulz, H.-M., 2011. Oil-oil and oil-source rock correlations in the Alpine Foreland Basin of Austria: Insights from biomarker and stable carbon isotope studies. Marine and Petroleum Geology 28, 1171-1186.

Grice, K., de Mesmay, R., Glucina, A., Wang, S., 2008. An improved and rapid 5A molecular sieve method for gas chromatography isotope ratio mass spectrometry of n-alkanes (C8–C30+). Org Geochem 39:284–288. https://doi.org/10.1016/j.orggeochem.2007.12.009

Gröcke, D.R., Hori, R.S., Trabucho-Alexandre, J., Kemp, D.B., Schwark, L., 2011. An open ocean record of the Toarcian oceanic anoxic event. Solid Earth 2(2):245–257.

Hallam, A., 1994. Strontium isotope profles of Triassic-Jurassic boundary sections in England and Austria. Geology 22(12):1079–1082

Heath, M.N., Cramer, B.D., Stolfus, B.M., Barnes, G.L., Clark, R.J., Day, J.E., Barnett, B.A., Witzke, B.J., Hogancamp, N.J., Tassier-Surine, S., 2021. Chemoautotrophy as the driver of decoupled organic and carbonate carbon isotope records at the onset of the Hangenberg (Devonian-Carboniferous Boundary) oceanic anoxic event. Palaeogeogr Palaeoclimatol Palaeoecol 577:11054.

Hoefs, J., 2009. Stable Isotope Geochemistry. 6th Edition. Springer, Göttingen. ISBN 978-3-540-70708-0

Hopmans, E.C., Schouten, S., Pancost, R.D., van der Meer, M.T.J., Sinninghe Damsté, J.S., 2000. Analysis of intact tetraether lipids in archaeal cell material and sediments by high performance liquid chromatography/atmospheric pressure chemical ionization mass spectrometry. Rapid Communications in Mass Spectrometry 14: 585-589, doi: 10.1002/(SICI)1097- 0231(20000415)14:7%3C585::AIDRCM913%3E3.0.CO;2-N.

Huang, C., Hesselbo, S.P., 2014. Pacing of the Toarcian oceanic anoxic event (Early Jurassic) from astronomical correlation of marine sections. Gondwana Res 25(4):1348–1356.

ICCP., 1998. The new vitrinite classification (ICCP System 1994). Fuel 77: 349–358. https://doi.org/10.1016/S0016-2361(98)80024-0.

ICCP., 2001. The new inertinite classification (ICCP System 1994). Fuel 80: 459–471. https://doi.org/10.1016/S0016-2361(00) 00102-2.

Izumi, K., Miyaji, T., Tanabe, K., 2012. Early Toarcian (Early Jurassic) oceanic anoxic event recorded in the shelf deposits in the northwestern Panthalassa: evidence from the Nishinakayama formation in the Toyora area, west Japan. Palaeogeogr Palaeoclimatol Palaeoecol 315:100–108.

Jenkyns, H., 1988. The early Toarcian (Jurassic) anoxic event-stratigraphic, sedimentary, and geochemical evidence. American Journal of Science, 288(2), 101-151.

Jenkyns, H.C. (1980). Cretaceous anoxic events: from continents to oceans. J Geol Soc 137(2):171–188.

Jenkyns, H.C., 2010. Geochemistry of oceanic anoxic events. Geochem Geophys Geosyst 11(3):Q03004.

Jenkyns, H.C., 2018. Transient cooling episodes during Cretaceous oceanic anoxic events with special reference to OAE 1a (Early Aptian). Philos Trans R Soc A Math Phys Eng Sci 376(2130):20170073.

Jenkyns, H.C., Forster, A., Schouten, S., Damsté, J.S.S., 2004. High temperatures in the Late Cretaceous Artic Ocean. Nature 432.

Kabanov, P., 2019. Devonian (c. 388–375 Ma) Horn River Group of Mackenzie Platform (NW Canada) is an open-shelf succession recording oceanic anoxic events. J Geol Soc 176(1):29–45

Kälin, O; Bernoulli, D., 1984. Schizosphaerella Deflandre and Dangeard in Jurassic deeper-water carbonate sediments, Mazagan Continental Margin (Hole 547B) and Mesozoic Tethys. In: Hinz, K; Winterer, EL; et al. (eds.), Initial Reports of the Deep Sea Drilling Project, Washington (U.S. Govt. Printing Office), 79, 411-435, https://doi.org/10.2973/dsdp.proc.79.112.1984

Karakitsios, V., Kafousia, N., Tsikos, H., 2010. A review of oceanic anoxic events as recorded in the Mesozoic sedimentary record of mainland Greece. Hellenic J Geosci 45:123.

Kassem, A.A., Sharaf, L.M., Baghdady, A.R., El-Naby, A.A., 2020. Cenomanian/Turonian oceanic anoxic event 2 in October oil feld, central Gulf of Suez, Egypt. J Afr Earth Sci 165:103817.

Keller, G., Adatte, T., Berner, Z., Chellai, E.H., Stueben, D., 2008. Oceanic events and biotic efects of the Cenomanian-Turonian anoxic event, Tarfaya Basin, Morocco. Cretac Res 29(5–6):976–994.

Keller, G., Nagori, M.L., Chaudhary, M., Reddy, A.N., Jaiprakash, B.C., Spangenberg, J.E., Mateo, P., Adatte, T., 2021. Cenomanian-Turonian sea-level transgression and OAE2 deposition in the Western Narmada Basin, India. Gondwana Res 94:73–86

Kemp, D.B., Selby, D., Izumi, K., 2020. Direct coupling between carbon release and weathering during the Toarcian oceanic anoxic event. Geology 48(10):976–980

Khan, S., Kroon, D., Wadood, B., Ahmad, S., and Zhou, X., 2021. Marine depositional signatures of the Aptian oceanic anoxic events in the Eastern Tethys, Lower Indus Basin, Pakistan Australia J Earth Sci 1-17.

Kuhlemann, J., Kempf, O., 2002. Post-Eocene evolution of the North Alpine Foreland Basin and its response to Alpinetectonics. Sedimentary Geology, 152, 45-78.

Kuypers, M. M. M., R. D. Pancost, I. A. Nijenhuis, and J. S. Sinninghe Damsté, 2002a. Enhanced productivity led to increased organic carbon burial in the euxinic North Atlantic basin during the late Cenomanian oceanic anoxic event, Paleoceanography, 17(4), 1051, doi:10.1029/2000PA000569.

Lafargue, E., Marquis, F., Pillot, D., 1998. Rock-Eval 6 applications in hydrocarbon exploration, production, and soil contamination studies. Revue de l'institut français du pétrole, 5, 4, 421-437.

Langsford, N., Raimondo, T., Jago, J. 2020. Red crust: evidence for an early Paleozoic oceanic anoxic event. Aust J Earth Sci 67(7):995–1001

Laubscher, H., 1987. Die tektonische Entwicklung der Nordschweiz. Eclogae Geologicae Helvetiae, 80, 287-303.

Lenniger, M., Nøhr-Hansen, H., Hills, L.V., Bjerrum, C.J., 2014. Arctic black shale formation during Cretaceous oceanic anoxic event 2. Geology 42(9):799–802

Leu, W., 2012. Swiss oil/gas exploration and lessons learnt. Swiss Bull. Angew. Geol., 17, 49-59.

Leu, W., 2014. Potenzial der Kohlenwasserstoff Ressourcen in der Nordschweiz. NAB 14-70 NAGRA.

Li, X., Wei, Y., Li, Y., Zhang, C., 2016. Carbon isotope records of the early Albian oceanic anoxic event (OAE) 1b from eastern Tethys (southern Tibet, China). Cretac Res 62:109–121

Li, Y-X., Bralower, T.J., Montañez, I.P., Osleger, D.A., Arthur, M.A., Bice, D.M., Herbert, T.D., Erba, E., Premoli Silva I., 2008. Toward an orbital chronology for the early Aptian oceanic anoxic event (OAE1a, ~120 ma), earth planet. Sci Lett 271:88–100

Madritsch, H., Naef, H., Meier, B., Franzke, H. J., Schreurs, G., 2018. Architecture and kinematics of the Constance-Frick Trough (northern Switzerland): Implications for the

formation of post-Variscan basins in the foreland of the Alps and scenarios of their Neogene reactivation. *Tectonics*, *37*. https://doi.org/10.1029/2017TC004945

Magoon, L.B., and Dow, W.G., eds., 1994a. The petroleum system—From source to trap: merican Association of Petroleum Geologists Memoir, 60, Tulsa, 655 pp.

Matsumoto, H., Kuroda, J., Coccioni, R., Frontalini, F., Sakai, S., Ogawa, N.O., Ohkouchi, N., 2020. Marine Os isotopic evidence for multiple volcanic episodes during Cretaceous oceanic anoxic event 1b. Sci Rep 10(1):1–10

Matter, A., 1987. Faciesanalyse und Ablagerungsmilieu des Permokarbons im Nordschweizer Trog. In: Eclogae Geologicae Helvetiae, Band 80, Heft 2.

Misch, D., Leu, W., Sachsenhofer, R. F., Gratzer, R., Rupprecht, B., Bechtel, A., 2017. Shallow hydrocarbon indications along the Alpine thrust belt and adjacent foreland basin: distribution and implications for petroleum exploration. Journal of Petroleum Geology, 40(4), 341-362.

Moiroud, M., Martinez, M., Deconinck, J.F., Monna, F., Pellenard, P., Riquier, L., Company, M., 2012. High-resolution clay mineralogy as a proxy for orbital tuning: example of the Hauterivian–Barremian transition in the Betic Cordillera (SE Spain). Sediment Geol 282:336–346

Mort, H., Jacquat, O., Adatte, T., Steinmann, P., Föllmi, K., Matera, V., Berner, Z., Stüben, D., 2007. The Cenomanian/Turonian anoxic event at the Bonarelli level in Italy and Spain: enhanced productivity and/ or better preservation? Cretac Res 28(4):597–612

Moscariello, A., 2019. Exploring for geo-energy resources in the Geneva Basin (Western Switzerland): opportunities and challenges. Swiss Bull. angew. Geol., 24/2, 105-124.

Moscariello, A., Ventra, D., Cervelli, M., Eruteya, O.E., Omodeo Salé, S., Makhloufi, Y., 2021. Revisiting the origin of the Carboniferous infill of Swiss post-Hercynian Throughs: Insights from the Weiach-1 borehole (northern Switzerland). Extended Abstract 19th Swiss Geoscience Meeting, Geneva 2021, Symposium 7: Stratigraphy and Sedimentology: processes and deposits through time. https://geoscience-meeting.ch/sgm2021

Naeher, S., Cui, X., Summons, R.E., 2022. Biomarkers: molecular tools to study life, environment, and climate. Elements 18: 79-85

Nagendra, R., Reddy, A.N., 2017. Major geologic events of the Cauvery Basin, India and their correlation with global signatures–a review. J Palaeogeogr 6(1):69–83

Najarro, M., Rosales, I., Moreno-Bedmar, J.A., de Gea, G.A., Barrón, E., Company, M., Delanoy, G., 2011. High-resolution chemo-and biostratigraphic records of the Early Aptian oceanic anoxic event in Cantabria (N Spain): Palaeoceanographic and palaeoclimatic implications. Palaeogeogr Palaeoclimatol Palaeoecol 299(1-2):137–158

Owens, J.D,, Lyons, T.W., Hardisty, D.S., Lowery, C.M., Lu, Z., Lee, B., Jenkyns, H.C., 2017. Patterns of local and global redox variability during the Cenomanian–Turonian Boundary Event (Oceanic Anoxic Event 2) recorded in carbonates and shales from central Italy. Sedimentology 64(1):168–185

Pedentchouk, N., Turich, C., 2017. Carbon and hydrogen isotopic compositions of n-alkanes as a tool in petroleum exploration. In: Lawson M, Formolo MJ, Eiler JM (eds) From source to seep: geochemical applications in hydrocarbon systems, Special Publications, vol 468. Geological Society, London, pp 105–125. https://doi.org/10.1144/SP468.1

Peters, K.E., Walters, C.C., Moldowan, J.M., 2005. The biomarker guide: biomarkers and isotopes in petroleum systems and earth history, 2nd edn. Cambridge University Press, Cambridge

Peters, K.E., Walters, C.C., Moldowan, J.M., 2004. The Biomarker Guide. Biomarkers and Isotopes in Petroleum Exploration and Earth History, Volume 2 (Second Edition). Cambridge University Press, 704 pp

Phillips Petroleum Colour Standard version no. 2., 1984.

Pickel, W., Kus, J., Flores, D., Kalaitzidis, S., Christanis, K., Cardott, B.J., Misz-Kennan, M., Rodrigues, S., Hentschel, A., Hamor-Vido, M., Crosdale, P., Wagner, N. ICCP., 2017. Classifcation of liptinite– ICCP system (1994). Int J Coal Geol 169:40–61. https://doi. org/10.1016/j.coal.2016.11.004

Radke, M., Schaefer, R.G., Leythaeuser, D., Teichmüller, M., 1980. Composition of soluble organic matter in coals: relation to rank and liptinite fuorescence. Geochim Cosmochim Acta 44:1787–1800.

Riegraf, W., 1985. Mikrofauna, Biostratigraphie und Fazies im Unteren Toarcium Sudwestdeutschlands und Vergleiche mit benachbarten Gebieten. Tubinger Mikropalaontologische Mitteilungen 3: 232 pp.

Röhl, H-J, Schmid-Röhl, A., 2005. Lower Toarcian (Upper Liassic) black shales of the Central European Epicontinental Basin: A sequence stratigraphic case study from the SW German Posidonia Shale. In: The Deposition of Organic-Carbon-Rich Sediments: Models, Mechanisms, and Consequences, SEPM (Society for Sedimentary Geology) Spec. Publ 82: 165-189. ISBN 1-56576-110-3

Sachse, V.F., Littke, R., Jabour H., Schümann, T., Kluth, O., 2012. Late Cretaceous (late Turonian, Coniacian and Santonian) petroleum source rocks as part of an OAE, Tarfaya Basin, Morocco. Mar Pet Geol 29(1):35–49

Sanchez-Hernandez, Y., Florentin, J.M.M., 2016. The infuence of regional factors in the expression of oceanic anoxic event 1a (OAE1a) in the semi-restricted Organyà Basin, south-Central Pyrenees, Spain. Palaeogeogr Palaeoclimatol Palaeoecol 441:582–598

Schegg, R., & Leu, W., 1998. Analysis of erosion events and palaeogeothermal gradients in the North Alpine Foreland Basin of Switzerland. In S. J. DuÈppenbecker, & J. E. Ili€ e, Basin modelling: Practice and progress, 141 (pp. 137±155). Geol. Soc. Special Publication.

Schlanger, S.O., Jenkyns, H.C., 1976. Cretaceous oceanic anoxic events: causes and consequences. Geologieenmijnbouw 55(3-4):179–184

Singh, B., Singh, S., & Bhan., U., 2022. Oceanic anoxic events in the Earth's geological history and signature of such event in the Paleocene-Eocene Himalayan foreland basin sediment records of NW Himalaya, India. Arab J Geosci 15, 317 https://doi.org/10.1007/s12517-021-09180-y

Stach, E., Mackowsky, M. Th., Teichmuller, M., Taylor, G. H., Chandra, D. and Teichmuller, R., 1982. Stack's Textbook of Coal Petrology (3rd edition), Gebrüder Borntraeger (Berlin & Stuttgart), 535 pp.

Suan, G., Mattioli, E., Pittet, B., Mailliot, S., Lécuyer, C., 2008. Evidence for major environmental perturbation prior to and during the Toarcian (Early Jurassic) oceanic anoxic event from the Lusitanian Basin, Portugal. Paleoceanography 23(1):PA1202

Sykes, R., Snowdon, L.R., 2002. Guidelines for assessing the petroleum potential of coaly source rocks using Rock-Eva pyrolysis. In: Organic Geochemistry, 33, 1441-1445.

Tewari, A., Hart, M.B. and Watkinson, M.P., 1996. Foraminiferal recovery after the mid-cretaceous oceanic anoxic events (OAEs) in the Cauvery Basin, Southeast India. Geological Society, London, Special Publications, 102(1), 237–244

Tissot, BP., Welte, D.H., 1984. Petroleum Formation and Occurrence. A New Approach to Oil and Gas Exploration. Springer, 702 pp.

Tissot, B.P., Pelet, R. & Ungerer, Ph., 1987. Thermal History of sedimentary basins, Muturation Indices and Kinetics of Oil and Gas generation. Bull. Am. Ass. Petr. Geol., 71/12, 1445-1466.

Tourtelot, H.A., 1979. Black Shale, Its Deposition and Diagenesis. Clays Clay Miner. 27, 313–321. https://doi.org/10.1346/CCMN.1979.0270501

Traverse, A., 2007. Paleopalynology. In: Topics in geobiology (Vol. 28). Dordrecht: Springer

Treibs, A., 1936. Chlorophyll- und Häminderivate in organischen Mineralstoffen. Angew. Chem. **49**, 682.

Tsikos, H., Jenkyns, H.C., Walsworth-Bell, B., Petrizzo, M.R., Forster, A., Kolonic, S., Erba, E., Silva, I.P., Baas, M., Wagner, T., Damsté, J.S., 2004. Carbon-isotope stratigraphy recorded by the Cenomanian–Turonian oceanic anoxic event: correlation and implications based on three key localities. J Geol Soc 161(4):711–719

Tyson, R. V., 1995. Sedimentary organic matter- Organic facies and palynofacies. London: Chapman and Hall.

Tyson, R.V., 1995. Sedimentary Organic Matter. Organic Facies and Palynofacies.

Veron, J., 2005. The Alpine Molasse Basin – Review of Petroleum Geology and Remaining Potential. Bull. Angew. Geol., 10, 75-86.

Voigt, S., Erbacher, J., Mutterlose, J., Weiss, W., Westerhold, T., Wiese, F., Wilmsen, M., Wonik, T.,2008. The Cenomanian-Turonian of the Wunstorf section-(North Germany): global stratigraphic reference section and new orbital time scale for oceanic anoxic event 2. Newsl Stratigr 43(1):65

Volkman, J.K., 2022. Future Outlook for Applications of Biomarkers and Isotopes in Organic Geochemistry. Elements ;18(2):115–120.
doi: https://doi.org/10.2138/gselements.18.2.115

Wang, C.S., Hu, X.M., Jansa, L., Wan, X.Q., Tao, R., 2001. The Cenomanian–Turonian anoxic event in southern Tibet. Cretac Res 22(4):481–490

Whiteside, J.H., Grice, K., 2016. Biomarker records associated with mass extinction events. Annual Review of Earth and Planetary Sciences 44: 581-612, doi: 10.1146/annurev-earth-060115-012501

Yule, B., Roberts, S., Marshall, J.E.A., Milton, J.A., 1998. Quantitative spore colour measurement using colour image analysis. Organic Geochemistry 28: 139-149

Ziegler, P.A., 1982. Geological Atlas of Central and Western Europe. Shell International Petroleum Maatschappij BV, Amsterdam 130 pp.

Ziegler, P.A., 1988. Evolution of the Arctic–North Atlantic and the Western Tethys. American Association of Petroleum Geologists, Memoirs 43: 197 pp

8 Publication I

Biomarker and compound-specific isotope records across the Toarcian CIE at the Dormettingen section in SW Germany

Stephen Ajuaba[1,*], Reinhard F. Sachsenhofer[1], Achim Bechtel[1], Francesca Galasso[2], Doris Gross[1], David Misch[1], Elke Schneebeli-Hermann[2]

International Journal of Earth Sciences (2022) 111:1631–1661
https://doi.org/10.1007/s00531-022-02196-z

[1] Lehrstuhl Erdölgeologie, Montanuniversitaet Leoben, Peter-Tunner-Strasse 5, A-8700 Leoben, Austria
[2] Paläontologisches Institut und Museum, Universität Zürich, Karl-Schmid-Strasse 4, CH-8006 Zürich, Switzerland

*corresponding author. E-mail address: stephen.ajuaba@unileoben.ac.at (Stephen Ajuaba)

Abstract

The Toarcian oceanic anoxic event (T-OAE) is associated with a prominent negative carbon isotope excursion (CIE; ~183 Myr). About 10-m-thick organic matter-rich sediments accumulated during the T-OAE in the Southwest German Basin (SWGB). Rock-Eval, maceral and biomarker analysis were used to determine variations of environmental conditions across the CIE interval. Carbon isotope records were determined for various *n*-alkanes, pristane and phytane to contribute to the reconstruction of the paleo-environment and to study the factors controlling molecular $\delta^{13}C$ values.

Geochemical redox indicators provide evidence for photic zone anoxia during the Toarcian CIE, which reached its maximum after deposition of the "Unterer Stein" marker horizon. The 2α-methylhopane index suggests enhanced activity of diazotrophic cyanobacteria, which is also supported by nitrogen isotope data. This distinguishes the SWGB from other basins with Toarcian black shale. Oxygen-depleted conditions, albeit with lower intensity continued after the CIE.

All investigated compounds replicate the negative CIE, but the magnitudes vary considerably. The largest shift is observed for *n*-C_{27} (9 ‰) and reflects the combined effect of the global

CIE and a major change in organic matter input (termination of terrigenous organic matter input). The shift for short-chain *n*-alkanes, pristane, and phytane, interpreted to reflect marine biomass, varies between 4.5 and 5.0 ‰. This is the highest value observed so far for any Toarcian section. $\delta^{13}C$ values of pristane and phytane reach a minimum near the base of the CIE interval and increase upsection. Thus, the maximum negative isotope shift predates the strongest basin restriction by about 450 kyr.

Keywords: organic geochemistry, photic zone anoxia, water column stratification, bacterial activity, oceanic anoxic event

Author contributions

SA, RFS, AB, and DG contributed to the study conception and design. FG and ESH took and prepared the samples. SA performed the analysis and interpreted the data. RFS, AB, FG, DG, DM and ESH helped interpret the data. SA wrote the first draft of the manuscript and all authors commented on previous versions of the manuscript. All authors read and approved the final manuscript.

Acknowledgments

The authors thank Annette Schmid-Röhl for providing access to the Dormettingen mine. FG and ESM acknowledge support by project n° 200021_175540/1 of the Swiss National Science Foundation. The paper benefited greatly from very detailed constructive reviews by W. Rübsam and an anonymous reviewer as well as by editorial comments by U. Riller.

Funding Swiss National Science Foundation (project n° 200021_175540/1 to Elke Schneebeli-Hermann).

Availability of data and materials Data in the manuscript and appendix will be published as replication data set in Pangaea.

Code availability Not applicable.

Declarations

Conflict of interest All authors declare that they have no conflict of interest.

Ethics approval Not applicable

Consent to participate Not applicable

Consent for publication Not applicable

Introduction

The Early Jurassic (Toarcian) is characterized by global climate change (Ruebsam and Schwark 2021 and references therein), a marine extinction event (e.g. Harries and Little 1999; Pálfy and Smith 2000; Dera et al. 2010; Caruthers et al. 2013), and a large (3-8‰) negative carbon isotope excursion (Toarcian CIE) (Hesselbo et al. 2000, 2007). Estimates on the duration of the Toarcian CIE range from 300-500 kyr (Boulila et al. 2014; Boulila and Hinnov 2017) to ~620 kyr (Huang and Hesselbo 2014) to 900-1200 ka (Suan et al. 2008, Ruebsam and Al-Husseini et al. 2020).

The Toarcian CIE reflects a perturbation of the global carbon cycle and is potentially associated with the coeval Karoo-Ferrar Large Igneous Province (LIP) (~183-182 Ma) (Pálfy et al. 2002; Burgess et al. 2015; Ivanov et al. 2017), but the ultimate trigger for the CIE, which affected the global oceanic and atmospheric carbon reservoirs (e.g. Hesselbo et al. 2000), is still disputed (Silva et al. 2021). Carbon degassing from the Karoo-Ferrar LIP (Pálfy and Smith 2000), generation and release of thermogenic methane during emplacement of the Karoo-Ferrar LIP (e.g. Wignall 2001; Svensen et al. 2007), recycling of isotopically light dissolved inorganic carbon from deeper levels of a stratified water body (e.g. Küspert 1982; Jenkyns 1985; van de Schootbrugge et al. 2005), dissociation of methane hydrate in marine sediments (e.g. Hesselbo et al. 2000, Kemp et al. 2005), increased methane emission from expanding swamps and wetlands (Them et al. 2017), melting of permafrost (Ruebsam et al. 2019; Ruebsam and Schwark 2021), or increased CO_2 release from the decomposition and oxidation of terrigenous organic matter associated with increased fungal activity (Pienkowski et al. 2016) have been discussed recently. Regardless of the trigger of the carbon release event, high temperatures and an enhancement of the hydrological cycle resulted in strongly (six-fold) increased global weathering rates (Cohen et al. 2004; Kemp et al. 2020).

Black shales with total organic carbon (TOC) contents exceeding 10 wt.% have been deposited during and after the Toarcian CIE in many European basins, characterizing the interval, which is known today as early Toarcian oceanic anoxic event (T-OAE; Jenkyns 1985, 1988; 2010; Neumeister et al. 2015; Silva et al. 2021). Lower Toarcian rocks with very high organic matter contents occur in the Central European Epicontinental Basin System (CEBS; Fig. 1) where they are important petroleum source rocks (e.g. Littke et al. 1991a, b; Cornford 1998; Song et al. 2015). These rocks are known as Posidonia Shale in Germany, Whitby Mudstone in England, or Schistes Carton in France (Jenkyns 1985; Baudin 1995; Röhl and Schmid-Röhl 2005). However, coeval sediment successions from southern Europe

(Italy, Portugal, Spain) and from northern Africa lack organic matter-rich deposits (e.g. de Oliveira et al. 2006; Hesselbo et al. 2007; Rodrigues et al. 2020; Silva et al. 2021).

Detailed carbon isotope records from carbonate minerals and bulk organic matter are available for a great number of sections across the Toarcian CIE (e.g. Röhl et al. 2001; Hesselbo et al. 2007; Kemp et al. 2005, 2020; Hermoso et al. 2012; Suan et al. 2015; Them et al. 2017; for a review see also Ruebsam and Al-Husseini et al. 2020). In contrast, few papers used carbon isotope data of specific organic compounds (e.g. Pedentchouk and Turich 2017), although Schouten et al. (2000), van Breugel et al. (2006), French et al. (2014), Ruebsam et al. (2020) and Xu et al. (2021) indicated their great potential as a proxy for marine and atmospheric carbon isotope ratios. The most complete data set has been published by French et al. (2014). These authors used molecular (biomarker) analysis to reconstruct the depositional environment of the Hawsker Bottoms section in the Cleveland Basin (England) and reported in parallel compound-specific $\delta^{13}C$ records of short- and long-chained n-alkanes and isoprenoids.

The present paper uses a similar approach and has several goals. The first goal is to reconstruct the depositional environment of the lower Toarcian rocks in the Southwest German Basin using biomarker data, the second goal is to study differences in carbon isotope trends of bulk organic matter and those of specific molecular fossils (*n*-alkanes, pristane, phytane). Finally, the comprehensive interpretation of biomarker and compound-specific isotope (CSI) data will help to determine the factors controlling CSI patterns and will improve the understanding of the time relation between the development of anoxia and processes, which influence carbon isotopy.

The study is based on sample material from the 12-m-long Dormettingen section, which has been investigated previously regarding bulk organic matter isotopy, palynofacies, and palynology (Galasso et al. 2021; Galasso et al. subm.; Fig. 2; for location see Fig. 1). In addition, Re-Os data are available for this section (van Acken et al. 2019). Another advantage of Dormettingen is its location only two kilometers northwest of the Dotternhausen section, which has been studied in great detail using different sedimentological, paleontological, and geochemical techniques (e.g. Riegraf 1985; Schouten et al. 2000; Röhl et al. 2001; Röhl and Schmid-Röhl 2005, van de Schootbrugge et al. 2005; Bour et al. 2007; Mattioli et al. 2008; Suan et al. 2008; 2015; Wang et al. 2020, 2021). This section is no longer accessible, but the presence of marker horizons allows the detailed correlation of data from Dotternhausen to the Dormettingen quarries.

Geological Setting

The epicontinental Central European Basin covered large parts of central and northern Europe during the Jurassic. It widened towards the Tethys Ocean and included several basins that were separated by submarine shoals and island of variable size (Ziegler 1982; 1988) (Fig. 1a). During Toarcian time, a pronounced topography together with climate change and eustatic sea level variations (see Ruebsam and Al-Husseini 2021 for a review) caused stratified water bodies with strongly depleted oxygen contents in a geographically wide area of the CEBS (e.g. Röhl et al 2021; Schwark and Frimmel 2004, Hermoso et al. 2013; Song et al. 2015; 2017).

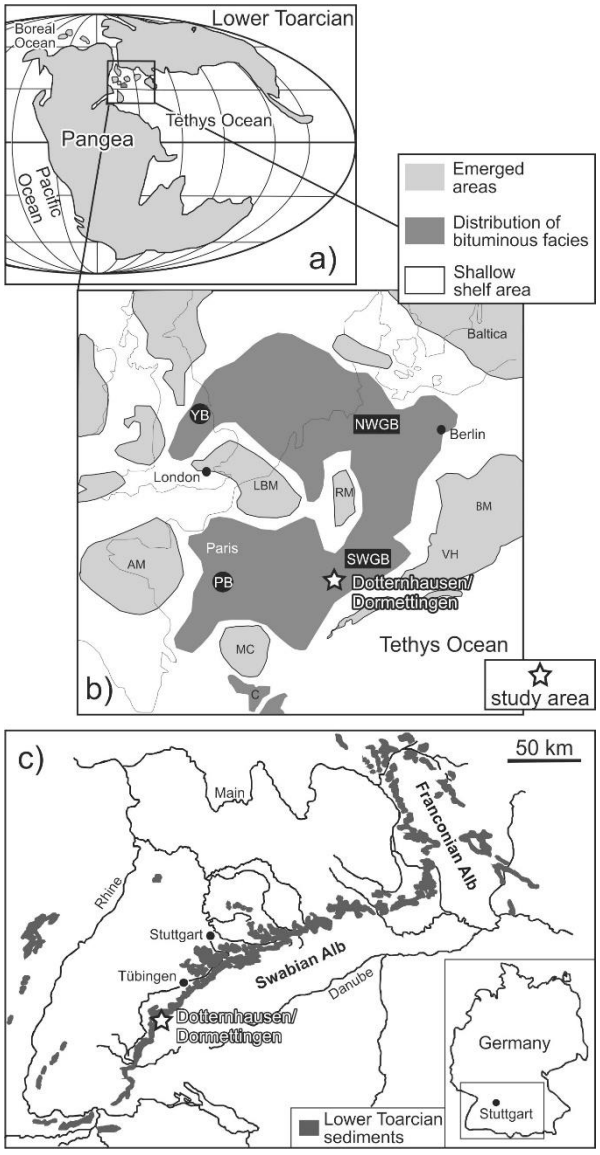

Fig. 1 a) Paleogeographic sketch of the early Toarcian; b) early Toarcian paleogeography of the epicontinental Central European Basin with the distribution of bituminous black shale across various sub-basins (SWGB: SW German Basin, NWGB: NW German Basin, YB: Yorkshire Basin and PB: Paris Basin); c) Outcrops of the lower Toarcian

sediments in southwestern Germany. The white star indicates the study area (Dormettingen). Maps are modified after Röhl et al. (2001), Ziegler (1982) and Galasso et al. (2021)

The Southwest German Basin, where the study site is located, was located at the southeastern fringes of the Central European Basin System (Fig. 1a). It was connected with the Paris Basin (Hollander et al. 1991, Hermoso et al. 2009; 2014; Song et al. 2014), the Northwest German Basin (e.g. Littke et al. 1991a) and the Cleveland Basin (Hesselbo et al. 2000; Bowden et al. 2006; Kemp et al. 2011; French et al. 2014). The Vindelician High (VH in Fig. 1b) separated the Southwest German Basin from the Tethys Ocean till ongoing transgression caused flooding of the Vindelician High in the Middle/Late Jurassic (Meyer and Schmidt-Kaler 1996).

The Posidonia Shale including the Toarcian CIE and the T-OAE in the Southwest German Basin has been described in great detail (e.g. Schouten et al. 2000; Röhl et al. 2001; Frimmel et al. 2004; Röhl and Schmid-Röhl 2005; van de Schootbrugge et al. 2005; Bour et al. 2007, Schwark and Frimmel 2004; Suan et al. 2008; 2015; Hougård et al. 2021). The following description of the Posidonia Shale in the Southwest German Basin is based on the Dormettingen section (van Acken et al. 2019; Galasso et al. 2021; Fig. 2), which is the focus of the present study.

The Posidonia Shale is underlain by light to dark grey bioturbated marls and marly limestones which are assigned to the Pliensbachian Amaltheenton Formation (*Pleuroceras spinatum* Zone). The presence of a diverse benthic fauna implies high oxygen availability (Röhl and Schmid-Röhl 2005). A limestone bed (Costatenkalk), tens of cm thick, marks the uppermost bed of the Amaltheenton Formation (Riegraf 1985; Röhl et al. 2001; Röhl and Schmid-Röhl 2005).

The Posidonia Shale follows above the Costatenkalk without a break in sedimentation (Galasso et al. 2021). The 12-m-thick succession includes the uppermost part of the *Dactylioceras tenuicostatum* ammonite zone, the *Harpoceras falciferum* and *Hildoceras bifrons* zones and their subzones (Fig. 2) (Riegraf 1985; Röhl et al. 2001; Röhl and Schmid-Röhl 2005).

Sediments of the *tenuicostatum* Zone are dominated by light-grey bioturbated marls with benthic fauna (Blaugraue Mergel, Aschgraue Mergel). Two black shale layers (Tafelfleins, Seegrasschiefer), each several centimeters thick, are intercalated between the marls. The

Fleins Bed near the top of the *tenuicostatum* Zone signals the onset of Toarcian CIE and continuous black shale deposition, which continued during the *falciferum* and *bifrons* Zones.

Black shales with wavy and lenticular lamination were deposited during the *falciferum* Zone, but lamination becomes less distinct in its upper part (*falciferum* Subzone; van Acken et al. 2019). The black shale succession is marked by the intercalation of five prominent limestone beds which form regional marker horizons. They are labelled from base to top: Unterer Stein (20-30 cm thick), Steinplatte (~10 cm thick), Oberer Stein (~ 20 cm thick), Obere Bank (~ 10 cm thick) and Inoceramenbank (~10 cm thick) (Fig. 2). The lowermost limestone bed (Unterer Stein; *exaratum* Subzone) is used as lower Toarcian marker horizon in the southern part of the Central European Basin (Riegraf 1982; van de Schootbrugge et al. 2005). The Inoceramenbank marks the boundary between the *falciferum* and *bifrons* Zones. Dark shales in the *bifrons* Zone show indistinct lamination.

Bulk organic carbon isotope data indicate that the Toarcian CIE in the Dormettingen section is located between 10.1 and 7.3 m (uppermost *semicelatum* to middle *elegans* Subzones; Fig. 2) and that the Steinplatte marker bed forms the top of the CIE (Galasso et al. 2021). This is in agreement with the extension of the CIE at Dotternhausen according to Mattioli et al. (2008). However, a slightly higher position (e.g. Suan et al. 2008) seems also possible. Using carbon isotope trends of bulk organic matter, Suan et al. (2008) subdivided the Toarcian CIE at Dotternhausen into three phases: A phase with strongly decreasing $\delta^{13}C$ values near the *tenuicostatum-falciferum* boundary (C1), a phase of rather constant negative values (C2) and a phase of marked $\delta^{13}C$ increase (C3) which starts near the top of the Unterer Stein marker bed (Fig. 2). Durations of ~150 kyr, ~450 kyr and 300 kyr have been estimated for C1, C2 and C3, respectively, by these authors. If these estimates are correct, accumulation rates were very low during the Toarcian CIE (~3 mm/kyr) (cf. Tyson, 2001). The amplitude of the CIE is very high (~7 ‰), but Suan et al. (2015) emphasized that part of the CIE is due to changes in organic matter composition.

Particulate organic matter (POM) data justify the subdivision of the Posidonia Shale into five palynofacies intervals, labelled from base to top A to E (Galasso et al. 2021; Fig. 2). Palynofacies A is documented in POM assemblages from below the Fleins Bed (*tenuicostatum* Zone) and is characterized by high amounts of terrigenous phytoclasts sporomorphs and dinoflagellate cysts. Palynofacies B coincides with the Toarcian CIE. Its assemblages are characterized by high amounts of amorphous organic matter and the lack of dinoflagellate cysts. Dinoflagellate cysts reappear in palynofacies C, which includes the

remaining part of the *falciferum* Zone. Palynofacies D and E occur within the *bifrons* Zone. They are marked by relatively higher (D) and lower (E) contributions of terrigenous phytoclasts and sporomorphs (Galasso et al. 2021).

A Re/Os age from the Dormettingen section (183.0 ± 2.0 Ma) agrees well with previous estimates of the age of the Toarcian CIE (van Acken et al. 2019). Low initial $^{187}Os/^{188}Os_i$ ratio (0.377 ± 0.065) is consistent with a significant influx of mantle-derived material into the Toarcian ocean from weathering of Karoo-Ferrar LIP basalts (van Acken et al. 2019).

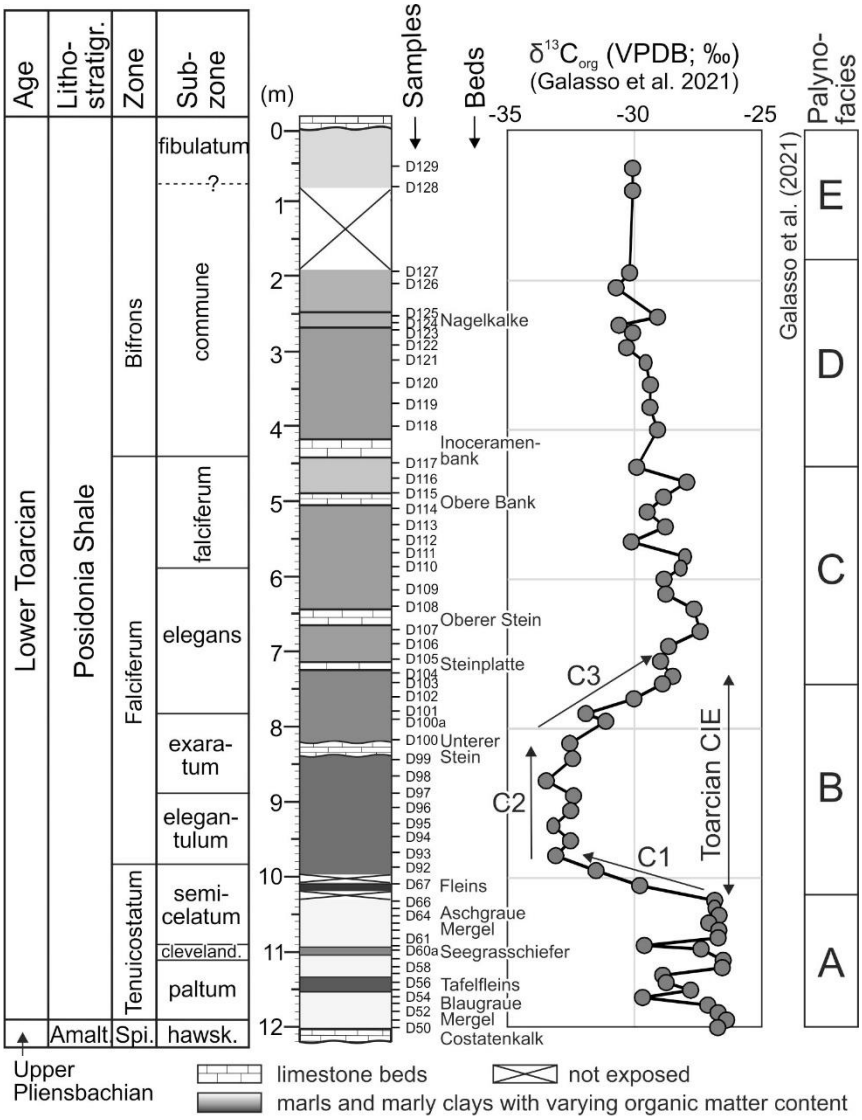

Fig. 2 Stratigraphy of the Dormettingen section with ammonite zones and subzones, bulk organic carbon isotope curve, and subdivision into palynofacies intervals (after Galasso et al. 2021). The subdivision of the Toarcian CIE into phases C1 to C3 follows Suan et al. (2008). Position of samples investigated by Galasso et al. (2021) (D50-D67; D92-D129) is shown. The identical samples are also used in the present study. (Because of limited space, some samples are unlabeled)

Samples and analytical methods

The present paper is based on rock samples which have been collected for palynological and carbon isotope studies (Galasso et al. 2021). The stratigraphic position of the samples within the Dormettingen section (D50-D67; D92-D129) is shown in Fig. 2. Samples D50-D127 were collected in October 2018 from freshly mined areas of the Dormettingen quarry, while the uppermost samples (D128-D129) are from older parts of the quarry, which was opened in 2008. The sample size is small, between 0.5 and 2.0 cm^3, to minimize time averaging effects. The remains of three samples (D92, D95; D123) were too small and did not allow geochemical investigations. Therefore, a total of 56 samples are included in the present study. Sample D99 represents the Unterer Stein, a limestone marker bed in the Toarcian CIE. As both the study of Galasso et al. (2021) and the present study focus on organic material, other limestone beds within the Posidonia Shale were not sampled.

Rock powders from all samples were analyzed for total carbon (TC; %), total sulfur (TS; %) and total organic carbon (TOC; %) using an Eltra Helios CS elemental analyzer. TOC contents were measured on samples pre-treated with concentrated phosphoric acid. TOC and TC were used to calculate the equivalent calcite content ($calcite_{equiv.}$ = 8.334 x [TC-TOC]).

Rock-Eval parameters S_1 and S_2 (mgHC/g rock) and T_{max} (°C) were determined using a "Rock-Eval 6" instrument. S_1 and S_2 are the amounts of hydrocarbons volatized at 300°C and during gradual heating from 300 to 650°C, respectively. T_{max} is a maturity parameter and corresponds to the temperature at which a maximum of S_2 hydrocarbons is formed. S_1 and S_2 were used to calculate the hydrogen index ($HI=100*S_2/TOC$) and the production index ($PI=S_1/[S_1+S_2]$) (Espitalié et al. 1977).

Based on the bulk geochemical data and their stratigraphic distribution, 24 samples were selected for organic petrography, biomarker, and isotope investigations. Semi-quantitative maceral analysis was performed on polished blocks using white and fluorescence light, a 50× oil immersion objective, and a Leica DM 4P microscope. Depending on TOC contents, 1000 to 1500 points were counted in a single scan and standardized to 100% organic matter. This maceral analysis was performed in accordance with the ICCP System (ICCP 1998, 2001; Pickel et al. 2017). Vitrinite reflectance measurements were performed on two samples (25-50 measurements per sample) using the same microscope and an yttrium-aluminiun-garnet standard (Rr: 0.899%).

For biomarker analysis, 5-10 g of powdered rock samples were extracted for ~1 h using a Dionex ASE 350 Accelerated Solvent Extractor with dichloromethane as solvent at 75°C and 100 bar. The extraction solvent was evaporated to ~0.5 ml total solution using a Zymark TurboVap 500 closed cell concentrator. Afterwards, asphaltenes were precipitated from a hexane:dichloromethane solution (80:1 according to volume) and separated by centrifugation.

The hexane-soluble fractions were split into NSO compounds and saturated and aromatic hydrocarbons using the medium pressure liquid chromatography (MPLC) device of Köhnen-Willsch (Radke et al. 1980).

n-Alkanes and isoprenoids within the saturated hydrocarbon fractions were analyzed using a gas chromatograph (Trace GC-Ultra) with a flame ionization detector (GC-FID). The gas chromatograph was equipped with a 50 m HP-PONA capillary column (inner diameter [i.d.] 0.20 mm, 0.50 µm film thickness). After sample injection (2 µl at 270°C), the oven temperature was increased from 70°C to 310°C and held constant for 35 min.

Biomarker molecules in the saturated and aromatic hydrocarbon fractions were analyzed by gas chromatography-mass spectrometry (GC-MS) using a Thermo Scientific Trace GC-Ultra equipped with a Triplus 100 liquid auto sampler and interfaced to a ThermoFischer ISQ single quadrupole mass spectrometer. The spectrometer was operated in the EI (electron ionization) mode scanning from *m/z* 50 to *m/z* 650 (0.7 s total scan time). Prior to analysis, proportionate amounts of internal standards (squalane for aliphatics; 1,1´-binaphthyl for aromatics) were added to each sample. Measurements were performed with a 60 m DB-5MS fused capillary column (i.d. 0.25 mm; 0.25 µm film thickness). The GC oven temperature was initially programmed from 40°C (held for 2 minutes) and ramped to 310°C with 4°C/min, followed by an isothermal period of 40 minutes. Sample injection was done in a split mode (split ratio 20) at 260°C using helium as carrier gas. The aliphatic fractions of selected samples were additionally analyzed with a Trace^{TM} 1300 GC (ThermoFisher) equipped with a 60 m TG-5MS fused silica capillary column (i.e. 0.25 mm; 0.25 µm film thickness) coupled to a ThermoFisher TSQ9000 triple quadrupole GC-MS/MS. The oven was programmed to hold 40°C for 2 minutes and then heated to 310°C with 4°C/min, followed by an isothermal period of 40 min. The sample was injected splitless with an injector temperature of 310°C. For the detection of methylsteranes isomers, a selected reaction monitoring process (SRM) was used. Different parent-to-daughter ion transitions (*m/z* 386–231, 400–231, 414–231, 414–98) were monitored to obtain C_{28} to C_{30} methylsteranes and dinosteranes.

Data was processed with Xcalibur and Chromeleon data system. Individual compound identification was based on their respective retention time within the mass spectra or total ion current (TIC) chromatogram and by comparing the mass spectra with published data. In the case of mass chromatograms, response factors were used to account for corrections of the fragment ions used for quantification of the total ion abundance while for TIC chromatograms, absolute concentrations were calculated for different saturated and aromatic compounds in relation to their internal standards per sample.

A semi-quantitative calculation of the target compounds was conducted based on results of total ion current (TIC) chromatograms. Thereby, methylsteranes which could be detected in TIC (total ions as well as *m/z* 231) and for which a calculation of the amount was possible were used for further calculations. Areas of specific compounds were taken then from the SRM mode and were set into relation to the TIC. With this relation, a proper estimation of the amount of methylsteranes was possible.

The *n*-alkanes were separated from branched/cyclic hydrocarbons by an improved 5 Å molecular sieve method (Grice et al. 2008) for the analysis of stable carbon isotope ratios on individual n-alkanes and isoprenoids. Compound specific carbon isotope measurements of the *n*-alkanes and isoprenoids were performed using a Trace GC-Ultra gas chromatograph attached to the ThermoFischer Delta-V isotope ratio mass spectrometer (IRMS) via a combustion and high temperature reduction interface (GC Isolink, ThermoFischer). The GC column is as described above, while the oven temperature was programmed to 70°C for 2 min followed by a 4°C/min increment to 300°C and held for 15 min. For calibration, a CO_2 standard gas was injected before and after each analysis. Each sample was analyzed in duplicate. The mean isotope composition is reported in the δ notation in permil (‰) relative to the V-PDB standard. Analytical reproducibility of the total procedure is in the range of 0.1 to 0.3 ‰.

Results

Bulk geochemistry

Inorganic and organic bulk parameters of the Dormettingen section are shown in Fig. 3. Calcite equivalent percentages below the Toarcian CIE range from 25 to 41 wt.%. Within the CIE carbonate contents are relatively low (20-40 wt.%), but high in the limestone marker bed (Unterer Stein: 91 wt.%). Calcite contents of marls above the CIE range from 27-60 wt.%. Limestone beds above the CIE have not been investigated, as the focus of the present study lies on the organic matter-rich rocks.

TOC contents in marls below the Toarcian CIE are typically low (0.2-0.9 wt.%). Only sediments related to the Tafelfleins and Seegrasschiefer contain high amounts of organic matter (max. 11.1 wt.%). Apart from the limestone marker (Unterer Stein: 1.1 wt.% TOC), TOC contents in the T-OAE range from 7.1 to 12.2 wt.%. TOC contents remain high above the CIE (4.0-10.4 wt.%).

Sulphur contents range from 0.6 to 4.4 wt.% and show a similar vertical trend than TOC contents. Only the two uppermost samples (*fibulatum* Subzone) contain very low amounts of sulphur (0.2-0.3 wt.%), probably due to weathering. TOC/S ratios below the Toarcian CIE interval are typically below 1, whereas higher ratios are observed in the organic-rich layers. Within the CIE interval TOC/S ratios vary between 2.0 and 4.0. Lower ratios are restricted to the limestone bed (Unterer Stein). Above the CIE interval TOC/S ratios range from 1.5 to 3.9. Very high ratios (~30) in the uppermost samples probably reflect weathering (cf Ruebsam et al. 2018).

Hydrogen index (HI) values of low-TOC samples below the Toarcian CIE increase upwards from 53 to 161 mgHC/gTOC. HI of the black shale layers varies between 459 and 649 mgHC/gTOC. Similar values are observed within the CIE (556-699 mgHC/gTOC) and above the CIE (612-728 mgHC/gTOC). HI values in the *fibulatum* Subzone (~480 mgHC/gTOC) may be reduced by weathering.

T_{max} values vary between 422 and 429°C (average 427°C) and show a subtle upward increasing trend (Table 1). The PI ranges from 0.01 to 0.09 (average 0.04).

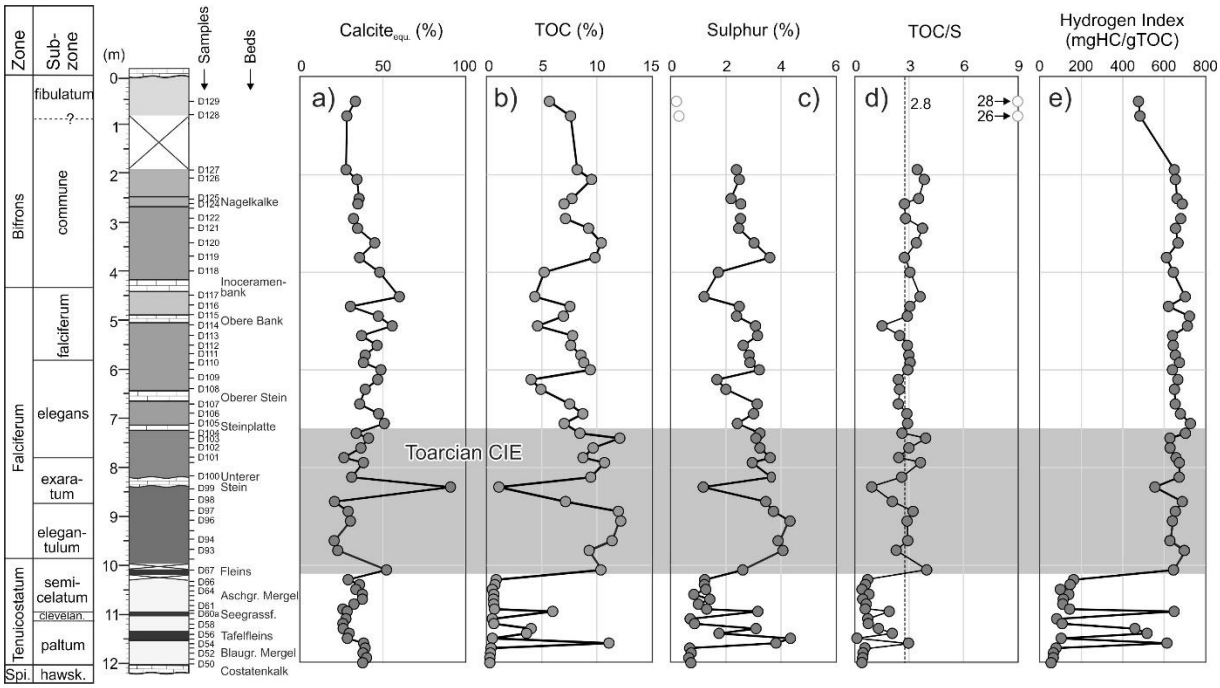

Fig. 3 Stratigraphic profile across the Dormettingen section (after Galasso et al. 2021) with calcite equivalent percentages, total organic carbon (TOC) and sulfur (S) contents, TOC/S ratios, and hydrogen index (HI). Sulphur contents and TOC/S ratios of samples D128/129 are probably influenced by weathering and, therefore, shown by open symbols

Organic petrography

Semi-quantitative maceral analysis shows that the organic matter of the Toarcian shales at Dormettingen is dominated by liptinite macerals (Table 2; Fig. 4), particularly alginite (50-81 vol.%) and liptodeterinite (14-41 vol.%). Telalginite dominates over lamalginite in samples below the CIE and in the upper part of the CIE (D98, D100, D101), while lamalginite prevails in most of the remaining samples. Telalginite includes Tasmanales algae beside of significantly smaller telalginite macerals (e.g. Fig. 4b,f). Tasmanales algae are especially abundant in sample D101 from the upper part of the CIE. Liptodetrinite (e.g. Fig. 4d) is probably also derived from algal material and occurs in high quantities (~40 vol%) in sample D57 (Tafelfleins) and in samples D98 and D100 from the Toarcian CIE interval. Sporinite is generally very rare and is observed in quantities exceeding 1 vol.% only in sediments above the CIE (Table 2).

Percentages of inertinite (including recycled vitrinite) and vitrinite macerals are typically below 10 vol.% (Table 2). Relatively high percentages of terrigenous macerals occur in marl samples below the CIE (e.g. D60; Fig. 4e). In contrast, terrigenous macerals occur in negligible amounts in most samples from the Toarcian CIE (Fig. 4). Primary vitrinite is rare in comparison with recycled vitrinite. Pyrite (mostly framboidal; e.g. Fig. 4f) is abundant in all samples, but rare in low-TOC samples below the CIE (D60, D62, D65) and in the uppermost sample (D128). Fish remains are abundant in some samples (e.g. D118). Vitrinite reflectance measurement gave values of 0.41 and 0.55 %Rr for samples D127 and D115, respectively.

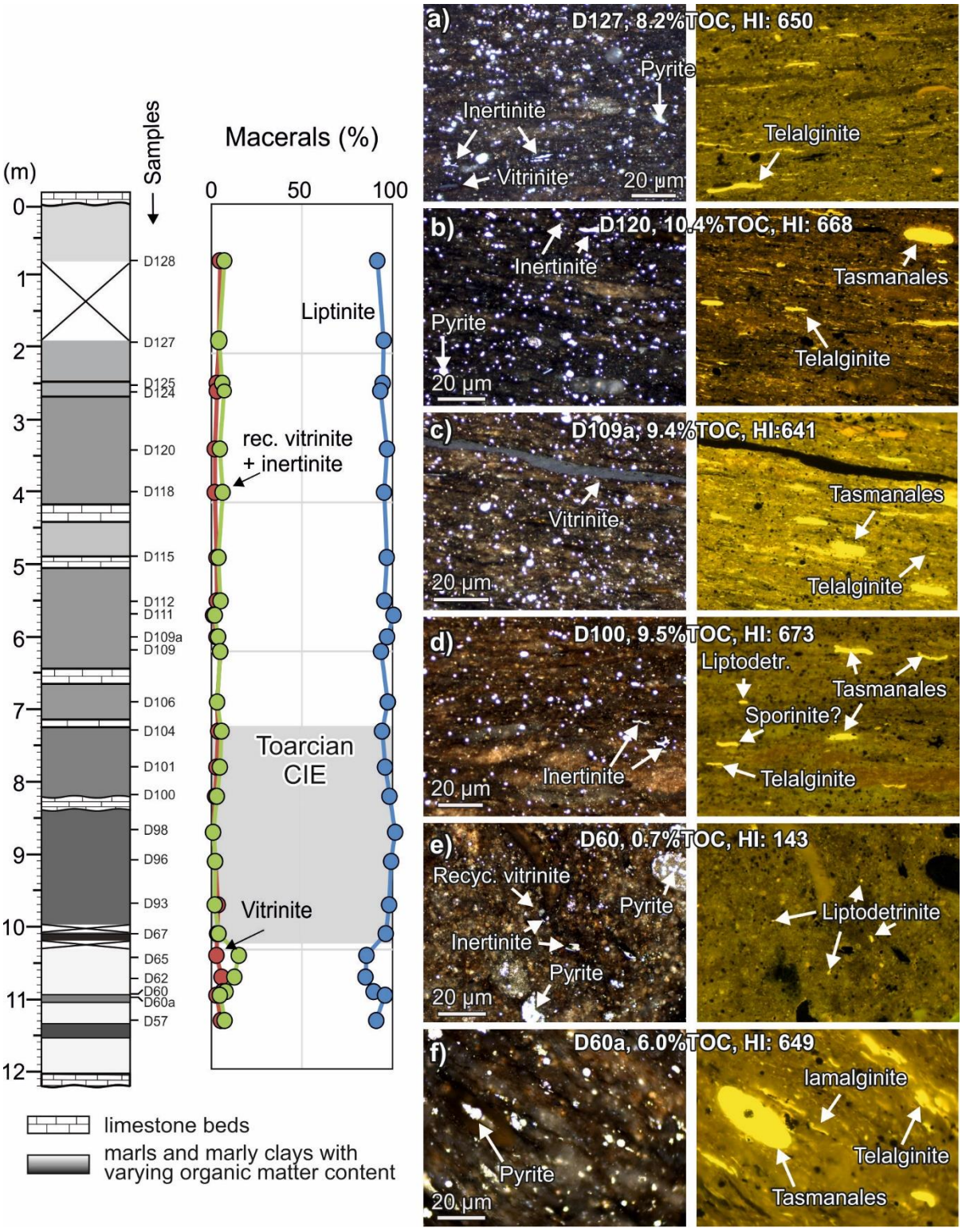

Fig. 4 Maceral composition of Dormettingen samples with micro-photomicrographs of selected samples (left: white light; right: fluorescence mode)

Molecular composition of hydrocarbons

GC-FID and GC-MS traces of representative samples are presented in Figs. 5 and 6. Concentrations and ratios of selected organic compounds are listed in Table 3 and are plotted versus stratigraphic height in Fig. 7.

n-alkanes and isoprenoids

n-Alkanes are abundant in all samples and show broad chain length distributions (*n*-C_{13-35}) (Fig. 5). Short-chain *n*-alkanes are always dominating (*n*-C_{15-19}/∑*n*-alkanes: 0.34-0.50) over mid- (*n*-C_{21-25}/∑n-alkanes: 0.19-0.28) and long-chain *n*-alkanes (*n*-C_{27-31}/∑*n*-alkanes: 0.08-0.16) (Fig. 7a). Three low-TOC samples below the Toarcian CIE (D60, D62, D65) show relative high concentrations of mid- and long-chain *n*-alkanes. The carbon preference index (CPI; according to Bray and Evans 1961) is close to 1 (0.95-1.13) in all samples except for the three low-TOC samples mentioned above (1.39-1.52) (Figs. 5, 7b).

The pristane/phytane (Pr/Ph) ratio (e.g. Didyk et al. 1978) decreases upwards in the lower part of the section (11.3-8.2 m) from 2.6 to 1.8 and reaches a minimum value in the upper part of the *exaratum* Subzone (D100). Between samples D100 (*exaratum* Subzone) and D106 *elegans* Subzone) Pr/Ph ratios increase again and are fairly constant (1.7-1.9) in the upper part of the section (Fig. 7c).

Below the Toarcian CIE the ratio of pristane and phytane versus *n*-C_{17} and *n*-C_{18} (e.g. Frimmel and Schwark 2004) decreases upwards and shows an opposite trend to the Pr/Ph ratio in the Toarcian CIE and the remaining part of the *falciferum* Zone (Fig. 7d). An increase is observed above the Inocermanenbank between samples D118 and D120. The uppermost part of the section is characterized by a constant decrease.

Steroids

Sterane concentrations range from 4 to 96 µg/g TOC (total organic carbon). C_{27} steranes dominate in all samples closely followed by C_{29} steranes (Fig. 5; Table 3). C_{28} steranes are typically less abundant, but relatively high concentrations are observed in samples D109a to D115 within the *falciferum* Subzone (Fig. 7e). The C_{29} sterane 20S/(20S+20R) ratio and C_{29} sterane αββ/(αββ+ααα) ratio are maturity parameters (Seifert and Moldowan 1986) and range from 0.19 to 0.29 (avg. 0.23) and from 0.28 to 0.38 (avg. 0.32), respectively. Both ratios show a subtle upward decrease (Table 3).

C_{27} Diasteranes are present in all samples in lower amounts than their C_{27} regular sterane counterparts (Fig. 5). The C_{27} diasterane/C_{27} regular sterane ratio varies between 0.11 and 0.63 and is especially high in samples below the CIE (Fig. 7f).

4-methylsteranes (C_{28}: 4α-methyl-5α-cholestane; C_{29}: 4α,24-dimethyl-5α-cholestane; C_{30}: 4α-methyl-24-ethyl-5α-cholestane) and dinosterane (4α,23S,24R-trimethyl-5α-cholestane) have been detected in many samples (Fig. 8). The highest concentrations occur in the CIE interval (Table 3; Fig. 7g,h).

Hopanoids and related compounds

The dominant non-aromatic cyclic triterpenoids are hopanes (3-30 µg/g TOC) (Fig. 6; Table 3). The sterane/hopane ratio shows an upward increase with a maximum in sample D120 followed by a decrease (Fig. 7i). Concentrations of C_{31} to C_{35} 17α,21β(H)-homohopanes decrease with increasing carbon number (Fig. 6). 22S/(22S+22R) isomer ratios of αβ C_{31} hopane range from 0.57 to 0.61 (Table 3). The moretane/hopane ratio ranges from 0.19 to 0.29 and is relatively low (≤0.21) within the CIE (Fig. 7j).

The C_{35} homohopane index (HHI = C_{35}/(C_{31}-C_{35}) homohopanes; Peters and Moldowan 2001) is below 0.02 for low TOC samples below the CIE and 0.3 to 0.5 for the rest of the samples without a specific depth trend (Table 3).

Methylhopanes occur in significant amounts in the studied samples and have been identified following Farrimond et al. (2004) and Pancost et al. (1998) (Figs. 7, 9). A minor overlap with regular hopanes occurs for some methylhopanes. Hence, a slight overestimation of the methylhopane concentrations cannot be excluded (Fig. 9, see also Farrimond et al. 2004). The 2α-methylhopane index (2α-MHI; 2α-methylhopane/[2α-methylhopane + hopanes]) and the 3β-methylhopane index (3β-MHI; 3β-methylhopane/[3β-methylhopane + hopanes]) have been calculated according to Summons et al. (1999) and Jiao et al. (2008). The 2α-MHI shows two maxima in the Toarcian CIE, while the 3β-MHI is slightly elevated below the CIE, but overall relatively constant (Fig. 7k).

The Ts/(Ts+Tm) ratio varies between 0.15 and 0.37 (Fig. 7l). The gammacerane index (gammacerane/ (gammacerane+C_{30} hopane) (Sinninghe Damsté et al. 1995) ranges from 0.1 to 0.2 and increases upwards (Fig. 7m).

Apart from hopanes, tricyclic terpanes (TT) also occur with significant concentrations (0.77-14.02 µg/g TOC; Fig. 6). C_{19} to C_{29} TTs are present, but C_{27} TT is absent. The dominant TT is C_{23} TT as reflected by low C_{19}/C_{23} TT (0.01-0.26) and C_{20}/C_{23} TT ratios (0.15-0.44) (Table 3).

Depth plot shows that low-TOC samples below the CIE (D60, D62, D65) are characterized by relatively high C_{19}/C_{23} TT and C_{20}/C_{23} TT ratios (Fig. 7n).

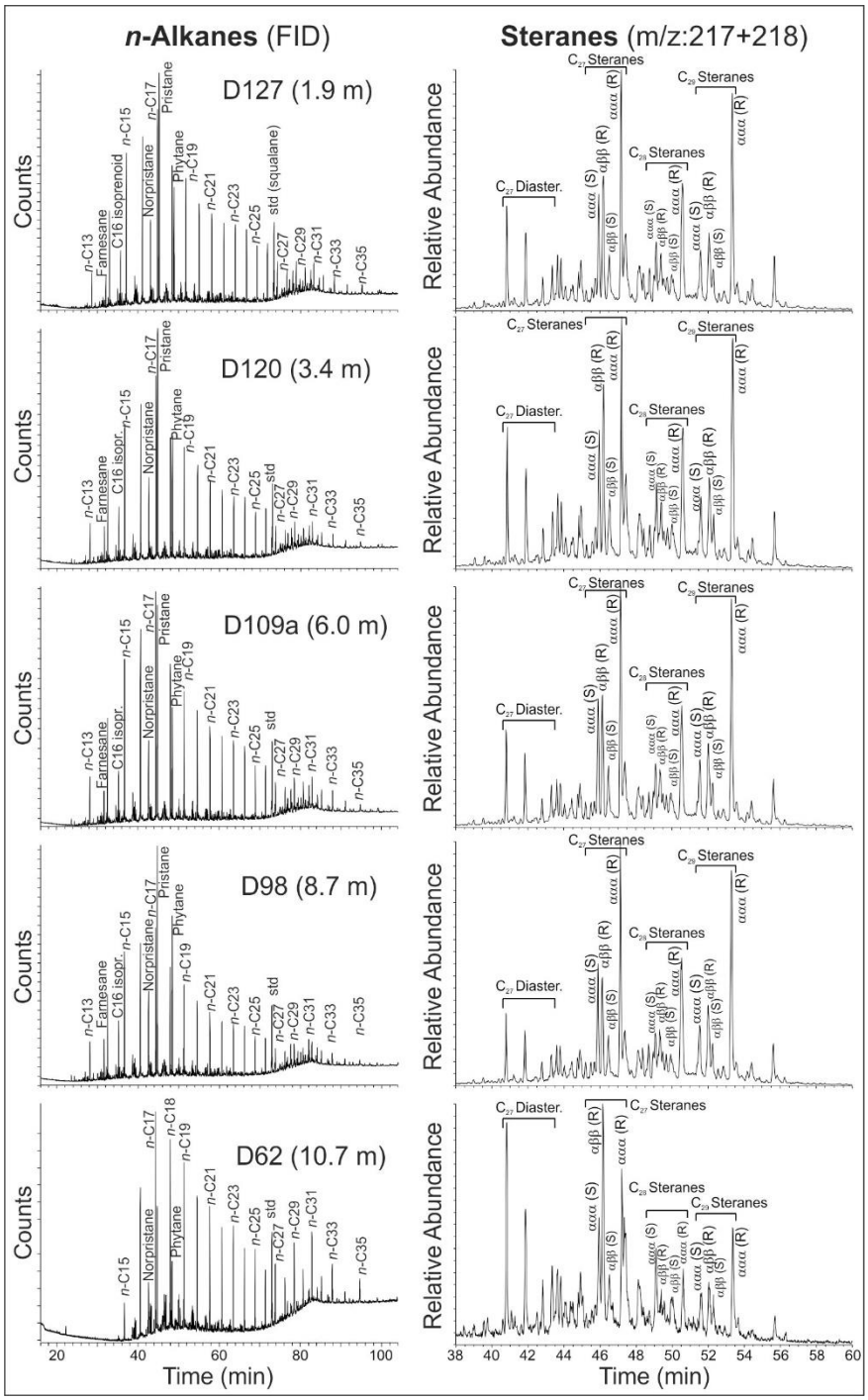

Fig. 5 FID (flame ionization detector) traces of the saturated hydrocarbon fraction, and mass chromatogram representations of steranes of samples from different stratigraphic positions within the Dormettingen section

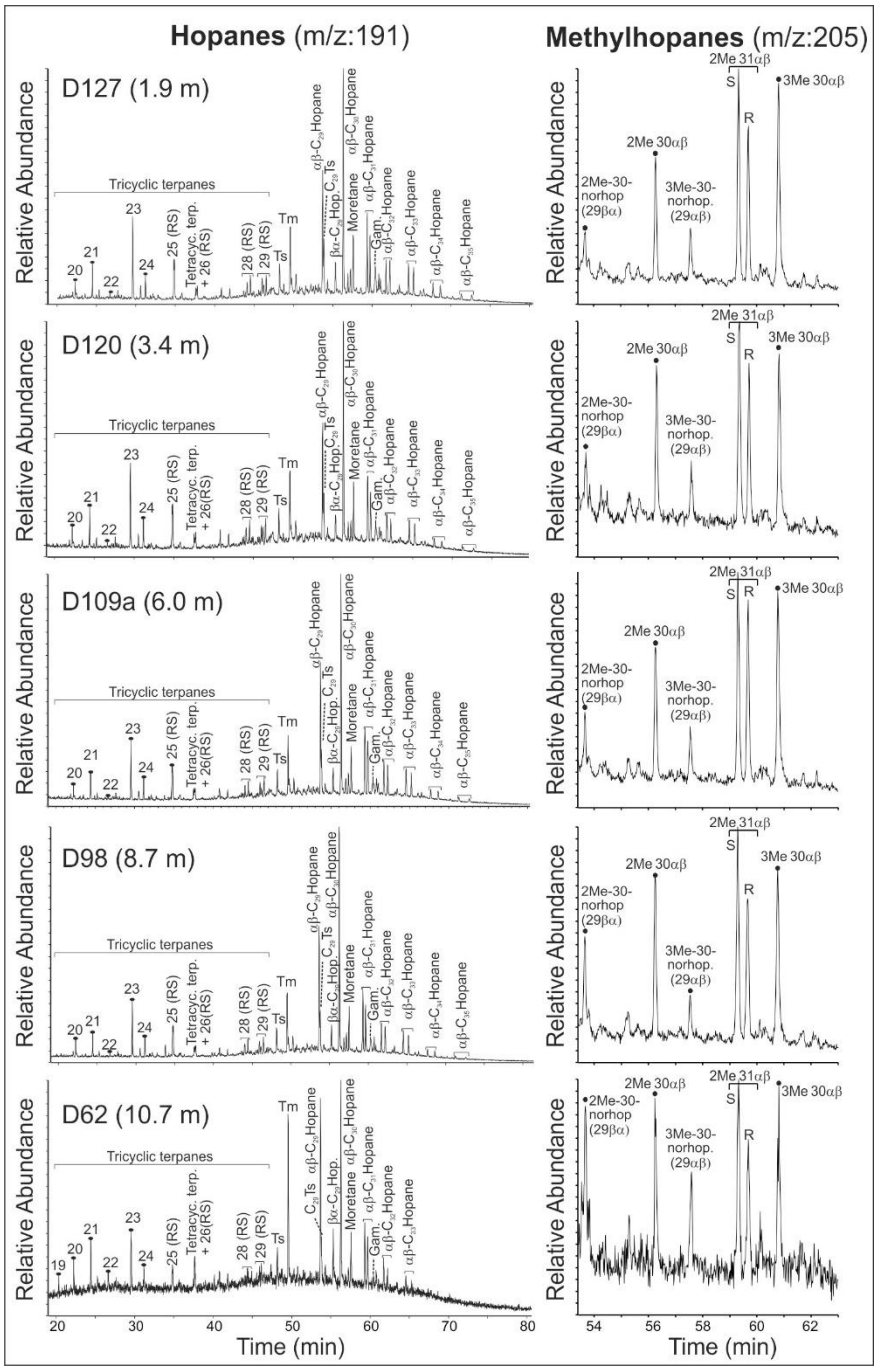

Fig. 6 Mass chromatogram representations of hopanes and methylhopanes of samples from different stratigraphic positions within the Dormettingen section.
2Me-30-norhop - (29βα)-2α(CH_3),17β(H),21a(H)-30-norhopane,
29αβ - 2α(CH_3),17α(H),21β(H)-hopane,
3Me-30-norhop (29αβ) - 3β(CH_3),17α(H),21β(H)-30-norhopane,
2Me 31αβ S - (22S)-2α(CH_3),17α(H),21β(H)-29-homohopane,
2Me 31αβ R - (22R)-2α(CH_3),17α(H),21β(H)-29-homohopane,
3Me 30αβ - 3β(CH_3),17α(H),21β(H)-30-hopane.

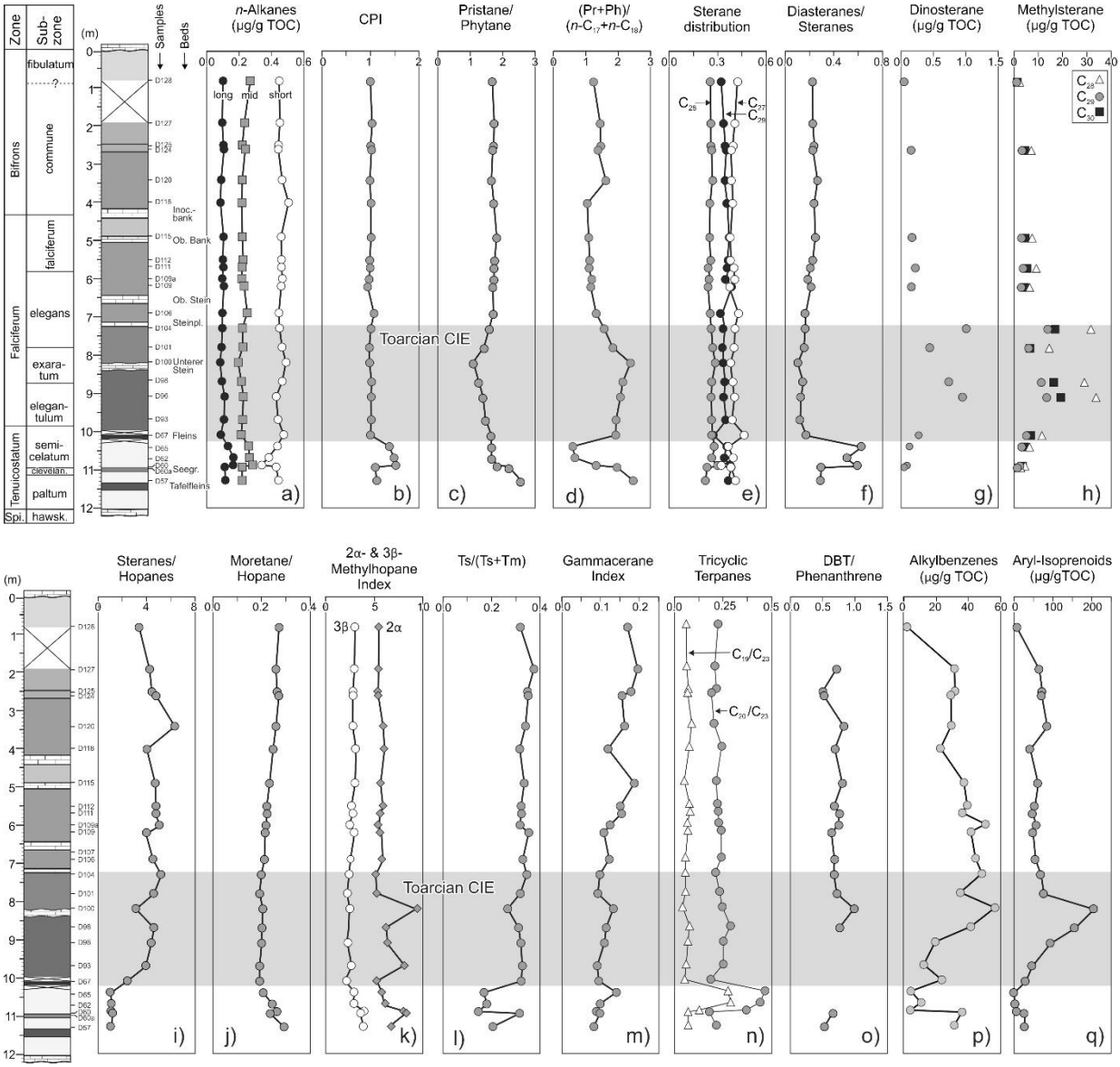

Fig. 7 Concentrations and ratios of selected organic compounds at Dormettingen. The position of the negative carbon isotope excursion (CIE) is shown after Galasso et al. (2021). Alkane distribution: short-chain: *n*-C_{15-19}/Σ *n*-alkanes; mid-chain: *n*-C_{21-25}/Σ *n*-alkanes; long-chain: *n*-C_{27-31}/Σ *n*-alkanes; CPI: Carbon Preference Index (Bray and Evans 1961), sterane distribution: C_{27}/C_{27-29} steranes, C_{28}/C_{27-29} steranes, C_{29}/C_{27-29} steranes; DBT: dibenzothiophene

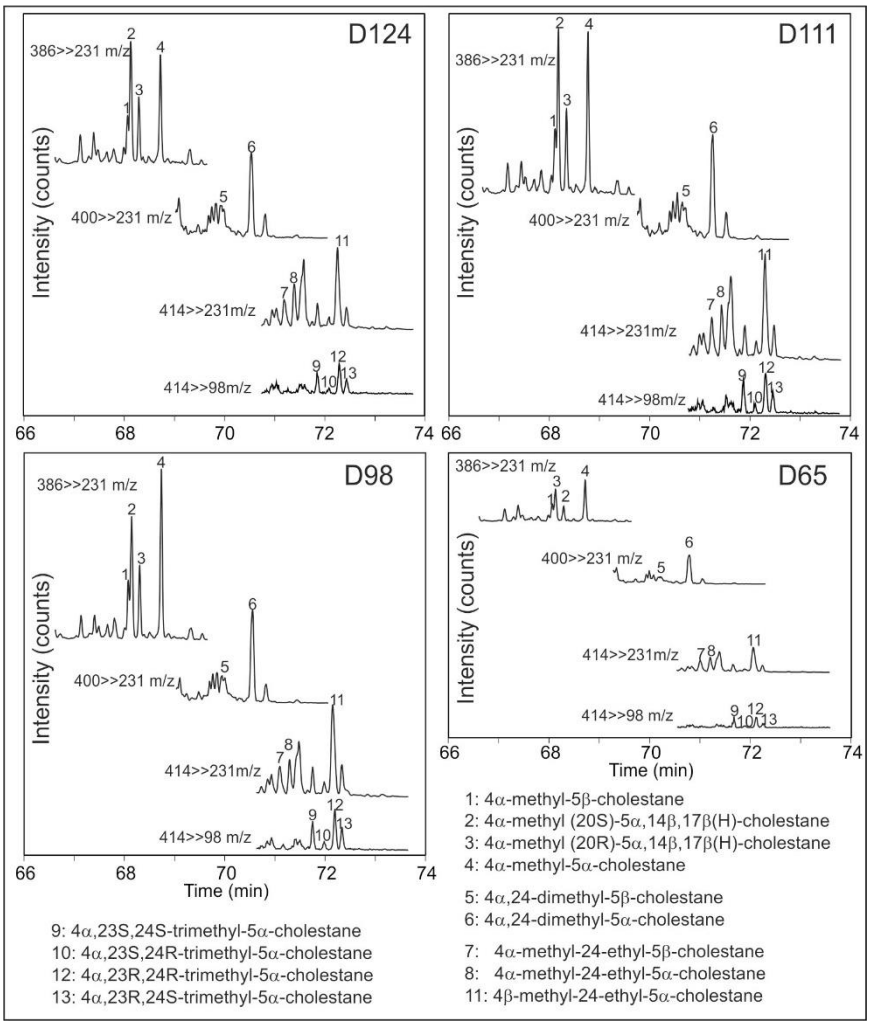

Fig. 8 4-Methylsterane distributions of four samples. Data were acquired by GC-MSMS. Identification of 4α-methylsteranes, 4β-methylsteranes is based on Goodwin et al. (1988) and Schouten et al. (2000)

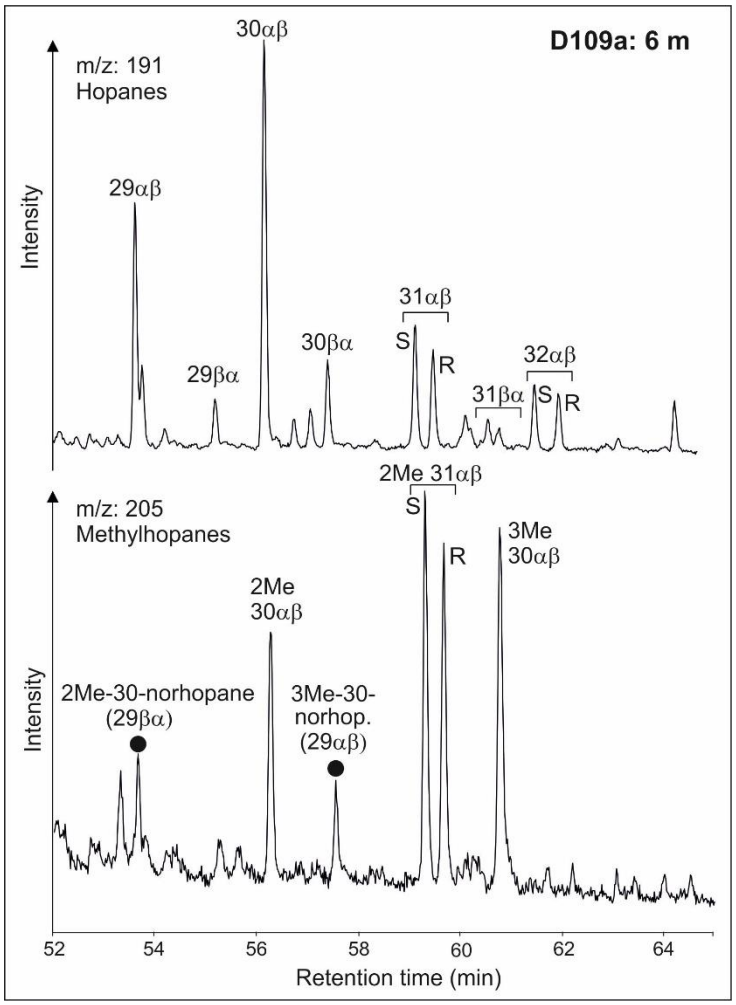

Fig. 9 Mass chromatograms of *m/z* 191 and 205 showing hopane and methylhopane distribution of sample D109a. Methylhopane peak identification of 2Me and 3Me is based on Farrimond et al. (2004) and Pancost et al. (1998).
2Me-30-norhop - (29βα)-2α(CH_3),17β(H),21a(H)-30-norhopane,
29αβ - 2α(CH_3),17α(H),21β(H)-hopane,
3Me-30-norhop (29αβ) - 3β(CH_3),17α(H),21β(H)-30-norhopane,
2Me 31αβ S - (22S)-2α(CH_3),17α(H),21β(H)-29-homohopane,
2Me 31αβ R - (22R)-2α(CH_3),17α(H),21β(H)-29-homohopane,
3Me 30αβ - 3β(CH_3),17α(H),21β(H)-30-hopane.

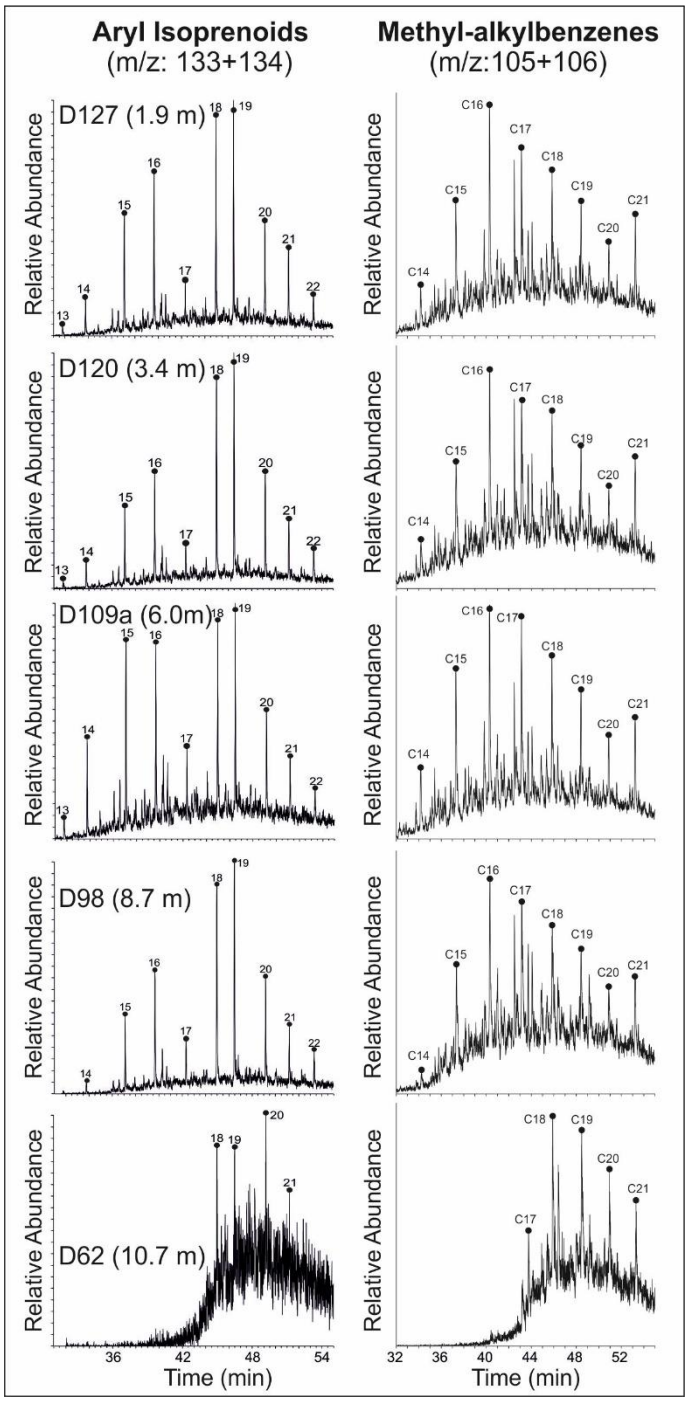

Fig. 10 Mass chromatogram representation of aryl isoprenoids and methyl-*n*-alkylbenzenes. Carbon number over the peaks refers total carbon in alkylbenzenes.

Aromatic hydrocarbons

The Posidonia Shale contains benzenes, napthalenes, phenanthrenes, dibenzothiophenes, and their alkylated equivalents in the aromatic fraction. Alkylphenanthrenes are present and include methylphenanthrene (MP), and dimethylphenanthrene (DMP). The methylphenanthrene index (MPI-1; Radke et al. 1986; Radke 1988) ranges from 0.17 to 0.68, but could not be determined for all samples.

Concentrations of methyldibenzothiophene range from 10.5 to 15.0 µg/g TOC (avg. 12.9). The methyldibenzothiophene ratio (MDR; Radke et al. 1986) varies between 0.26 and 0.38. Dibenzothiophene (DBT) and phenanthrene (Phen) contents are also high with DBT/Phen ratios (Hughes et al. 1995; Fig. 7p) ranging from 0.22-1.01 (avg. 0.70; Table 3). Methyl-*n*-alkylbenzenes (e.g. Zhang et al., 2014) are present in considerable amounts in the aromatic fraction (2.1-56.5 µg/g TOC; avg. 31.2; Table 3) and reach maximum concentrations within the CIE (8.2 m; D100; Fig. 10).

C_{13} to C_{22} aryl isoprenoids are observed in significant amounts in most samples. The maximum peaks are formed by C_{18} and C_{19} aryl isoprenoid (Fig. 10). Concentrations of aryl isoprenoids increase upwards in the lower part of the CIE and reach a maximum (210 µg/g TOC) in sample D100 (Fig. 7q). Above sample D100 aryl isoprenoid concentrations are lower and decrease gradually towards the top of the section. The ratio between $C_{13\text{-}17}$ and $C_{18\text{-}22}$ aryl isoprenoids (aryl isoprenoid ratios (AIR) following Schwark and Frimmel 2004) are typically low and exceed 1 only in the Tafelfleins (D57) and the Seegrasschiefer (D60a) below the CIE (Fig. 11). However, AIR could not be determined reliably for samples D60 to D65. In contrast to aryl isoprenoids, isorenieratane was not detected.

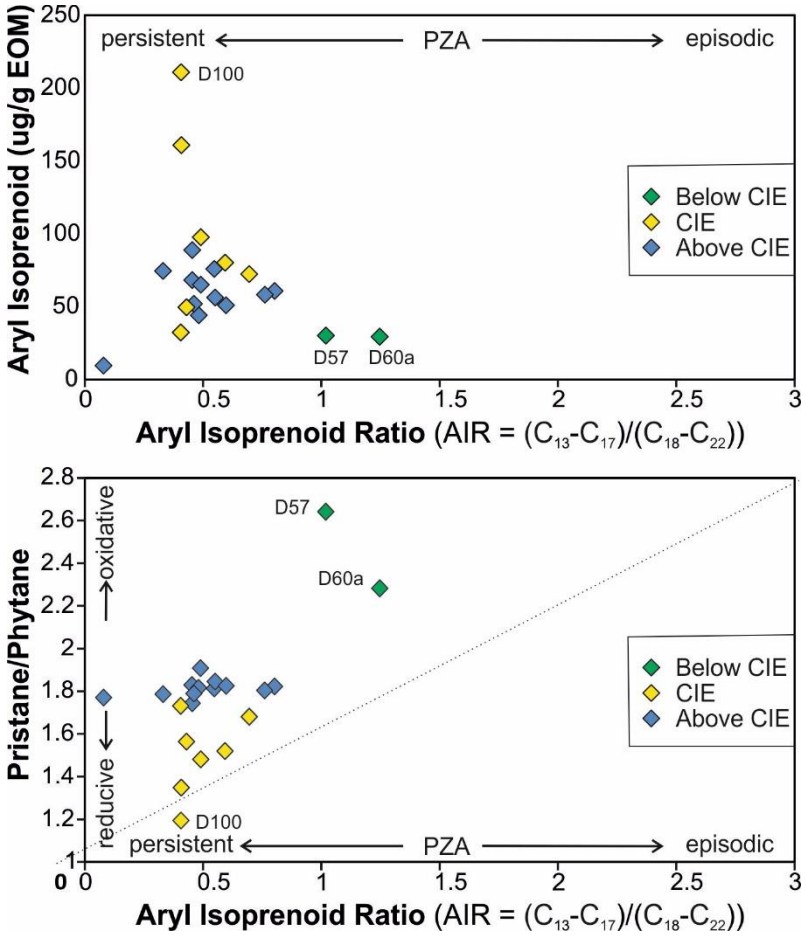

Fig. 11 Redox conditions (photic zone anoxia) represented by aryl isoprenoid *versus* aryl isoprenoid ratio ($C_{13\text{-}17}$/ $C_{18\text{-}22}$) and pristane/phytane ratio *versus* aryl isoprenoid ratio ($C_{13\text{-}17}$/ $C_{18\text{-}22}$) (after Schwark and Frimmel 2004)

Stable carbon isotope composition of organic matter

Compound-specific carbon isotope ratios have been determined for *n*-alkanes with chain length ranging from C_{15} to C_{29} as well as for norpristane, pristane and phytane. Stratigraphic variations of $\delta^{13}C$ values of individual compounds are presented in Figure 12. It is obvious that the negative CIE is visible in all compounds. The strongest negative isotope shift is observed for *n*-C_{27}. Reliable $\delta^{13}C$ values for *n*-C_{28} and *n*-C_{29} could be obtained only for a few samples. However, these data show a similar strong shift. In contrast, the shift is less prominent for *n*-alkanes in the range of *n*-C_{17} to *n*-C_{25}. Pristane and phytane display similar trends. With the exception of sample D62, carbon in phytane is isotopically slightly heavier than that in pristane. The most negative $\delta^{13}C$ value for pristane and phytane is recorded for sample D93, near the base of the CIE (9.7 m), whereas the most negative $\delta^{13}C$ values for *n*-alkanes (and C_{org}; Galasso et al. 2021) are found in its middle part (samples D96 and D98).

Figure 13 shows plots of $\delta^{13}C$ values versus chain length of *n*-alkanes. Apart from the differences in absolute values (lower values compared to $\delta^{13}C_{org}$), samples from different depth intervals show different isotope patterns:

- Samples below the CIE (11.3-10.4 m) are characterized by a trend towards less negative $\delta^{13}C$ values with increasing chain length. This trend is observed both, in organic-lean sediments and in organic-rich Tafelfleins and Seegrasschiefer samples. $\delta^{13}C$ values of isoprenoids are similar to those of long-chain *n*-alkanes or even more negative.
- Samples within the CIE (10.1-7.8 m) show very negative $\delta^{13}C$ values, which decrease with increasing chain length. Only the lowermost (D67) and uppermost sample (D104) show more or less constant $\delta^{13}C$ values. $\delta^{13}C$ values of isoprenoids are typically heavier than n-alkanes in this interval.
- Samples above the CIE show either a negative trend (10.1-7.8 m; 2.6-0.8 m) or rather constant values (5.5-3.4 m) whereby n-C_{22} often shows the most negative $\delta^{13}C$ value. Isotope ratios of isoprenoids in these intervals are rather uniform and less negative than *n*-alkanes.

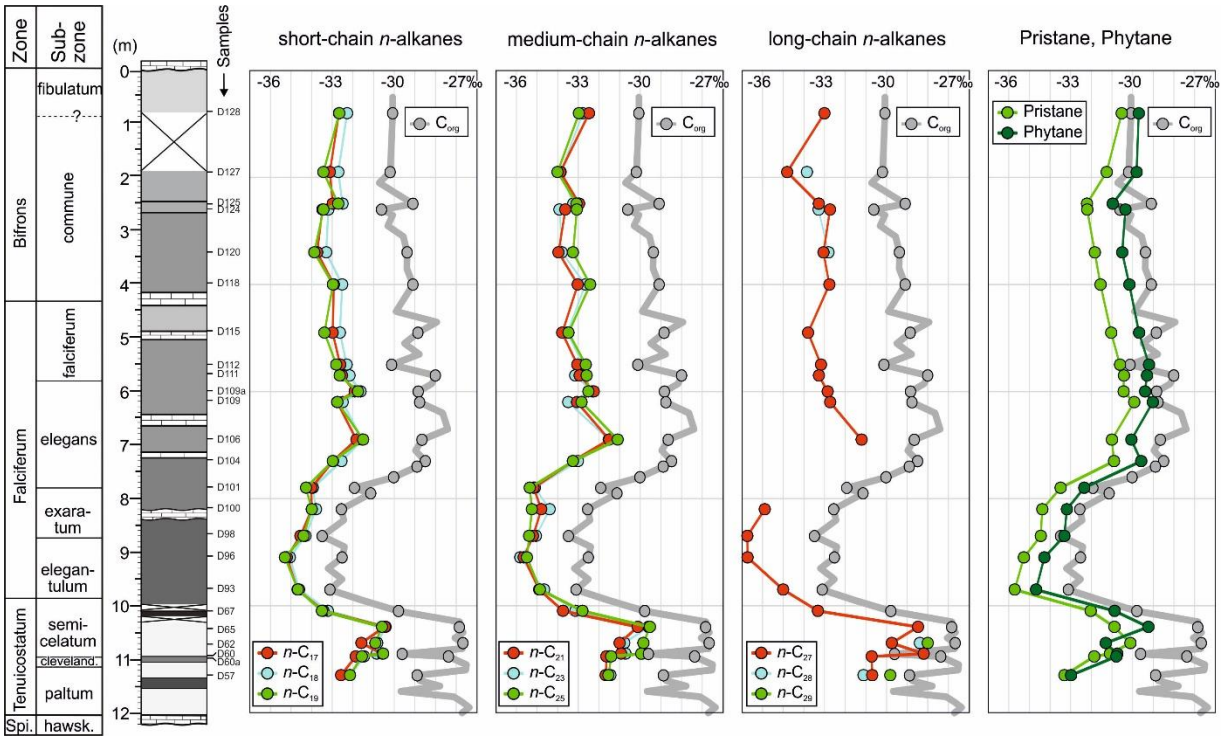

Fig. 12 Depth plot representation of variation in $\delta^{13}C$ of *n*-alkanes, pristane and phytane. Vertical variation of bulk carbon isotope values ($\delta^{13}C_{org}$) is shown for comparison after Galasso et al. (2021)

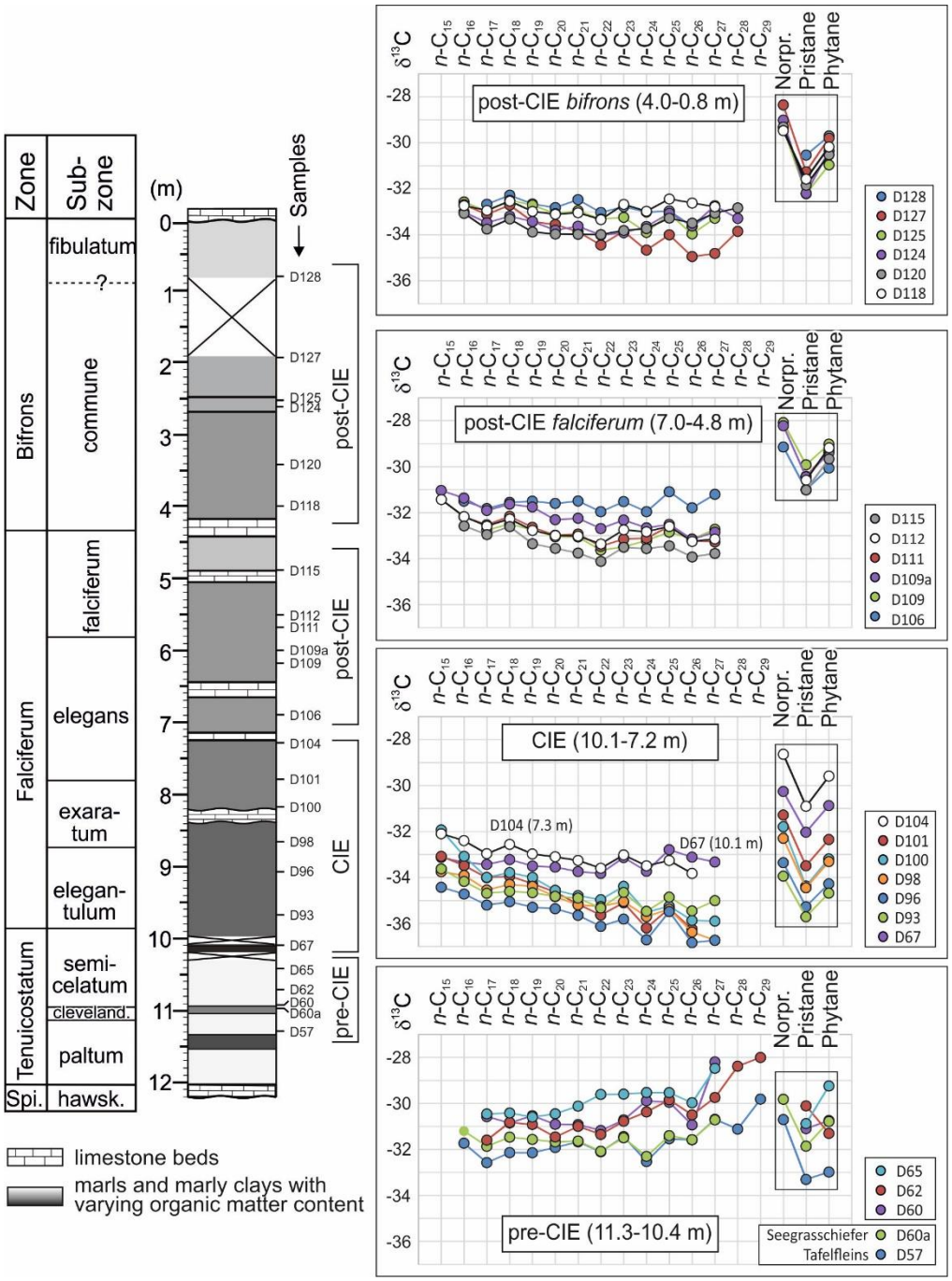

Fig. 13 Carbon isotope composition of individual *n*-alkanes and isoprenoids for samples from different stratigraphic intervals in the Dormettingen section

Discussion

Thermal maturity

Vitrinite reflectance (0.40-0.54 %Rr), T_{max} (avg. 427°C), and the low isomerization ratio of C_{29} steranes (avg. 0.23) suggest that the Dormettingen section is thermally immature. In contrast, early oil window maturity is suggested by the αββ/(αββ+ααα) ratios of C_{29} steranes (avg. 0.32) and the C_{31} hopane isomerisation values, which are at equilibrium (avg. 0.6).

Maturity variations cannot be expected within the thin (~12 m) stratigraphic interval. All depth trends of maturity parameters (e.g. upward increase in T_{max}; slight upward decrease of sterane isomerisation ratios; low moretane/hopane ratios in the CIE [Fig. 7j]; low Ts/(Ts+Tm) below the CIE [Figs. 7l, 14]) reflect facies variations (see also Moldowan et al. 1986; 1994). Similar thermal maturity values were determined for the neighbouring Dotternhausen section (Schmid-Röhl 1999; Frimmel et al. 2004).

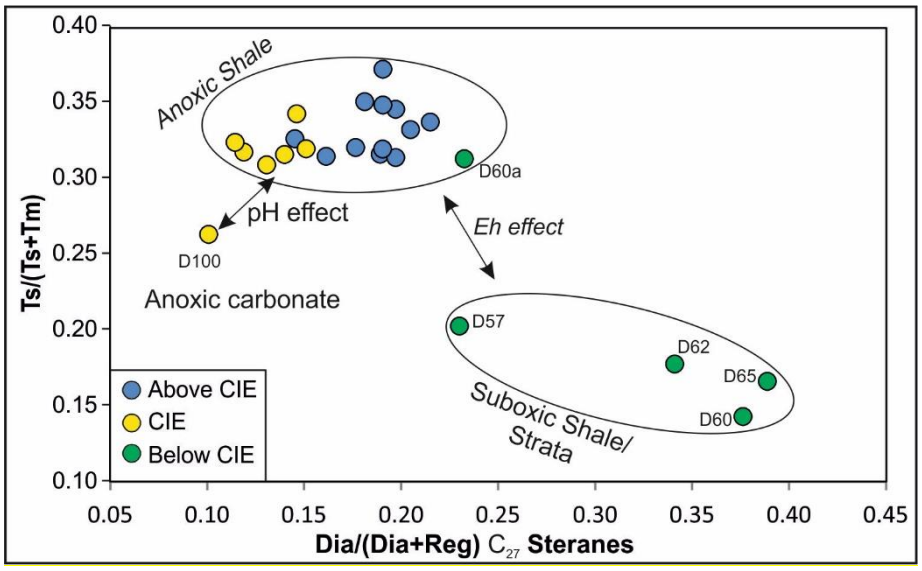

Fig. 14 C_{27} diasteranes/C_{27} regular sterane versus Ts/(Ts+Tm) (plot after Moldowan et al. 1994). In case of the immature Posidonia Shale, differences in Ts/(Ts+Tm) ratios are not controlled by maturity but the depositional environment (Moldowan et al. 1994)

Depositional environment

In the following, geochemical proxies are used to reconstruct the depositional environment of the Dormettingen section considering the wealth of information provided by previous studies (van Acken et al. 2019; Galasso et al. 2021), including those on the Dotternhausen section (e.g. Röhl et al. 2001; Schmid-Röhl and Röhl 2002; Frimmel et al. 2004; Schwark and Frimmel 2004; Röhl and Schmid-Röhl 2005; van den Schootbrugge et al. 2005; Bour et al. 2007; Wang et al. 2020, 2021).

Before discussing the depositional environment of individual units, geochemical parameters based on pristane and phytane will be examined. The Pr/Ph ratio, a widely used redox proxy (e.g. Didyk et al. 1978), is unusually high in the Posidonia Shale of the SWGB (e.g. Schouten et al. 2000; Frimmel et al. 2004). Nevertheless, Frimmel et al. (2004) found a clear relationship between Pr/Ph and (Pr+Ph)/(*n*-C_{17}+*n*-C_{18}) ratios with various paleoecological redox indicators. They showed that strictly anoxic conditions are associated with Pr/Ph ratios <1.6 and (Pr+Ph)/(*n*-C_{17}+*n*-C_{18}) ratios >1.75. Environments with very short (weeks, month) and short (month, years) oxygen supply to the sediment surface are related to Pr/Ph ratios of about 1.7 and 1.75, respectively. The corresponding values for the (Pr+Ph)/(*n*-C_{17}+*n*-C_{18}) ratios are ~1.6 and ~1.3. The unusual high Pr/Ph ratios were attributed to an additional input of pristane from tocopherols or chromans (Frimmel et al. 2004). Since tocopherols are formed by the same biochemical pathway as chlorophyll, tocopherol-derived pristane has the same $\delta^{13}C$ as the phytol side chain (Hughes et al. 1995; Peters et al. 2005). This also applies to the chromans (Grice et al. 1998; Zhang et al. 2012). Thus it is not surprising that (with the exception of samples below the Toarcian CIE) $\delta^{13}C_{pristane}$ and $\delta^{13}C_{phytane}$ show an excellent correlation (Fig. 15).

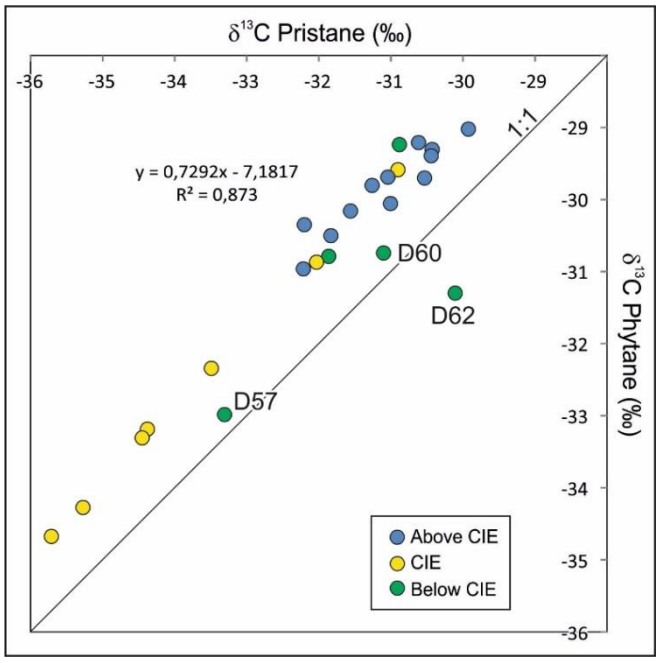

Fig. 15 Cross-plot of $\delta^{13}C$ values of pristane and phytane. $\delta^{13}C$ values of pristane are generally about 1 ‰ more negative than $\delta^{13}C$ values of phytane. No good correlation exists for samples below the Toarcian CIE.

Pre-CIE (12.0-10.2 m)

The *tenuicostatum* Zone is dominated by light-grey marls (Blaugraue Mergel; Aschgraue Mergel) with low TOC contents (<0.9 wt.%; Fig. 3). An oxygenated environment is indicated by bioturbation and the presence of a relatively diverse benthic macrofauna (Schmid-Röhl and Röhl 2002; Frimmel et al. 2004; Schwark and Frimmel 2004; Röhl and Schmid-Röhl 2005; van Acken et al. 2019). HI values (53-162 mgHC/gTOC) reflect the poor preservation conditions and/or suggest a high contribution of terrigenous organic matter. Indeed, a significant contribution of terrigenous phytoclasts (up to 65 %) is characteristic for this interval (palynofacies A of Galasso et al. 2021). A high amount of terrigenous organic matter is also indicated by maceral analysis and geochemical proxies. The latter include elevated amounts of long-chain *n*-alkanes, high CPI values (Bray and Evans 1961), and high ratios of C_{19}/C_{23} and C_{20}/C_{23} tricyclic terpanes (Noble et al. 1986; Peters et al. 2005; French et al. 2014; Fig. 7a,b,n). HI values of the light-grey marls increase upwards (Fig. 3). Since the ratio of aquatic to terrigenous phytoclasts does not vary in a systematic way (Galasso et al. 2021), the observed HI values probably reflect a trend towards better preservation conditions. In addition, the upward decreasing Pr/Ph ratios (Fig. 7c) support a general trend towards less oxic conditions. Oxic to suboxic conditions are also reflected by very low values of the C_{35} homohopane index (C_{35} HHI $\leq$ 0.02) (Table 3).

High TOC contents (3.6-11.1 wt.%) in the *tenuicostatum* Zone below the CIE are restricted to distinct black shale layers (Tafelfleins, Seegrasschiefer) (Fig. 3). HI values ranging from 459 to 614 mgHC/gTOC in these beds reflect a high amount of amorphous aquatic organic matter in these layers (Galasso et al. 2021). Strongly anoxic conditions are suggested by the presence of low concentrations of aryl isoprenoids, high (Pr+Ph)/(*n*-C_{17}+*n*-C_{18}) ratios (Fig. 7) and C_{35} HHI values (~0.04; Table 3), which are similar to those in the strongly anoxic CIE. However, various degrees of bioturbation described by van Acken et al. (2019), show that the redox proxies have to be interpreted with caution. Nevertheless, Pr/Ph ratios pretending dysoxic to oxic conditions (Didyk et al. 1978) are surprisingly high (2.2-2.7; see also Schouten et al. 2000; Frimmel et al. 2004). Frimmel et al. (2004) suggested that high Pr/Ph ratios reflect additional input of terrigenous pristane and/or secondary oxidation. However, both explanations appear unsatisfactory because neither an increased input of terrigenous phytoclasts (Galasso et al. 2021) nor secondary oxidation phenomena on pyrite can be observed. Very low steranes/hopanes ratios may reflect input of heterotrophic bacterial biomass involved in the degradation of algae (Peters et al. 2005).

Toarcian CIE (10.2-7.4 m)

The presence of black shales with a distinct lamination and the widespread absence of benthic organisms is evidence for strongly oxygen-depleted conditions in the Toarcian CIE interval (Röhl and Schmid-Röhl 2005). Consequently, TOC contents increase sharply to values higher than 10 wt.% at the base of the Toarcian CIE (D67, Fleins). TOC contents remain high during the CIE and are low only in a limestone layer ("Unterer Stein"). Below and above the limestone layer, the average HI is 657 mgHC/gTOC reflecting very high amounts of aquatic organic matter as documented by macerals analysis (Fig. 4), palynofacies (palynofacies B of Galasso et al. 2021), and reduced ratios of C_{19}/C_{23} and C_{20}/C_{23} tricyclic terpanes.

Marine aquatic macerals include telalginite and lamalginite (Fig. 4c). Tasmanales alginite is present in all samples, but is especially abundant in sample D67 from the uppermost *tenuicostatum* Zone. Terrigenous macerals including vitrinite (Fig. 4c), recycled vitrinite, and inertinite are very rare. Fish remains (Fig. 4g) are especially abundant in samples from the *exaratum* Subzone of the *falciferum* Zone.

Pr/Ph ratios decrease gradually from 1.73 to 1.18 between 10.1 m (D67) and 8.2 m (D100) and increase to a value of 1.68 at 7.3 m (D104). The (Pr+Ph)/(*n*-C_{17}+*n*-C_{18}) ratio shows the opposite trend. Following Frimmel et al. (2004), these data suggest strictly anoxic conditions

with only very short intervals with oxygen availability at the sea floor during the uppermost *tenuicostatum* Zone (D67).

High concentrations of aryl isoprenoids, markers for photosynthetic sulphide-oxidizing bacteria (Summons and Powell 1987), suggest photic zone anoxia, which were previously postulated for the Dotternhausen section (Schouten et al. 2000; Frimmel et al. 2004; Schwark and Frimmel 2004). At Dotternhausen (Schwark and Frimmel 2004) and at Dormettingen the highest degree of oxygen depletion is reached in the upper part of the negative CIE, during and after deposition of the "Unterer Stein" (Fig. 7). This level is also characterized by maxima in gammacerane index and DBT/Phen ratios supporting that oxygen depletion was linked to salinity stratification (see also Schouten et al. 2000) probably due to strong basin restriction and increased run-off (e.g. Röhl et al. 2001; Schwark and Frimmel 2004; McArthur et al. 2008). Remarkably, the most severe photic zone anoxia occurs just at the onset of the carbon isotope recovery phase (C3 after Suan et al. 2008). The abundance of methyl-alkylbenzenes is highest in samples showing the negative CIE and co-varies with the concentrations of aryl isoprenoids (Fig. 7), suggesting the formation of both compound groups through degradation of carotenoids (e.g., isorenieratene). However, in difference to Schouten et al. (2000), the presence of the isoprenoid chain could not be detected in the present study. Sinninghe-Damsté et al. (1993) and Chairi et al. (2010) reported increased contents of alkylbenzenes in sediments deposited during periods of enhanced salinity. Therefore, the formation of the methyl-alkylbenzenes, found in elevated abundances in the Toarcian CIE samples, is considered to have been accelerated in response to salinity stratification and water column anoxia. Beside degradation of carotenoids, direct cyclization and aromatization of the straight chain fatty acids are suggested as responsible mechanism (Derenne et al., 1990; Chairi et al., 2010).

Concentrations of 4-methylsteranes including dinosterane, which is generally ascribed to dinoflagellates (Withers 1987; Moldowan and Talyzina 1998; Volkman et al. 1990), are high (Fig. 7f). Galasso et al. (2021) showed that anoxic conditions resulted in a complete disappearance of dinoflagellates cysts in palynofacies B. This apparent discrepancy, which was also observed by Schouten et al. (2000), suggests the presence of specific non-cyst forming dinoflagellate species. Palynological evidence shows that dinoflagellates cysts were replaced by green algae (prasinophytes) with a high tolerance to fresh-water input and periodic photic zone anoxia and by *Spheropollenites* (Prauss et al. 1991; Galasso et al. 2021).

The sterane/hopane ratio increases within the CIE as algal biomass is better preserved. However, the sterane/hopane ratio is locally decreased in sample D100 (Fig. 7i). This is mainly attributed to high hopane concentrations, which reflect strong bacterial activity (e.g. Fonseca et al. 2021).

The 2α-methylhopane index (2-MHI) and the 3β-methylhopane index (3-MHI) have been introduced as proxies for specific bacteria. 2-MHI was used as a marker for cyanobacteria by Summons et al. (1999), but Rashby et al. (2007) added additional sources. 3-MHI was used as a marker for methanotrophs and acetic acid bacteria (Zundel and Rohmer 1985; Talbot et al. 2003; Farrimond et al. 2004). Similar to a section in the Cleveland Basin (French et al. 2014), the vertical variation of the 3-MHI is minor. However, a distinct increase of 2-MHI within the Toarcian CIE with a maximum in sample D100 above the Unterer Stein limestone marker bed (Fig. 7k) indicates enhanced activity of diazotrophic cyanobacteria at Dormettingen. Activity of diazotrophic cyanobacteria during the Toarcian CIE is also indicated by $\delta^{15}N$ values near 0 recently reported from the Dotternhausen section (Wang et al. 2021) and the Rietheim section, about 90 km south of Dotternhausen/Dormettingen (Montero-Serrano et al. 2015). This is in contrast to locations in England, Wales, and Italy, where positive nitrogen isotope excursions suggest denitrification of anoxic bottom waters (Jenkyns et al. 2001).

post-CIE

TOC contents remain high above the CIE and vary between 4.0 and 10.4 wt.% (Fig. 3). HI values are partly very high and values between 700 and 730 mgHC/gTOC are observed near the base of this interval and near the top of the *falciferum* Zone. Slightly lower HI values (640-680 mgHC/gTOC) occur between 7.0 and 5.2 m. This interval (below and above the "Oberer Stein" limestone bed) coincides with a few thin bioturbated layers and a moderately diverse benthic fauna (van Acken et al. 2019). Hence the slightly lower HI values might be related to increased oxygen availability. Relatively low HI values near the top of the succession (D128, D129) might be due to weathering.

Vertical trends of Pr/Ph (1.7-1.9; Fig. 7c) and (Pr+Ph)/(n-C_{17}+n-C_{18}) ratios (1.6-1.0; Fig. 7d) and the concentrations of aryl isoprenoids (89-44 µg/g EOM) (Fig. 7q) indicate that the oxygen availability increased gradually after the CIE till deposition of the lowermost part of the *bifrons* Zone (sample D118 at 4.0 m). Sample D120 (3.4 m) marks a return to strongly oxygen-depleted conditions (Pr/Ph: 1.7; (Pr+Ph)/(n-C_{17}+n-C_{18}): 1.6; aryl isoprenoids: 89 µg/g EOM). Above this level, oxygen concentrations increased again. Overall, the biomarker

ratios suggest anoxic to temporarily oxic conditions. The proposed redox trend fits well with the occurrence of benthic fossils around the Inoceramenbank (*falciferum/bifrons* boundary) and in the upper part of the *commune* Subzone (Röhl et al. 2001). Interestingly, the redox trend is not reflected in the C_{35} HHI (Table 3) and the DBT/Phen ratio (Fig. 7o), which suggests fairly constant availability of free H_2S in the depositional/diagenetic environment (Hughes et al. 1995).

The increase in oxygen availability following the CIE allowed the recovery of dinoflagellate cysts, although with low numbers and diversity (palynofacies C of Galasso et al. 2021). The return of dinoflagellate cysts has been attributed to a reconnection of the German Basin to the open ocean, low numbers and diversity might be indicative of persistent adverse environment, probably due to low levels of water column mixing (Galasso et al. 2021). The latter is supported by a moderately high gammacerane index in post-CIE sediments (0.10-0.20; Fig. 7m), which suggests that the water column remained at least temporarily stratified. Despite the re-appearance of dinoflagellate cysts, concentrations of dinosteranes (and other 4-methylsteranes) are low supporting the observation that dinosteranes are probably not derived from the cyst-forming dinoflagellates.

Probably, the change in redox conditions in the lowermost *bifrons* Zone also influenced TOC and S contents, which increase in the same depth interval (4.0 to 3.7 m) from 5.2 to 9.8 % and from 1.7 to 3.6 %), respectively (Fig. 3). The sterane/hopane ratio is also raised at 3.4 m depth (Fig. 7i), suggesting the high productivity of eukaryotic organisms or enhanced degradation of algal organic matter.

Diasterane/sterane ratios are higher in post-CIE sediments (0.17-0.27) than in sediments deposited during the CIE (0.11-0.18; Fig. 7f). As carbonate contents are even lower in the CIE, higher diasterane/sterane ratios probably result from the less strictly anoxic conditions during deposition of post-CIE sediments (Fig. 14; Moldowan et al. 1994) rather than the clay catalytic effect (van Kaam-Peters et al. 1998).

Compound Specific Carbon Isotope Data

Compound-specific isotope data were measured for short-chain (*n*-C_{17} to *n*-C_{19}), mid-chain (*n*-C_{21} to *n*-C_{25}), and long-chain *n*-alkanes (*n*-C_{27} to *n*-C_{29}). Short- and long-chain *n*-alkanes are typically attributed to marine and terrigenous organic matter, respectively (e.g. French et al. 2014). Especially interesting are isotope data for pristane and phytane, which are considered representative of marine photoautotrophic biomass (e.g. Schouten et al. 2000).

In this section, stratigraphic variations of compound-specific isotope data are investigated and discussed in relation to changes in the depositional environment. Thereafter the compound-specific isotope record is compared to that of coeval sections in the Central European Epicontinental Basin System.

Stratigraphic variations of compound-specific isotope patterns

pre-CIE - $\delta^{13}C$ values of *n*-alkanes in five samples from the *tenuicostatum* Zone range from -28 to -33 ‰ (Table 4) and are characterized by an increase in $\delta^{13}C$ values with increasing chain length ("positive pattern"; Fig. 13). Thus, $\delta^{13}C$ values of long-chain *n*-alkanes are less negative than in any other sample. A high CPI, especially in low-TOC samples from the *tenuicostatum* Zone (D60, D62, D95), suggests that the long-chain *n*-alkanes are derived mainly from terrigenous organic matter. Therefore, it is reasonable to assume that the positive isotope pattern caused by relatively high $\delta^{13}C$ values of long-chain *n*-alkanes reflects terrigenous input.

$\delta^{13}C$ values of pristane and phytane range typically from -29 to -32 ‰ (Fig. 15). Only the $\delta^{13}C$ values of sample D57 (Tafelfleins) are characterized by $\delta^{13}C$ values, which are more negative than *n*-alkanes in the same sample and more negative than pristane and phytane in any sample outside the Toarcian CIE. Similar values have been determined by Schouten et al. (2000) for their sample T6, located at the same stratigraphic level in the Dotternhausen section. This indicates that pristane and phytane are derived from aquatic organisms using very light, probably recycled carbon sources.

Toarcian CIE - The lowermost sample (D67; Fleins) represents the uppermost *tenuicostatum* Zone and the transition from palynofacies A to B (Galasso et al. 2021). $\delta^{13}C$ values of *n*-alkanes in this sample (-33 to -34 ‰) are rather uniform. Relatively high $\delta^{13}C$ values of pristane and phytane (-31 to -32 ‰), which are in the order of those from the underlying rocks

are another peculiarity of sample D67. The overlying samples from the main part of the Toarcian CIE (D93 to D101; lower *falciferum* Zone) represent palynofacies B. Their *n*-alkanes are isotopically light (-33 to -37 ‰; Figs. 12, 13) and $\delta^{13}C$ values decrease significantly with increasing chain length (negative trend; Fig. 13). Isoprenoids of these samples are also isotopically light (-31 to -36 ‰), but $\delta^{13}C$ values in some of these samples are distinctly less negative than those from *n*-alkanes (Figs. 12, 13).

The uppermost sample (D104; middle *falciferum* Zone) has been attributed by Galasso et al. (2021) to palynofacies C, but still contains very little terrigenous organic matter. It includes *n*-alkanes with a similar distribution of $\delta^{13}C$ values like sample D67, but $\delta^{13}C$ values of isoprenoids are less negative (Fig. 13).

Stratigraphic trends of $\delta^{13}C$ values of *n*-alkanes and isoprenoids (pristane, phytane) across the CIE show remarkable differences (Fig. 12). Short- and mid-chain *n*-alkanes show comparable trends within minimum $\delta^{13}C$ values in sample D96 (9.1 m). The record for long-chain *n*-alkanes is incomplete because of their low abundance in the CIE, but $\delta^{13}C$ values of *n*-C_{27} reach minima (-36.7 ‰) in samples D96 and D98 (8.7 m) producing an overall symmetric depth trend across the CIE. In contrast, $\delta^{13}C$ values from pristane and phytane show a clear asymmetric trend. $\delta^{13}C$ values in sample D67 (Fleins) are still relatively high and similar to that of pre-CIE sediments. The minimum values are reached already at a depth of 9.7 m in sample D93 (Pr: -35.7 ‰; Ph: -34.7 ‰). Following the subdivision of the CIE by Suan et al. (2008), this sample coincides with the end of phase C1. Above this level, $\delta^{13}C$ values increase slowly during phase C2 (sample D100; 8.2 m; Pr: 34.4 ‰; Ph 33.2 ‰) and more rapidly during phase C3 (sample D104; 7.3 m; Pr: -30.9 ‰; Ph: -29.6 ‰).

The data show that there is an obvious time lag (~450 kyr according to the calibration of Suan et al. 2008) between the minimum of $\delta^{13}C_{CO2}$ in the photic zone as reflected by the $\delta^{13}C_{isoprenoid}$ minimum and the maximum of oxygen depletion, related to the shallowest position of the chemocline, represented by sample D100 (Fig. 7). This suggests that there might be an external source for isotopically light CO_2 (e.g. dissociation of methane hydrate; e.g. Hesselbo et al. 2000, Kemp et al. 2005). Apart from that, recycling of isotopically light carbon from deeper levels of the stratified water body ("Küspert model"; e.g. Küspert 1982; Jenkyns 1985; van de Schootbrugge et al. 2005) certainly also contributed to the light isotopy, especially during the time of maximum oxygen-restriction.

The amplitude of the CIE varies significantly for different compounds (Fig. 12). It is about 4.5 ‰ for short-chain *n*-alkanes, about 5-6 ‰ for mid-chain *n*-alkanes, and up to 9 ‰ for *n*-

C_{27}. Pristane and phytane show a negative shift of ~5 ‰. A slightly higher shift (~6 ‰) is found for bulk organic carbon. As discussed in a following section, the very high negative shift for *n*-C_{27} may be related to the combined effect of atmospheric CO_2 levels and climatic factors (e.g. Lomax et al. 2019; Ruebsam et al. 2020) or to the described change from terrestrial (pre-CIE) to marine organic matter input (CIE; see also Suan et al. 2015). These mechanisms are probably not valid for short-chain *n*-alkanes, pristane, and phytane. Therefore, an amplitude of 4.5 to 5.0 ‰ seems realistic for the Toarcian CIE at Dormettingen. This value is slightly higher than the one proposed by Suan et al. (2015) for Dotternhausen, based on correlations between HI and $\delta^{13}C$ values (3-4 ‰).

post-CIE - Sediments deposited after the Toarcian CIE contain *n*-alkanes with $\delta^{13}C$ values between -31 to 34 ‰. These values either remain constant with increasing chain length (e.g. D106, D120) or decrease slightly (e.g. D109a). $\delta^{13}C$ values of isoprenoids are less negative (-28 to -32 ‰; Fig. 13).

n-Alkanes with varying chain lengths exhibit similar vertical trends (Fig. 12). $\delta^{13}C$ values reach a maximum in sample D106 (6.9 m) near the top of the CIE and decrease upwards to sample D127 (1.9 m). The uppermost sample (D128, 0.8 m) has less negative values than the underlying sample D127. A shift towards less negative $\delta^{13}C$ values in mid- and long-chain *n*-alkanes is observed between samples D115 (4.9 m) and D118 (4.0 m), which coincides with the boundary between palynofacies C and D according to Galasso et al. (2021). Therefore, the isotope record may reflect slightly enhanced input of terrigenous organic matter.

Pristane and phytane show a different trend. Their $\delta^{13}C$ maximum is observed at 6.2 m (sample D109) and there is a remarkably uniform decrease in $\delta^{13}C$ values to sample D125 at 2.5 m (Fig. 12). Apart from the change of palynofacies C to D, additional environmental changes occurred during deposition of the post-CIE sediments. These include the decrease in oxygen availability between samples D118 and D120 (4.0-3.4 m). Moreover, Mattioli et al. (2009) showed a strong increase in nannofossil flux within the lower part of the *falciferum* Subzone in the Dotternhausen section. At Dormettingen this position corresponds to a depth of ~5.9 m (sample D110). Apparently, none of these events had a significant effect on isotope ratios of pristane and phytane (Fig. 12). There is an excellent agreement between the isotope data of isoprenoids measured by Schouten et al. (2000) and the new data. However, data from a sample, which falls into the gap between sample D127 and D128 (their sample T45) is isotopically lighter than these samples. This may indicate that $\delta^{13}C$ values in the uppermost

part of the section might be more strongly varying than indicated by our data. Overall the data suggest that the carbon pool in the photic zone following the Toarcian CIE changed more gradually than indicated by the strongly varying $\delta^{13}C$ values of bulk organic matter.

Comparison with compound-specific carbon isotope records from other basins

Apart from the pioneering work of Schouten et al. (2000), compound-specific isotope records across the Toarcian CIE are rare. $\delta^{13}C$ values have been determined for phytane and isorenieratane in the Paris Basin (ANDRA Core HTM 102) (van Breugel et al. 2006). The most detailed record has been provided from the Hawsker Bottoms section (Cleveland Basin) by French et al. (2014) (see also Sælen 2000). Data for long-chain *n*-alkanes in the Sichuan Basin (China) and the Iberian Basin (La Cerradura; Spain) were published by Xu et al. (2017) and Ruebsam et al. (2020).

The comparison of the Dormettingen section with those in the Cleveland, Paris, Iberian, and Sichuan basins shows major differences in the amount of the negative CIE:

The negative CIE of bulk organic matter at Dormettingen (6-7 ‰) and in the Cleveland Basin (~5-7 ‰) is similar, whereas the negative CIE in the sections in the Paris (3.7 ‰), Iberian (~3 ‰) and Sichuan basins (~4 %) is smaller.

Short-chain *n*-alkanes (*n*-C_{17}, *n*-C_{18}, *n*-C_{19}) and the isoprenoids pristane and phytane are considered as derived from marine organisms. They display relatively small negative CIEs of only ~2-3 (*n*-alkanes) and ~2 ‰ (isoprenoids) at Hawsker Bottoms and larger CIEs of ~4.5 ‰ and ~5 ‰ at Dormettingen. The higher CIE magnitude results in isotopically lighter pristane and phytane at Dormettingen (Pr: -35.7 ‰; Ph: -34.7 ‰) compared to those at Hawsker Bottoms (Pr: -33.0 ‰; Ph: -33.9 ‰). Probably the higher CIE magnitude reflects more severe restriction in the SWGB. Another difference between the isoprenoid records at Hawsker Bottoms and Dormettingen concerns the vertical trend of pristane and phytane $\delta^{13}C$ values. At Hawsker Bottoms, $\delta^{13}C$ values decrease sharply already in the middle part of the *semicelatum* Subzone and remain constant across the *tenuicostatum/falciferum* boundary and within the entire CIE. At Dormettingen, the main shift is at the *tenuicostatum/falciferum* boundary, and $\delta^{13}C$ increases upwards within the main part of the CIE. A CIE with intermediate magnitude has been observed in the phytane record (3.3 ‰) in the Paris Basin (van Breugel et al. 2006).

At the latter locality, the relative abundance of isorenieratane increased after the $\delta^{13}C$ of phytane and bulk organic matter return to more positive values (van Breugel et al. 2006). This

suggests that the temporal decoupling of the maximum isotope excursion and the peak in oxygen-depletion is not restricted to the SWGB. In the Cleveland Basin, the time shift of the maximum oxygen-depletion and maximum isotope excursion is less obvious, as $\delta^{13}C$ values of pristane and phytane remained constant during the entire CIE.

Long-chain n-alkanes (*n*-C_{27}, *n*-C_{28}, *n*-C_{29}) are typically derived from terrigenous organic matter. In pre-CIE sediments their $\delta^{13}C$ values are similar at Dormettingen (-28.2 to -31.1 ‰; Table 4) and in the Cleveland Basin (-27.8 to -30.0; French et al 2014), but significantly higher in the Iberian Basin (-23.8 to -25.5; Ruebsam et al. 2020). Differences in absolute $\delta^{13}C$ values of terrigenous *n*-alkanes in the Cleveland Basin, located in a winter-wet temperate climate belt, and the Iberian Basin, located in a winter-wet to semi-arid climate belt (Rees et al. 2000), have been related to different precipitation rates and floral assemblages (Ruebsam et al. 2020). Thus, a winter-wet temperate climate during the *tenuicostatum* Zone at Dormettingen is in agreement with the isotope data.

Long-chain *n*-alkanes in pre-CIE sediments show a much larger negative CIE of ~8-9 ‰ in Dormettingen (Fig. 12) than in the Cleveland Basin (~4-5 ‰; French et al. 2014). Even smaller shifts (~3.7 ‰) are reported for the sections in the Iberian Basin and lacustrine rocks in the Sichuan Basin (Ruebsam et al. 2020; Xu et al. 2021). Interestingly the vertical trends in these basins are very different and show rather uniform values (Cleveland Basin), two minima (Iberian Basin), or a slow decrease followed by a rapid increase (Sichuan Basin). Assuming that the amount of CO_2 in the atmosphere and its $\delta^{13}C$ value changed uniformly worldwide, the observed differences may reflect regional climate (e.g. precipitation) variations (e.g. Schubert and Jahren 2013; Lomax et al 2019). In addition, the extraordinarily high shift at Dormettingen may be influenced by a major change in organic matter input (see also Suan et al. 2015). Whereas a terrigenous source of the long-chain *n*-alkanes in the pre-CIE rocks is proven based on biomarker and palynological evidence, *n*-C_{27} in the Toarcian CIE may have an algal origin.

Conclusion

The paper presents a comprehensive organic geochemical study of the Dormettingen section (SW Germany). It expands the knowledge of the Toarcian evolution in the Southwest German Basin and provides new insights into the factors controlling carbon isotopy on a molecular level. The most important results are summarized below and displayed in a cartoon (Fig. 16).

The evolution of the depositional environment at Dormettingen was similar to that in nearby Dotternhausen. In both sections, photic zone anoxia, indicated by a variety of different biomarkers, prevailed during the Toarcian CIE. As postulated by previous authors, anoxia was caused by basin restriction and a stratified water column. The chemocline reached its shallowest position above the "Unterer Stein" marker horizon (sample D100; 8.2 m).

Elevated 2α-methylhopane index values in this interval reflect the enhanced activity of diazotrophic cyanobacteria. This interpretation is strongly supported by nitrogen isotope values at Dotternhausen (Wang et al. 2021). Obviously, denitrification, which controlled nitrogen isotopy in other basins during the Toarcian CIE, played a subordinate role emphasizing differences in geological settings (basin restriction versus upwelling).

Pristane and phytane are derived from photoautotrophic marine biomass. Their $\delta^{13}C$ values show a very strong negative excursion (~5 ‰) and are partly very low (minimum: -35.7 ‰) in the lower part of the Toarcian CIE (sample D93; 9.7 m). Above this point an increase in $\delta^{13}C$ values of pristane and phytane is observed. Hence, there is an obvious time shift of about 450 kyr between the isotopic minimum and peak anoxic conditions. This suggests that recycled isotopically light dissolved inorganic carbon from deeper levels of the stratified water body ("Küspert model") is probably not the only source for isotopically light carbon.

n-C_{27} displays the largest negative CIE (~9 ‰). This very high magnitude is due to the combined effect of the global CIE and a major change in the source of the organic matter. While *n*-C_{27} in pre-CIE sediments is mainly derived from terrigenous organic matter, *n*-C_{27} within the CIE is derived from marine organic matter.

Despite that, the actual magnitude of the CIE, as reflected by short-chain *n*-alkanes (~4.5 ‰) and isoprenoids, is higher in the Southwest German Basin (Dormettingen) than in other subbasins of the Central European Epicontinental Basin.

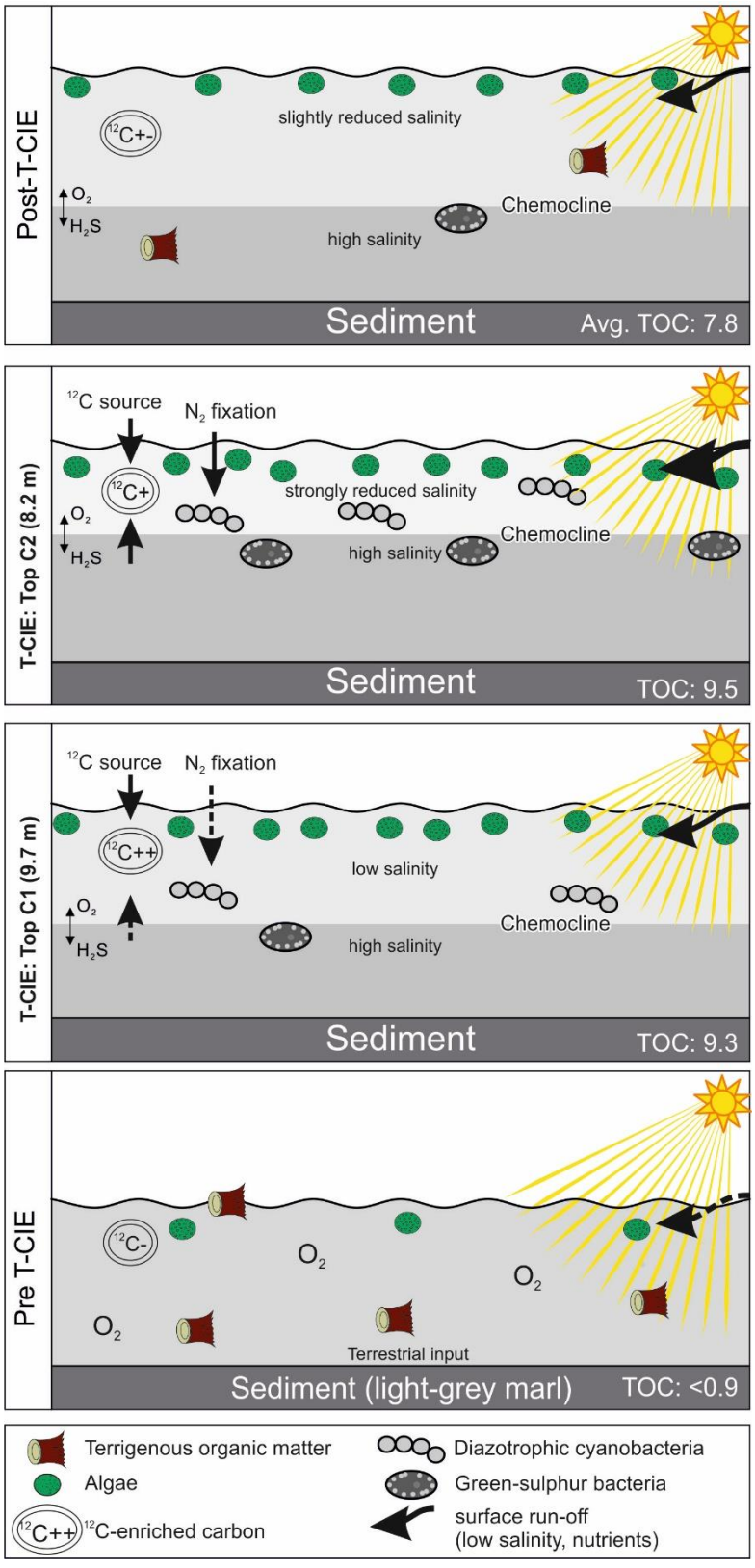

Fig. 16 Cartoon showing amount and type of organic matter input, changes in salinity and the position of the chemocline, as well as the degree of surface run-off, nitrogen fixation by cyanobacteria, and the source of isotopically light CO_2. Photic zone anoxia allowed the life of green sulfur bacteria.

References

Baudin F (1995) Depositional controls on Mesozoic source rocks in the Tethys. In: Huc, A-Y (ed.), Paleogeography, Paleoclimate, and Source Rock. American Association of Petroleum Geologists Studies in Geology 40: 191–211 Houston.

Boulila S, Hinnov L (2017) A review of tempo and scale of the early Jurassic Toarcian OAE: implications for carbon cycle and sea level variations. Newsletters on Stratigraphy 50: 363-389.

Boulila S, Galbrun B, Huret E, Hinnov L, Rouget I, Gardin S, Bartolini A (2014) Astronomical calibration of the Toarcian Stage: implications for sequence stratigraphy and duration of the early Toarcian OAE. Earth Planet Sci Let 386: 98–111.

Bour I, Mattioli E, Pittet B (2007) Nannofacies analysis as a tool to reconstruct paleoenvironmental changes during the Early Toarcian anoxic event. Palaeogeography, Palaeoclimatology, Palaeoecology 249: 58-79.

Bowden SA, Farrimond P, Snape CE, Love GD (2006) Compositional differences in biomarker constituents of the hydrocarbon, resin, asphaltene and kerogen fractions: An example from the Jet Rock (Yorkshire, UK). Organic Geochemistry 37: 369-383.

Bray EE, Evans ED (1961) Distribution of n-parafins as a clue to recognition of source beds. Geochimica et Cosmochimica Acta 22: 2-15.

Burgess SD, Bowring SA, Fleming TH, Elliot DH (2015) High-precision geochronology links the Ferrar large igneous province with early-Jurassic anoxia and biotic crisis. Earth Planet Sci Lett 415: 90–99. https://doi.org/10.1016/j.epsl.2015.01.037

Caruthers AH, Smith PL, Gröcke DR (2013) The Pliensbachian–Toarcian (Early Jurassic) extinction, a global multi-phased event. Palaeogeography, Palaeoclimatology, Palaeoecology 386: 104–118. https://doi.org/10.1016/j.palaeo.2013.05.010

Chairi R, Derenne S, Largeau C (2010) Alkylbenzene origin in recent sediments from the hypersaline environment of Moknine Sebkha, Tunisi. Rapp Comm int Mer Médit 39:233

Cohen AS, Coe AL, Harding SM, Schwark L (2004) Osmium isotope evidence for the regulation of atmospheric CO2 by continental weathering. Geology 32: 157-160.

Cornford C (1998) Source rocks and hydrocarbons of the North Sea. In: Glennie, K.W. (ed.) Petroleum geology of the North Sea: Basic concepts and recent advances. Blackwell Science Geology & Petroleum Geology, Oxford, United Kingdom, pp 376-462.

de Oliveira LCV, Rodrigues R, Duarte LV, Lemos VB (2006) Oil generation potential assessment and paleoenvironmental interpretation based on biomarkers and stable carbon isotopes of the Pliensbachian - lower Toarcian (Lower Jurassic) of the Peniche region (Lusitanian Basin, Portugal). Bull Geosci 14: 207–234.

Dera G, Neige P, Dommergues J-L, Fara E, Laffont R, Pellenard P (2010) High resolution dynamics of Early Jurassic marine extinctions: the case of Pliensbachian-Toarcian

ammonites (Cephalopoda). Journal of the Geological Society of London 167: 21–33. https://doi.org/10.1144/0016-76492009-068

Derenne S, Largeau C, Casadevall E, Sinninghe-Damsté JS, Tegelaar EW, de Leeuw JW (1990) Characterisation of Estonian Kukeriste by spectroscopy and pyrolysis: Evidence for abundant alkyl phenolic moieties in an Ordovician, marine, Type II/I kerogen. Org Geochem 16:873–888

Didyk B, Simoneit B, Brassell S, Eglinton G (1978) Organic geochemical indicators of palaeoenvironmental conditions of sedimentation. Nature 272: 216–222.

Espitalié J, Laporte JL, Madec M, Marquis F, Leplat P, Paulet J, Boutefeu A (1977) Méthode rapide de caractérisation des roches mètres, de leur potentiel pétrolier et de leur degré d´éevolution. Rev. l'Institut Français du Pétrole 32: 23-42. https://doi.org/10.2516/ogst:1977002

Farrimond P, Talbot HM, Watson DF, Schulz LK, Wilhelms A (2004) Methylhopanoids: Molecular indicators of ancient bacteria and a petroleum correlation tool. Geochimica et Cosmochimica Acta 68: 3873-3882.

Fonseca C, Mendonça Filho JG, Lézin C, Baudin F, de Oliveira AD, Torres Souza J, Duarte LV (2021) Boosted microbial productivity during the Toarcian Oceanic Anoxic Event in the Paris Basin, France: new evidence from organic geochemistry and petrographic analysis. In: Reolid M, Duarte LV, Mattioli E and Ruebsam W (eds) (2021) Carbon Cycle and Ecosystem Response to the Jenkyns Event in the Early Toarcian (Jurassic). Geological Society, London, Special Publications 514: 309-334.

French K.L, Sepulveda J, Trabucho-Alexandre J, Gröcke DR, Summons RE (2014) Organic geochemistry of the early Toarcian oceanic anoxic event in Hawsker Bottoms, Yorkshire, England. Earth and Planetary Science Letters 390: 116-127. https://doi.org/10.1016/j.epsl.2013.12.033

Frimmel A, Oschmann W, Schwark L (2004) Chemostratigraphy of the Posidonia Black Shale, SW Germany I. Influence of sea-level variation on organic facies evolution, Chemical Geology 206: 199-230.

Galasso F, Schmid-Röhl A, Fesit-Burkhardt S, Bernasconi SM, Schneebeli-Hermann E (2021) Changes in organic matter composition during the Toarcian Oceanic Anoxic Event (T-OAE) in the Posidonia Shale Formation from Dormettingen (SW-Germany). Palaeogeography, Palaeoclimatology, Palaeoecology 569: 110327. https://doi.org/10.1016/j.palaeo.2021.110327

Goodwin NS, Mann AL, Patience RL (1988) Structure and significance of C_{30} 4-methylsteranes in lacustrine shales and oils. Organic Geochemistry 12: 495-506.

Goossens H, de Leeuw JW, Schenck PA, Brassell SC (1984) Tocopherols as likely precursors of pristane in ancient sediments and crude oils. Nature 312: 440-442.

Grice K, de Mesmay R, Glucina A, Wang S (2008) An improved and rapid 5A molecular sieve method for gas chromatography isotope ratio mass spectrometry of n-alkanes (C_8-

C_{30+}). Organic Geochemistry 39: 284–288. https://doi.org/10.1016/j.orggeochem.2007.12.009

Grice K, Schouten S, Peters KE, Sinninghe Damsté JS (1998) Molecular isotopic characterisation of hydrocarbon biomarkers in Palaeocene-Eocene evaporitic, lacustrine source rocks from the Jianghan Basin, China. Organic Geochemistry 29: 1745–1764.

Harries PJ and Little CTS (1999) The early Toarcian (Early Jurassic) and Cenomanian–Turonian (Late Cretaceous) mass extinctions: similarities and contrasts. Palaeogeography, Palaeoclimatology, Palaeoecology 154: 39–66. https://doi.org/10.1016/S0031-0182(99)00086-3

Hermoso M, Minoletti F, Le Callonnec L, Jenkyns HC, Hesselbo SP, Rickaby REM, Renard M, de Rafélis M, Emmanuel L (2009) Global and local forcing of Early Toarcian seawater chemistry: A comparative study of different paleoceanographic settings (Paris and Lusitanian basins), Paleoceanography 24: 1-15. https://doi:10.1029/2009PA001764

Hermoso M, Minoletti F, Rickaby REM, Hesselbo SP, Baudin F, Jenkyns HC (2012) Dynamics of a stepped carbon-isotope excursion: Ultra high-resolution study of Early Toarcian environmental change. Earth Planet. Sci. Lett. 319-320: 45-54. https://doi.org/10.1016/j.epsl.2011.12.021

Hermoso M, Minoletti F, Pellenard P (2013) Black shale deposition during Toarcian super-greenhouse driven by sea level. Climate of the Past 9: 2703.2712.

Hermoso M, Delsate D, Baudin F, Le Callonnec L, Minoletti F, Renard M, Faber A (2014) Record of Early Toarcian carbon cycle perturbations in a nearshore environment: the Bascharage section (easternmost Paris Basin). Solid Earth 5: 793–804. https://doi:10.5194/se-5-793-2014

Hesselbo SP, Gröcke DR, Jenkyns HC, Bjerrum CJ, Farrimond P, Morgans Bell HS, Green OR (2000) Massive dissociation of gas hydrate during a Jurassic oceanic anoxic event. Nature 406: 392–395. https://doi.org/10.1038/35019044

Hesselbo SP, Jenkyns HC, Duarte LV, Oliveira LCV (2007) Carbon-isotope record of the Early Jurassic (Toarcian) Oceanic Anoxic Event from fossil wood and marine carbonate (Lusitanian Basin, Portugal). Earth Planet Sci Lett 253: 455–470.

Hesselbo SP, Gröcke, DR, Jenkyns HC, Bjerrum CJ, Farrimod P, Morgens Bell HS, Green OR (2000) Massive dissociation of gas hydrate during the Jurassic oceanic anoxic event. Nature 406: 392-395.Hollander DJ, Bessereau G, Belin S, Huc AY, Houzay JP (1991) Organic matter in the early Toarcian shales, Paris Basin, France: A response to environmental changes. Reve de l´institut francais du pétrole 46: 543-562.

Hougård IW, Bojese-Koefoed JA, Vickers ML, Ullmann CV, Bjerrum CJ, Rizzi M, Korte C (2021) Redox element record shows that environmental perturbations associated with the T-OAE were of longer duration than the carbon isotope record suggests – the Aubach section, SW Germany. Newsletters on Stratigraphy 54: 229-246.

Huang C, Hesselbo SP (2014) Pacing of the Toarcian Oceanic Anoxic Event (Early Jurassic) from astronomical correlation of marine sections. Gondwana Research 25: 1348-1356.

Hughes WB, Holba AG, Dzou LIP (1995) The ratios of dibenzothiophene to phenanthrene and pristane to phytane as indicators of depositional environment and lithology of petroleum source rocks. Geochimica et Cosmochimica Acta 59: 3581–3598. https://doi.org/10.1016/0016-7037(95)00225-O

ICCP (1998) The new vitrinite classification (ICCP System 1994). Fuel 77: 349-358. https://doi.org/10.1016/S0016-2361(98)80024-0

ICCP (2001) The new inertinite classification (ICCP System 1994). Fuel 80: 459-471. https://dx.doi.org/10.1016/S0016-2361(00)00102-2

Ivanov AV, Meffre S, Thompson J, Corfu F, Kamenetsky VS, Kamenetsky MB, Demonterova EI (2017) Timing and genesis of the Karoo-Ferrar large igneous province: New high precision U-Pb data for Tasmania confirm short duration of the major magmatic pulse. Chemical Geology 455: 3243.

Jenkyns HC (1985) The early Toarcian and Cenomanian–Turonian Anoxic Events in Europe: comparisons and contrasts. Geologische Rundschau 74: 505-518.

Jenkyns HC (1988) The early Toarcian (Jurassic) anoxic event: Stratigraphic, sedimentary, and geochemical evidence. Am. J. Sci 288: 101-151.

Jenkyns HC (2010) Geochemistry of oceanic anoxic events. Geochem. Geophys. Geosyst 11: 1–30. https://doi.org/10.1029/2009GC002788.

Jenkyns HC, Gröcke DR, Hesselbo SP (2001) Nitrogen isotope evidence for water mass denitrification during the early Toarcian (Jurassic) oceanic anoxic event. Paleoceanography 16: 593-603.

Jiao D, Perry RS, Engel M-H, Sephton MA (2008) Biomarker indicators of bacterial activity and organic fluxes during end Triassic mass extinction event Proc SPIE 7097, Instruments, Methods, and Missions for Astrobiology XI: 709709. https://doi.org/10.1117/12.796160

Kemp DB, Coe AL, Cohen AS, Schwark L (2005) Astronomical pacing of methane release in the Early Jurassic period. Nature 437: 396-399. https://doi:10.1038/nature04037

Kemp DB, Coe AL, Cohen AS, Weedon GP (2011) Astronomical forcing and chronology of the early Toarcian (Early Jurassic) oceanic anoxic event in Yorkshire, UK. Palaeogeogr. Palaeoclimatol. Palaeoecol 530: 90-102.

Kemp DB, Selby D, Izumi K (2020) Direct coupling between carbon release and weathering during the Toarcian oceanic anoxic event. Geology 48: 976–980. https://doi.org/10.1130/G47509.1

Küspert W (1982) Environmental change during oil shale deposition as deduced from stable isotope ratios, in Cyclic and Event Stratification, edited by S. Einsele and A. Seilacher pp. 482-501. Springer, New York.

Littke R, Baker DR, Leythaeuser D, Rullkötter J (1991a) Keys to the depositional history of the Posidonia Shale (Toarcian) in the Hils Syncline, northern Germany. In: Tyson RV & Pearson TH (eds) Modern and Ancient Continental Shelf Anoxia, Geological Society, London, Special Publications 58: 311–333. https://doi.org/10.1144/GSL.SP.1991.058.01.20

Littke R, Rotzal H, Leythaeuser D, Baker DR (1991b) Lower Toarcian Posidonia Shale in Southern Germany (Schwaebische Alb). Organic Facies, Depositional Environment and maturity. Erdöl Kohle Erdgas Petrochem./Hydrocarbon Technol 44: 407–414.

Lomax BH, Lake JA, Leng MJ, Jardine PE (2019) An experimental evaluation of the use of $\Delta^{13}C$ as a proxy for palaeoatmospheric CO_2. Geochimica et Cosmochimica Acta 247: 162–174. https://doi.org/10.1016/j.gca.2018.12.026

Mattioli E, Pittet B, Suan G, Mailliot S (2008) Calcareous nannoplankton changes across the early Toarcian oceanic anoxic event in the Western Tethys. Paleoceanography 23: PA3208. https://doi:10.1029/2007PA001435.

McArthur JM, Algeo TJ van de Schootbrugge B, Li Q, Howarth RJ (2008) Basinal restriction, black shales, Re-Os dating, and the Early Toarcian (Jurassic) oceanic anoxic event, Paleoceanography 23: PA4217. https://doi:10.1029/2008PA001607.

Meyer RKF, Schmidt-Kaler H (1996) Jura. In Freudenberger W, Schwerd K, (eds.) Erläuterungen zur Geologischen Karte von Bayern 1 : 500 000. Bayrisches Geologisches Landesamt. 4th ed., München 90-111.

Moldowan JM, Talyzina NM (1998) Biogeochemical evidence for dinoflagellate ancestors in the Early Cambrian. Science 281: 1168-70.

Moldowan JM, Seifert WK, Gallegos EJ (1985) Relationship between petroleum composition and depositional environment of petroleum source rocks. American Association of Petroleum Geologists Bulletin 69: 1255–68.

Moldowan JM, Sundararaman P, Schoell M (1986) Sensitivity of biomarker properties to depositional environment and/or source input in the Lower Toarcian of SW-Germany. Org. Geochem 10: 915- 926.

Moldowan JM, Peters KE, Carlson RMK, Schoell M, Abu-Ali MA (1994) Diverse applications of petroleum biomarker maturity parameters. Arabian Journal for Science and Engineering 19: 273-98.

Montero-Serrano J-C, Föllmi KB, Adatte T, Spangenberg JE, Tribovillard N, Fantasia A, Suan G (2015) Continental weathering and redox conditions during the early Toarcian Oceanic Anoxic Event in the northwestern Tethys: Insight from the Posidonia Shale section in the Swiss Jura Mountains. Palaeogeography, Palaeoclimatology, Palaeoecology 429: 83-99. http://dx.doi.org/10.1016/j.palaeo.2015.03.043

Neumeister S, Gratzer R, Algeo TJ, Bechtel A, Gawlick H-J, Newton R, Sachsenhofer RF (2015) Oceanic response to Pliensbachian and Toarcian magmatic events: Implications from an organic-rich basinal succession in the NW Tethys. Global and Planetary Change 126: 62-83.

Noble RA, Alexander R, Kagi RI, Knox J (1986) Identification of some diterpenoid hydrocarbons in petroleum. Org. Geochem. 10: 825–829.

Pálfy J, Smith PL (2000) Synchrony between Early Jurassic extinction, oceanic anoxic event, and the Karoo-Ferrar flood basalt volcanism. Geology 28: 747-750. https://doi.org/10.1130/0091-7613(2000)028<0747:SBEJEO>2.3.CO;2.

Pálfy J, Smith PL, Mortensen JK (2002) Dating the end-Triassic and Early Jurassic mass extinctions, correlative large igneous provinces, and isotopic events. Geol. Soc. Am. Spec. Pap. 356: 523-532. https://doi.org/10.1130/0-8137-2356-6.523

Pancost RD, Freeman KH, Patzkowsky ME, Wavrek DA, Collister JW (1998) Molecular indicators of redox and marine photoautotroph composition in the late Middle Ordovician of Iowa, USA. Org. Geochem. 29: 1649-1662.

Pedentchouk N, Turich C (2017) Carbon and hydrogen isotopic compositions of n-alkanes as a tool in petroleum exploration. In: Lawson M, Formolo MJ, Eiler JM, (Eds.): From Source to Seep: Geochemical Applications in Hydrocarbon Systems. Geological Society, London, Special Publications 468: 105-125. https://doi.org/10.1144/SP468.1

Peters KE, Moldowan JM (2001) Effects of source, thermal maturity, and biodegradation on the distribution and isomerization of homohopanes in petroleum. Org. Geochem. 17: 47-61.

Peters KE, Walters CC, Moldowan JM (2005) The Biomarker Guide: Biomarkers and Isotopes In Petroleum Systems and Earth History, 2nd ed. Cambridge University Press.

Pickel W, Kus J, Flores D, Kalaitzidis S, Christanis K, Cardott BJ, Misz-Kennan M, Rodrigues S, Hentschel A, Hamor-Vido M, Crosdale P, Wagner N, ICCP (2017) Classification of liptinite–ICCP System (1994) Int. J. Coal Geol 169: 40-61. https://doi.org/10.1016/j.coal.2016.11.004

Pienkowski G, Hodbod M, Ullmann CV (2016) Fungal decomposition of terrestrial organic matter accelerated Early Jurassic climate warming. Sci Rep 6: 319-330. https://doi.org/10.1038/srep31930

Prauss M, Ligouis B, Luterbacher H (1991) Organic matter and palynomorphs in the 'Posidonienschiefer' (Toarcian, lower Jurassic) of southern Germany. Evidence from phytoplankton associations Radke M (1988) Application of aromatic compounds as maturity indicators in source rocks and crude oils. Marine Petroleum Geology 5: 224-236.

Radke M, Schaefer RG, Leythaeuser D, Teichmüller M (1980) Composition of soluble organic matter in coals: relation to rank and liptinite fluorescence. Geochimica et Cosmochimica Acta 44: 1787-800.

Radke M, Welte DH, Willsch H (1986) Maturity parameters based on aromatic hydrocarbons: Influence of the organic matter type. Organic Geochemistry 10: 51-63.

Rashby SE, Sessions AL, Summons RE, Newman DK (2007) Biosynthesis of 2-methylbacteriohopanepolyols by an anoxygenic phototroph. PNAS 104: 15099-15104. https://doi_10.1073_pnas.0704912104

Rees PM, Ziegler AM, Valdes PJ (2000) Jurassic phytogeography and climates: new data and model comparisons. In: Huber BT, Macleod KG, Wing SL, (Eds.): Warm climates in Earth history. Cambridge University Press, Cambridge: 297‑318. https://doi.org/10.1017/CBO9780511564512.011

Riegraf W (1982) The bituminous Lower Toarcian at the Truc-de-Balduc near Mende (Departement de la Lozere, S-France). In: Einsele S, Seilacher A (Eds.): Cyclic and event stratification, Springer, New York: 506-511.

Riegraf W (1985) Mikrofauna, Biostratigraphie und Fazies im Unteren Toarcium Südwestdeutschlands und Vergleiche mit benachbarten Gebieten. Tübinger Mikropaläontologische Mitteilungen 3: 232 p.

Rodrigues B, Duarte LV, Silva RL, Mendonça Filho JG (2020) Sedimentary organic matter and early Toarcian environmental changes in the Lusitanian Basin (Portugal). Palaeogeogr. Palaeoclimatol. Palaeoecol. 554: 109781. https://doi.org/ 10.1016/j.palaeo.2020.109781.

Röhl H-J, Schmid-Röhl A (2005) Lower Toarcian (Upper Liassic) black shales of the Central European Epicontinental Basin: A sequence stratigraphic case study from the SW German Posidonia Shale. In: The Deposition of Organic-Carbon-Rich Sediments: Models, Mechanisms, and Consequences, SEPM (Society for Sedimentary Geology) Spec. Publ 82: 165-189. ISBN 1-56576-110-3

Röhl H-J, Schmid-Röhl A, Oschmann W, Frimmel A, Schwark L (2001) Erratum to "The Posidonia Shale (Lower Toarcian) of SW-Germany: an oxygen-depleted ecosystem controlled by sea level and palaeoclimate". Palaeogeogr. Palaeoclimatol. Palaeoecol. 169: 273–299.

Ruebsam W, Al-Hussein, M (2020) Calibrating the Early Toarcian (Early Jurassic) with stratigraphic black holes (SBH). Gondwana Research 82: 317–336, https://doi.org/10.1016/j.gr.2020.01.011

Ruebsam W, Müller T, Kovács J, Pálfy J, Schwark L (2018) Environmental response to the early Toarcian carbon cycle and climate perturbations in the northeastern part of the West-Tethys shelf. Gondwana Research 59: 144-158. https://doi.org/10.1016/j.gr.2018.03.013

Ruebsam W, Mayer B, Schwark L (2019) Cryosphere carbon dynamics control early Toarcian global warming and sea level evolution. Global and Planetary Change 172: 440–453. https://doi.org/10.1016/j.gloplacha.2018.11.003

Ruebsam W, Reolid M, Schwark L (2020) $\delta^{13}C$ of terrestrial vegetation records Toarcian CO_2 and climate gradients. Nature Scientific Reports 10: 117, https://doi.org/10.1038/s41598-019-56710-6.

Ruebsam W, Schwark L (2021) Impact of a northern-hemispherical cryosphere on late Pliensbachian–early Toarcian climate and environment evolution. Geological Society, London, Special Publications 514: 359-385. https://doi.org/10.1144/SP514-2021-11

Sælen G, Tyson RV, Telnæs N, Talbot MR (2000) Contrasting water mass conditions during deposition of the Whitby Mudstone (Lower Jurassic) and Kimmeridge Clay (Upper Jurassic) formations, UK, Palaeogeogr. Palaeoclimatol. Palaeoecol. 163: 163-196.

Schmid-Röhl A, Röhl H-J, Oschmann W, Frimmel A, Schwark L (2002) Palaeoenvironmental reconstruction of Lower Toarcian epicontinental black shales (Posidonia Shale, SW Germany): global versus regional control. Geobios 35: 13-20.

Schmid-Röhl A (1999) Hochauflösende geochemische Untersuchungen im Posidonienschiefer (Lias e) von SW-Deutschland: Tübinger Geowissenschaftliche Arbeiten A v. 48: 189 p.

Schwark L, Frimmel A (2004) Chemostratigraphy of the Posidonia Black Shale, SW Germany II. Assessment of extent and persistence of photic-zone anoxia using aryl isoprenoid distribution. Chemical Geology 206: 231– 248.

Schouten S, van Kaam-Peters HME, Rijpstra WIC, Schoell M, Sinninghe Damste JS (2000) Effects of an oceanic anoxic event on the stable carbon isotopic composition of early Toarcian carbon. American Journal of Science 300: 1-22.

Schubert BA, Jahren AH (2013) Reconciliation of marine and terrestrial carbon isotope excursions based on changing atmospheric CO2 levels. Nature Communications, https://doi.org/10.1038/ncomms2659

Seifert WK, Moldowan JM (1986) Use of biological markers in petroleum exploration. In: Methods in Geochemistry and Geophysics Vol 24 (R. B. Johns, ed.), Elsevier, Amsterdam, pp. 261–90.

Silva RL, Duarte LV, Wach GD, Ruhl M, Sadki D, Gómez JJ, Hesselbo SP, Xu W, O´Connor D, Rodrigues B, Mendoca Filho JG (2021) An Early Jurassic (Sinemurian–Toarcian) stratigraphic framework for the occurrence of Organic Matter Preservation Intervals (OMPIs). Earth-Science Reviews 221: 103780. https://doi.org/10.1016/j.earscirev.2021.103780

Sinninghe Damsté J, Kenig F, Koopmans M, Köster J, Schouten S, Hayes J, de Leeuw J (1995) Evidence for gammacerane as an indicator of water column stratification. Geochim. Cosmochim. Acta 59: 1895–1900.

Song J, Littke R, Maquil R, Weniger P (2014) Organic facies variability in the Posidonia Black Shale from Luxembourg: implications for thermal maturation and depositional environment. Palaeogeography, Palaeoclimatology, Palaeoecology 410: 316–336.

Song J, Littke R, Weniger P, Ostertag-Henning C, Nelskamp S (2015) Shale oil potential and thermal maturity of the Lower Toarcian Posidonia Shale in NW Europe. Int. J. Coal Geol. 150-151, 127-153.

Song J, Littke R, Weniger P (2017) Organic geochemistry of the Lower Toarcian Posidonia Shale in NW Europe. Organic Geochemistry 106 (2017): 76–92.

Suan G, Pittet B, Bour I, Mattioli E, Duarte LV, Mailliot S (2008) Duration of the Early Toarcian carbon isotope excursion deduced from spectral analysis: Consequence for its possible causes. Earth and Planetary Science Letters 267: 666–679.

Suan G, van de Schootbrugge B, Adatte T, Fiebig J, Oschmann W (2015) Calibrating the magnitude of the Toarcian carbon cycle perturbation. Paleoceanography 30: 495-509, https://doi:10.1002/2014PA002758

Summons RE, Powell TG (1987) Identification of aryl isoprenoids in source rocks and crude oils: Biological markers for the green sulphur bacteria. Geochimica et Cosmochimica Acta 51: 557-566.

Summons RE, Jahnke L, Hope J, Logan G (1999) 2-Methylhopanoids as biomarkers for cyanobacterial oxygenic photosynthesis. Nature 23: 85-88.

Svensen H, Planke S, Chevallier L, Malthe-Sørenssen A, Corfu F, Jamtveit B (2007) Hydrothermal venting of greenhouse gases triggering Early Jurassic global warming. Earth Planet. Sci. Letters 256: 554–566.

Talbot HM, Watson DF, Pearson EJ, Farrimond P (2003) Diverse biohopanoid composition of non-marine sediments. Org. Geochem 34: 1353-1371.

Them TR II, Gill BC, Caruthers AH, Gröcke DR, Tulsky ET, Martindale RC, Poulton TP, Smith PL (2017) High-resolution carbon isotope records of the Toarcian Oceanic Anoxic Event (Early Jurassic) from North America and implications for the global drivers of the Toarcian carbon cycle. Earth and Planetary Science Letters 459: 118–126, https://doi.org/10.1016/j.epsl.2016.11.021

Tyson RV (2001). Sedimentation rate, dilution, preservation and total organic carbon: Some results of a modelling study. Organic Geochemistry 32: 333-339.

van Acken D, Tütken T, Daly JS, Schmid-Röhl A, Orr PJ (2019) Rhenium-osmium geochronology of the Toarcian Posidonia Shale, SW Germany. Palaeogeography, Palaeoclimatology, Palaeoecology 534: 109294.

van Breugel Y, M. Baas, S. Schouten, E. Mattioli, and J S Sinninghe Damste´ (2006) Isorenieratane record in black shales from the Paris Basin, France: Constraints on recycling of respired CO_2 as a mechanism for negative carbon isotope shifts during the Toarcian oceanic anoxic event, Paleoceanography 21: PA4220. https://doi:10.1029/2006PA001305

Van de Schootbrugge B, McArthur JM, Bailey TR, Rosenthal Y, Wright JD, Miller KG (2005) Toarcian oceanic anoxic event: An assessment of global causes using belemnite C isotope records. Paleoceanography 20: 1-10 PA3008. https://doi:10.1029/2004PA001102

Van Kaam-Peters HME, Köster J, van der Gaast SJ, Dekker M, de Leeuw JW, Sinninghe Damesé JS (1998) The effect of clay minerals on diasterane/sterane ratios. Geochimica et Cosmochimica Acta 62: 2923-2929. https://doi.org/10.1016/S0016-7037(98)00191-4

Volkman JK, Kearney P, Jeffrey SW (1990) A new source of 4-methyl and 5α(H)-stanols in sediments: prymnesiophyte microalgae of the genus *Pavlova*. Organic Geochemistry 15: 489-497.

Wang Y, Ossa Ossa F, Wille M, Schurr S, Saussele M, Schmid-Röhl A, Schoenberg R (2020) Evidence for local carbon-cycle perturbations superimposed on the Toarcian carbon isotope excursion. Geobiology 18: 682-709. https://doi.org/10.1111/gbi.12410

Wang Y, Ossa Ossa F, Spangenberg JE, Wille M, Schoenberg R (2021) Restricted oxygen-deficient basins on the Northern European epicontinental shelf across the Toarcian carbon isotope excursion interval. Paleoceanography and Paleoclimatology 36: e2020PA004207. https://doi.org/10.1029/2020PA004207

Wignall PB (2001) Large igneous provinces and mass extinctions. Earth Sci. Rev. 53: 1-33.

Withers N (1987) Dinoflagellate sterols. In: Taylor, FJR (Ed.) The Biology of Dinoflagelltes. Blackwell Scientific Oxford pp. 316–359.

Xu W, Ruhl M, Jenkyns HC, Hesselbo SP, Riding JB, Selby D, Naafs BDA, Weijers JWH, Pancost RD, Tegelaar EW, Idiz EF (2017) Carbon sequestration in an expanded lake system during the Toarcian oceanic anoxic event. Nature Geoscience 10: 129-134. https://doi.org/10.1038/ngeo2871

Xu W, Weijers JWH, Ruhl M, Idiz EF, Jenkyns HC, Riding JB, Gorbanenko O, Hesselbo SP (2021) Molecular and petrographical evidence for lacustrine environmental and biotic change in the palaeo-Sichuan mega-lake (China) during the Toarcian Oceanic Anoxic Event. In: Reolid M, Duarte LV, Mattioli E, Ruebsam W (Eds) Carbon Cycle and Ecosystem Response to the Jenkyns Event in the Early Toarcian (Jurassic). Geological Society, London, Special Publications 514: 335–357.

Zhang S, Huang H, Su J, Liu M, Zhang H (2014) Geochemistry of alkylbenzenes in the Paleozoic oils from the Tarim Basin, NW China. Organic Geochemistry 77: 126-139.

Zhang YD, Jiang AZ, Sun YG, Xie LJ, Chai PX (2012) Stable carbon isotope compositions of isoprenoid chromans in cenozoic saline lacustrine source rocks from the Western Qaidam Basin, NW China: Source implications. Chinese Science Bulletin 57: 560–570.

Ziegler PA (1982) Geological Atlas of Central and Western Europe. Shell International Petroleum Maatschappij BV, Amsterdam 130 pp.

Ziegler PA (1988) Evolution of the Arctic–North Atlantic and the Western Tethys. American Association of Petroleum Geologists, Memoirs 43: 197 p.

Zundel M, Rohmer M (1985) Prokaryotic triterpenoids 1. 3β-methylhopanoids from Acetobacter species and Methylococcus capsulatus. European Journal of Biochemistry 150: 23-27.

Table 1 Bulk geochemical parameters for Toarcian sediments from the Dormettingen section

Sample ID	Depth [m]	TOC [wt%]	Sulphur [wt%]	Calcite [wt%]	S1 [mg HC/g rock]	S2 [mg HC/g rock]	HI [mg HC/g TOC]	PI [--]	T_{max} [°C]
D129	0.5	5.69	0.20	33.4	0.29	27.11	476	0.01	426
D128	0.8	7.62	0.29	28.3	0.48	36.81	483	0.01	422
D127	1.9	8.21	2.38	27.8	1.63	53.39	650	0.03	427
D126	2.1	9.52	2.48	34.3	2.50	62.36	655	0.04	428
D125	2.49	7.74	2.18	35.6	1.60	51.35	663	0.03	428
D124	2.6	7.02	2.54	34.9	1.58	48.39	689	0.03	428
D122	2.9	7.16	2.53	32.2	1.78	48.74	681	0.04	429
D121	3.1	9.26	2.46	34.8	2.58	60.74	656	0.04	429
D120	3.4	10.42	3.02	45.1	3.70	69.55	668	0.05	429
D119	3.7	9.83	3.59	35.9	2.86	60.22	612	0.05	429
D118	4	5.22	1.72	48.1	1.13	33.69	645	0.03	429
D117	4.5	4.37	1.20	60.0	1.10	30.75	703	0.03	429
D116	4.7	7.56	2.49	30.4	1.85	47.02	622	0.04	428
D115	4.9	6.97	2.39	47.3	2.24	50.42	723	0.04	428
D114	5.1	4.62	3.07	55.8	1.19	32.95	713	0.03	427
D113	5.3	7.80	3.15	37.1	2.18	50.07	642	0.04	429
D112	5.5	7.63	2.63	46.5	2.25	49.15	644	0.04	429
D111	5.7	8.54	2.84	39.4	2.63	55.98	655	0.04	428
D110	5.85	8.82	2.87	38.3	2.75	59.55	675	0.04	428
D109a	6	9.40	3.21	48.8	3.42	60.27	641	0.05	428
D109	6.2	4.02	1.67	46.9	0.86	26.87	668	0.03	427
D108	6.4	4.92	2.00	39.4	1.05	32.02	650	0.03	428
D107	6.7	7.53	3.14	36.0	2.11	49.31	655	0.04	427
D106	6.9	8.73	3.00	47.4	3.01	59.35	680	0.05	428
D105	7.1	7.04	2.42	50.9	2.44	51.30	728	0.05	428
D104	7.3	8.47	3.23	33.9	2.42	59.59	704	0.04	427
D103	7.4	12.09	3.09	41.4	4.14	76.04	629	0.05	428
D102	7.6	9.67	3.23	36.8	3.15	60.84	629	0.05	427
D101	7.8	8.75	3.61	26.5	2.44	57.62	658	0.04	429
D101a	7.9	10.70	2.95	38.3	4.48	72.18	674	0.06	426
D100	8.2	9.45	3.65	31.2	3.54	63.64	673	0.05	427
D99	8.4	1.10	1.17	91.0	0.49	6.11	556	0.07	424
D98	8.7	7.16	3.44	20.7	2.33	49.30	689	0.05	426
D97	8.9	11.97	3.73	29.0	4.83	78.45	655	0.06	427
D96	9.1	12.18	4.33	30.4	5.00	78.03	640	0.06	427
D94	9.5	11.38	3.89	20.6	4.19	71.53	628	0.06	427
D93	9.7	9.30	4.07	22.7	3.65	65.02	699	0.05	425
D67	10.1	10.36	2.61	52.2	3.94	66.98	646	0.06	426
D66	10.3	0.85	1.23	29.0	0.04	1.38	162	0.03	428
D65	10.4	0.75	1.22	35.9	0.04	1.08	145	0.04	426
D64	10.5	0.50	1.26	33.7	0.03	0.49	98	0.05	424
D63	10.6	0.65	0.83	37.6	0.04	0.90	139	0.04	427
D62	10.7	0.61	1.42	37.7	0.04	0.69	111	0.05	425
D61	10.8	0.63	1.00	32.6	0.03	0.69	110	0.04	426
D60	10.9	0.70	1.30	25.8	0.04	1.00	143	0.03	426
D60a	10.95	5.99	3.16	28.4	1.25	38.88	649	0.03	427
D59	11.1	0.50	0.70	27.6	0.03	0.40	80	0.07	425
D58	11.2	0.64	0.86	25.8	0.04	0.68	107	0.05	424
D57	11.3	4.03	3.09	26.0	0.48	18.51	459	0.03	425
D56	11.4	3.61	1.75	29.7	0.42	18.70	518	0.02	425
D55	11.5	0.51	4.34	28.5	0.03	0.53	102	0.05	423
D54	11.6	11.10	3.82	38.4	3.06	68.16	614	0.04	425
D53	11.7	0.38	0.68	39.3	0.02	0.29	77	0.06	427
D52	11.8	0.34	0.74	38.0	0.02	0.22	64	0.07	425

D51	11.9	0.28	0.65	40.2	0.02	0.18	63	0.08	426
D50	12	0.28	0.73	37.8	0.02	0.15	53	0.09	425

Table 2 Maceral percentages of Toarcian sediments from the Dormettingen section

Sample	**Depth**	**Vitrinite**	**Inertinite (+recycled vitrinite)**	**Sporinite**	**Tasmanales telalginite**	**undefined telalginite**	**Lamalginite**	**Liptodetrinite**
ID	[m]	[vol%]	[vol%]	[vol%]	[vol%]	[vol%]	[vol%]	[vol%]
D128	0.8	4	6	1	1	17	55	16
D127	1.9	3	3	0	4	19	39	32
D125	2.49	2	5	0	2	29	36	25
D124	2.6	2	6	0	5	26	35	25
D120	3.4	1	4	1	5	32	39	19
D118	4	1	5	2	9	21	35	28
D115	4.9	2	3	1	2	18	43	32
D112	5.5	2	4	1	4	30	31	29
D111	5.7	0	1	1	1	22	44	32
D109a	6	2	3	1	8	27	46	14
D109	6.2	4	4	0	0	17	44	31
D106	6.9	2	2	0	2	19	45	30
D104	7.3	3	5	0	3	21	47	23
D101	7.8	2	4	0	20	39	4	31
D100	8.2	1	2	0	2	30	24	41
D98	8.7	0	0	0	1	36	22	41
D96	9.1	1	1	0	0	24	41	33
D93	9.7	3	1	0	0	22	42	32
D67	10.1	2	3	0	11	24	35	25
D65	10.4	2	14	0	2	56	5	21
D62	10.7	5	12	0	2	49	12	21
D60	10.9	5	7	0	3	42	19	24
D60a	10.95	2	4	0	2	37	29	26
D57	11.3	4	6	0	2	25	23	40

Table 3 Concentrations and concentration ratios of compounds and compound groups within the hydrocarbon fractions of Toarcian sediments from the Dormettingen section

Sample ID	Depth [m]	*n*-C_{15-19}/ *n*-alkanes	*n*-C_{21-25}/ *n*-alkanes	*n*-C_{27-31}/ *n*-alkanes	CPI	Pr/Ph	(Pr+Ph)/ (*n*-C_{17+18})	Steranes [mg/g EOM]	C_{27}/ C_{27-29} steranes	C_{28}/ C_{27-29} steranes	C_{29}/ C_{27-29} steranes	S/(S+R) C_{29} Steranes	αββ/(αββ+ααα) C_{29} Steranes	C_{27} Diasteranes/ C_{27} Sterane	Methylsteranes [µg/g EOM] C_{28}	C_{29}	C_{30}	Dino-steranes
D128	0.8	0.45	0.27	0.10	1.00	1.77	1.25	46	0.42	0.25	0.32	0.21	0.29	0.23	2.23	1.01	1.27	0.05
D127	1.9	0.45	0.23	0.10	1.04	1.83	1.46	77	0.41	0.26	0.34	0.19	0.31	0.23	n.d	n.d	n.d	n.d
D125	2.49	0.44	0.22	0.10	1.01	1.81	1.48	75	0.40	0.26	0.35	0.20	0.31	0.24	n.d	n.d	n.d	n.d
D124	2.6	0.44	0.24	0.11	1.03	1.79	1.39	66	0.38	0.26	0.35	0.20	0.31	0.23	7.02	3.24	4.38	0.16
D120	3.4	0.46	0.22	0.09	0.99	1.74	1.63	80	0.38	0.27	0.35	0.23	0.32	0.27	n.d	n.d	n.d	n.d
D118	4	0.50	0.22	0.08	1.02	1.82	1.06	44	0.39	0.25	0.36	0.24	0.32	0.24	n.d	n.d	n.d	n.d
D115	4.9	0.46	0.22	0.10	1.02	1.91	1.10	72	0.38	0.25	0.37	0.23	0.33	0.26	7.37	3.03	4.55	0.18
D112	5.5	0.46	0.23	0.10	0.99	1.84	1.13	70	0.38	0.26	0.36	0.23	0.32	0.23	n.d	n.d	n.d	n.d
D111	5.7	0.46	0.22	0.10	1.00	1.82	1.11	77	0.40	0.24	0.36	0.23	0.32	0.21	9.10	3.65	5.30	0.23
D109a	6	0.47	0.22	0.10	0.98	1.82	1.20	97	0.41	0.25	0.35	0.23	0.33	0.19	n.d	n.d	n.d	n.d
D109	6.2	0.46	0.23	0.11	0.95	1.79	1.17	86	0.37	0.24	0.39	0.23	0.32	0.22	6.35	2.92	4.23	0.17
D106	6.9	0.44	0.25	0.10	1.08	1.80	1.33	91	0.43	0.25	0.32	0.23	0.31	0.17	n.d	n.d	n.d	n.d
D104	7.3	0.45	0.22	0.10	1.01	1.68	1.58	84	0.41	0.26	0.33	0.24	0.30	0.17	31.56	13.81	16.78	1.02
D101	7.8	0.46	0.22	0.09	0.98	1.52	1.85	50	0.40	0.27	0.33	0.22	0.30	0.16	14.42	5.96	6.50	0.45
D100	8.2	0.49	0.19	0.08	0.99	1.18	2.39	85	0.38	0.29	0.33	0.23	0.28	0.11	n.d	n.d	n.d	n.d
D98	8.7	0.47	0.21	0.09	1.03	1.35	2.15	92	0.39	0.26	0.34	0.22	0.31	0.15	28.90	11.18	16.28	0.75
D96	9.1	0.43	0.23	0.11	1.02	1.48	2.08	93	0.40	0.26	0.34	0.22	0.31	0.13	33.71	13.41	19.11	0.96
D93	9.7	0.44	0.22	0.11	1.02	1.56	1.95	91	0.39	0.26	0.35	0.22	0.31	0.13	n.d	n.d	n.d	n.d
D67	10.1	0.47	0.21	0.09	1.00	1.73	1.94	20	0.46	0.26	0.27	0.26	0.38	0.18	11.41	5.05	6.74	0.28
D65	10.4	0.44	0.26	0.13	1.39	1.75	0.61	3	0.37	0.28	0.36	0.22	0.36	0.63	6.30	3.07	4.28	0.14
D62	10.7	0.38	0.26	0.16	1.49	1.75	0.68	4	0.40	0.26	0.34	0.24	0.35	0.52	n.d	n.d	n.d	n.d
D60	10.9	0.34	0.28	0.16	1.52	1.92	1.33	11	0.32	0.30	0.38	0.28	0.37	0.60	4.42	2.33	3.35	0.10
D60a	10.95	0.43	0.22	0.11	1.10	2.28	1.97	36	0.38	0.23	0.38	0.27	0.36	0.30	2.68	1.28	1.81	0.06
D57	11.3	0.44	0.22	0.11	1.13	2.64	2.47	19	0.41	0.22	0.37	0.29	0.34	0.30	n.d	n.d	n.d	n.d

EOM - extractable organic matter CPI – Carbon preference index (Bray and Evans 1961); Pr – pristane; Ph – phytane

Table 3 continued

Sample ID	Depth [m]	Hopanes [mg/g EOM]	Steranes/ Hopanes	S/(S+R) C_{31} Hopanes	Moretane / Hopane	Homohopane Index	2α Methyhopane Index	3β	Ts/ (Ts+Tm)	Gammacerane/ (Gamm.+C_{30} Hopane)	Tricyclic terpanes Σ [µg/g EOM]	C_{19}/C_{23}	C_{20}/C_{23}
D128	0.8	14	3,37	0.59	0.27	0.04	5.67	3.12	0.32	0.17	5.44	0.03	0.20
D127	1.9	18	4,25	0.60	0.26	0.05	5.70	3.11	0.37	0.20	7.84	0.04	0.18
D125	2.49	17	4,43	0.60	0.26	0.04	5.54	2.90	0.35	0.18	7.17	0.04	0.19
D124	2.6	14	4,78	0.59	0.27	0.03	5.56	2.90	0.35	0.16	5.93	0.04	0.16
D120	3.4	13	6,32	0.59	0.26	0.04	6.10	2.90	0.34	0.16	6.62	0.06	0.18
D118	4	11	4,02	0.58	0.25	0.04	6.24	3.20	0.32	0.12	3.86	0.05	0.22
D115	4.9	15	4,71	0.59	0.23	0.04	5.89	3.15	0.33	0.19	5.29	0.02	0.19
D112	5.5	15	4,77	0.58	0.22	0.04	6.05	2.74	0.32	0.15	5.10	0.05	0.19
D111	5.7	16	4,77	0.59	0.22	0.04	5.84	2.93	0.32	0.15	5.67	0.05	0.20
D109a	6	19	5,04	0.57	0.22	0.03	5.54	2.56	0.32	0.12	7.55	0.04	0.20
D109	6.2	21	3,99	0.58	0.22	0.03	5.79	3.05	0.35	0.11	4.98	0.04	0.21
D106	6.9	20	4,51	0.58	0.21	0.03	5.94	2.63	0.33	0.12	6.98	0.03	0.22
D104	7.3	16	5,17	0.59	0.20	0.04	5.27	2.48	0.34	0.10	7.28	0.03	0.18
D101	7.8	11	4,57	0.58	0.19	0.03	5.37	2.29	0.32	0.09	4.68	0.03	0.21
D100	8.2	27	3,10	0.60	0.21	0.03	9.67	2.49	0.27	0.13	14.02	0.01	0.22
D98	8.7	20	4,59	0.58	0.20	0.04	6.37	2.43	0.31	0.11	7.43	0.05	0.26
D96	9.1	21	4,37	0.59	0.20	0.03	6.53	2.30	0.32	0.11	8.02	0.04	0.22
D93	9.7	23	3,93	0.59	0.19	0.03	8.31	2.67	0.33	0.09	7.86	0.03	0.22
D67	10.1	8	2,40	0.62	0.19	0.04	5.35	2.16	0.32	0.10	5.74	0.03	0.16
D65	10.4	3	0,98	0.69	0.21	0.02	5.77	2.91	0.17	0.14	0.77	0.25	0.44
D62	10.7	4	1,07	0.59	0.24	0.01	6.11	2.91	0.18	0.10	0.84	0.26	0.42
D60	10.9	11	1,05	0.61	0.26	0.00	8.04	3.98	0.15	0.09	2.68	0.10	0.34
D60a	10.95	30	1,18	0.59	0.24	0.05	8.70	3.78	0.32	0.10	6.35	0.04	0.15
D57	11.3	19	1,01	0.59	0.29	0.04	6.88	3.96	0.20	0.08	4.15	0.04	0.19

Table 3 continued

Sample ID	Depth [m]	MP [µg/g EOM]	DMP [µg/g EOM]	MPI-1	Rc [%]	MDBT [µg/g EOM]	MDR	DBT/Phen	Methylated Alkylbenzenes [µg/g EOM]	Aryl-Isoprenoids [µg/g EOM]	AIR C_{13-17}/C_{18-22}
D128	0.8	n.d	n.d	n.d	n.d	n.d	0.32	n.d	2.07	9.51	0.08
D127	1.9	9.59	20.18	0.36	0.62	10.55	0.32	0.74	31.51	68.14	0.45
D125	2.49	12.43	19.87	0.46	0.67	11.88	0.31	0.53	31.75	75.81	0.55
D124	2.6	9.13	20.56	0.40	0.64	11.66	0.26	0.55	29.22	74.48	0.33
D120	3.4	9.44	12.96	0.17	0.50	12.92	0.29	0.85	29.53	88.77	0.45
D118	4	10.97	18.93	0.39	0.64	12.12	0.35	0.72	22.76	44.07	0.48
D115	4.9	12.19	23.47	0.28	0.57	11.38	0.36	0.83	37.31	64.88	0.49
D112	5.5	13.57	18.91	0.31	0.58	13.20	0.35	0.71	39.40	56.13	0.55
D111	5.7	9.85	9.25	0.19	0.51	12.52	0.38	0.79	36.30	50.87	0.60
D109a	6	12.33	20.45	0.32	0.59	15.00	0.36	0.78	50.65	60.56	0.80
D109	6.2	12.68	24.69	0.33	0.60	14.26	0.33	0.66	41.69	51.74	0.46
D106	6.9	13.99	12.37	0.25	0.55	13.81	0.35	0.71	44.49	58.09	0.76
D104	7.3	12.10	15.22	0.29	0.57	12.16	0.32	0.70	48.48	72.28	0.70
D101	7.8	10.22	15.66	0.43	0.66	10.53	0.30	0.75	35.08	80.06	0.59
D100	8.2	14.75	12.47	0.51	0.70	14.45	0.29	1.02	56.52	210.86	0.41
D98	8.7	18.94	8.20	0.52	0.71	14.20	0.29	0.79	41.57	160.77	0.41
D96	9.1	0.00	12.49	n.d	n.d	n.d	n.d	n.d	19.56	97.47	0.49
D93	9.7	0.00	7.50	n.d	n.d	n.d	n.d	n.d	12.42	49.53	0.43
D67	10.1	0.00	11.67	n.d	n.d	n.d	n.d	n.d	23.57	32.26	0.41
D65	10.4	n.d	n.d	n.d	n.d	n.d	n.d	n.d	4.39	1.79	n.d
D62	10.7	n.d	n.d	n.d	n.d	n.d	n.d	n.d	10.83	4.98	n.d
D60	10.9	n.d	n.d	n.d	n.d	n.d	n.d	0.22	4.09	6.92	n.d
D60a	10.95	12.30	19.67	0.24	0.54	13.10	0.33	0.68	36.15	29.24	1.25
D57	11.3	16.50	25.94	0.68	0.81	14.74	0.34	0.56	31.29	29.98	1.02

MP – Methylphenathrene; DMP – Dimethylphenanthrene; MPI – Methylphenathrene Index (Radke et al. 1986); MDBT – Methyldibenzothiophene; MDR - Methyldibenzothiophene ratio (Radke et al. 1986); Rc – calculated vitrinite reflectance; DBT – Dibenzothiophene; Phen – phenanthrene; AIR - aryl isoprenoid ratio (Schwark and Frimmel 2004)

Table 4 Compound specific carbon isotope ratios ($\delta^{13}C$; ‰) of Toarcian sediments from the Dormettingen section.

Sample ID	Depth [m]	*n*-C_{15}	*n*-C_{16}	*n*-C_{17}	*n*-C_{18}	*n*-C_{19}	*n*-C_{20}	*n*-C_{21}	*n*-C_{22}	*n*-C_{23}	*n*-C_{24}	*n*-C_{25}	*n*-C_{26}	*n*-C_{27}	*n*-C_{28}	*n*-C_{29}	Nor-pristane	Pristane	Phytane
D128	0.8	*n.d*		-32.68	-32.28	-32.66	-32.82	-32.48	-33.03	-32.78	-33.02	-32.97	-33.63	-33.00			*n.d*	-30.53	-29.70
D127	1.9	*n.d*	-32.69	-33.12	-32.71	-33.43	-33.55	-33.87	-34.44	-33.85	-34.67	-34.01	-34.95	-34.81	-33.85		-28.36	-31.26	-29.81
D125	2.49	*n.d*	-32.58	-32.98	-32.50	-32.71	-33.08	-32.96	-33.31	-33.24	-33.90	-33.09	-33.96	-33.28			-29.36	-32.22	-30.97
D124	2.6	*n.d*	-33.02	-33.48	-33.19	-33.43	-33.80	-33.63	-34.02	-33.91	-33.64	-33.07	-33.62	-32.74	-33.29		-29.02	-32.20	-30.35
D120	3.4	*n.d*	-33.05	-33.73	-33.29	-33.87	-33.95	-33.96	-33.98	-33.80	-33.71	-33.26	-33.48	-33.05	-32.81		-29.29	-31.83	-30.51
D118	4	*n.d*	-32.71	-32.93	-32.52	-32.97	-33.09	-33.03	-33.32	-32.66	-32.96	-32.43	-32.61	-32.77			-29.46	-31.56	-30.16
D115	4.9	*n.d*	-32.60	-32.98	-32.63	-33.38	-33.58	-33.78	-34.14	-33.53	-33.59	-33.47	-33.95	-33.80			*n.d*	-31.04	-29.69
D112	5.5	-31.46	-32.20	-32.61	-32.30	-32.80	-33.02	-33.05	-33.39	-32.78	-32.86	-32.63	-33.28	-33.17			*n.d*	-30.62	-29.21
D111	5.7	*n.d*	-32.18	-32.53	-32.16	-32.64	-32.99	-32.93	-33.47	-33.15	-33.11	-32.60	-33.22	-33.28			*n.d*	-30.42	-29.31
D109a	6	-31.04	-31.37	-31.91	-31.63	-31.75	-32.31	-32.25	-32.69	-32.32	-32.66	-32.51	-33.16	-32.85			-28.22	-30.44	-29.40
D109	6.2	*n.d*		-32.76	-32.50	-32.75	-33.06	-33.06	-33.63	-33.49	-33.22	-32.84	-33.15	-32.73			-28.09	-29.92	-29.03
D106	6.9	*n.d*	-31.50	-31.83	-31.56	-31.50	-31.60	-31.50	-31.96	-31.52	-31.96	-31.09	-31.79	-31.21			-29.15	-31.01	-30.06
D104	7.3	-32.10	-32.39	-32.96	-32.56	-32.97	-33.09	-33.25	-33.60	-33.02	-33.49	-33.26	-33.82				-28.63	-30.90	-29.59
D101	7.8	-33.08	-33.48	-34.01	-33.94	-34.27	-34.63	-35.16	-35.63	-35.10	-36.20	-35.35	-36.24				-31.28	-33.49	-32.35
D100	8.2	-31.93	-33.08	-34.00	-33.79	-33.99	-34.56	-34.79	-34.97	-34.39	-35.52	-35.25	-35.87	-35.90			-31.79	-34.38	-33.19
D98	8.7	-33.75	-33.91	-34.54	-34.30	-34.39	-34.84	-35.20	-35.26	-35.05	-35.71	-35.38	-36.38	-36.74			-32.30	-34.45	-33.31
D96	9.1	-34.43	-34.72	-35.20	-35.05	-35.30	-35.36	-35.65	-36.13	-35.81	-36.71	-35.48	-36.83	-36.73			-33.36	-35.27	-34.28
D93	9.7	-33.62	-34.17	-34.69	-34.61	-34.66	-34.82	-34.90	-35.33	-34.65	-35.47	-34.86	-35.45	-35.01			-33.94	-35.71	-34.68
D67	10.1	-33.13	-33.35	-33.43	-33.22	-33.50	-33.55	-33.74	-33.83	-33.14	-33.73	-32.79	-33.11	-33.33			-30.26	-32.03	-30.87
D65	10.4	*n.d*		-30.46	-30.42	-30.59	-30.45	-30.12	-29.61	-29.60	-29.53	-29.54	-29.97	-28.47			*n.d*	-30.88	-29.24
D62	10.7	*n.d*		-31.59	-30.83	-30.92	-31.46	-31.00	-31.35	-30.77	-30.37	-29.85	-30.50	-29.75	-28.38	-28.00	*n.d*	-30.11	-31.30
D60	10.9	*n.d*		-30.58	-30.85	-30.54	-30.91	-30.92	-31.18	-30.72	-29.89	-29.95	-30.93	-28.20			*n.d*	-31.10	-30.74
D60a	10.95	*n.d*	-31.21	-31.87	-31.47	-31.57	-31.68	-31.64	-32.08	-31.50	-32.30	-31.41	-31.58	-30.72			-29.82	-31.86	-30.79
D57	11.3	*n.d*	-31.73	-32.57	-32.14	-32.15	-31.92	-31.67	-32.11	-31.44	-32.53	-31.54	-31.59	-30.69	-31.11	-29.82	-30.70	-33.31	-32.99

9 Publication II

Coaly and lacustrine hydrocarbon source rocks in Permo-Carboniferous graben deposits (Weiach well, Northern Switzerland)

Stephen Ajuaba[1,*], Reinhard F. Sachsenhofer[1], Verena Meier[1,2], Doris Gross[1], Johann Schnyder[3], Silvia Omodeo-Salé[4], Andrea Moscariello[4], David Misch[1]

Marine and Petroleum Geology 150 (2023) 106147
https://doi.org/10.1016/j.marpetgeo.2023.106147

[1] Lehrstuhl Erdölgeologie, Montanuniversitaet Leoben, Peter-Tunner-Strasse 5, 8700 Leoben, Austria
[2] present address: Institute of Hydrogeology, Engineering Geology and Applied Geophysics, Charles Univesity Prague, Czech Republic
[3] Sorbonne Université, CNRS-INSU, Institut des Sciences de la Terre de Paris, iSTeP, 4 place Jussieu, 75005 Paris, France
[4] Department of Earth Sciences, University of Geneva, Switzerland

*corresponding author. E-mail address: stephen.ajuaba@unileoben.ac.at

Highlights:

- Carboniferous coals in the Constance-Frick trough were deposited in low-lying freshwater mires and hold a significant gas potential.
- Permian lacustrine shales were deposited in anoxic lakes with a stratified water column and contain an abundance (up to 10 wt.% TOC) of Type II kerogen.
- Permian shales can generate considerable amounts of liquid hydrocarbons.
- Oil generated from Permian shales can be distinguished from oils with Jurassic and Oligocene source rocks using biomarker and isotope ratios.

Abstract

Permo-Carboniferous graben sediments in the North Alpine Foreland Basin (NAFB) include Upper Carboniferous (Stephanian) coal-measures and lower Permian (lower Autunian) lacustrine shales with high organic matter contents. Coals are probably the source for a gas accumulation in Switzerland, while the bituminous shales are potential source rocks for oil. In order to study the hydrocarbon potential of coal and bituminous shales and to contribute to the understanding of their depositional environment, 90 core samples from the Weiach-1 well (northern Switzerland) were investigated using organic petrographic, palynofacies, Rock-Eval pyrolysis, and geochemical techniques (incl. biomarker analysis and compound-specific carbon isotopy). Carboniferous coal seams are up to 10 m thick and were deposited in low-lying freshwater mires. They contain a significant gas potential and reached a maturity stage related to the onset of gas generation. Sapropelic rocks were not observed in the coal-bearing succession. Organic matter-rich Permian shales (Autunian shales) were deposited in anoxic lakes with a stratified water column. The organic matter is of mixed aquatic and terrigenous origin. $\delta^{13}C$ values of chlorophyll-derived isoprenoids provide evidence for reworking of organic matter in the water column. The Autunian shales have a strongly varying, but locally very good oil potential. They reached early oil window maturity, but did not yet generate significant amounts of hydrocarbons. The main shale interval in the studied borehole is about 12 m thick and will generate about 0.35 tHC/m² when mature. A comparison with literature data shows that it is possible to distinguish oils generated from Permian, Jurassic and Oligocene source rocks based on biomarker ratios and isotope data.

Keywords: Permo-Carboniferous sediments, Permian lacustrine shales, Carboniferous coals, hydrocarbon potential, gas potential, palynofacies, anoxic lake, stratified water column

Author contributions

SA, RFS and DG contributed to the study conception and design. SA, VM and SOS prepared the samples. SA performed the analysis and interpreted the data in collaboration with VM. JS performed part of the analysis and interpreted the corresponding data. RFS, VM, DG, JS, SOS, AM, and DM, helped interpret the entire data. SA wrote the first draft of the manuscript and all authors commented on previous versions of the manuscript. All authors read and approved the final manuscript.

Acknowledgments

The authors thank Swisstopo for the permission to take core samples from the Weiach-1 well, at the Swisstopo core shed located in Hochdorf (Switzerland), in the framework of the UNCONGEO project. The authors also thank François Baudin from Sorbonne University for some rock eval analysis and scientific discussion. Careful reviews by the journal reviewers P. Hackley and B. Katz helped to improve the paper significantly.

Funding

The study was supported in the frame of the UNCONGEO project (University of Geneva).

Availability of data and materials All data are published in the paper. Samples are stored at Department of Earth Sciences, University of Geneva.

Code availability Not applicable.

Declarations

Conflict of interest All authors declare that they have no conflict of interest.

Ethics approval Not applicable

Consent to participate Not applicable

Consent for publication Not applicable

1. Introduction

Post-Variscan tectonics resulted in the formation of a series of Permo-Carboniferous strike-slip and extensional basins in central and western Europe (e.g., McCann et al., 2006). Many of these basins are filled with latest Carboniferous coal-bearing sediments and early Permian lacustrine deposits (McCann et al., 2006; Mercuzot et al., 2022). Elongated Permo-Carboniferous coal-bearing basins are also present in the basement of the North Alpine Foreland Basin (NAFB; Fig. 1) (e.g., Bachmann et al., 1987; Madritsch et al., 2018).

The extension and sedimentary infill of the Permo-Carboniferous grabens are poorly known. This is because high resolution seismic data illuminating the grabens are scarce and only very few wells penetrated the graben deposits. The most intensively studied graben structure is named the Constance-Frick Trough and is located in northern Switzerland (Diebold et al., 1991; Laubscher, 1987; Madritsch et al., 2018; Moscariello et al., 2021). At present, the Constance-Frick Trough is buried beneath Cenozoic and Mesozoic sediments, more than 1 km thick. Only few wells have reached the Permian and Carboniferous sediments in the Constance-Frick Trough and only the Weiach-1 well, drilled by NAGRA (National Cooperative for the Disposal of Radioactive Waste) in 1983, has crossed the entire Permo-Carboniferous succession. With a total depth of 2482 m, this well penetrates Cenozoic Molasse sediments, Mesozoic sediments and the entire Permo-Carboniferous succession down to the crystalline basement (Fig. 2).

In the past century, the Constance-Frick area has been the object of different exploration activities, triggered by the economic interest in potential resources in the Carboniferous and Permian deposits, first by the coal mining industry and afterwards by the oil and gas industry (Diebold et al., 1991; Thury et al., 1994; Lahusen and Wyss, 1995; Greber et al., 1997). Currently, there is renewed interest in the area thanks to the development of deep geothermal and CO_2 storage projects that envisage new targets in these deposits (Swiss Office of Energy; Energy strategy 2050).

The NAFB contains a number of hydrocarbon deposits in its eastern (Austrian) and central (German) sectors. In addition, shallow hydrocarbon indications are present along the entire NAFB, and are especially abundant in the western (Swiss) sector (Misch et al., 2017). The main source rocks for oil and gas in the NAFB are the lower Oligocene Schöneck Formation and the Lower Jurassic Posidonia Shale (Wehner and Kuckelkorn, 1995; Schulz et al., 2002; Véron, 2005; Gratzer et al., 2011; Bechtel et al., 2019). In the Swiss western part, Carboniferous coal is probably the source rock of the Entlebuch gas field (for location see

Fig. 1; Vollmayr and Wendt, 1987; Leu, 2012) and gas encountered by the St. Gallen GT-1 geothermal well (Omodeo-Salé et al., 2020). Permian lacustrine shales, together with the Toarcian Posidonia black shales, have been discussed as potential source rock for oil in the western part of the NAFB (Schegg and Leu 1998; Véron, 2005; Leu, 2014; Misch et al., 2017; Moscariello, 2019; Do Couto et al., 2021) including the Jura Mountains (Pullan and Berry, 2019).

Hydrocarbon occurrence and migration at shallow and deep depths can represent a serious risk for the geothermal exploration activity and for the nuclear waste storage (Moscariello, 2019; Moscariello et al., 2020; Omodeo-Salé et al., 2020 and reference herein related to the St.Gallen incident while drilling a deep geothermal well). Therefore, to assess the type and the amount of hydrocarbons that can be generated at various depths is essential to properly evaluate this risk.

The hydrocarbon potential of the Permo-Carboniferous deposits in Switzerland is poorly known, based on few published data on their maturity and organic carbon content (Matter, 1987; Leu, et al., 2001; NAGRA, 2002; Omodeo-Salé et al., 2020). The main goal of this study is to characterize coaly and shaly rocks, from the Weiach-1 well core material, using a wide array of techniques, including bulk geochemical data, organic petrology, biomarker, and compound-specific isotope data. Apart from a realistic assessment of the hydrocarbon potential, the study will also provide a basis for future oil to source correlation.

2. Geological Setting

The Late Carboniferous consolidation of the Variscan orogen was followed by latest Carboniferous (Stephanian) to early Permian wrench-induced collapse (Ziegler et al., 2006). Across Europe, Permo-Carboniferous graben structures resulted from the post-Variscan transtensional activity (McCann et al., 2006). In Switzerland, several Permo-Carboniferous grabens have been recognized, segmenting the crystalline basement of the NAFB (Madritsch et al., 2018; Diebold et al., 1991, Leu, 2008). One of the most extended and best studied grabens is the Constance-Frick-Trough, extending along the northern rim of the NAFB (Laubscher, 1987; Diebold, 1988; Diebold et al., 1991; McCann et al., 2006; Fig. 1b).

A detailed description of the architecture and evolution of the Constance-Frick Trough (CFT) was provided by Madritsch et al. (2018). According to these authors, the 10 to 12 km wide CFT consists of two segments probably with opposing half-graben geometries, the eastern

Weiach segment and the deeper western Riniken segment. The basin fill was subdivided into a lower, middle, and upper trough fill, which correspond to the Upper Carboniferous, Lower and Upper Permian clastic successions, respectively (Matter, 1987; Madritsch et al., 2018).

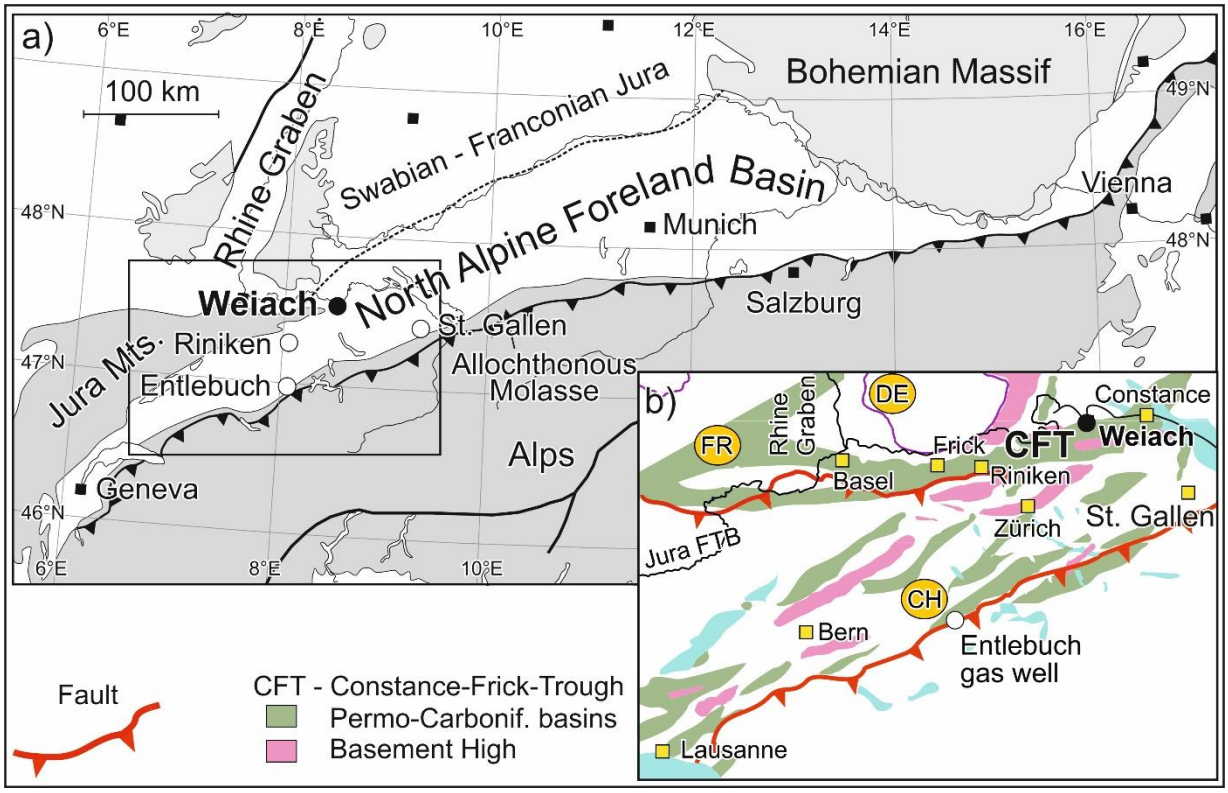

Fig. 1. a) Sketch map of the North Alpine Foreland Basin (NAFB) with location of the Weiach-1, Riniken-1 and St. Gallen wells, and the Entlebuch gas field in Switzerland, b) Distribution of Permo-Carboniferous graben structure in the basement of the NAFB (after Madritsch et al., 2018). CFT - Constance-Frick Trough.

The Constance-Frick Trough was penetrated by two wells: Weiach-1 (Matter, 1987; Matter et al., 1988; Moscariello et al. 2021) and Riniken-1 (Matter et al., 1988). The 2482-m-deep Weiach-1 well penetrates the entire Permo-Carboniferous stratigraphic record (Matter, 1987; Matter et al., 1988; Moscariello et al. 2021). In contrast, the Riniken-1 well, drilled to a depth of 1618 m, only penetrated the coarse-grained upper Permian unit.

This study focuses on the Weiach-1 well. A lithostratigraphic sketch of the well is show in Fig. 2. The Permo-Carboniferous succession in this well starts with coarse-grained sediments (2020-1388 m) was originally interpreted as an anastomosing fluvial system. Recently, a detailed sedimentological study of the same sequence (Cervelli, 2022; Moscariello et al., 2021) indicated dominant deposition associated with a braided delta front prograding periodically into a relatively deep (below wave base) lacustrine environment. This stratigraphic interval has been subdivided into six lithostratigraphic units and includes a Coal

Series between 1752 and 1551 m (Fig. 2). Based on palynological data, Hochuli (1985) dated the main part of fluvial succession as Stephanian (*Angulisporites splendidus-Latensina trilete* [ST] and *Potonieisporites novicus-bhardwajii-Cheiledonites major* [NBM] zones; Clayton et al. (1977). The boundary to the early "Autunian" *Vittatina costabilis* [VC] zone (Carboniferous/Permian boundary) is within the interval from 1443.0-1451.5 m. The fluvial deposits are overlain by lacustrine sediments (Autunian Lacustrine Series; 1388-1252 m). The upper part of the Permian succession was deposited in alluvial fan and playa lake environments and is characterized by red colours. Mesozoic sediments follow above a major unconformity.

The Coal Series comprises nine fining-upward cycles, which include coarse gravels and sandstones, six groups of coal seams (from bottom to top #10 to #4, according to Matter et al., 1988; Fig. 2) and laminated shale. The main coal seam (#6; 1585.01-1591.23 m) is about 6 m thick. The laminated shale has been described as bituminous (e.g. Matter, 1987; Diebold, 1988). The depositional environment of the Coals Series was originally interpreted as belonging to a flood plain (Matter, 1987; Matter et al., 1988) whereas more recent investigation revealed the occurrence of several indicators of reworking processes associated with subacqueous sedimentary facies (i.e. slumps, sedimentary gravity flows) suggesting the likely resedimentation of the coal units in a delta front environment (Moscariello et al., 2021).

The Autunian Lacustrine Series (1388-1252 m) overlies the delta front sediments. The following description is based on Matter et al. (1988). The sedimentologically highly variable series is characterized by frequent facies changes, resulting from rapid shifting of the facies areas in the lakeshore area. It includes debris-flow conglomerates, fining-upward cycles, turbiditic graded siltstone rhythmites, black shales and stromatolithic layers. Matter et al. (1988) describe two "megacycles" which start with fluvial to deltaic channel sands and grade into lacustrine shales. The lacustrine shales often contain fish scales and ostracodes, indicating oxygen-rich water. In contrast, the laminated bituminous shales contain very high amounts of organic matter proving oxygen-deficient or even anoxic conditions (Matter, 1987). Probably the lake sediments were deposited in a complex and extensive early Permian lakescape (Matter, 1987).

Grey and subsequently red coarse-grained clastic sediments representing alluvial fans follow above the lacustrine deposits (1252.07-1058.03 m). Fine-grained red-coloured playa sediments (1058.03-991.50 m) are the youngest Permian deposits preserved (Diebold, 1988).

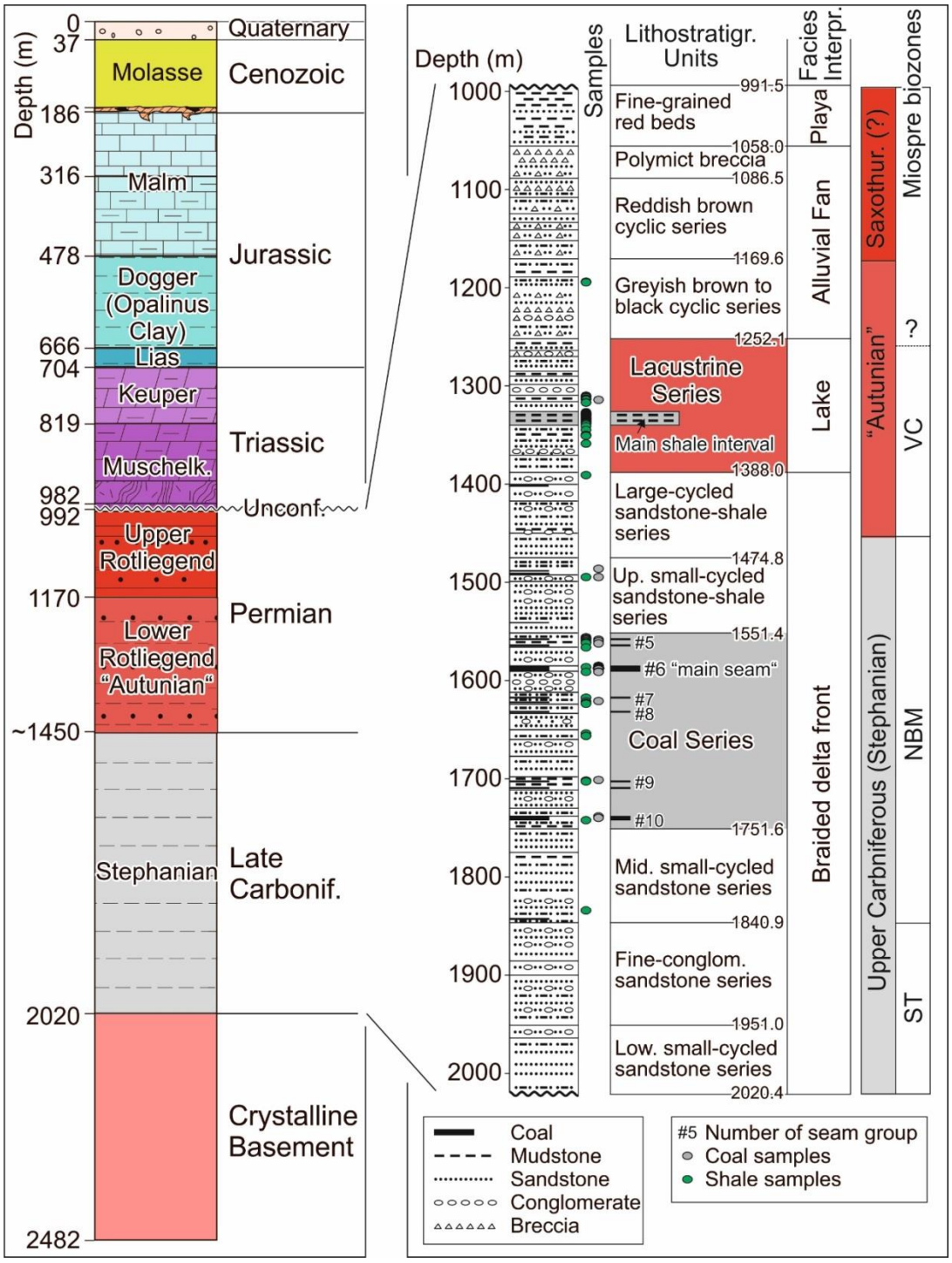

Fig. 2. Stratigraphy of the Weiach-1 borehole (modified after Matter et al., 1988 and Moscariello et al., 2021). The position of shale and coal samples is shown. Subdivision into biozones follows Hochuli (1985). ST – *Angulisporites spledidus-Latensina trilete* zone; NBM - *Potonieisporites novicus-bhardwajii-Cheiledonites major* zone; VC - *Vittatina costabilis* zone.

Random vitrinite reflectance (%Rr) data of the Weiach-1 well was provided by Leu et al. (2001) and NAGRA (2002). Vitrinite reflectance increases from ~0.7 %Rr at the top of the Permo-Carboniferous succession to ~1.25 %Rr at 1950 m depth. Mazurek et al. (2006), Leu (2012) and Omodeo-Salé et al. (2021) used these reflectance data to calibrate the heat flow history of the Weiach area. Based on these models, it is likely that Permian heat flow was high (125 mW/m²; Omodeo-Salé et al., 2021) and that gas generation from Permo-Carboniferous coals occurred already during Permian time (Leu, 2012).

Based on the palynological data of Hochuli (1985), the Coal Series (late Stephanian NBM zone) and the Lacustrine Series (early "Autunian" VC zone) can be correlated with the Igornay Formation and the Muse Formation in the Autun Basin, respectively (Mercuzot et al., 2022).

3. Samples and analytical methods

3.1 Sampling

The present study is based on 90 core samples from the Weiach-1 well, taken with the permission of Swisstopo at the core shed of NAGRA in Hochdorf in the frame of the UNCONGEO project (University of Geneva). The samples were collected in the Carboniferous (Stephanian) Coal Series (22 shale and 22 coal samples) and the Permian ("Autunian") Lacustrine Series (46 shales samples; Fig. 2).

Samples were taken from different coal seams and shale intervals to provide information on stratigraphic variations. In order to study variations at high resolution, 13 coal samples were taken from the 5-m-thick "main seam #6" (1585.0-1591.2 m; Wolf et al., 1988; see Fig. 2), which is the most important seam in the succession, and 25 samples were taken from the thickest black shale interval in the Lacustrine Series (1326.9-1338.4 m), which is termed the main shale interval in this paper (Fig. 2).

Bulk parameters were determined for all samples. A sample subset was selected for organic petrographic, biomarker, and isotope investigations. This subset includes six coal samples from the main seam #6 together with a sample from underlying shale and 21 samples from the Permian Lacustrine Series. The latter samples cover all organic matter-rich shale intervals with a special focus on the main shale interval (13 samples).

3.2 Analytical methods

With the exception of palynological investigations, the analytical work was performed at the laboratories of the Chair Petroleum Geology at Montanuniversitaet Leoben (Austria). Palynological preparations were made at the iSTEP laboratory from Sorbonne Université, Paris (France).

3.2.1 Bulk parameters

All samples were analyzed for total carbon (TC; %), total sulphur (TS; %) and total organic carbon (TOC; %) using an Eltra Helios CS elemental analyzer. Samples pre-treated with concentrated phosphoric acid were used for the TOC measurements. The difference between TC and TOC was used to calculate calcite equivalent percentages ($calcite_{equiv.}$ = 8.334*(TOC-TIC).

Rock-Eval parameters (S_1, S_2 [mgHC/g rock]; T_{max} [°C]) were determined using a "Rock-Eval 6" instrument. S_1 and S_2 peaks are hydrocarbons volatized at 300°C and hydrocarbons pyrolyzed from kerogen during gradual heating from 300 to 650°C, respectively. T_{max} is the temperature of maximum S_2 hydrocarbon generation and serves as a maturity indicator. The hydrogen index (HI = $100\times S_2/TOC$), the production index (PI = $S_1/[S_1+S_2]$) and the petroleum potential (PP = S1+S2) were calculated (Espitalié et al. 1977). A bitumen index (BI = $100xS_1/TOC$) and a quality index (QI = $100x(S_1+S_2)/TOC$) were calculated for coal samples (Sykes and Snowdon, 2002).

3.2.2 Organic petrography

Organic petrographic investigations were performed using a Leica DM 4P microscope with a 50x oil immersion objective. Semi-quantitative macerals analysis was carried out in white and fluorescence light using a single scan method. Approximately 1500 and 550 points were counted for the shale and coal samples, respectively. The results were normalized to 100 % organic matter. The maceral terminology used follows the ICCP system (ICCP 1998, 2001; Pickel et al. 2017), with te exception that fusinite is subdivided into pyro- and degradofusinite. Random vitrinite reflectance (%Rr) of four shale and two coal samples was determined in non-polarized light with a wavelength of 546 nm (Taylor et al., 1998). At least 50 particles were measured for shale samples and 100 particles for coals. The microscope was calibrated with a synthetic reflectance standard (N-LASF46A; Rr: 1.311%).

3.2.3 Palynofacies

The palynofacies approach allows the assessment of the origin and preservation state of particulate organic matter in sedimentary deposits (e.g., Steffen and Gorin, 1993; Tyson, 1995; McArthur et al., 2016; Schnyder et al. 2017). Twelve bulk samples from the Permian main shale interval (1326.9-1338.4 m) were selected and treated at the iSTEP laboratory from Sorbonne Université, Paris, France by HCl-HF using the standard procedure of Steffen and Gorin (1993). The resulting organic residues were used to make a first set of non-filtered slides. An aliquot of each sample was also filtered with a 10 µm sieve mesh and the >10 µm fraction was used to prepare a second set of filtered slides. Qualitative palynofacies observations were performed on all slides using an Axioplan2 Imaging Zeiss microscope in transmitted light. The filtered slides only were used for quantitative observations. For each filtered slide, at least 30 fields were counted yielding more than 500 particles, the threshold considered to be relevant to obtain a statistically valid count (Tyson, 1995). In this study, continental particles correspond to opaque and translucent vascular plant fragments, to a palynomorph group consisting of spores and pollen grains, and to rare occurrences of *Botryococcus*, a colonial algae indicative of freshwater to brackish water masses (e.g Tyson, 1995). Some hyphae from fungi are also observed. Amorphous organic matter (AOM) has also been observed. It correspond to orange to dark brown or even grey flakes, the origin of which cannot be determined at the microscopic scale. AOM is generally considered as deriving from algal/bacterial phytoplankton, although a higher plant tissue origin has also been proposed in some cases (Burdige, 2007; Tyson, 1995).

3.2.4 Biomarker analysis

Solvent extraction of powdered shale (5-10 g) and coal material (~1.5 g) was performed for ~1 h on a Dionex ASE 350 instrument using dichloromethane at 75°C and 100 bar. A Zymark TurboVap 500 closed cell concentrator was used to concentrate the extract to ~0.5 ml. This was followed by asphaltene precipitation using a hexane:dichloromethane solution (80:1, v/v) and separation using centrifugation. The hexane-soluble fractions were further separated into polar fractions (NSO compounds), saturated and aromatic hydrocarbons using a Köhnen-Willsch MPLC (medium pressure liquid chromatography) instrument (Radke et al., 1980). Before the GC-MS measurement, equivalent amounts of internal standards (squalane for aliphatics; 1,1´-binaphthyl for aromatics) were added to each sample.

The saturated hydrocarbon fractions were analyzed for *n*-alkanes and isoprenoids by a gas chromatograph (Trace GC-Ultra) attached to a flame ionization detector (GC-FID), equipped

with a 50 m HP-PONA capillary column (inner diameter [i.d.] 0.20 mm, 0.50 µm film thickness). The sample was injected splitless at 270 °C, and oven temperature increased from 70 to 310 °C followed by 35 min isothermal period.

Analysis of specific biomarker molecules in the saturated and aromatic fractions was performed using gas chromatography-mass spectrometry (GC-MS) by a Thermo Scientific Trace GC-Ultra installed with a 60 m TG/DB-5MS fused silica capillary column (i.d. 0.25 mm; 0.25 µm film thickness) coupled to ThermoFisher ISQ mass spectrometer. The oven temperature was initially programed from 40°C/min, held for 2 minutes and raised up to 310°C with 4°C/min followed by an isothermal period of 40 min. The sample was injected in split mode with a split ratio of 20 at 260°C using helium as carrier gas. The spectrometer was operated in the EI (electron ionization) mode with a mass-to-charge ratio (*m/z*) scan range from *m/z* 50 to *m/z* 650 (0.7 s total scan time). Xcalibur and Chromeleon data systems were used for data processing. Identification of individual compounds was based on their respective retention time within the mass spectra or total ion current (TIC) chromatogram and comparing the mass spectra with published data as reference. From the distinct compound groups in the aliphatic and aromatic fraction, absolute concentrations were determined using peak areas in the TIC chromatograms comparable to that of internal standards while in the case of mass chromatograms, response factor were used to correct the intensities of the fragment ions used for quantification of the total ion abundance per sample. The sample concentrations were standardized to their respective TOC.

3.2.5 Compound-specific carbon isotopy

For the analysis of stable carbon isotope ratios on individual *n*-alkanes and isoprenoids, the *n*-alkanes were separated from the *iso*-alkanes within the saturated hydrocarbon fraction by an improved 5 Å molecular sieve method (Grice et al., 2008). Isotope analysis was performed using a Trace GC-Ultra gas chromatograph attached to the ThermoFisher Delta-V isotope ratio mass spectrometer (IRMS) via a combustion and high temperature reduction interface (GC Isolink, ThermoFisher). The GC column is as described above, while the oven temperature was programmed to 70°C for 2 min followed by a 4°C/min increment to 300°C and held for 15 min. For calibration, a CO_2 standard gas was injected before and after each analysis. Each sample was analyzed twice. The mean isotope composition is reported in the δ notation in permil (‰) relative to the V-PDB standard. The average values of duplicate runs and analytical reproducibility per sample is less than 0.3‰.

4. Results

4.1 Carboniferous coal measures

In this section, bulk geochemical data for Carboniferous shale and coal samples are presented (Table 1). Detailed petrographic and geochemical data exist only for coal samples.

4.1.1 Bulk geochemical data of Carboniferous samples

TOC contents of coal samples range from 51.5 to 77.0 wt.% and reflect different mineral contents. Hence, shaly coal (28.8 and 33.5 wt.%), coaly shale (12.7-17.1 wt.%) and shale samples (2.0-7.3 wt.%) have lower TOC contents. In the main seam (#6), the TOC contents decrease towards the top (Fig. 3b) reflecting ash yields, which increase from the relative clean lower part of the seam (10 wt.% ash yield dry basis [db]) to 46 wt.%db (ash data are from Wolf et al., 1988).

Sulphur contents of coal samples are generally low. In the main seam, sulphur content (0.39 wt.% in average) correlates well with TOC content (Fig. 3c). Somewhat higher sulphur contents (0.55-0.85 wt.%) occur in seams below and above the main seam. Sulphur contents of shale samples are also very low (0.01-0.47 wt.%). Consequently, TOC/S ratios for coal (81.2-193.1) and shale samples are very high (5.3-133.1).

HI values of shaly coal and coal samples vary between 143 and 261 mg HC/g TOC. The average HI in the main seam (#6) is 220 mgHC/gTOC (Fig. 3d). Between 1600 and 1740 m, a slight decrease in HI from ~240 to ~200 mgHC/gTOC is observed. HI values of coaly shale samples (149 and 181 mgHC/gTOC) are of similar order of magnitude, and those of shale samples (<10 wt.%TOC) are generally lower (25-124 mgHC/gTOC; see also Fig. 4a). A plot of S_2 against TOC displays a good correlation (correlation coefficient for shale samples: r^2=0.91). The slope of the regression line gives a graphic solution of an average "true HI" (sensu Langford and Blanc-Valleron, 1990) of 131 mg HC/gTOC (Fig. 4b).

T_{max} values of coal (440-461°C, average 450°C) and shale samples (443-480°C, avg. 456°C) are similar and do not show a distinct depth trend in the interval between 1485 and 1835 m.

Shales samples are largely carbonate-free. Carbonate contents in coal samples reflect the presence of calcitic veins. The maximum carbonate content (11.2 wt.%) is recorded in a sample from the main seam (#6; Fig. 3a).

Table 1. Bulk geochemical parameters for Carboniferous sediments. Samples from the main seam (#6) are highlighted by grey shading.

Sample ID[m]	Lithology/ Seam (#)	Calcite [Wt%]	TOC [Wt%]	Sulphur [Wt%]	TOC/S [--]	S_1 [mg HC/g rock]	S_2 [mg HC/g rock]	HI [mg HC/ g TOC]	T_{max} [°C]	PI [--]	PP [mg HC/ g TOC]
1486.40	Coal	8.25	62.93	0.60	105	6.26	89.97	143	459	0.07	96
1494.74	Coal	3.07	69.33	0.85	81	5.75	135.12	195	450	0.04	141
1494.82	Shale	0.57	4.98	0.05	110	0.24	3.72	75	449	0.06	3.96
1556.00	Shale	0.46	3.79	0.03	108	0.24	2.04	54	466	0.11	2.28
1557.10	Shale	0.13	2.78	0.04	62	0.16	1.48	53	455	0.10	1.63
1557.40	Shale	0.08	3.79	0.06	61	0.24	2.81	74	450	0.08	3.05
1558.37	Shale	0.01	6.80	0.06	120	0.54	8.45	124	443	0.06	8.99
1558.50	Coal # 5	3.29	70.51	0.84	84	12.30	184	261	440	0.06	197
1559.40	Shale	0.74	7.29	0.05	133	0.61	6.50	89	457	0.09	7.11
1560.00	Coal # 5	6.75	72.19	0.55	130	10.15	168.32	233	448	0.06	178
1560.65	Shale	0.31	4.35	0.12	37	0.27	3.54	81	447	0.07	3.81
1561.95	Shale	0.00	5.82	0.07	86	0.48	5.74	99	452	0.08	6.22
1562.40	Coal #?	3.25	66.14	0.72	92	10.56	144.69	219	450	0.07	155
1566.50	Shale	0.20	2.01	0.38	5	0.09	0.50	25	459	0.15	0.58
1585.10	Coal # 6	0.00	57.06	0.43	133	8.39	126.56	222	447	0.06	135
1585.50	Shaly coal #6	11.23	33.52	0.23	147	5.57	68.75	205	448	0.07	74
1586.00	Coal # 6	0.00	51.47	0.41	126	7.38	116.89	227	451	0.06	124
1586.70	Coal # 6	0.12	54.81	0.31	178	7.34	116.43	212	449	0.06	124
1586.95	Coal # 6	0.00	74.78	0.44	170	9.83	154.60	207	451	0.06	164
1587.35	Coal # 6	0.00	69.53	0.40	175	9.35	145.63	209	448	0.06	155
1587.48	Coal # 6	1.68	65.27	0.41	159	10.01	147.23	226	453	0.06	157
1587.70	Coal # 6	0.00	74.51	0.44	169	10.48	171.90	231	447	0.06	182
1588.10	Coal # 6	3.64	53.38	0.30	176	7.11	118.34	222	448	0.06	125
1588.40	Coal # 6	0.00	69.54	0.50	139	9.56	164.43	236	448	0.05	174
1588.63	Coal # 6	1.26	66.10	0.40	163	9.52	162.03	245	448	0.06	172
1590.95	Coal # 6	0.00	75.69	0.44	170	9.64	166.55	220	451	0.05	176
1591.19	Coal # 6	0.00	76.95	0.40	193	10.14	156.86	204	448	0.06	167
1591.25	Shale	0.14	1.98	0.03	64	0.14	1.15	58	457	0.11	1.29
1617.60	Coaly Shale	0.87	17.05	0.25	69	1.54	30.83	181	448	0.05	32.36
1620.99	Shaly coal	1.32	28.84	0.24	119	3.06	52.49	182	451	0.06	56
1621.50	Shale	0.67	5.31	0.05	106	0.42	3.98	75	460	0.10	4.40
1623.00	Shale	0.37	3.17	0.05	67	0.22	1.66	52	465	0.11	1.88
1623.80	Shale	0.26	8.05	0.41	19	0.61	7.89	98	449	0.07	8.50
1654.04	Shale	0.21	6.31	0.05	126	0.55	5.33	84	462	0.09	5.87
1656.45	Shale	0.00	7.04	0.09	80	0.51	5.94	84	451	0.08	6.45
1656.67	Shale	0.04	3.69	0.05	76	0.19	1.67	45	457	0.10	1.86
1701.30	Coal # 9	4.36	75.52	0.62	122	11.75	157.21	208	459	0.07	169
1702.00	Shale # 9	0.48	5.70	0.05	118	0.55	5.57	98	451	0.09	6.11
1703.00	Coaly shale	0.12	12.72	0.15	83	1.53	19.00	149	457	0.07	20.52
1738.46	Coal # 10	0.76	68.55	0.58	118	9.40	132.37	193	455	0.07	142
1739.90	Coal # 10	0.00	65.31	0.66	100	8.28	132.08	202	461	0.06	140
1742.30	Shale	0.14	3.51	0.04	88	0.21	1.29	37	488	0.14	1.50
1834.15	Shale	0.04	5.10	0.06	85	0.37	4.82	95	456	0.07	5.19

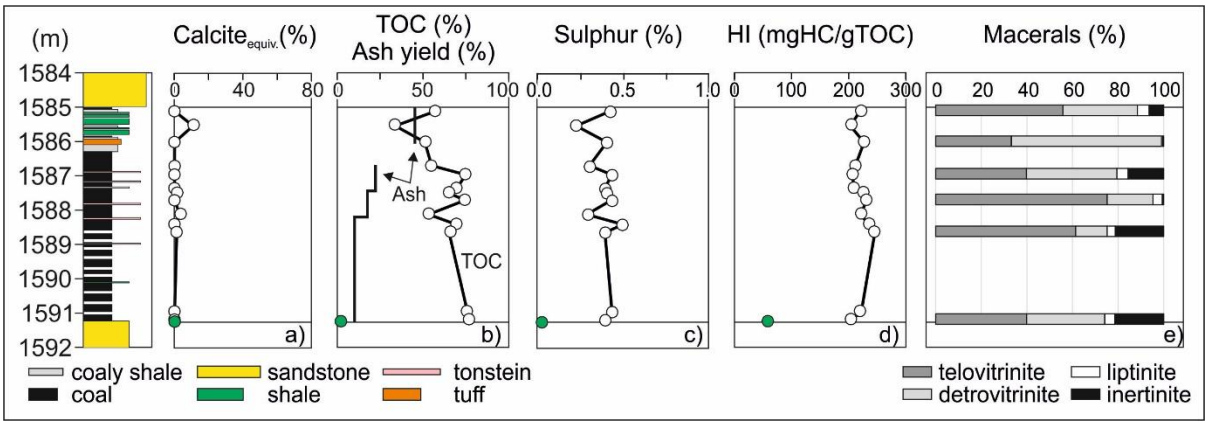

Fig. 3. Sketch of the main coal seam (#6) with vertical variation of bulk geochemical parameters and maceral percentages. Lithology and ash yield are from Wolf et al. (1988). Data from a shale sample from the underlying fine-grained sandstone are shown by green symbols.

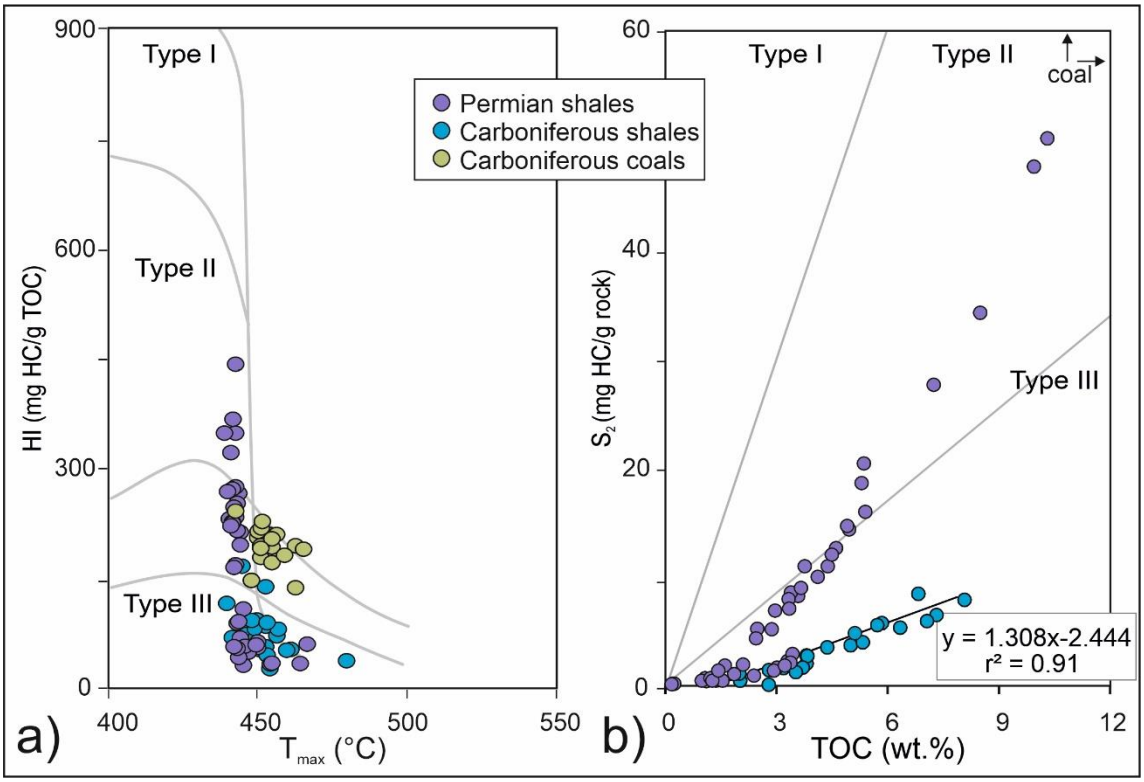

Fig. 4. Cross-plots of a) HI versus T_{max} and b) S_2 versus TOC. Data from coaly shales and coals (TOC >12 wt.%) are not displayed in Fig. 4b. A regression line is plotted for Carboniferous shale samples. (Regression lines for different subsets of Permian shales are shown in Fig. 17).

4.1.2 Organic petrography

Maceral percentages of six samples from the main seam (#6) are presented in Table 2 and Fig. 3. The prevailing maceral group is vitrinite (74-99 vol.%; 85 vol.% in average). Telovitrinite (mainly collotelinite; Fig. 5) is more abundant than detrovitrinite (except in the sample from 1586.00 m depth). Inertinite macerals occur in significant amounts (up to 22 vol.%; 11 vol.% in average). Pyrofusinite (fossil charcoal; 6 vol.% average; Fig. 5) dominates amongst the macerals of the inertinite group. Degradofusinite (fusinite formed due to degradation; 3 vol.%), highly degraded macrinite (1.4 vol.%), and intertodetrinite (0.7 vol.%) are less abundant. Significant amounts of secretinite (oxidized plant excretions [ICCP, 1998]; Fig. 5) are limited to sample 1588.63 m (1.2 vol.%). Liptinite contents range from 0.4 to 5.2 vol.% (3.7 vol.% in average). Sporinite (3.1 vol.% in average) is the dominant liptinite macerals. Sporangia and macrosporinite are present (Fig. 5). Liptodetrinite, cutinite, resinite, and exsudatinite (solid residue of originally petroleum-like substances; Pickel et al., 2017) are rare. Vitrinite reflectance of two samples from the main seam is 0.91 and 0.95 %Rr (Table 2).

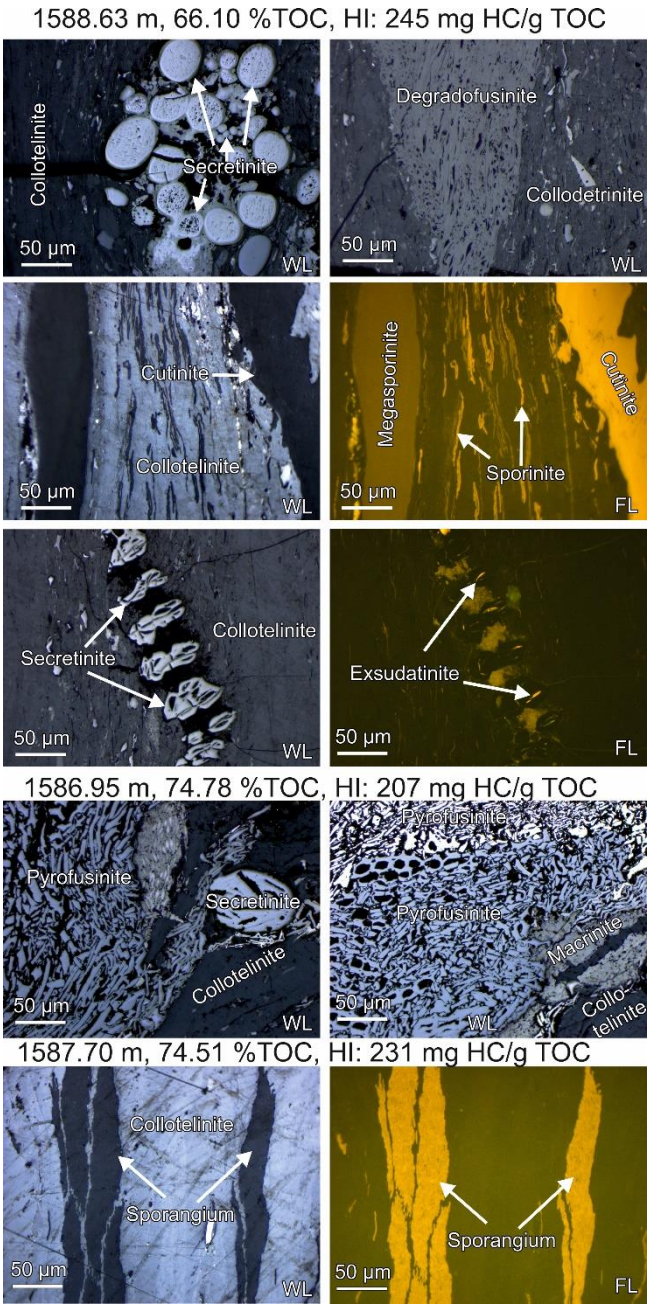

Fig. 5. Microphotographs of typical macerals in Carboniferous coal samples. (WL: white light, FL: fluorescent light)

Table 2. Maceral percentages and vitrinite reflectance in Carboniferous coals from the main seam #6.
Std – standard deviation, n – number of measurements

Sample ID [m]	Telo-vitrinite [Vol%]	Detro-vitrinite [Vol%]	Degrado-fusinite [Vol%]	Pyro-fusinite [Vol%]	Inerto-detrinite [Vol%]	Macri-nite [Vol%]	Secreti-nite [Vol%]	Spori-nite [Vol%]	Cuti-nite [Vol%]	Resi-nite [Vol%]	Exsuda-tinite [Vol%]	Lipto-detrinite [Vol%]	Vitrinite Reflect. [%Rr]	Std. dev	n
1585.10	55.9	32.6	0.2	5.0	0.8	0.4	0.0	3.4	0.2	1.0	0.0	0.6	0.95	0.04	100
1586.00	33.2	65.9	0.0	0.2	0.4	0.0	0.0	0.2	0.2	0.0	0.0	0.0			
1586.95	39.8	39.7	4.9	8.0	0.5	2.3	0.0	4.0	0.0	0.0	0.7	0.2			
1587.70	75.2	20.2	0.2	0.0	0.0	0.4	0.0	3.8	0.0	0.0	0.0	0.2			
1588.63	61.4	13.8	10.6	6.8	0.4	2.2	1.2	3.2	0.4	0.0	0.0	0.0	0.91	0.04	100
1591.19	39.9	34.3	2.2	14.0	2.2	3.1	0.0	4.0	0.0	0.0	0.2	0.2			

4.1.3 Biomarker

Representative GC-traces of three coal and one shale sample from the main coal seam #6 are shown in Fig. 6. Biomarker results of six coal and the shale sample from the main coal seam #6 are shown in Table 3. Depth plots of selected parameters are provided in Fig. 7. The extractable organic matter (EOM) content ranges from 18.2 to 29.0 mg/gTOC and is dominated by asphaltenes (avg. 66 wt.%), followed by NSO compounds (avg. 24 %), aromatic (avg. 6 wt.%) and aliphatic (avg. 4 wt.%) hydrocarbons, respectively.

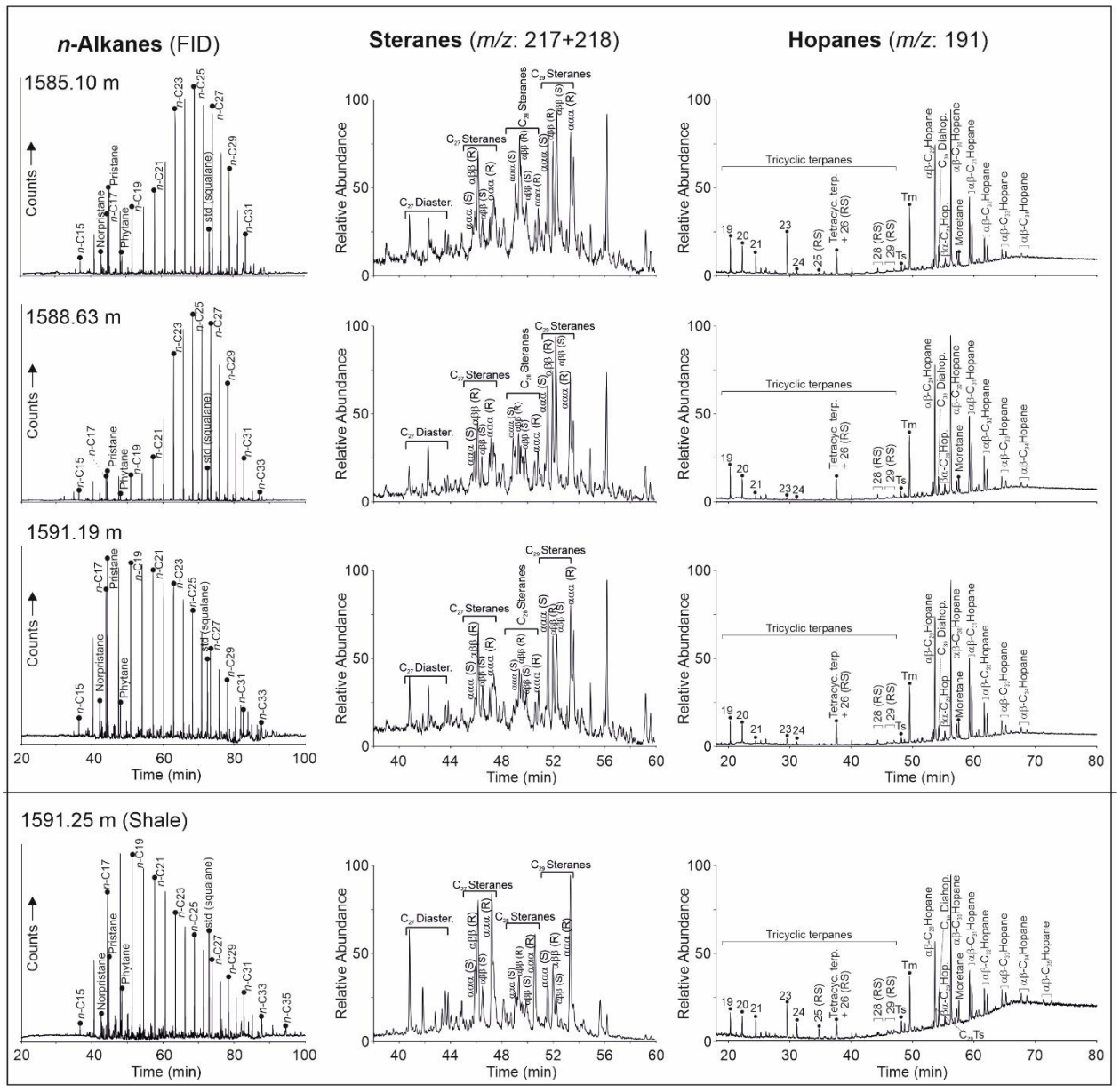

Fig. 6. Representative gas chromatograms of samples from the main coal seam (#6).

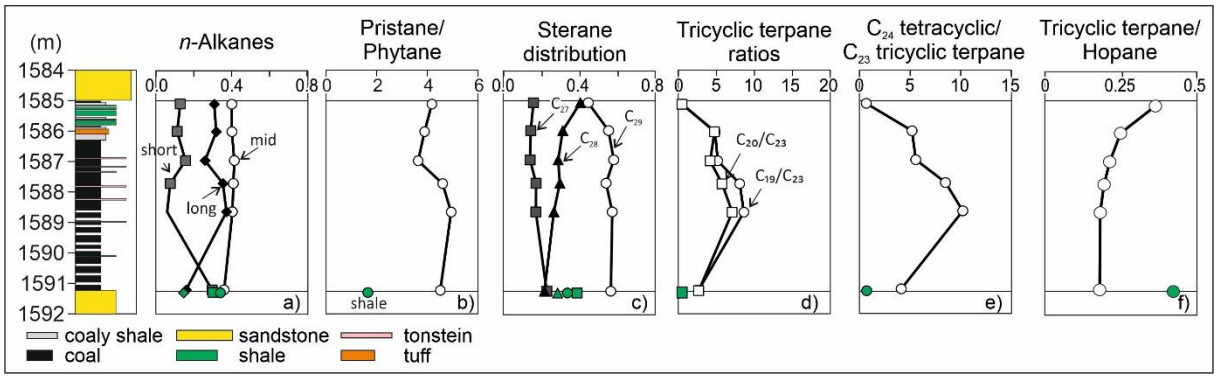

Fig. 7. Depth plots of selected geochemical parameters in the main seam (#6). Data from the underlying shale are shown by green symbols.

The samples contain moderate concentrations of *n*-alkanes (73-612 µg/g TOC) ranging in chain length from *n*-C_{15} to *n*-C_{35} (Fig. 6). With the exception of the lowermost sample (1591.19 m), the unimodal distribution patterns show a peak at C_{24} or C_{25}. Mid-chain *n*-alkanes (*n*-$C_{21–25}$/∑*n*-alkanes: 0.40-0.42) are typically more abundant than long-chain (*n*-$C_{27–31}$/∑*n*-alkanes: 0.31-0.37) and short-chain *n*-alkanes (*n*-$C_{15–19}$/∑*n*-alkanes: 0.06-0.16; Table 3; Fig. 7a). The lowermost sample shows a peak at *n*-C_{17} and contains a relatively high amount of short-chain *n*-alkanes (0.30), but relatively low amounts of mid- (0.36) and long-chain *n*-alkanes (0.16). No marked odd-even predominance could be seen and the carbon preference index (CPI after Bray and Evans, 1961) ranges from 1.02 to 1.16 (Table 3).

The concentrations of isoprenoids are low (6-25 µg/g TOC). The pristane/phytane (Pr/Ph) ratios (Didyk et al., 1978) are very high, but slightly lower in the upper three samples (3.6-4.2) than in the lower three samples (4.5-4.9; Fig. 7b). The samples are characterized by moderate pristane/*n*-C_{17} ratios (0.90-2.00) and very low phytane/*n*-C_{18} ratios (0.20-0.43; Table 3).

In all samples, sterane concentrations are very low (4-9 µg/g TOC) and C_{29} steranes significantly dominate over C_{28} and C_{27} steranes (C_{29} >> C_{28} > C_{27}; Fig. 7c). The C_{29} ααα sterane 20S/(20S+20R) ratio ranges from 0.43 to 0.49 (avg. 0.45), while ratios of αββ/(αββ+ααα) C_{29}-steranes range from 0.43 to 0.60 (Table 3).

Hopanes are significantly more abundant (28-76 µg/g TOC) than steranes. Regular αβ hopanes from C_{27} to C_{35} dominated the distribution with C_{30} being most abundant, while C_{28} was absent. The Ts/(Ts+Tm) and moretane/hopane ratios are both ~0.1. The C_{35} homohopane index (HHI = C_{35}/C_{31-35}) is very low. The 22S/(22S+22R) isomerization ratios of C_{31} hopanes (0.6) reached the equilibrium value (Peters et al., 2005). Tricyclic terpanes (TT) are present in low amounts (3-13 µg/g TOC). Prominent among them are the C_{19}, C_{20}, and C_{23} TTs (Fig. 6).

C_{24} Tetracyclic terpane (TeT) is also present in significant amounts. The ratios of C_{19}/C_{23} TT (2.66-8.66) and C_{20}/C_{23} TT (2.71-7.12) are indicators for land-plants input (Noble et al., 1986; Peters et al., 2005) and are very high in all samples with exception of the uppermost coal sample (1581.10 m) and the shale sample from the floor of the seam (1591.25 m) where they are approximately 0.5 (Fig. 7d). Consequently, these ratios show an upward increasing-decreasing trend.

The dominant aromatic hydrocarbon compounds (Table 3) are naphthalene and its methylated counterparts (di, tri and tetra methyl-naphthalenes) followed by phenanthrene and its methylated counterparts (methyl-phenanthrenes (MP) and dimethyl-phenanthrenes (DMP)). The methyl-phenanthrene index (MPI-1 according to Radke et al., 1986; Radke, 1988) varies from 0.49 to 0.56 for the coals. Equivalent vitrinite reflectance values calculated from MPI-1 (Radke and Welte, 1983) range from 0.69 to 0.74 %Rr. The concentration of methyl-dibenzothiophene (MDBT; 0.77-1.55 µg/g TOC) and the dibenzothiophene/phenathrene (DBT/P; 0.01-0.02) ratio are very low.

Table 3. Concentration and concentration ratios of compound groups within the hydrocarbon fractions of Permian and Carboniferous sediments from the Weiach-1 well. Carboniferous coal samples in grey highlight. *n.d* = not detected.

Sample ID [m]	EOM [mg/gTOC]	Aliphatic [wt.%]	Aromatic [wt.%]	NSO compounds [wt.%]	Asphaltene [wt.%]	*n*-C_{15-19}/	*n*-C_{21-25}/ *n*-alkanes	*n*-C_{27-31}/	CPI	Pr/Ph	Pr/ C_{17}	Pr/C_{18}	Steranes [µg/g TOC]	C_{27}/ C_{27-29} steranes	C_{28}/ C_{27-29} steranes	C_{29}/ C_{27-29} steranes
1310.08	15.31	8.28	10.11	60.46	21.15	0.35	0.29	0.19	1.17	1.17	0.73	0.58	54	0.34	0.29	0.37
1310.58	18.25	16.71	22.28	50.93	10.08	0.37	0.33	0.12	0.97	1.72	0.93	0.48	238	0.38	0.28	0.34
1311.55	24.47	12.05	16.33	62.25	9.37	0.45	0.29	0.12	1.13	3.01	2.66	1.00	146	0.36	0.26	0.38
1312.95	48.88	31.88	17.69	48.37	2.06	0.44	0.26	0.09	1.05	2.53	0.75	0.31	117	0.32	0.24	0.45
1313.37	61.42	38.44	13.26	45.71	2.59	0.40	0.29	0.11	1.17	2.55	0.66	0.26	99	0.39	0.32	0.29
1326.95	16.31	14.53	18.44	44.69	22.35	0.36	0.33	0.12	1.07	1.05	0.67	0.42	242	0.35	0.30	0.35
1328.65	29.33	12.46	6.09	53.62	27.83	0.33	0.39	0.10	1.17	0.85	0.08	0.06	29	0.45	0.19	0.37
1329.35	69.20	27.65	11.22	46.79	14.34	0.54	0.25	0.04	1.15	1.89	0.13	0.07	1	0.51	0.11	0.38
1330.15	39.20	21.72	7.81	53.15	17.32	0.58	0.24	0.03	1.10	2.11	0.08	0.03	14	0.47	0.13	0.40
1331.10	41.97	21.33	6.58	55.75	16.34	0.59	0.23	0.02	1.11	2.21	0.08	0.03	12	0.50	0.13	0.37
1332.43	48.11	23.33	7.39	50.39	18.88	0.58	0.24	0.02	1.26	0.99	0.07	0.06	17	0.52	0.13	0.35
1333.30	53.24	27.70	7.12	48.18	17.00	0.56	0.24	0.03	1.11	1.95	0.07	0.03	15	0.54	0.12	0.34
1334.22	51.80	25.16	8.01	50.38	16.46	0.55	0.26	0.04	1.11	1.54	0.13	0.07	24	0.48	0.16	0.36
1335.75	41.95	11.46	7.80	45.49	35.24	0.55	0.26	0.04	1.31	1.36	0.07	0.04	8	0.49	0.19	0.32
1336.12	57.53	24.45	5.94	56.73	12.88	0.53	0.26	0.05	1.14	1.98	0.14	0.06	27	0.46	0.15	0.40
1337.40	68.67	24.81	7.77	57.22	10.20	0.53	0.26	0.05	1.15	1.81	0.17	0.09	27	0.46	0.15	0.39
1338.35	63.96	23.78	12.21	53.75	10.26	0.53	0.26	0.06	1.15	2.49	0.19	0.08	27	0.39	0.15	0.45
1339.20	60.35	20.51	8.87	52.13	18.50	0.45	0.30	0.09	1.25	2.45	0.27	0.10	2	0.44	0.21	0.35
1350.70	25.98	20.29	14.54	59.74	5.43	0.43	0.31	0.10	1.20	1.74	0.33	0.20	23	0.38	0.26	0.36
1350.95	27.85	26.29	13.73	55.15	4.83	0.36	0.34	0.13	1.20	2.13	0.49	0.22	56	0.33	0.30	0.37
1358.90	11.75	9.03	10.11	63.54	17.33	0.41	0.30	0.13	1.37	1.06	0.46	0.38	9	0.43	0.26	0.31
1585.10	23.82	2.97	5.80	24.60	66.63	0.13	0.40	0.31	1.14	4.17	2.00	0.43	9	0.15	0.40	0.44
1586.00	21.95	4.72	7.81	25.17	62.30	0.11	0.40	0.32	1.16	3.88	1.36	0.29	7	0.14	0.31	0.55
1586.95	27.12	1.44	4.12	14.99	79.44	0.16	0.42	0.26	1.11	3.63	0.90	0.20	4	0.14	0.28	0.58
1587.70	28.96	5.13	6.40	19.77	68.70	0.08	0.41	0.36	1.14	4.60	1.31	0.27	8	0.17	0.29	0.54
1588.63	26.27	7.92	8.31	30.95	52.81	0.06	0.41	0.37	1.14	4.93	1.77	0.34	8	0.17	0.26	0.57
1591.19	22.01	2.06	6.53	26.20	65.21	0.30	0.36	0.16	1.02	4.51	1.65	0.30	7	0.22	0.21	0.56
1591.25	18.16	3.31	10.22	62.71	23.76	0.30	0.34	0.16	1.08	1.65	0.85	0.43	35	0.38	0.28	0.33

Table 3. Continued

Sample ID[m]	S/(S+R) C_{29} Steranes	αββ/(αββ+ααα) C_{29} Steranes	C_{27} (Diast./Reg. Sterane)	Hopane [µg/g TOC]	Steranes/ Hopanes	S/(S+R) C_{31} Hopanes	Moretane/ Hopane	Ts/ (Ts+Tm)	Gam./ (Gam. + C_{30} Hopane)	C_{35}/C_{31-35} Hopanes	Tricyclic terpanes Σ [µg/g TOC]	C_{19}/C_{23}	C_{20}/C_{23}
1310.08	0.25	0.37	0.21	96	0.56	0.59	0.36	0.07	0.06	0.05	12	0.46	0.83
1310.58	0.32	0.29	0.21	1697	0.14	0.58	0.45	0.03	0.06	0.02	77	0.61	1.10
1311.55	0.40	0.29	0.24	2305	0.06	0.59	0.41	0.02	0.10	0.01	160	0.99	1.63
1312.95	0.68	0.35	0.30	2963	0.04	0.58	0.19	0.67	0.17	0.08	281	0.78	1.04
1313.37	0.46	0.48	0.37	943	0.10	0.60	0.21	0.71	0.27	0.05	163	0.58	0.84
1326.95	0.25	0.29	0.16	262	0.92	0.59	0.25	0.27	0.12	0.09	42	0.19	0.36
1328.65	0.63	0.63	0.70	391	0.08	0.57	0.39	0.05	0.05	0.02	90	6.18	18.74
1329.35	0.64	0.36	1.25	8	0.07	0.55	0.19	0.76	0.31	n.d	2	0.54	0.32
1330.15	0.63	0.41	0.86	122	0.11	0.57	0.26	0.58	0.24	0.02	24	1.66	2.80
1331.10	0.57	0.42	0.82	102	0.11	0.57	0.26	0.63	0.24	0.02	21	1.84	1.34
1332.43	0.55	0.38	0.82	191	0.09	0.58	0.25	0.61	0.21	0.03	25	1.45	0.43
1333.30	0.71	0.28	0.79	153	0.10	0.57	0.23	0.68	0.28	0.03	25	1.15	0.31
1334.22	0.60	0.34	0.92	305	0.08	0.58	0.19	0.70	0.40	0.04	46	0.74	0.32
1335.75	0.68	0.47	0.87	64	0.12	0.57	0.27	0.34	0.23	0.03	12	0.92	0.35
1336.12	0.70	0.36	0.94	234	0.12	0.58	0.20	0.72	0.41	0.04	40	0.70	0.98
1337.40	0.58	0.34	0.88	272	0.10	0.58	0.20	0.70	0.31	0.03	54	0.72	0.37
1338.35	0.54	0.29	0.71	380	0.07	0.58	0.23	0.71	0.15	0.04	62	1.10	0.75
1339.20	0.70	0.54	1.10	10	0.16	0.58	0.27	0.50	0.14	0.04	3	1.38	2.26
1350.70	0.45	0.33	0.33	113	0.21	0.60	0.34	0.29	0.18	0.06	48	1.16	1.15
1350.95	0.27	0.32	0.25	86	0.65	0.61	0.33	0.46	0.23	0.07	35	0.58	0.86
1358.90	0.29	0.35	0.28	24	0.39	0.59	0.32	0.07	0.05	0.07	9	0.53	0.86
1585.10	0.44	0.49	0.45	72	0.13	0.61	0.10	0.07	*n.d*	0.01	13	0.52	0.52
1586.00	0.49	0.60	0.32	53	0.13	0.61	0.10	0.08	*n.d*	0.02	7	4.87	4.80
1586.95	0.44	0.56	0.41	28	0.15	0.61	0.12	0.09	*n.d*	0.01	3	5.21	4.22
1587.70	0.45	0.57	0.31	63	0.12	0.61	0.12	0.10	*n.d*	0.02	6	8.10	5.78
1588.63	0.43	0.53	0.26	63	0.13	0.61	0.12	0.09	*n.d*	0.02	6	8.66	7.12
1591.19	0.47	0.43	0.29	76	0.09	0.61	0.11	0.09	*n.d*	0.02	7	2.66	2.71
1591.25	0.22	0.33	0.26	38	0.92	0.60	0.15	0.18	0.11	0.09	8	0.47	0.53

Table 3. Continued

Sample ID[m]	MP [µg/g TOC]	DMP	MPI-1	Rc	MDBT [µg/g TOC]	DBT/ Phen	Aryl-isoprenoid [µg/g TOC]	AIR C_{13-17}/C_{18-22}	C_{30} (Diahop./Hop.)	Σ Tricyclic terpane / Σ Hopane	Retene [µg/g TOC]	Simonellite [µg/g TOC]
1310.08	33	39	0.37	0.62	1	0.00	2	0.21	0.05	0.13	*n.d*	*n.d*
1310.58	21	3	0.22	0.53	*n.d*	0.00	3	0.08	0.04	0.05	*n.d*	*n.d*
1311.55	14	7	0.19	0.51	2	0.02	15	0.44	0.05	0.07	*n.d*	*n.d*
1312.95	11	41	0.24	0.54	12	0.12	58	2.55	0.31	0.09	*n.d*	*n.d*
1313.37	21	75	0.48	0.69	14	0.16	81	2.18	0.48	0.17	*n.d*	*n.d*
1326.95	24	17	0.35	0.61	1	0.01	6	0.08	0.11	0.16	*n.d*	*n.d*
1328.65	21	41	0.61	0.77	3	0.02	2	0.17	0.05	0.23	17.47	74.84
1329.35	32	70	0.53	0.72	7	0.02	24	1.01	0.40	0.23	5.78	21.29
1330.15	28	61	0.52	0.71	4	0.02	6	0.61	0.35	0.20	6.23	42.61
1331.10	25	48	0.53	0.72	3	0.02	7	0.65	0.41	0.20	5.87	17.69
1332.43	32	68	0.52	0.71	3	0.02	7	0.38	0.36	0.13	1.53	1.10
1333.30	33	82	0.52	0.71	3	0.02	9	0.55	0.44	0.16	1.41	0.76
1334.22	34	76	0.51	0.71	4	0.04	9	0.62	0.39	0.15	1.91	1.61
1335.75	26	62	0.55	0.73	4	0.02	3	0.21	0.22	0.19	1.78	0.75
1336.12	26	65	0.54	0.72	3	0.02	7	0.47	0.42	0.17	1.26	0.33
1337.40	22	59	0.53	0.72	3	0.03	11	0.59	0.48	0.20	1.33	1.09
1338.35	25	71	0.56	0.74	6	0.03	21	0.97	0.56	0.16	4.30	10.61
1339.20	38	110	0.57	0.74	8	0.03	21	0.58	0.36	0.34	6.12	22.26
1350.70	28	13	0.16	0.50	2	0.00	12	0.42	0.29	0.42	*n.d*	*n.d*
1350.95	17	18	0.17	0.50	*n.d*	0.01	14	0.18	0.35	0.40	*n.d*	*n.d*
1358.90	38	29	0.48	0.69	1	0.01	1	0.33	0.07	0.39	*n.d*	*n.d*
1585.10	47	58	0.54	0.73	1	0.01	*n.d*	*n.d*	0.17	0.18	*n.d*	*n.d*
1586.00	66	84	0.53	0.72	2	0.01	*n.d*	*n.d*	0.10	0.12	*n.d*	*n.d*
1586.95	52	55	0.53	0.72	1	0.02	*n.d*	*n.d*	0.12	0.11	*n.d*	*n.d*
1587.70	45	53	0.56	0.74	1	0.02	*n.d*	*n.d*	0.13	0.10	*n.d*	*n.d*
1588.63	48	71	0.52	0.71	1	0.02	*n.d*	*n.d*	0.13	0.09	*n.d*	*n.d*
1591.19	52	74	0.49	0.69	1	0.02	*n.d*	*n.d*	0.12	0.09	*n.d*	*n.d*
1591.25	76	71	0.53	0.72	2	0.02	3	0.08	0.23	0.21	*n.d*	*n.d*

Table 4. Compound specific carbon isotope ratios ($\delta^{13}C$; ‰) of Permo-Carboniferous samples of Weiach-1. Coal samples in grey highlight.

Sample ID [m]	*n*-C_{15}	*n*-C_{16}	*n*-C_{17}	*n*-C_{18}	*n*-C_{19}	*n*-C_{20}	*n*-C_{21}	*n*-C_{22}	*n*-C_{23}	*n*-C_{24}	*n*-C_{25}	*n*-C_{26}	*n*-C_{27}	*n*-C_{28}	*n*-C_{29}	Pristane	Phytane
1312.95	*n.d*	-27.63	-28.07	-28.43	-28.90	-29.59	-29.86	-30.13	-30.43	-29.80	-30.99	*n.d*	*n.d*	*n.d*	*n.d*	-25.90	-26.36
1313.37	*n.d*	-28.15	-28.52	-28.94	-29.63	-29.69	-30.21	-30.52	-30.69	-30.60	-31.24	-30.15	-30.32	*n.d*	*n.d*	-26.74	-27.63
1328.65	*n.d*	*n.d*	*n.d*	-30.31	-30.31	-30.90	-30.22	-30.72	-30.67	-30.68	-31.08	-31.07	-30.65	-30.32	*n.d*	*n.d*	*n.d*
1329.35	-28.58	-28.99	-29.23	-29.79	-29.93	-30.00	-30.21	-30.25	-29.93	-29.49	-29.81	-29.51	-28.97	-29.12	-28.87	-28.47	-28.87
1330.15	*n.d*	-28.44	-29.09	-29.89	-29.74	-29.95	-29.89	-29.74	-29.24	-29.03	-29.00	-28.90	-28.27	-28.77	-28.89	-28.65	-28.80
1331.10	*n.d*	-28.68	-28.94	-29.52	-29.75	-29.85	-29.69	-29.64	-29.38	-29.18	-29.04	-28.22	-27.96	-28.32	-28.18	-29.10	-29.22
1332.43	*n.d*	-29.15	-29.38	-29.11	-28.93	-28.91	-28.77	-28.74	-29.19	-29.26	-29.37	-28.67	-27.86	-28.16	-28.32	-28.92	-28.79
1333.30	*n.d*	-29.45	-29.44	-29.19	-29.06	-29.18	-29.11	-29.42	-29.25	-29.17	-29.18	-29.39	-29.35	-29.01	-29.21	-28.83	-29.00
1334.22	-29.95	-29.21	-29.64	-29.63	-29.49	-29.63	-29.30	-29.31	-29.17	-28.70	-28.79	-29.24	-28.85	-28.51	-28.72	-29.58	-29.53
1335.75	*n.d*	-28.89	-29.17	-29.41	-29.44	-29.81	-30.00	-30.42	-30.18	-29.83	-30.28	-30.03	-29.65	-29.78	-30.05	-29.43	-29.79
1336.12	-29.43	-29.38	-29.86	-30.03	-30.07	-30.27	-30.43	-30.82	-31.20	-30.50	-30.27	-30.61	-31.03	-31.12	-30.73	-30.21	-30.21
1337.40	-29.54	-29.63	-30.04	-30.32	-30.29	-30.50	-30.62	-31.10	-30.64	-30.99	-30.40	-30.88	-30.88	-31.07	-30.87	-30.17	-29.93
1338.35	-28.90	-29.32	-29.78	-29.71	-29.59	-29.47	-29.87	-30.12	-30.91	-30.51	-30.37	-30.64	-31.14	-30.62	-30.45	-29.91	-30.28
1339.20	-29.08	-30.17	-29.96	-29.92	-29.97	-30.04	-30.61	-31.09	-31.22	-30.72	-30.67	-30.63	-31.03	-30.93	-31.15	-30.27	-30.33
1350.95	*n.d*	*n.d*	*n.d*	-28.10	-29.37	-29.64	-30.10	-29.72	-30.94	-31.15	-31.49	-28.94	-30.96	-30.39	*n.d*	*n.d*	-28.76
1585.10								-26.33	-26.82	-26.85	-27.03	-26.60	-27.00	-27.09	-27.82	*n.d*	*n.d*
1586.00								-27.65	-27.85	-27.47	-27.72	-27.83	-27.94	-27.45	-27.32	*n.d*	-27.06
1586.95								-26.84	-26.87	-25.97	-26.80	-26.31	-27.05	-27.31	*n.d*	*n.d*	*n.d*
1587.70								-26.94	-27.43	-27.76	-28.42	-28.58	-28.55	-28.53	*n.d*	-28.10	-26.48
1588.63								*n.d*	-27.12	-28.03	-28.08	-28.02	-28.20	-28.09	*n.d*	-27.93	-27.28

4.1.4 Compound-specific stable carbon isotopy

Carbon isotope compositions of *n*-alkanes with 22 to 29 carbon atoms and of pristane and phytane were determined (Table 4). The $\delta^{13}C$ values of *n*-alkanes and isoprenoids ranges from -26.33 ‰ to -28.58 ‰. In most samples, $\delta^{13}C$ values of *n*-alkanes decrease slightly (get isotopically lighter) with increasing carbon numbers. Only in the sample from 1586.00 m depth, $\delta^{13}C$ values remain constant or get slightly heavier (Fig. 8).

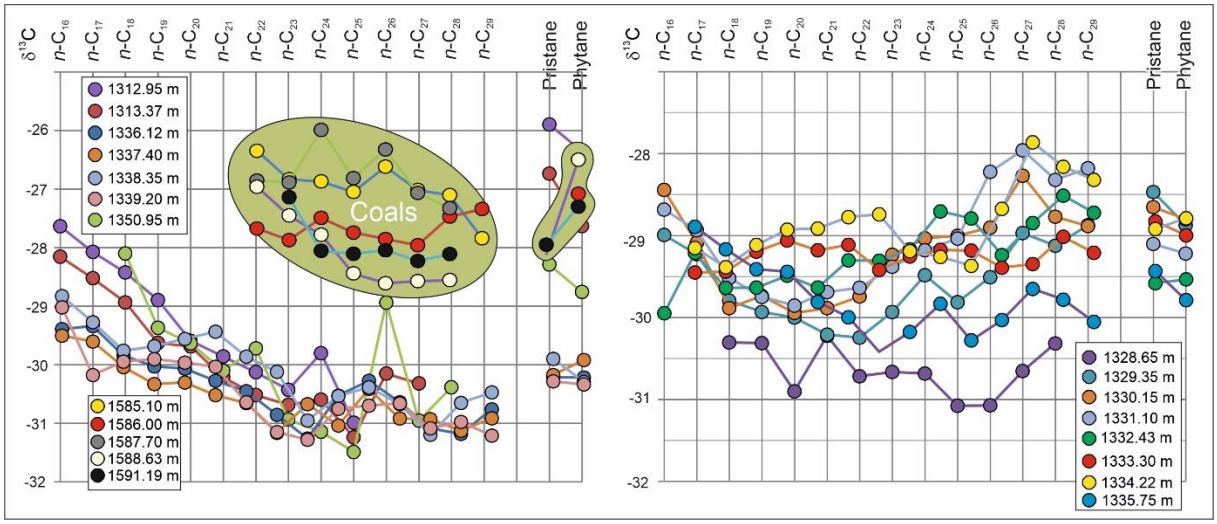

Fig. 8. Carbon isotope composition of individual *n*-alkanes, pristane and phytane for Permian shales and Carboniferous coal samples from different stratigraphic intervals in the Weiach-1 well.

4.2 Permian Lacustrine Series

Forty-five shale samples and one driftwood sample (1314.23 m) from the Permian Lacustrine Series, covering the depth range from 1391.00 to 1194.08 m, were investigated. The shales are light grey, dark grey or dark brown and often contain fish scales and plant remains. Sampling gaps are due to the presence of sandy layers. The main focus is on the thickest shale interval in the lacustrine series (main shale interval; 1339.20-1326.95 m).

4.2.1 Bulk geochemical data of samples from the Permian Lacustrine Series

Largely carbonate-free shale samples with very low TOC contents (≤0.21 wt.%), sulphur contents (≤0.10 wt.%) and HI values (~20 mgHC/gTOC) occur near the base (1391.00 m) and in the upper part of the lacustrine series (1149.58-1194.08 m; Table 5).

Significantly higher TOC contents (0.95-10.25 wt.%, 4.7 wt.% in average) are observed in shale samples in the depth interval between 1358.90 and 1310.08 m (Table 5; Fig. 9). HI values in this interval range from 24 to 488 mgHC/gTOC and indicate the presence of Type II, III and IV kerogen (Fig. 4a). The plot of S_2 versus TOC also reflects the presence of different kerogen types (Fig. 4b). As expected in fresh water lacustrine sediments, sulphur contents are generally low (<0.8 wt.%), despite high TOC contents. This results in high TOC/S ratios (5.8-197). Carbonate contents are often very low (<1.0 wt.%), but significantly higher values occur between 1351.0 and 1350.3 m (max. 31 wt.%), at the base (1339.2-1338.3 m; max. 37 wt.%), near the top of the main shale interval (1328.7-1327.6 m; max. 8 wt.%), and in the shale interval between 1310.5 and 1314.3 m (max: 23 wt.%). Both, TOC and HI decrease upwards in the main shale interval (1326.9-1339.2 m), although a TOC and HI peak occurs at 1329.35 m depth, briefly interrupting this trend (Fig. 9).

The investigated driftwood (1314.23 m) has a very high TOC content (51.20 wt.%) and a low HI (155 mgHC/gTOC). The sulphur content of the driftwood is relatively high (1.46 wt.%).

The average T_{max} values of Permian samples with S_2 >0.2 mgHC/g rock is 442°C (435-460°C). No depth trend is visible in the depth interval between 1310 and 1391 m.

Table 5. Bulk geochemical parameters of samples from the Permian Lacustrine Series. Samples from the main shale interval are highlighted by grey shading.

Sample ID [m]	Lithology	Calcite [Wt.%]	TOC [Wt.%]	Sulphur [Wt.%]	TOC/S [--]	S_1 [mg HC/g rock]	S_2 [mg HC/g rock]	HI [mg HC/ g TOC]	T_{max} [°C]	PI [--]	PP [mg HC/ g TOC]
1194.08	Shale	0.00	0.16	0.01	17	0.00	0.03	16	488?	0.00	0.03
1194.50	Shale	0.13	0.17	0.09	2	0.01	0.04	21	487?	0.22	0.05
1194.58	Shale	0.22	0.21	0.04	5	0.01	0.04	19	480?	0.20	0.05
1310.08	Shale	1.23	2.97	0.03	97	0.11	1.52	51	447	0.06	1.62
1310.58	Shale	5.58	3.26	0.08	42	0.11	2.12	65	441	0.05	2.23
1310.80	Shale	4.47	2.89	0.05	59	0.12	1.26	43	444	0.08	1.37
1311.55	Shale	9.05	3.39	0.12	29	0.13	2.78	82	435	0.04	2.91
1312.95	Shale	23.39	10.25	0.48	21	3.31	50.07	488	440	0.06	53.38
1313.37	Shale	14.44	5.31	0.75	7	1.57	20.28	382	440	0.07	21.85
1314.16	Shale	1.50	3.33	0.08	42	0.22	1.99	60	447	0.10	2.21
1314.23	Driftwood	5.13	51.20	1.46	35	5.95	79.12	155	445	0.07	85.07
1316.88	Shale	0.27	1.33	0.07	20	0.05	0.34	26	451	0.12	0.39
1317.25	Shale	0.03	1.51	0.04	42	0.04	0.36	24	442	0.10	0.40
1326.95	Shale	0.67	1.07	0.02	50	0.05	0.29	27	451	0.14	0.33
1327.67	Shale	2.22	1.04	0.04	23	0.04	0.55	53	443	0.07	0.59
1328.10	Shale	5.87	0.95	0.16	6	0.04	0.34	35	441	0.09	0.37
1328.65	Shale	8.31	1.18	0.04	30	0.04	0.58	49	440	0.06	0.62
1328.85	Shale	2.05	1.57	0.03	58	0.13	1.73	110	442	0.07	1.86
1329.35	Shale	0.00	8.44	0.78	11	2.31	34.08	404	439	0.06	36.39
1329.71	Shale	0.02	3.54	0.28	13	0.46	8.11	229	441	0.05	8.56
1330.15	Shale	0.50	2.83	0.17	17	0.31	5.05	178	440	0.06	5.36
1330.70	Shale	0.00	3.35	0.21	16	0.45	8.43	252	440	0.05	8.88
1331.10	Shale	0.19	4.91	0.18	27	0.86	14.20	289	441	0.06	15.06
1331.66	Shale	0.10	4.34	0.56	8	0.69	10.84	250	438	0.06	11.53
1332.43	Shale	0.72	3.62	0.22	16	0.56	8.86	245	439	0.06	9.41
1333.10	Shale	1.17	4.56	0.27	17	0.87	12.48	273	440	0.06	13.35
1333.30	Shale	1.85	4.86	0.26	19	1.02	14.53	299	440	0.07	15.55
1333.85	Shale	0.39	2.92	0.21	14	0.44	6.76	231	440	0.06	7.20
1334.22	Shale	0.31	4.07	0.41	10	0.61	9.88	243	439	0.06	10.49
1334.85	Shale	1.81	3.29	0.13	25	0.57	7.83	238	438	0.07	8.40
1335.30	Shale	0.37	2.44	0.14	17	0.30	5.12	210	441	0.05	5.41
1335.75	Shale	0.09	2.06	0.09	23	0.21	1.82	88	440	0.10	2.03
1336.12	Shale	0.15	4.45	0.29	15	0.80	11.92	268	439	0.06	12.72
1336.90	Shale	0.00	5.35	0.59	9	1.09	15.81	295	439	0.06	16.90
1337.40	Shale	1.25	5.25	0.46	11	1.18	18.46	351	438	0.06	19.64
1338.00	Shale	0.65	7.19	0.72	10	1.73	27.46	382	436	0.06	29.19
1338.35	Shale	18.09	9.89	0.43	23	2.99	47.52	480	441	0.06	50.51
1339.20	Shale	36.54	3.30	0.03	99	0.67	6.93	210	438	0.09	7.60
1341.20	Shale	0.82	3.18	0.04	80	0.26	1.73	54	446	0.13	2.00
1345.00	Shale	0.28	1.23	0.02	63	0.08	0.32	26	460	0.19	0.39
1350.00	Shale	0.88	1.39	0.02	86	0.05	1.27	91	441	0.03	1.31
1350.30	Shale	5.05	1.82	0.11	17	0.11	0.94	52	439	0.10	1.05
1350.70	Shale	7.94	2.41	0.09	28	0.14	4.21	175	439	0.03	4.34
1350.95	Shale	30.69	3.72	0.02	197	0.33	10.84	291	437	0.03	11.16
1358.90	Shale	0.84	2.35	0.03	86	0.14	0.81	34	457	0.15	0.95
1391.00	Shale	0.10	0.13	0.10	1	0.01	0.03	22	442?	0.14	0.04

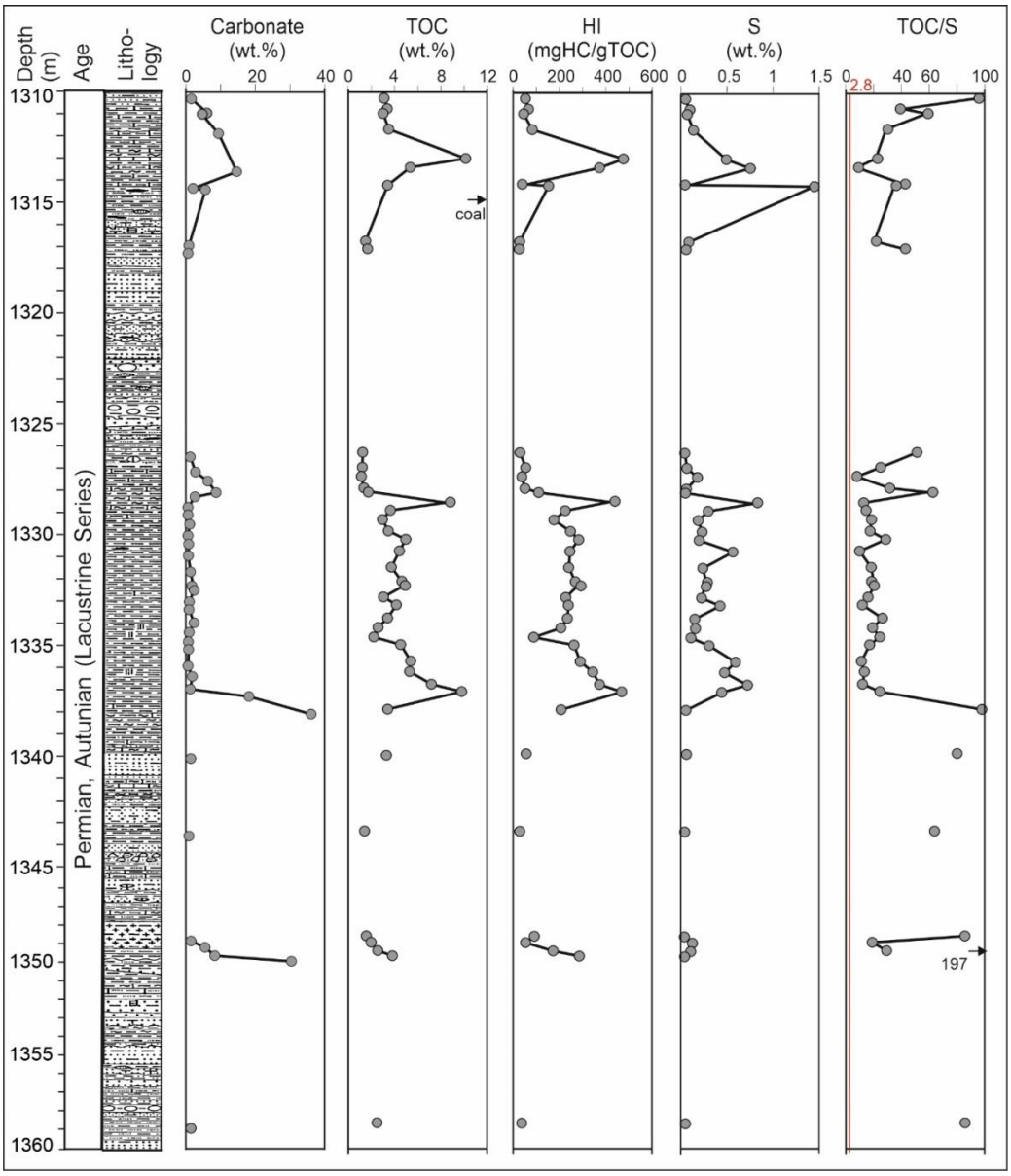

Fig. 9. Depth *versus* bulk geochemical parameters for the Permian lacustrine shales

4.2.2 Organic Petrography and Palynofacies

Organic petrographic and palynofacies investigations have been performed on twelve samples from the main shale interval (1339.20-1328.65 m).

The prevailing maceral group within the main shale interval is liptinite (18-79 vol.%) closely followed by inertinite (8-63 vol.%) and vitrinite (5-43 vol.%; Table 6; Fig. 10). Main liptinite macerals include alginite and liptodetrinite (Fig. 10a,b,c). Telalginite is typically more abundant than lamalginite and includes some *Botryococcus*-type algal bodies (Fig.10c). Sporinite (Fig. 10d) is typically rare. The mineral matrix is strongly fluorescing (e.g. Fig. 10a) suggesting that not all organic matter is visible microscopically. Five samples were selected for vitrinite reflectance measurements (Table 6). Strongly varying reflectance values with high standard deviations show that the reflectance of vitrinite particles varies considerably within and between the samples. Thus, vitrinite reflectance in the short interval varies from 0.56 (±0.19) to 0.78 (±0.11) %Rr. The mean value is 0.66 %Rr. This value is consistent with previously published data (NAGRA, 2002) and is lower than that of the deeper coal seams.

Amorphous organic matter (AOM; Fig. 11) is the main component in palynofacies in both non-filtered and filtered slides. It represents 55 to 98 vol.% (avg. 70 vol.%) of the particles in the filtered slides (Table 6; Fig. 12), but may be invisible in reflected light mcroscopy. Two types of AOM particules were observed in the Weiach-1 samples. The first AOM type corresponds to large, grey particles with a sub-rectangular shape. Such sub-rectangular shape organic forms of AOM are known to possibly originate from degraded translucent phytoclast tissues such as cuticles or lignocellulosic tissues (Laggoun-Défarge et al., 1999; Sebag et al., 2006). The second AOM type is characterized by orange to grey-orange fluffy clouds. This AOM type is generally interpreted as deriving from algal/bacterial matter living in the upper part of the water column (Tyson, 1995). Transitional forms exist between these two AOM types. Therefore, in some slides it is not easy to distinguish between these two end members. The two AOM types co-occur in many samples (Fig. 12), but grey, sub-rectangular AOM tends to dominate in deeper samples (1339.20-1334.22 m), whereas orange cloudy AOM particles dominate from 1333.30 m to 1328.65 m (Table 6). However, sub-rectangular AOM again shortly dominates at 1329.35 m (Fig. 12), corresponding to a peak in TOC and HI values (see above). Palynomorphs (spores and pollen) represent 0.5 to 22 vol.% (10.6 vol.% in average) of the particles in palynofacies. Opaque phytoclasts represent 1.4 % to 23.30 % (average 12.4 vol.%) of palynofacies and are much more abundant than translucent phytoclasts (0.5-10.4 vol.%; avg. 5.7 vol.%) (Table 6). Some opaque phytoclasts show

recognizable biological wood structures. Opaque and translucent phytoclast proportions increase regularly from 1338.35 to 1331.1 m/1330.15 m (Fig. 12). *Botryococcus* algae are observed in trace amounts (<1 vol.%) within half of the studied slides. Hyphae from fungi also appear in trace amounts (<1 vol.%) within most slides.

In general there is no good relationship between maceral percentages and HI. However, moderate positive and negative correlations between HI and AOM (r^2=0.58) and opaque phytoclasts (r^2=0.60) can be observed, respectively.

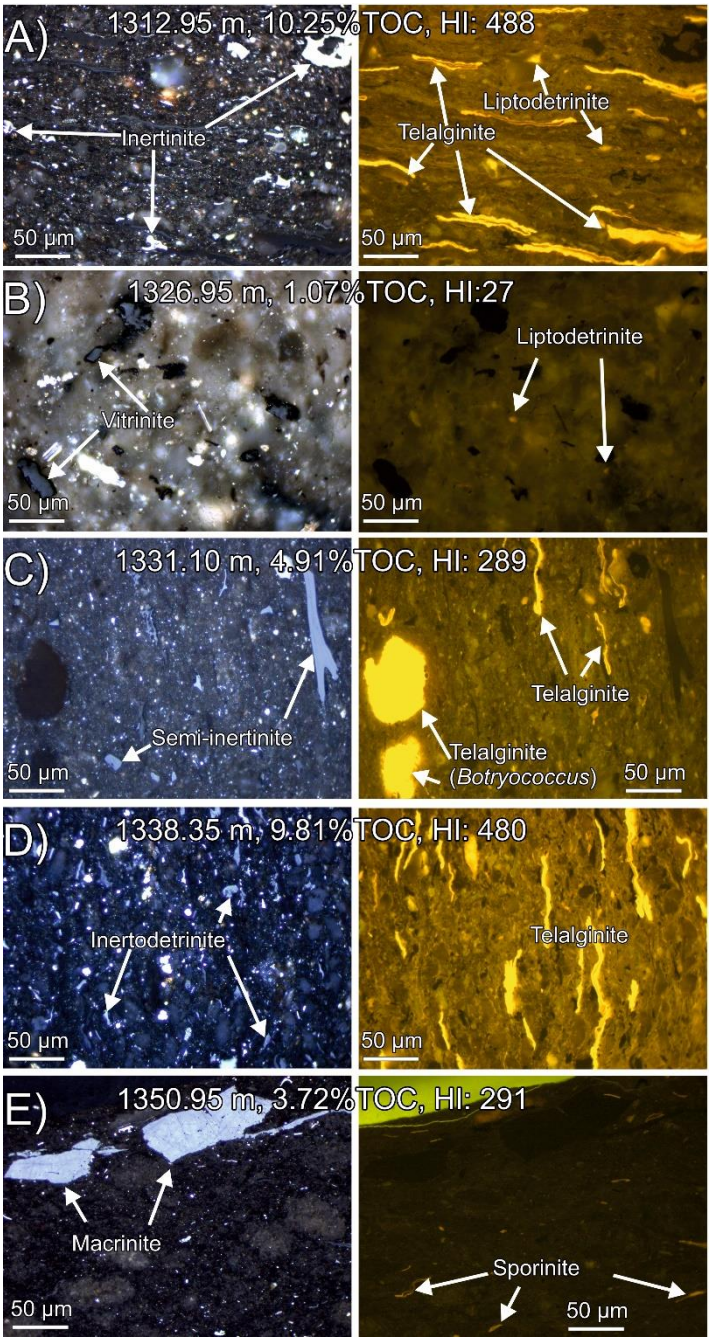

Fig. 10. Photomicrographs of maceral composition of selected samples (Left: white light; right: fluorescent mode).

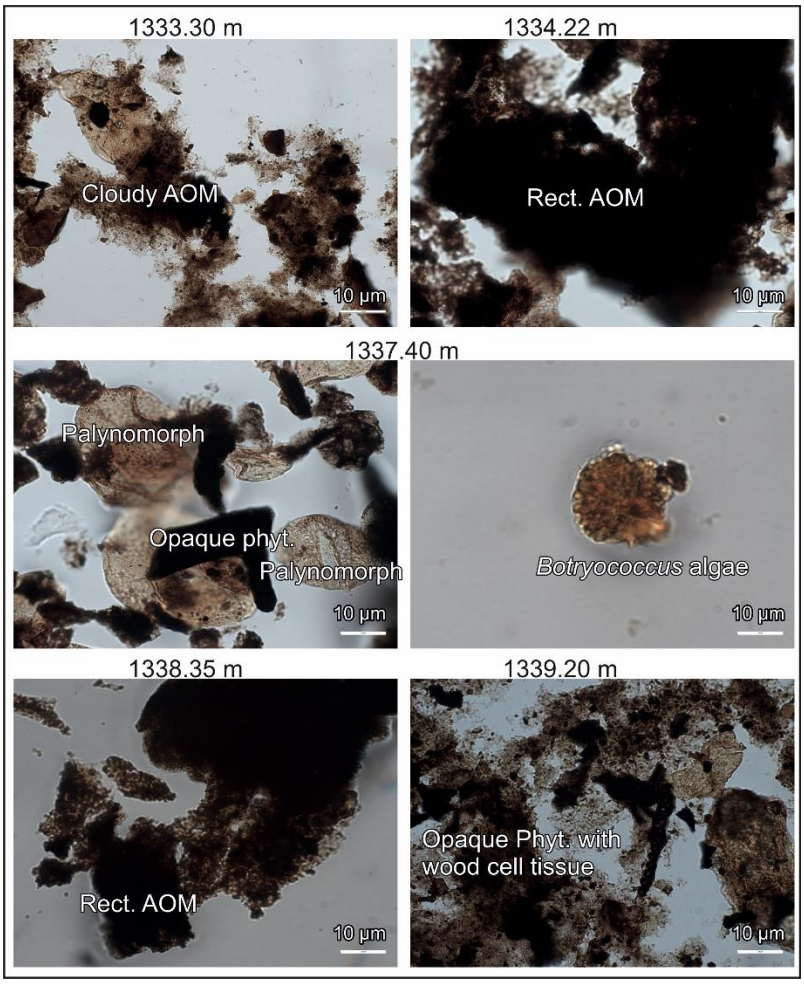

Fig. 11. Photomicrographs of palynofacies for selected samples from the main shale interval in the Lacustrine Series.

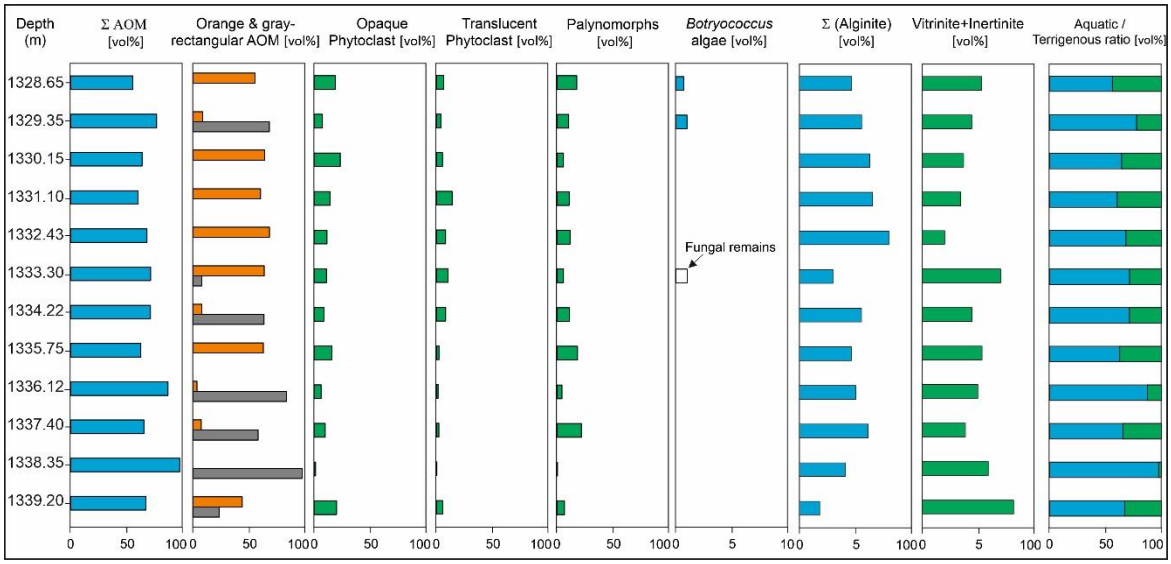

Fig. 12. Depth plot of palynofacies and maceral composition for selected samples from the main lacustrine shale succession. (Aquatic: Σ AOM+Botryococcus; Terrigenous: Phytoclasts+palynomorphs).

Table 6. Palynofacies, maceral pecentages and vitrinite reflectance of samples from the Permian Lacustrine Series.
Std – standard deviation, n – number of measurements

Sample	Palynofacies								Macerals						VR	Std. dev	n
ID[m]	Orange AOM [Vol%]	Grey, rectangular-shape AOM [Vol%]	∑ (AOM) [Vol%]	Opaque Phytoclasts [Vol%]	Translucent Phytoclasts [Vol%]	Palyno-morphs [Vol%]	*Botryococcus algae* [Vol%]	Fungal remains [Vol%]	Vitrinite [Vol%]	Inertinite [Vol%]	Sporinite [Vol%]	Tel-alginite [Vol%]	Lam-alginite [Vol%]	Lipto-detrinite [Vol%]	[%Rr]		
1310.08															0.71	0.05	50
1312.95															0.58	0.11	50
1328.65	55.6	0.0	55.6	19.0	6.5	17.8	0.7	0.4	43	10	0	37	3	7	0.78	0.11	61
1329.35	8.7	68.3	77.0	7.5	4.0	10.5	1.0	0.0	16	29	0	41	5	11			
1330.15	64.0	0.0	64.0	23.3	5.4	6.0	0.0	0.5	18	20	0	25	16	22			
1331.10	60.4	0.0	60.4	14.2	14.0	11.0	0.2	0.2	12	22	1	36	8	21			
1332.43	68.4	0.0	68.4	11.6	8.2	11.8	0.0	0.0	12	8	0	23	5	51			
1333.30	63.7	7.9	71.6	11.0	10.4	6.0	0.0	1.0	41	28	1	25	0	5			
1334.22	8.0	63.5	71.5	8.7	8.3	11.2	0.0	0.3	27	18	0	16	11	28	0.56	0.19	50
1335.75	62.9	0.0	62.9	16.0	2.3	18.5	0.0	0.3	5	48	1	13	12	21			
1336.12	3.6	83.5	87.1	6.3	1.5	4.5	0.4	0.2	18	31	0	22	7	21			
1337.40	7.4	58.2	65.6	9.9	2.2	22.0	0.1	0.2	16	22	0	23	17	22			
1338.35	0.0	97.6	97.6	1.4	0.5	0.5	0.0	0.0	18	41	0	21	16	3	0.63	0.11	50
1339.20	44.0	23.3	67.3	20.1	5.5	6.8	0.1	0.2	19	63	0	16	0	2			

4.2.3 Biomarker

Rock extracts from 21 Permian shale samples (1310-1360 m) were investigated, twelve of which come from the main shale interval. The EOM ranges from 11.7 to 69.2 mg/gTOC (41.7 mg/gTOC on average) and is dominated by NSO compounds (53 wt.% in average). Aliphatic hydrocarbons (21 wt.% in average), asphaltenes (15 wt.% in average) and aromatic hydrocarbons (11 wt.% in average) occur in lower amounts. A positive correlation exists between EOM and HI (r^2 = 0.65). Representative GC-FID and GC-MS traces are shown in Fig. 13. Concentrations and ratios of selected molecular compounds are listed in Table 3 and plotted versus depth in Fig. 14.

n-Alkanes and isoprenoids

The concentrations of *n*-alkanes (> *n*-C_{15} fraction) vary significantly between 82 and 7392 µg/gTOC. Typically, their chain lengths range from *n*-C_{15} to *n*-C_{35} and show a unimodal chain length distribution (Fig. 13). Short-chain *n*-alkanes (*n*-$C_{15–19}$/∑*n*-alkanes: 0.33-0.59) are more abundant than mid-chain (*n*-$C_{21–25}$/∑*n*-alkanes: 0.23-0.39), while low long-chain *n*-alkanes are rare (*n*-$C_{27–31}$/∑*n*-alkanes: 0.02-0.19) (Table 3; Fig. 14a). The maximum amounts of long chain *n*-alkanes (>0.5) and the minimum amounts of long chain *n*-alkanes (<0.07) are observed in the middle part of the main shale interval. CPI values (Bray and Evans, 1961) vary from 0.97 to 1.37 and show a clear upward decrease (Fig. 14b).

Isoprenoid concentrations vary from 9 to 822 µg/gTOC. The Pr/Ph ratio ranges between 0.85 and 3.01. Similar to CPI, Pr/Ph ratios in the main shale interval decrease upwards (Fig. 14c). However, no clear trend is visible below and above this interval. The Pr/*n*-C_{17} (0.07-2.66) and the Ph/*n*-C_{18} (0.03-1.0) ratios (Fig. 14o) show similar depth trends as the relative amount of long chain *n*-alkanes.

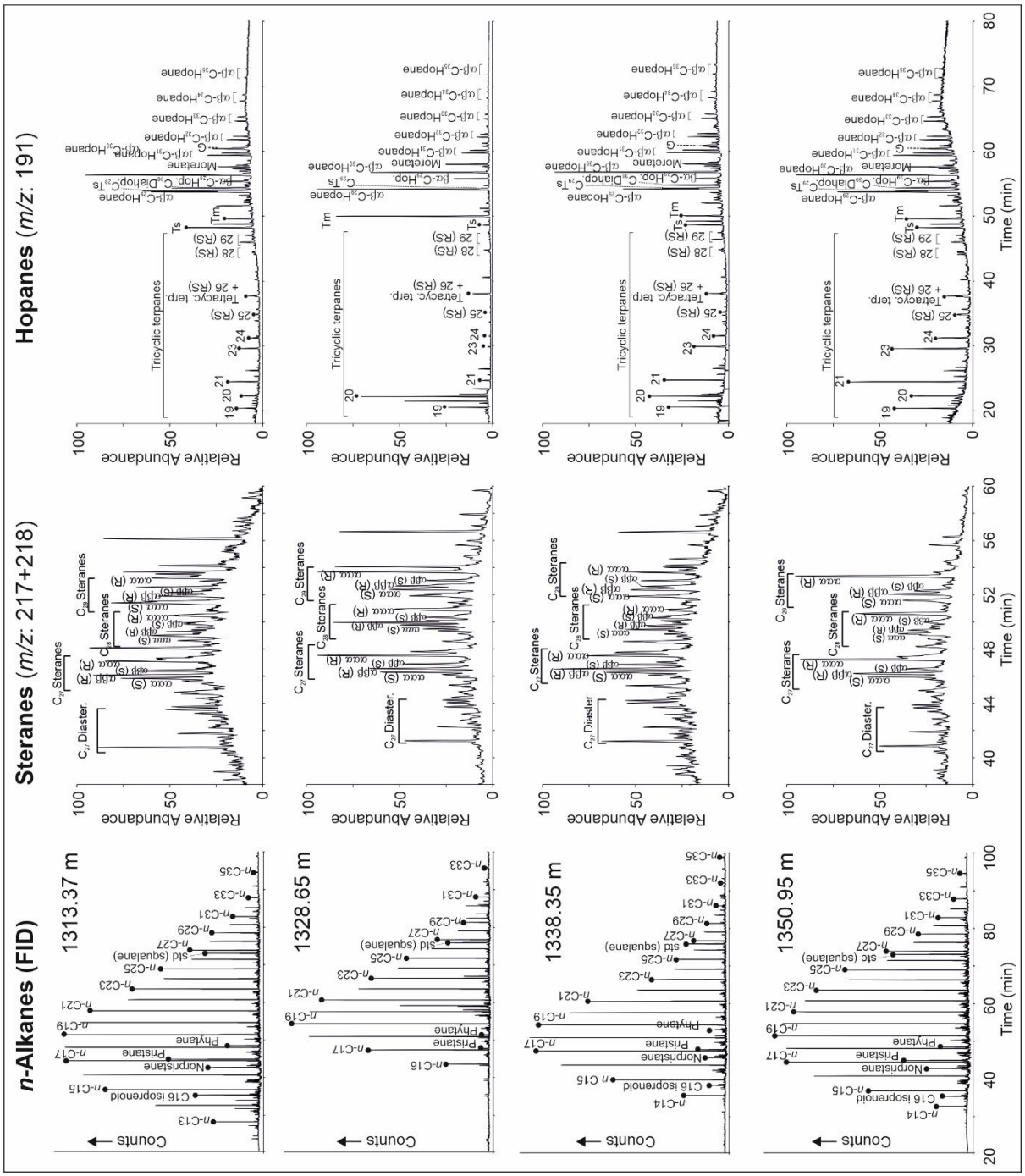

Fig. 13. Mass chromatograms of selected shale samples from the Permian Lacustrine Series.

Steroids distribution

Sterane concentrations are low within and below the main shale interval (1-56 µg/g TOC) and relatively high above it (54-242 µg/g TOC). Sterane distributions are generally dominated by C_{27} steranes. This is especially true for the central part of the main shale interval (1337.40-1328.65 m), where C_{29} and C_{28} steranes occur in significantly lesser amounts. Below and above of this interval, concentrations of C_{27} and C_{29} steranes are similar (Fig. 14d; Table 3). The C_{29} ααα sterane 20S/(20S+20R) ratio ranges from 0.25 to 0.71, while ratios of

αββ/ (αββ+ααα) C_{29}-steranes range from 0.28 to 0.63 (Fig. 14p,q; Table 3). Low 20S/(20S+20R) ratios are mainly found in samples with high proportions of long chain *n*-alkanes.

Penta- and Tricyclic Triterpanes

Similar to the Carboniferous coal samples, hopanes are significantly more abundant than steranes. Especially high hopane concentrations (943-2963 µg/g TOC) are found in four samples between 1310.58 and 1313.37 m depth. Elsewhere, hopane concentrations range from 8 to 391 µg/g TOC.

Their mass chromatograms (Fig. 13) show the presence of similar compounds as in the Carboniferous succession. The C_{35} homohopane index (HHI = C_{35}/C_{31-35}) decreases upwards in the lower part of the lacustrine series, including the main part of the main shale interval. However, the C_{34} to C_{35} peaks are extremely small in most cases. The C_{31} hopane 22S/(22S+22R) isomerization ratios (0.55-0.61; Table 3) are close to the end-point value (Mackenzie and Maxwell, 1981). The Ts/(Ts+Tm) ratios vary between 0.02 to 0.76 with the lowest values occurring below and above the main shale interval (Fig. 14h). Moretane/hopane ratios (0.20-0.45) and Ts/(Ts+Tm) ratios (0.02-0.76) show a strong negative correlation (r^2=0.82). The latter also shows a moderate negative correlation with the relative percentage of long chain *n*-alkanes (r^2=0.50). The Gammacerane Index ranges from 0.05 to 0.41 and reaches maximum values in the main shale interval (Fig. 14i).

Concentrations of tricyclic terpanes (TT) are low (2-281 µg/g TOC; Table 3) and positively correlated with hopanes (r^2=0.82). Similar to hopanes, the highest concentrations occur above the main shale interval. In most samples, tricyclic terpanes occur within the C_{19} to C_{29} chain length with C_{19}, C_{20}, C_{23} being the most prominent and C_{27} being absent. Ratios for C_{19}/C_{23} TT and C_{20}/C_{23} TT were plotted against depth (Fig. 14j; Table 3).

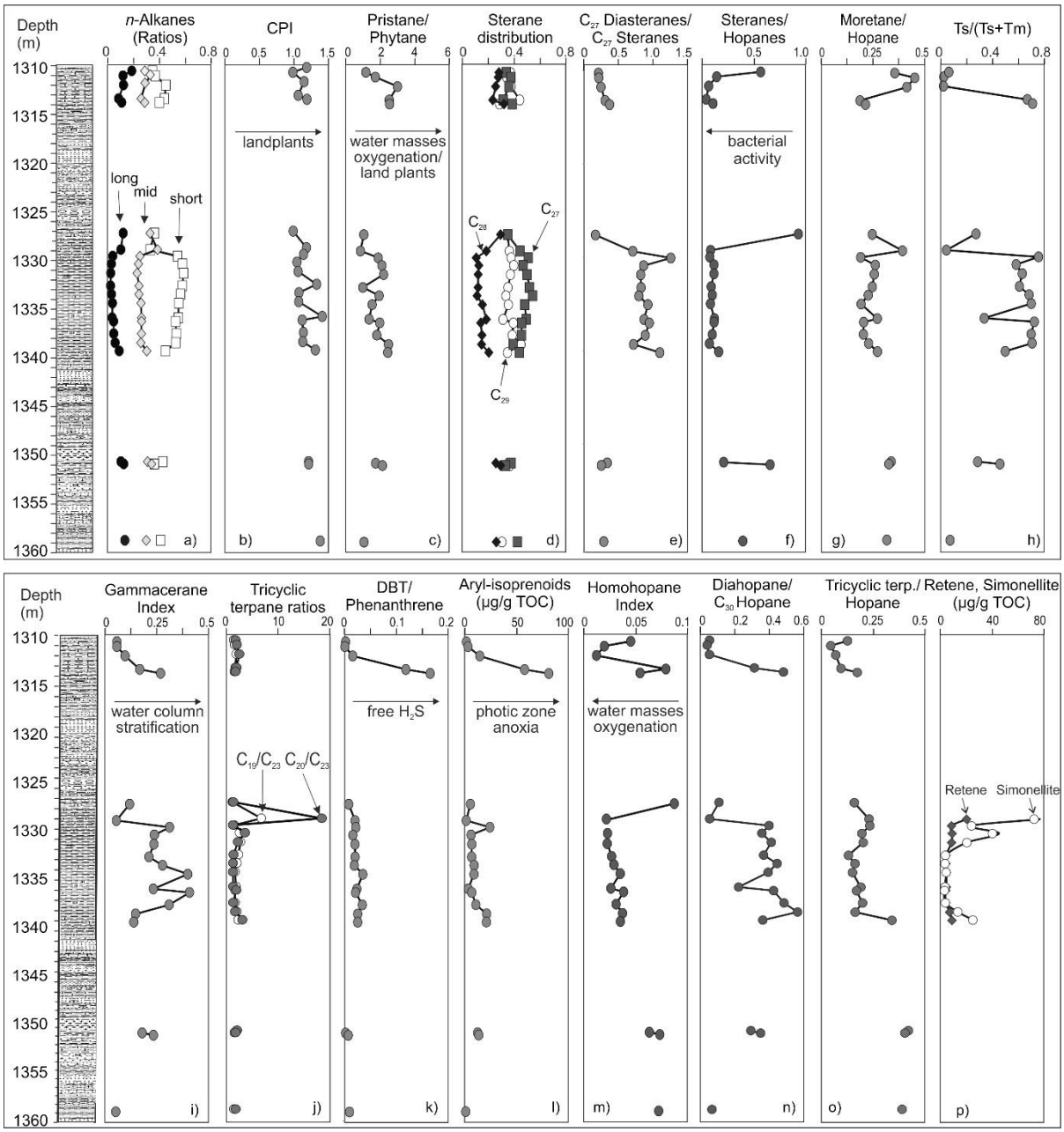

Fig. 14. Concentrations and ratios of selected organic compounds (a-p). Alkane distribution: short-chain: *n*-C_{15-19}/Σ*n*-alkanes; mid-chain: *n*-C_{21-25}/Σ*n*-alkanes; long-chain: *n*-C_{27-31}/Σ*n*-alkanes; CPI: Carbon Preference Index (Bray and Evans 1961), sterane distribution: C_{27}/C_{27-29} steranes, C_{28}/C_{27-29} steranes, C_{29}/C_{27-29} steranes; DBT: dibenzothiophene.

Aromatic Hydrocarbons

The Permian shales contain very low concentrations of benzenes, naphthalenes, phenanthrenes, dibenzothiophenes and their alkylated equivalents (Table 3). The methyl phenanthrene index (MPI-1) in the main shale interval varies from 0.51 to 0.61, while lower values (0.16-0.48) occur below and above this interval. Equivalent vitrinite reflectance values calculated from MPI-1 within the main shale interval range from 0.71 to 0.74% and are slightly lower (0.51-0.69) below and above this interval. Methyl dibenzothiophene (MDBT) concentrations are very low (1.16-14.34 µg/g TOC), the highest values occur in two samples above the main shale interval. The dibenzothiophene/phenathrene (DBT/P) ratios are generally low (<0.05), higher values are limited to the depth between 1313.37 and 1312.95 m (Fig. 14k). Low amounts of mono- (0.15-1.39 µg/g TOC) and tri-aromatic steroids (0.07-1.29 µg/g TOC) are present.

Aryl isoprenoids with C_{13} to C_{23} chain length are present and have low to moderate concentrations (1.06-81.14 µg/g TOC; Fig. 14m). Maximum concentrations occur in the depth interval (1313.37-1312.95 m) with high DBT/P ratios. The aryl isoprenoid ratio (AIR=$C_{13\text{-}17}/C_{18\text{-}22}$) (0.08-2.55; Table 3) shows a strong positive correlation with the total amount of aryl isoprenoids (r^2=0.85).

Polycyclic aromatic hydrocarbons (PAHs), such as simonellite and retene, were determined within the main shale interval with significant concentrations (0.33-74.84 µg/g TOC and 1.26-17.47 µg/g TOC, respectively). Both compounds exhibit similar depth trends (Fig. 14p).

4.2.4 Compound-specific stable carbon isotopy

Carbon isotope ratios of *n*-alkanes with 15 to 29 carbon atoms and for pristane and phytane were determined for twelve samples within the main shale interval, one sample below and two samples above (Table 4). In Fig. 8, $\delta^{13}C$ values of *n*-alkanes are plotted versus their chain length. Two different patterns can be recognized: Samples from the lower part of the shale interval (1350.95-1336.12 m), as well as of samples above (1313.37-1312.95 m) and below this interval (1350.95 m) are characterized by *n*-alkanes, which become isotopically lighter with increasing chain length. In addition, the $\delta^{13}C$ values of specific *n*-alkanes vary in a relatively narrow range. In contrast, $\delta^{13}C$ values of *n*-alkanes from samples from the upper part of the main shale interval (1335.75-1328.65 m) vary considerably and long chain n-alkanes typically have less negative $\delta^{13}C$ values than shorter chain *n*-alkanes.

Stratigraphic variations of $\delta^{13}C$ values of *n*-alkanes and isoprenoids are shown in Fig. 15. Different depth trends are observed for *n*-alkanes with different chain lengths, pristane and phytane:

- $\delta^{13}C$ values of pristane and phytane are about -28 to -29 ‰ at 1350.95 m depth and increase approximately from -30 to -25 ‰ in the depth interval from 1339.20 to 1312.95 m. The correlation between $\delta^{13}C$ values of pristane and phytane is excellent (r^2=0.96).
- Short chain *n*-alkanes (*n*-C_{15-17}) show a similar depth trend as isoprenoids, although the $\delta^{13}C$ values are more negative at shallow depth.
- $\delta^{13}C$ values of long chain *n*-alkanes (*n*-C_{27-29}) are often very negative (-30 to -31 ‰). However, a positive isotope excursion to -28 ‰ occurs in the upper part of the main shale interval (1335.75-1329.35 m).
- *n*-alkanes with intermediate chain lengths (*n*-C_{18-25}) occupy an intermediate position.

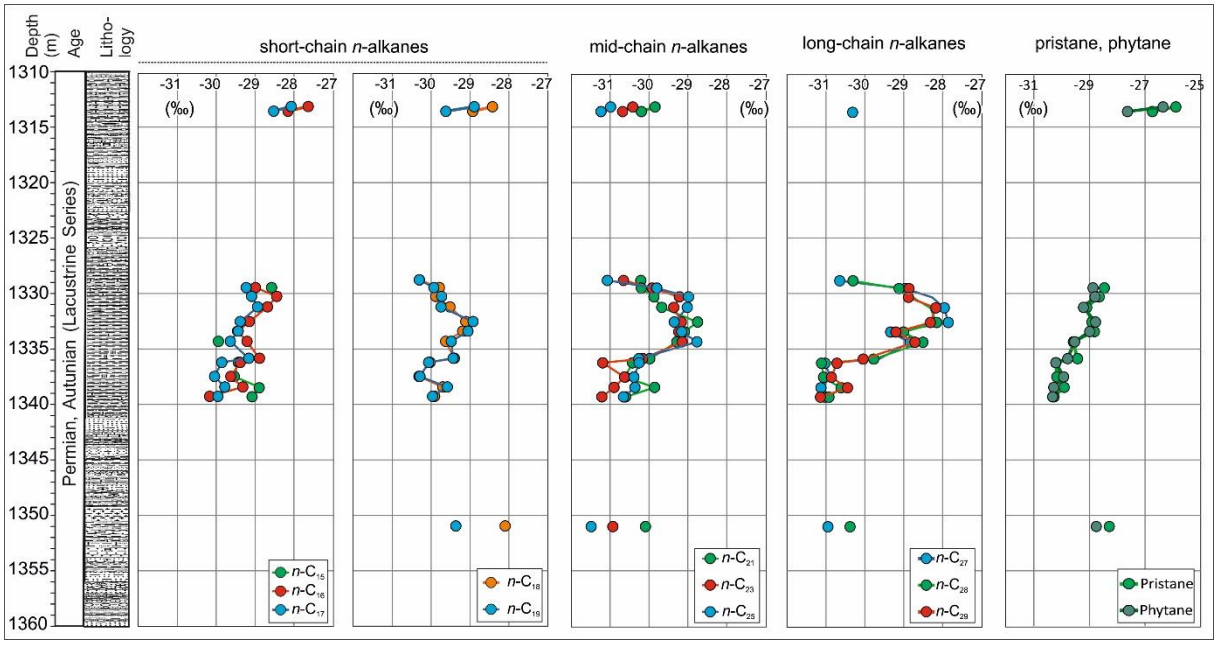

Fig. 15. Vertical variation of $\delta^{13}C$ values of *n*-alkanes, pristane and phytane.

5. Discussion

5.1 Thermal Maturity

Thermal maturity was deduced using T_{max} values from the entire studied succession and vitrinite reflectance data from the main coal seam and the main shale interval. T_{max} values increase in the depth interval from 1300 to 1850 m from ~440 to 465°C. Random vitrinite reflectance in the main shale interval (1326.95-1339.20 m) is lower (0.56-0.78 %Rr, avg. 0.66 %Rr) than in the main coal seam (#6; 1585.0-1591.2 m; 0.91-0.95%Rr).

This range of T_{max} and random vitrinite reflectance values agrees well with the increase of vitrinite reflectance in the same depth interval (1300-1850 m) from ~0.70 to 1.15 %Rr (NAGRA, 2002). In the following maturity issues are discussed separately for Carboniferous coals and the Permian lacustrine series.

5.1.1 Carboniferous coal

Cross-plots of bitumen index (BI = 100*S1/TOC), hydrogen index (HI = 100*S2/TOC) and quality index (QI = [100*(S1+S2)/TOC] versus T_{max} provide information on the petroleum potential and maturity of coal samples (Fig. 16, Sykes and Snowdon, 2002). According to these plots, the coals from the main seam (#6) reached maturity values close to the onset of gas generation. These data agree well with vitrinite reflectance measured for this seam (0.91-0.95 %Rr; this study; 0.86-0.91 %Rr; NAGRA, 2002). Gas generation already occurred in deeper coal samples (1620-1740 m) where vitrinite reflectance is 0.91 to 1.03 %Rr according to NAGRA (2002).

In contrast to vitrinite reflectance and T_{max}, biomarker parameters suggest lower maturity for the main seam (#6). For example, MPI-1 values (0.49-0.56) suggest 0.69 to 0.74 % $Rc_{(MPI\ 1)}$ (Radke and Welte, 1983). This maturity corresponds to the maturity of the lacustrine shale unit. However, downward migration (or upward migration from low-maturity deeper shales) is considered unlikely.

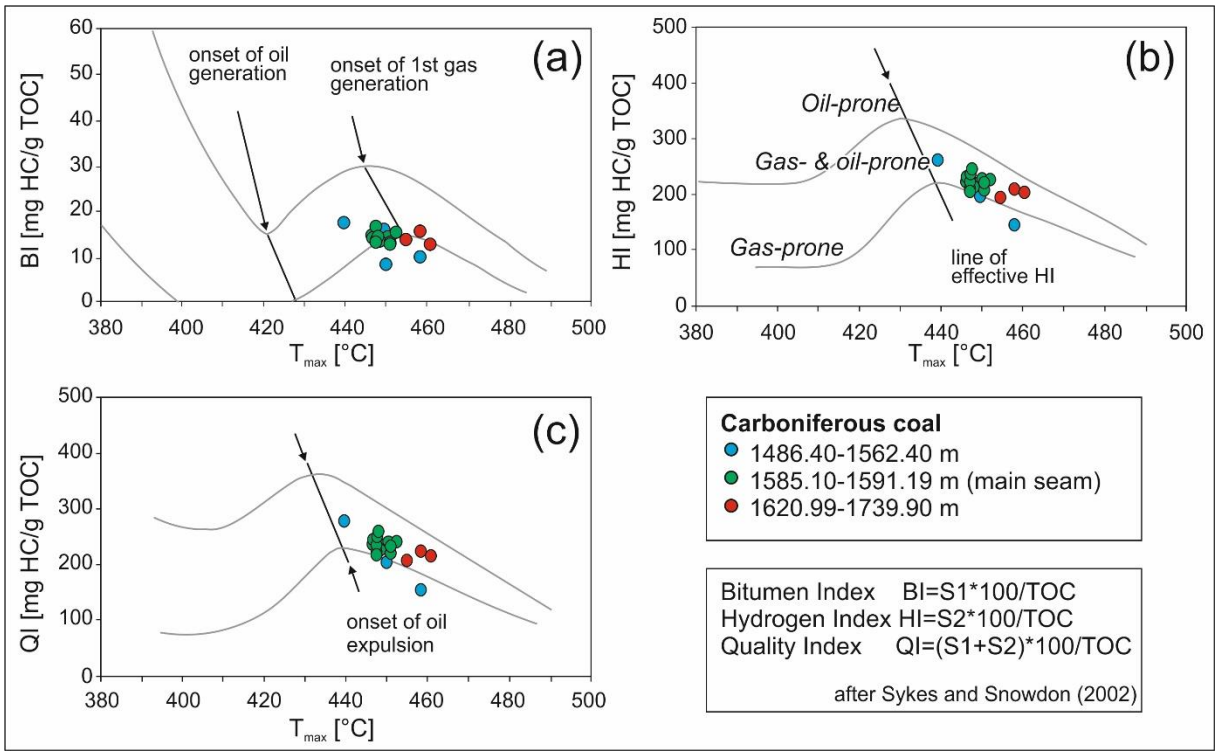

Fig. 16. Cross-plots of T_{max} versus (a) bitumen index (BI), (b) hydrogen index (HI), and (c) quality index (QI) for the interpretation of Rock-Eval data from coals (according to Sykes and Snowdon, 2002).

5.1.2 Permian Lacustrine Series

T_{max} values of samples from the lacustrine series (1252-1388 m) with S_2 >1.0 mgHC/gTOC (435-447°C; avg. 440°C) and vitrinite reflectance of samples between 1310 and 1339 m depth (avg. 0.66 %Rr) suggest early oil window maturity. An average PI of 0.07 shows that major oil generation did not yet start in the Lacustrine Series.

Biomarker maturity parameters show strong vertical variations and are probably influenced by facies variations. However, average values generally support early oil window maturity. For example the average MPI-1 value (0.44) suggests an average vitrinite reflectance of 0.66 % $Rc_{(MPI\ 1)}$ (Radke and Welte, 1983).

5.2 Hydrocarbon source potential

5.2.1 Carboniferous coal measures

The plot of hydrogen index versus T_{max} (Fig. 16b) suggests that the coals are mainly gas prone, but may also generate minor amounts of oil. However, low percentages of liptinite macerals (avg. 3.7 vol.%; Table 2) and relatively high percentages of inertinite macerals (up to 14 vol.%) indicate that the oil potential is limited. Surprisingly, a strong positive correlation ($r^2 = 0.93$) exists between vitrinite macerals and HI. This suggests that HI may be controlled by hydrogen-rich substances adsorbed in the vitrinite matrix. Similarly, Wolf et al. (1988) noted a relatively high hydrogen content of the Weiach coals and assumed that this is due to secondary bitumen impregnations. As noted, based on HI, generation of minor amounts of liquid hydrocarbons cannot be excluded. The Upper Carboniferous coals are the most likely source rock for the Entlebuch gas field beneath the Molasse sediments (Vollmayr and Wendt, 1987; Leu, 2012) and the gas found at great depth during the drilling of the geothermal St. Gallen GT-1 well (Omodeo-Salé et al., 2020 and references). This shows that the knowledge of deeply buried Carboniferous rocks is important for eventual future hydrocarbon exploration in northern Switzerland (e.g., Leu, 2012), but also to derisk the geothermal exploration activity (Omodeo-Salé et al., 2020).

Carboniferous shales have been described as bituminous (e.g. Matter, 1987; Diebold, 1988). However, based on S_2 and HI values the organic matter in all investigated samples is classified as Type III kerogen (Fig. 2). Hence, these shales are coaly rather than bituminous. Consequently, these samples may hold some additional gas potential, but no oil potential.

5.2.2 Permian Lacustrine Series

Shales near the base and the top of the lacustrine series with TOC contents below 0.25 wt.% do not hold any hydrocarbon potential. The following discussion therefore focuses on the depth range between 1358.90 and 1310.08 m, where TOC contents are significantly higher (0.95-10.25 wt.%). For these samples, the plots of S_2 against TOC for different depth intervals are shown separately in Fig. 17. The interval between 1358.90 and 1341.20 m contains mainly Type III kerogen, but a single sample is classified as Type II kerogen (Fig. 4a).

The plot for samples from the main shale interval (1339.20-1326.95 m; Fig. 17b) shows that Type III kerogen predominates in the uppermost part (above 1328.85 m). The remaining samples follow a linear trend in the S_2 versus TOC diagram. The slope and the intercept of the

regression line show a high percentage (~2 wt.%) of inert carbon (e.g. inertinite, vitrinite) and that the HI of the reactive organic matter is about 550 mgHC/gTOC (cf. Dahl et al., 2004). This indicates the presence of highly oil prone Type II kerogen also in samples with relative low measured HI.

A similar plot for samples from the upper interval shows an even slightly higher amount of inert carbon and a slightly higher HI (685 mgHC/gTOC) of the reactive kerogen (Fig. 17a). However, this plot is based on a low sample number.

Overall, data plotted in Fig. 17 reflects that the organic matter is a mixture of terrigenous and aquatic organic matter (see palynofacies and maceral data; Table 6).

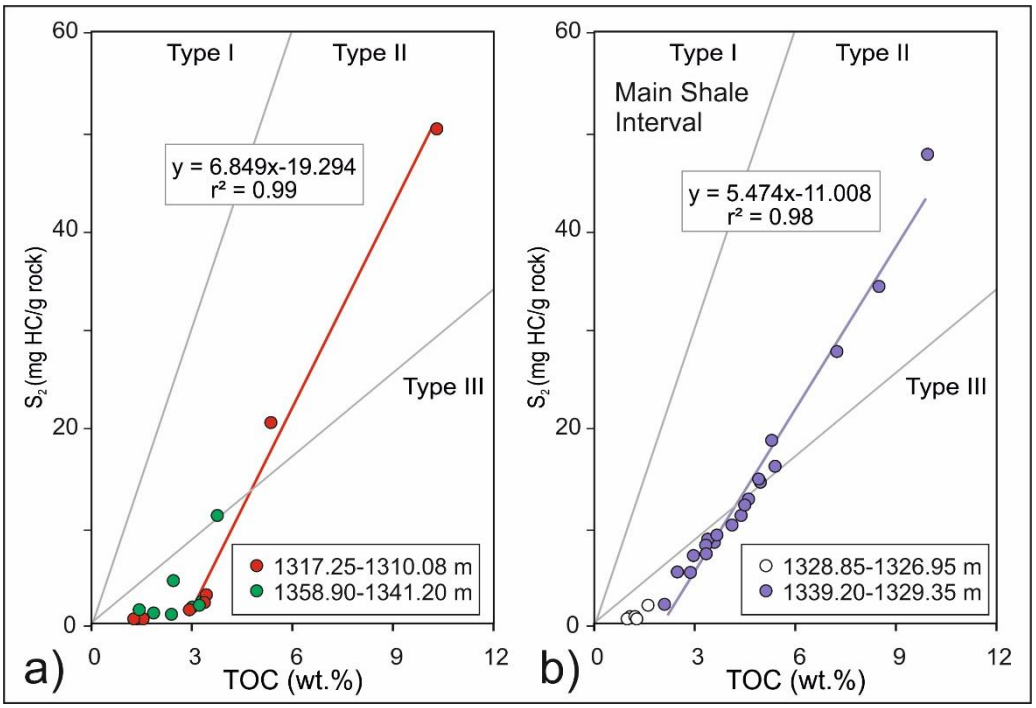

Fig. 17. Plots of S_2 against TOC for the lacustrine series. a) Samples from the lower depth interval (1358.90-1341.20 m) and upper depth interval (1317.25-1310.08 m); b) samples from the main shale interval (1339.20-1326.95 m). Regression lines are shown for samples with TOC contents >2 wt.% from the upper depth interval and the main shale interval in order to determine the amount of inert kerogen and the HI of reactive organic matter (see Dahl et al., 2004).

The plot of Petroleum Potential (S_1+S_2) versus TOC (Fig. 18) is often used to quantify the generation potential. It shows that good to very good source rocks exist in the main shale interval, but also in underlying and overlying Permian shale layers.

The source potential index (SPI=(S1+S2 [mgHC/g rock])*thickness [m]*rock density [g/cm³]/1000) can be used to quantify the amount of hydrocarbon generated beneath one square meter of surface area (Demaison and Huizinga, 1994). The SPI has been calculated for the 12.25 m thick main shale interval, considering the average petroleum potential (11.92 mgHC/g rock) and an estimated rock density of 2.4 g/cm³. With these input parameters, the calculation results in a SPI of 0.35 tHC/m². However, this value neglects the presence of additional layers with high oil potential in the lacustrine series. Therefore, the total SPI might be higher. Based on the work of Demaison and Huizinga (1994), an SPI of 0.35 tHC/m² is classified as low. However, it is equal to the SPI of the Schöneck Formation, the main source rock in the NAFB (Sachsenhofer et al., 2010).

In the eastern (Austrian) and central (German) sectors of the basin, the extension of the Permian succession in the basement of the NAFB is limited, suggesting that the lacustrine series is not a main source rock interval in these parts of the basin. In contrast, the extension in the eastern (Swiss) sector is probably larger, but poorly known. This suggests that Permian lacustrine source rocks may have contributed locally to hydrocarbon accumulations (e.g. Do Couto et al., 2021; Pullan and Berry, 2019).

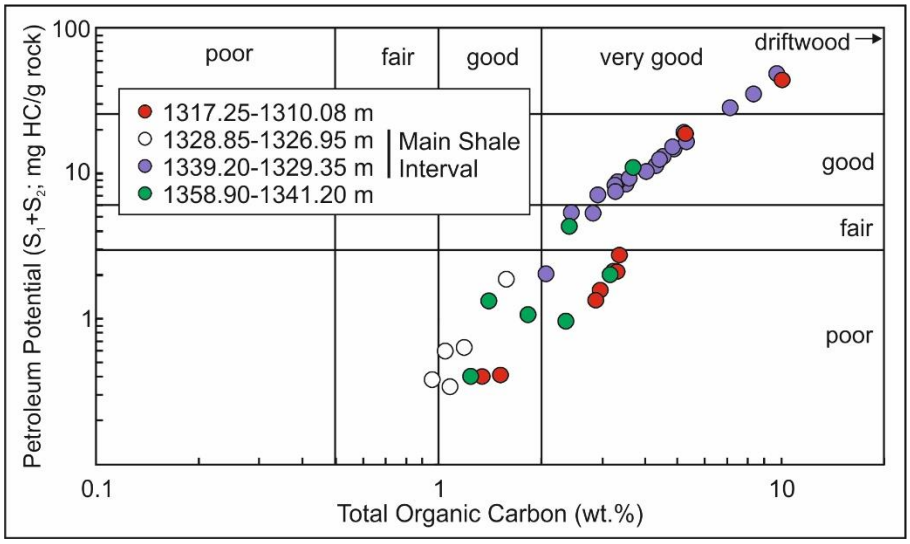

Fig. 18. Plot of petroleum potential (Rock-Eval S1+S2) versus total organic carbon for samples from the Permian lacustrine series.

5.2.3 Possibilites to distinguish oil of Permo-Carboniferous origin

The main source rocks in the NAFB are the Oligocene Schöneck Formation (Schulz et al., 2002; Sachsenhofer and Schulz, 2006; Gratzer et al., 2011; Bechtel et al., 2013) and the Toarcian Posidonia Shale (Littke et al., 1991; Wehner and Kuckelkorn, 1995; Bechtel et al., 2019).

Biomarker ratios and isotope patterns that can help distinguish oil shows derived from Permo-Carboniferous source rocks from those derived from the main Jurassic and Oligocene source rocks are defined below. Box plots summarizing biomarker ratios of Permo-Carboniferous and Jurassic source rock extracts and of oil samples generated from Oligocene source rocks are shown in Fig. 19. In the case of Permian shales, non-source rock samples (S1+S2: < 1 mgHC/gTOC) are neglected.

The distinction of Permo-Carboniferous (and Jurassic) oils from oil generated by the Oligocene Schöneck Formation is simple. Unique features of Oligocene-source oils include the presence of considerable amounts of oleanane, a biomarker characteristic for angiosperms which only evolved after the Late Cretaceous (Moldowan et al., 1994) and relatively high C_{28}/C_{29} sterane ratios (~1; Fig. 19) reflecting the young age of the source rock (Grantham and Wakefield, 1988). Moreover, Oligocene source rocks and their oils are characterized by a very specific ("V-shaped") CSI pattern, characterized by very negative $\delta^{13}C$ values of mid-chain *n*-alkanes (especially *n*-C_{21}; -Gratzer et al., 2011; Bechtel et al., 2013).

The Stephanian coals probably will generate only minor amounts of liquid hydrocarbons. Any coal-generated oil, however, should be identified easily based on very high Pr/Ph ratios (3.6-5.0) and very high C_{19}/C_{23} and C_{20}/C_{23} tricyclic terpane ratios (Table 3; Fig. 19).

Permian lacustrine and Lower Jurassic marine source rocks contain comparable Pr/Ph ratios and sterane distributions and display similar CSI patterns (e.g., Ajuaba et al., 2022). However, a distinction of Permian oils should be possible based on the fact that Permian rock extracts contain significantly higher amounts of tricyclic terpenates (TT; tricyclic terpenates/hopanes ratio) and higher ratios of C_{19}/C_{23} TT (avg. 1.16) and C_{20}/C_{23} TT ratios (1.8) than Posidonia Shale extracts (0.06 and 0.22, respectively; Fig. 19). Moreover, the C_{30} diahopane/hopane ratio is significantly higher for Permian extracts (0.29) than for Jurassic extracts (0.06). Finally, the sterane/hopane ratio is lower in Permian rocks extracts (0.20 on average) than in Jurassic ones (3.69 on average; Fig. 19).

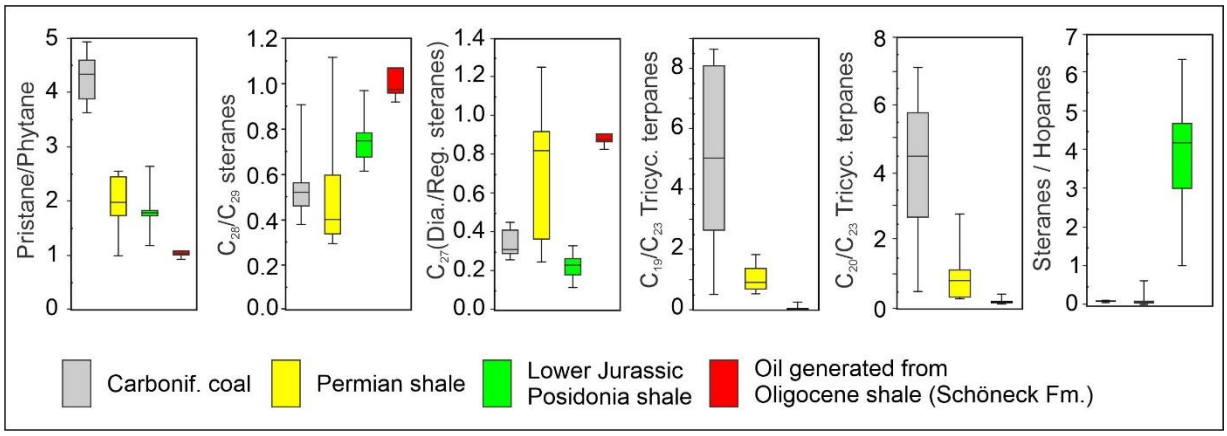

Fig. 19. Box plots (statistical representation from bottom to top are: minimum, first quartile, median, second quartile and maximum) showing distributions of biomarker ratios in extracts from Carboniferous coals (main seam #6; this study), Permian shales (main shale interval; this study), and Toarcian (Lower Jurassic Posidonia shale; Ajuaba et al., 2022). Biomarker ratios of oil samples from the Austrian sector of the NAFB, generated by Oligocene source rocks are shown for comparison (data from Gratzer et al., 2011).

5.3 Implications of study results for the reconstruction of the depositional environment

The results presented in this work provide indications on the depositional environment of the main coal seam in the Carboniferous succession and the Permian lacustrine deposits.

5.3.1 Carboniferous coal measures

The lithological log of the main seam (#6) is shown in Fig. 3 after Wolf et al. (1988) and Matter et al. (1988). The seam overlies laminated fine-grained, shaly sandstone. It contains relatively clean coal in the lower part (10 wt.% ash, db) with ash yields increasing upwards to 46 wt.%db (Fig. 3b). High ash yields are reflected by low TOC contents (77.0-35.5 wt.%; Fig. 3b). Based on the absence of rooted horizons and high mineral matter contents, Wolf et al. (1988) assumed an hypautochthonous to allochthonous origin of the coal seams. High ash yields together with low sulphur contents (<0.5 wt.% in the main seam; Fig. 3c; <0.9 wt.% in other seams) support an origin in a non-marine low-lying mire. A thick tuff and several thin (1-30 mm) tonstein layers occur in the seam (Wolf et al., 1988) and reflect strong contemporary volcanic activity, whereas alteration to kaolinite testifies to acidic conditions.

The top of the seam (1585.01 m) is overlain by cross-bedded conglomeratic sandstones, several metres thick (Matter et al., 1988). The presence of coaly shales and shales in the upper part of the seam and the lithology of the overlying rocks suggest that peat accumulation ended due to channel(s) avulsion.

A detailed petrographic study using polished blocks of 120 samples was performed by Wolf et al. (1988). They reported a relatively high percentage of inertinite (17 vol.%) and low percentage of liptinite macerals (3 vol.%). Although only six samples were investigated in the present study, the overall results are similar (inertinite: 11 vol.%; liptinite: 4 vol.%). Despite the low liptinite contents, Wolf et al. (1988) noted that the coal samples are relatively rich in hydrogen (5.3 wt.%$_{daf}$) and concluded that this is due to secondary bitumen. In agreement with this observation, HI values are also relatively high and not related to liptinite contents. Alternatively, HI may be enhanced due to migration of hydrocarbons from adjacent shale source beds (see section 5.1.1).

Geochemical parameters are within the range expected for coal samples. High Pr/Ph ratios (3.6-5.0) and high amounts of C_{29} steranes (44-58 wt.%) reflect the predominant input of land-plants. Very low sterane/hopane ratios (≤0.15; Table 3) indicate high bacteria activity, characteristic for many peat-forming environments (Dai et al., 2020). High concentrations of

hopanoids in these environments have been related to wood-degrading bacteria (e.g. Bechtel et al., 2007a,b; 2008).

5.3.2 Lacustrine series

The postulated lacustrine setting is evidenced by low sulphur contents and high TOC/S ratios (Table 5, Fig. 9). This is also supported by the regular occurrence of the freshwater to brackish water algae *Botryococcus*, albeit in trace amounts, and the absence of any marine organic particles, like dinoflagellate cysts or foraminifer linings.

The most detailed information is available for the main shale interval, which can be subdivided into a lower organic matter-rich part (1339.20-1329.35 m) and a thin, less organic matter-rich upper part (1328.85-1326.95 m; Fig. 9). The organic material of the lower organic matter-rich part is dominated by aquatic organisms, as shown by the prevailing Type II kerogen (Figs. 4; 17b) and high concentrations of short-chain *n*-alkanes (Fig. 14a) and C_{27} steranes (Fig. 14b). The Pr/Ph ratio is a widely used redox parameter (e.g. Didyk et al., 1978). However, in the present case, the good correlation between Pr/Ph ratio and CPI (cf. Fig. 14b, c) suggests that the Pr/Ph ratio is mainly controlled by the input of land-plants rather than by oxygen availability. Hence, the concentration of aryl-isoprenoids (Fig. 14l) and the homohopane index (HHI; Fig. 14m) may be the better redox proxies. Both parameters indicate strongly anoxic conditions and probably even photic zone anoxia during the early stage of shale deposition followed by gradually increasing oxygen availability. Apart from the main shale interval, strongly anoxic conditions also occurred during deposition of the sediments at about 1314 m depth (Fig. 14l, m).

Vertical trends of the gammacerane index (Fig. 14i) suggest that oxygen restriction was caused by water column stratification. A low energy environment is a prerequisite for water column stratification. Preservation of delicate biological structures observed in several opaque phytoclasts is an additional indication of a low-energy setting. As expected in a lacustrine environment, the availability of free H_2S was very low as suggested by low DBT/Phenanthrene ratios (Fig. 14k). Despite of the generelly low values, the DBT/Phenanthrene ratios (Fig. 14k) show similar depth trends as the other redox parameters. With few exceptions, the sterane/hopane is below 0.2 indicating high bacterial activity (Fig. 14f). At least partly, high concentrations of hopanes are related to bacteria degrading plant tissues in terrigenous environments (Bechtel et al., 2007a,b).

Additional insight into the origin of organic matter is provided by palynofacies data, especially by the abundance of different types of AOM. Proportions of rectangular AOM

show a moderate positive correlation between HI and TOC (r^2=0.50 and 0.59, respectively), while proportions of orange, cloudy AOM shows moderate to weak negative correlations (r^2=0.51 and 0.40, respectively) (Fig. 20). This suggests that a large part of the organic productivity in the lake facies from Weiach-1 was associated with the rectangular AOM source, while production of the orange, cloudy AOM was associated with reduced paleoproductivity levels in the lake and/or increased oxygen availability.

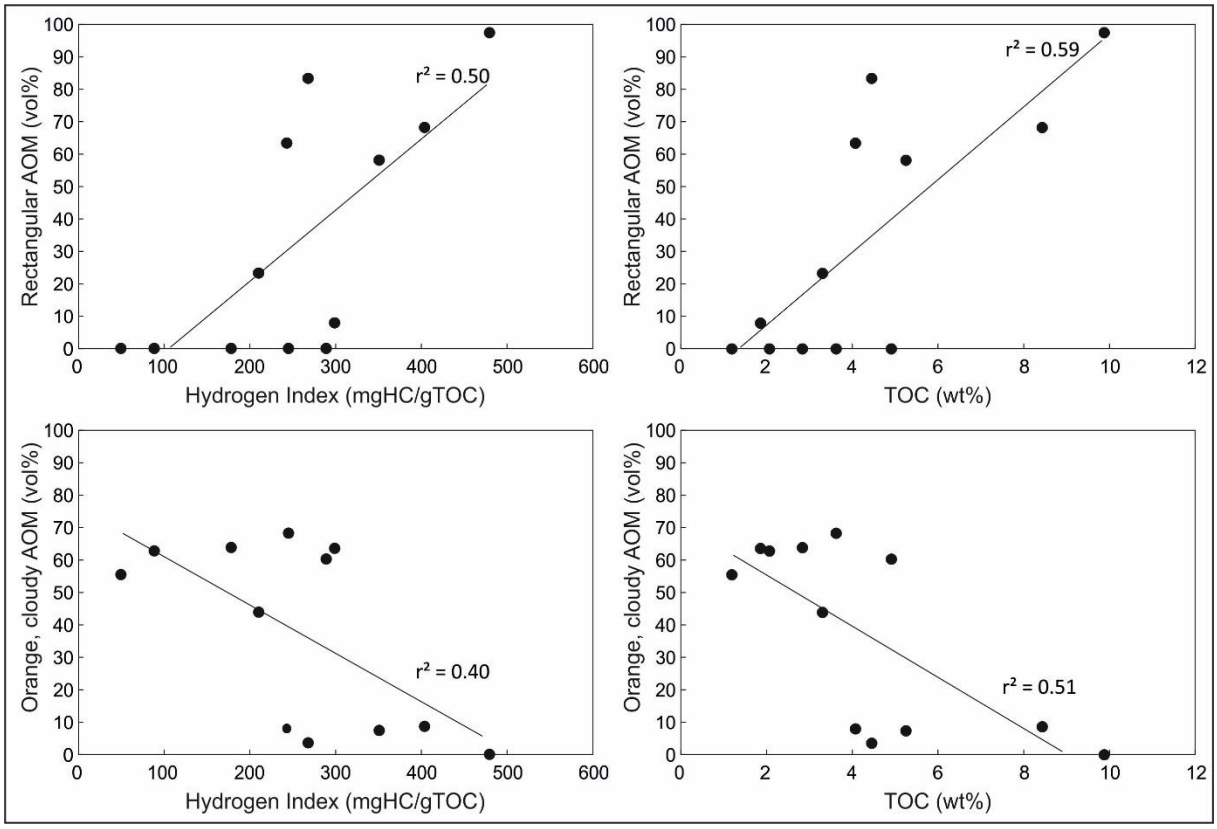

Fig. 20. Plots of the amount of rectangular and orange, cloudy amorphous organic matter (AOM) against hydrogen index and TOC. Percentages of rectangular AOM shows moderate positive correlations, while cloudy AOM shows moderate negative correlations.

Sub-rectangular AOM is known to be formed in peat and marsh environments through amorphization and gelification processes in low-energy locations (Laggoun-Défarge et al., 1999; Sebag et al., 2006; Garel et al., 2013; Storme et al., 2012) and, therefore, our results suggest the greater occurrence of such paleoenvironmetal conditions between 1339.20 m and 1334.22 m. These paleoenvironmental conditions seem to have been the most favourable for organic production and preservation in the Weiach-1 core. The exact nature of the higher plants sources leading to the sub-rectangular AOM are not known in Weiach-1. Based on the high amount of short-chain *n*-alkanes and C_{27} steranes, the sub-rectangular AOM are probably

not related to emerged land-plants in vegetated areas at the boarders parts of the lake system. In contrast, submerged (or floating) aquatic plants are a more likely source.

From 1333.30 to 1328.65 m, the increasing proportions of orange, cloudy AOM in palynofacies suggest enhanced algal/bacterial surface production, however associated with lower organic fluxes as TOC and HI values are lower than between 1339.20 m up to 1334.22 m. The lake system may have been more open and enlarged, possibly deeper, favoring surface algal/bacterial productivity in the photic waters of the lake.

5.3.3 Stable carbon isotope data in Permo-Carboniferous terrigenous environments

Main coal seam

Carbon and nitrogen isotope data from coals and black shales in the Permo-Carboniferous Igornay and Muse formations in the Autun Basin (Massif Central) have been reported recently by Mercuzot et al. (2021). They observed background $\delta^{13}C$ values of aquatic and dispersed terrigenous organic matter of around -23.5 ‰ and -20.0 ‰, respectively, and of coal of around -24 to -25 ‰. These data can be compared with the compound-specific stable carbon isotope data from the coeval coal series and the lacustrine series.

The average $\delta^{13}C$ value of long-chain *n*-alkanes (*n*-C_{25-29}; -27.6 ‰) and isoprenoids (-27.4 ‰) in the coal samples is slightly more negative than bulk ^{13}C values of the coeval coals in the Autun Basin. The difference (~3 ‰) is about the same as that observed between coal and the saturated hydrocarbon fraction for Carboniferous coals in Poland (Kotarba and Clayton, 2003). Hence, the bulk coal data from the Massif Central and the CSI data from Weiach match well. They also agree with isotope data from Upper Carboniferous coal samples in other parts of the world (Peters-Kottig et al., 2006; Zdravkov et al., 2017). A clear vertical trend of $\delta^{13}C$ values, which may reflect temporal changes in atmospheric CO_2, is neither expected nor observed in the 10-m-thick seam.

Lacustrine Series

$\delta^{13}C$ values of *n*-alkanes and isoprenoids in the lacustrine series show a larger variability and significant stratigraphic trends (Fig. 15). $\delta^{13}C$ values of pristane and phytane are similar in most samples (difference ≤0.4 ‰). Although the difference is slightly greater (0.46-0.89 ‰)

in two samples above the main shale interval, this suggests a common chlorophyll precursor and that non-chlorophyll-derived phytane is largely absent (e.g. Aghayeva et al., 2021).

Pristane and phytane show the same stratigraphic $\delta^{13}C$ trend as the short-chain *n*-alkanes *n*-C_{15} and *n*-C_{16}, which are derived mainly from aquatic organisms, including bacteria and algae (Cranwell et al., 1987). In contrast, mid- and long-chain *n*-alkanes, derived at least partly from submergent plants (e.g. Ficken et al., 2000) and land plants (e.g. Eglinton et al., 1962), show different stratigraphic trends (Fig. 15). This suggests that pristane and phytane are derived from the chlorophyll of aquatic plants. Consequently, the uniform upward increase in $\delta^{13}C$ values of pristane and phytane reflects a change in the isotopic composition within the water column. The most negative $\delta^{13}C$ values of pristane and phytane (-30.3 ‰) are observed at the base of the main shale interval (1339.20 m). Based on the amount of aryl-isoprenoids (Fig. 10m) and the homohopane index (HHI; Fig. 10n), this level corresponds to the most anoxic part of the main shale interval. While various factors, like climatic variations or productivity, may affect the lacustrine carbon reservoir, the observed very negative $\delta^{13}C$ values are probably related to remineralization of organic matter in the anoxic water column beneath a strong chemocline (e.g. Küspert 1982; Jenkyns 1985; Hayes, 2001). Similarly, Mercuzot et al. (2021) observed strong negative bulk organic carbon excursions in coeval black shales from the Autun Basin. In addition, these authors noted a positive nitrogen isotope excursion in these intervals indicating denitrification and anammox processes. An upward increase in oxygen availability within the main shale interval and a trend towards less negative $\delta^{13}C$ values (Fig. 15) may reflect a weakening of water column stratification, which is also supported by the gammacerane index (Fig. 10i). Mid- and long-chain *n*-alkanes with relatively high $\delta^{13}C$ values probably reflect terrigenous input.

$\delta^{13}C$ values of pristane and phytane in organic-rich layers above the main shale interval (1313.37-1312-95 m) are relatively high (about -26 ‰; Fig. 15), despite partly strictly anoxic conditions. Apparently, the effect of recycling of isotopically light dissolved inorganic carbon from deeper levels of the stratified water body was limited during deposition of the younger layer.

Whereas pristane and phytane are derived from chlorophyll, short-chain *n*-alkanes (*n*-C_{15-17}) are produced by primary producers (algae, cyanobacteria) and heterotrophs. Consequently, their $\delta^{13}C$ values represent a weighted average of these (Grice et al., 2005). If derived from primary producers, short-chain *n*-alkanes should be depleted in ^{13}C compared with the co-occurring isoprenoids by 1.5 ‰ (Schouten et al., 1998; Hayes, 2001; Grice et al., 2005). In

contrast, enrichment in ^{13}C result from heterotrophic processing of primary photosynthate or dominant contribution of isotopically heavy bacterial biomass (Grice et al., 2005; Fox et al., 2020). In the main shale interval, $\delta^{13}C$ values of short-chain *n*-alkanes and of pristane and phytane are similar (difference <0.8 ‰). In contrast, $\delta^{13}C$ values of short-chain *n*-alkanes in organic-rich layers above the main shale interval are 1.1 to 1.7 ‰ more negative. This suggests that short-chain *n*-alkanes in the upper layer are mainly derived from primary producers, whereas both auto- and heterotrophs contributed to the short-chain *n*-alkanes in the main shale layer.

4. Conclusion

A total of 90 core samples from the Weiach-1 well, located in the Permo-Carboniferous Constance-Frick-Trough beneath the Northern Alpine Foreland Basin (NAFB; Northern Switzerland), have been investigated to study the petroleum potential of coals and shales and to contribute to the understanding of the depositional environment of the main Carboniferous coal seam and the main Permian (Autunian) shale horizon. The most relevant findings of the detailed petrographic and geochemical investigation are summarized below.

- Carboniferous coaly shales, classified as bituminous in earlier studies, do not hold a significant hydrocarbon potential, despite relatively high TOC contents.
- Coals in the Carboniferous coal series are potential source rocks for natural gas. The maturity of the oal series reached the onset of gas generation. The coal would have generated only very limited amounts of oil, which could be identified easily based on biomarker ratios (e.g., high Pr/Ph ratios).
- The petroleum potential of shales in the Permian Lacustrine Series varies considerably. While some intervals do not exhibit a petroleum potential (TOC <0.3 wt.%), bituminous shales in the "main shale interval" (1339.20-1326.95 m) contain very high amounts of organic matter TOC (max. 10.3 wt.% TOC) with a high HI (max. 488 mgHC/gTOC). These sediments display "good" to "very good" oil potential. The calculated SPI (Source Potential Index) suggests that the main shale interval may generate about 0.35 tHC/m².
- The lacustrine series is probably not a main source rock interval in the NAFB, but it may have contributed to hydrocarbon accumulations. A clear distinction of oil generated from Permian, Jurassic and Oligocene source rocks is possible based on biomarker ratios and CSI data.

- The main seam (#6) was deposited in a low-lying, freshwater mire. Upward increasing mineral matter contents are probably due to delta channel(s) avulsion process in a floodplain setting. Biomarker ratios reflect the high amount of terrigenous organic matter.
- The non-marine environment of the acustrine eries is supported by the presence of the freashwater algae *Botryococcus* and very high TOC/S ratios throughout the main shale interval. The organic matter is mainly of aquatic (algal) origin but with a significant terrigenous input. Bacterial activity was high. Biomarker and palynofacies data show a strongly oxygen-depleted depositional environment, controlled by water column stratification, which even caused photic zone anoxia, and associated with a low energy environment as supported by palynofacies data. In the study interval, these environmental conditions, then changed to a more oxygenated, less stratified and probably deeper and more open lacustrine environment.
- $\delta^{13}C$ values of pristane and phytane in the main shale interval reflect anoxic conditions and remineralization of organic matter.

References

Aghayeva, V., Sachsenhofer, R.F., van Baak, C.G.C., Bechtel, A., Hoyle, T.M., Selby, D., Shiyanova, N., Vincent, S.J. (2021). New geochemical insights into Cenozoic source rocks in Azerbaijan: Implications for petroleum systems in the South Caspian Region. Journal Petroleum Geology, 44, 349-384.

Ajuaba, S., Sachsenhofer, R.F., Galasso, F., Bechtel, A., Gross, D., Misch, D., Schneebeli-Hermann, E. (2022). Biomarker and compound-specific isotope records across the Toarcian CIE at the Dormettingen section in SW Germany. Int. J. Earth Sciences, 111:1631–1661. https://doi.org/10.1007/s00531-022-02196-z.

Bachmann, G.H., Müller, M., Weggen, K. (1987). Evolution of the Molasse basin (Germany. Switzerland). Tectonophysics, 137. 77 92.

Bechtel, A., Reischenbacher, D., Sachsenhofer, R.F., Gratzer, R., Lücke, A., (2007a). Paleogeography and paleoecology of the upper Miocene Zillingdorf lignite deposit (Austria). Int. J. Coal Geol., 69, 119–143.

Bechtel, A., Hámor-Vidó, M., Sachsenhofer, R.F., Reischenbacher, D., Gratzer, R., Püttmann, W. (2007b). The middle Eocene Márkushegy sub-bituminous coal (Hungary): Paleoenvironmental implications from petrographical and geochemical studies. Int. J. Coal Geol., 72, 33-52.

Bechtel, A., Gratzer, R., Sachsenhofer, R.F., Gusterhuber, J., Lücke, A., Püttmann, W. (2008). Biomarker and carbon isotope variation in coal and fossil wood of Central Europe through the Cenozoic. Palaeogeography, Palaeoclimatology, Palaeoecology, 262, 166-175.

Bechtel, A., Gratzer, R., Linzer, H.-G., Sachsenhofer, R.F. (2013). Influence of migration distance, maturity and facies on the stable isotopic composition of alkanes and on carbazole distributions in oils and source rocks of the Alpine Foreland Basin of Austria. Organic Geochemistry, 62, 74-85.

Bechtel, A., Berling, M., David, P., Dax, F., Garlichs, T.U., Gratzer, R.; Groß, D., Köhler, V., Oriabure, J.E., Sachsenhofer, R.F. (2019). Oil-source correlation in the German Molasse Basin. 29th Int. Meeting on Org. Geochem. (IMOG 2019). https://doi.org/10.3997/2214-4609.201902720

Bray, E.E., Evans, E.D. (1961). Distribution of n-paraffins as a clue to recognition of source beds. Geochim. Cosmochim. Acta, 22, 2–5. https://doi.org/10.1016/0016-7037(61)90069-2.

Burdige, D.J. (2007). Preservation of organic matter in marine sediments: controls, Mechanisms, and an imbalance in sediment organic carbon budgets? Chem. Rev., 107, Chapman and Hall, 615 pp.

Cervelli, M. (2022) Reservoir Sedimentology, Mineralogy and Chemostratigraphy of a Permo – Carboniferous trough infill in NE Switzerland. Implication for geo-energy exploration. MSc Thesis, Departmen of Geosciences, University of Padoue, Italy, 118 pp.

Clayton, G., Coquel, R., Doubinger, J., Gueinn, K.J., Loboziak, S., Owen, B., Streel, M. (1977). Carboniferous miospores of Western Europe: illustration and zonation. Meded. Rijks geol. Dienst, 29, 1-71.

Cranwell, P., Eglinton, G., Robinson, N. (1987). Lipids of aquatic organisms as potential contributors to lacustrine sediments—II. Org. Geochem., 11, 513–527.

Dahl, B., Bojesen-Koefoed, J., Holm, A., Justwan, H., Rasmussen, E., Thomsen, E. (2004). A new approach to interpreting Rock-Eval S2 and TOC data for kerogen quality assessment. Org. Geochem., 35, 1461–1477.

Dai, S., Bechtel, A., Eble, C.F., Flores, R.M., French, D., Graham, I.T., Hood, M.M., Hower, J.C., Korasidis, V.A., Moore, T.A., Püttman, W., Wei, Q., Zhao, L., O'Keefe, J. M.K. (2020). Recognition of peat depositional environments in coal: a review. Int. J. Coal Geol., 210, 103383, 67.

Demaison, G., Huizinga, B.J. (1994). Genetic classification of petroleum systems using three factors: charge, migration and entrapment. In: Magoon, L.B., Dow, W.G. (Eds.): The Petroleum System, from Source to Trap. AAPG Memoir, 60, 73-89.

Didyk, B., Simoneit, B., Brassell, S., Eglinton, G. (1978). Organic geochemical indicators of palaeoenvironmental conditions of sedimentation. Nature, 272, 216–222.

Diebold, P. (1988). Der Nordschweizer Permokarbon-Trog und die Steinkohlefrage der Nordschweiz. In: Vierteljahrsschrift der Naturforschenden Gesellschaft in Zürich, 133/1, 143-174.

Diebold, P., Naef, H., Ammann, M. (1991). Zur Tektonik der zentralen Nordschweiz: Interpretation aufgrund regionaler Seismik, Oberflächengeologie und Tiefbohrungen. Nagra Tech. Ber. NTB 90-04, Nagra, Wettingen, 277.

Do Couto, D., Garel, S., Moscariello, A., Bou Daher, S., Littke, R., Weniger, P. (2021). Origins of hydrocarbons in the Geneva Basin: insights from oil, gas and source rock organic geochemistry. Swiss Journal of Geosciences, 114(1), 1-28.

Eglinton, G., Gonzalez, A., Hamilton, R., Raphael, R. (1962). Hydrocarbon constituents of the wax coatings of plant leaves: A taxonomic survey. Phytochemistry, 1, 89-102.

Espitalié, J., Marquis, F., Barsony, I. (1984). Geochemical logging. In: Voorhess, K.J. (Eds.): Analytical Pyrolysis. Butterworths, Boston, 53-79.

Ficken, K.J., Li, B., Swain, D., Eglinton, G. (2000). An n-alkane proxy for the sedimentary input of submerged/floating freshwater aquatic macrophytes. Org. Geochem., 31, 745–749. https://doi.org/10.1016/S0146-6380(00)00081-4.

Fox, C.P., Cui, X., Whiteside, J.H., Grice, K. (2020). Molecular and isotopic evidence reveals the end-Triassic carbon isotope excursion is not from massive exogenous light carbon. PNAS, 117(48), 30171-30178. https://doi.org/10.1073/pnas.1917661117.

Garel, S., Schnyder, J., Jacob, J., Dupuis, C., Boussafir, M., Le Milbeau, C., Storme, J.-Y., Iakovleva, A., Yans, J., Baudin, F., Fléhoc, C, Quesnel, F. (2013). Paleohydrological and paleoenvironmental changes recorded in terrestrial sediments of the Paleocene–Eocene boundary (Normandy, France). Palaeogeography, Palaeoclimatology, Palaeoecology, 376, 184-199.

Grantham, P.J., Wakefield, L.L. (1988). Variations in the sterane carbon number distribution of marine source rocks derived crude oils through geological time. Organic Geochemistry, 12, 61-74.

Gratzer, R., Bechtel, A., Sachsenhofer, R.F., Linzer H.-G., Reischenbacher, D., Schulz, H.-M. (2011). Oil-oil and oil-source rock correlations in the Alpine Foreland Basin of Austria: Insights from biomarker and stable carbon isotope studies. Marine and Petroleum Geology 28, 1171-1186.

Greber, E., W. Leu, D. Bernoulli, M. E. Schumacher, and Wyss, R. (1997). Hydrocarbon provinces in the Swiss Southern Alps—a gas geochemistry and basin modelling study. Marine and Petroleum Geology, 14, 3-25.

Grice, K., Cao, C., Love, G.D., Böttcher, M.E., Twitchett, R.J., Grosjean, E., Summons, R.E., Turgeon, S.C., Dunning, W., Jin, Y. (2005). Photic zone euxinia during the Permian-Triassic superanoxic event. Science, 307, 706-709.

Grice, K., de Mesmay, R., Glucina, A., Wang, S. (2008). An improved and rapid 5A molecular sieve method for gas chromatography isotope ratio mass spectrometry of n-alkanes (C8–C30+). Org Geochem 39:284–288. https://doi.org/10.1016/j.orggeochem.2007.12.009

Hayes, J.M. (2001). Fractionation of Carbon and Hydrogen Isotopes in Biosynthetic Processes. Rev. Mineral. Geochem., 43, 225–277. doi:10.2138/gsrmg.43.1.225

Hochuli, P.A. (1985): Palynostratigraphische Gliederung und Korrelation des Permokarbons der Nordschweiz. Eclogae Geol. Helv., 78, 719-831.

ICCP (1998) The new vitrinite classification (ICCP System 1994). Fuel 77: 349–358. https://doi.org/10.1016/S0016-2361(98)80024-0.

ICCP (2001) The new inertinite classification (ICCP System 1994). Fuel 80: 459–471. https://doi.org/10.1016/S0016-2361(00) 00102-2.

Jenkyns, H.C. (1985). The early Toarcian and Cenomanian-Turonian Anoxic Events in Europe: comparisons and contrasts. Geol. Rundschau, 74, 505-518.

Kotarba, M.J., Clayton, J.L. (2003). A stable carbon isotope and biological marker study of Polish bituminous coals and carbonaceous shales. Int. J. Coal Geol., 55, 73-94.

Küspert, W. (1982). Environmental change during oil shale deposition as deduced from stable isotope ratios. In: Einsele, S., Seilacher, A. (eds.) Cyclic and event stratification. Springer, New York, pp 482-501.

Laggoun-Défarge, F., Bourdon, S., Chenu, C., Défarge, C. and Disnar, J.R. (1999). Etude des transformations morphologiques précoces des tissus végétaux dans la tourbe du marécage de Tritrivakely (Madagascar). Apports des techniques de marquage histochimique en MET et du cryo-MEB haute résolution. In: Structure et Ultrastructure des Sols et des Organismes (V.F. Elsass and A.-M. Jaunet, eds), Les Colloques No. 92, pp. 169–182. INRA, Versailles.

Lahusen, P. H., and Wyss, R. (1995). Erdöl- und Erdgasexploration in der Schweiz: Ein Rückblick: Bulletin Association Suisse des Geologues et Ingnieurs du Petrole, 62, 43-72.

Langford, F.F., Blanc-Valleron, M.-M. (1990). Interpreting Rock–Eval pyrolysis data using graphs of pyrolyzable hydrocarbons vs. total organic carbon. American Association of Petroleum Geologists Bulletin, 74, 799–804.

Laubscher, H. (1987). Die tektonische Entwicklung der Nordschweiz. Eclogae Geologicae Helvetiae, 80, 287-303.

Leu, W. (2008). Permokarbon-Kartenskizze (Rohstoffe) Kompilation eines GIS-Datensatzes auf der Basis von bestehenden Unterlagen (Bereich Schweizer Mittelland). Arbeitsbericht NAB 08-49, NAGRA.

Leu, W., Greber, E., Schegg, R. (2001). Basin modeling NE-Switzerland, burial, erosion and temperature history of wells Benken, Weiach and Herdern-1. Unpubl. Nagra Int. Rep.

Leu, W. (2014). Potenzial der Kohlenwasserstoff Ressourcen in der Nordschweiz. NAB 14-70 NAGRA.

Leu, W. (2012). Swiss oil/gas exploration and lessons learnt. Swiss Bull. Angew. Geol., 17, 49-59.

Littke, R., Rotzal, H., Leythaeuser, D., Baker, D.R. (1991). Lower Toarcian Posidonia Shale in Southern Germany (Schwaebische Alb). Organic Facies, Depositional Environment and maturity. Erdöl Kohle Erdgas Petrochemie Hydrocarbon Technol., 44, 407-414.

Mackenzie, A.S., Maxwell, J.R. (1981). Assessment of thermal maturation in sedimentary rocks by molecular measurements. In: Brooks, J. (Ed.), Organic Maturation Studies and Fossil Fuel Exploration. Academic Press, London, pp. 239e254.

Madritsch, H., Naef, H., Meier, B., Franzke, H. J., Schreurs, G. (2018). Architecture and kinematics of the Constance-Frick Trough (northern Switzerland): Implications for the formation of post-Variscan basins in the foreland of the Alps and scenarios of their Neogene reactivation. *Tectonics*, *37*. https://doi.org/10.1029/2017TC004945

Matter, A. (1987). Faciesanalyse und Ablagerungsmilieu des Permokarbons im Nordschweizer Trog. In: Eclogae Geologicae Helvetiae, Band 80, Heft 2.

Matter, A., Peters, T., Bläsi, H.-R., Meyer, J., Ischi, H., Meyer, C. (1988). Sondierbohrung Weiach – Geologie. Text- und Beilagenband. Nagra Tech. Ber. NTB 86–01. Nagra, Wettingen.

Mazurek, M., Hurford, A.J., Leu, W. (2006). Unravelling the multi-stage burial history of the Swiss Molasse Basin: Integration of apatite fission track, vitrinite reflectance and biomarker isomerisation analysis. Basin Res. 2006, 18, 27–50.

McArthur, A.D., Kneller, B.C., Wakefield, M.I., Souza, P.A., Kuchle, J. (2016). Palynofacies classification of the depositional elements of confined turbidite systems: examples from the Gres d'Annot, SE France. Mar. Pet. Geol. 77, 1254-1273.

McCann, T., Pascal, C., Timmerman, M. J., Krzywiec, P., López-Gómez, J., Wetzel, A., Krawczyk, C.M., Rieke, H., Lamarch, J. (2006). Post-Variscian (end Carboniferous – Early Permian) basin evolution in Western and Central Europe. In D. G. Gee, R. A. Stephenson (Eds.), European Lithosphere Dynamics (pp. 355–388). London: Geological Society.

Mercuzot, M., Bourquin, S., Pellenard, P., Beccaletto, L., Schnyder, J., Baudin, F., Ducassou, C., Garel, S., Gand, G. (2022). Reconsidering Carboniferous–Permian continental paleoenvironments in eastern equatorial Pangea: facies and sequence stratigraphy investigations in the Autun Basin (France). International Journal of Earth Sciences, 111, 1663–1696. https://doi.org/10.1007/s00531-022-02200-6

Mercuzot, M., Thomazo, C., S., Schnyder, J., Pellenard, P., Baudin, F., Pierson-Wickmann, A.-C.,, Sans-Jofre, P., Bourquin, S., Beccaletto, L., Santoni, A.-L., Gand, G., Buisson, M., Glé, L., Muiner, T., Saloume, A., Boussaid, M., Boucher, T. (2021). Carbon and Nitrogen Cycle Dynamic in Continental Late-Carboniferous to Early Permian Basins of Eastern Pangea (Northeastern Massif Central, France). Front. Earth Sciences, 9, 705351. https://10.3389/feart.2021.705351

Misch, D., Leu, W., Sachsenhofer, R. F., Gratzer, R., Rupprecht, B., Bechtel, A. (2017). Shallow hydrocarbon indications along the Alpine thrust belt and adjacent foreland basin: distribution and implications for petroleum exploration. Journal of Petroleum Geology, 40(4), 341-362.

Moldowan, J.M., Dahl, J., Huizinga, B.J., Fago, F.J., Hickey, L.J., Peakman, T.M., Taylor, D.W. (1994). The molecular fossil record of oleanane and its relation to angiosperms. Science, 265, 768-771.

Moscariello A. (2019). Exploring for geo-energy resources in the Geneva Basin (Western Switzerland): opportunities and challenges. Swiss Bull. angew. Geol., 24/2, 105-124.

Moscariello, A., Guglielmetti, L., Omodeo-Salé, S., De Haller, A., Eruteya, O.E., Lo, H.Y., Clerc, N., Makloufhi, Y., Do Couto, D., Ferreira De Oliveira, G., Perozzi, L., Hollmuller, P., Quiquerez, L., Nawratil De Bono, C., Martin, F., Meyer, M. (2020). Heat production and storage in Western Switzerland: advances and challenges of intense multidisciplinary geothermal exploration activities, an 8 years progress report. In: Proceedings World Geothermal Congress. Reykjavik, Iceland.

Moscariello, A., Ventra, D., Cervelli, M., Eruteya, O.E., Omodeo Salé, S., Makhloufi, Y. (2021). Revisiting the origin of the Carboniferous infill of Swiss post-Hercynian Throughs: Insights from the Weiach-1 borehole (northern Switzerland). Extended Abstract 19th Swiss Geoscience Meeting, Geneva 2021, Symposium 7: Stratigraphy and Sedimentology: processes and deposits through time. https://geoscience-meeting.ch/sgm2021

Naef, H., Birkhäuser, P., Roth, P. (1995). Interpretation der Reflexionsseismik im Gebiet nördlich Lägeren – Zürcher Weinland (Nagra Tech. Ber. NTB 94–14). Wettingen: Nagra.

NAGRA, 2002: Technischer Bericht - Projekt Opalinuston: Konzept für die Anlagen und den Betrieb eines geologischen Tiefenlagers. Entsorgungsnachweis für abgebrannte Brennelemente, verglaste hochaktive sowie langlebige mittelaktive Abfälle. Nagra Tech. Ber. NTB 02-02.

Noble, R.A., Alexander, R., Kagi, R.I., Knox, J. (1986). Identification of some diterpenoid hydrocarbons in petroleum. Org. Geochem., 10, 825–829.

Omodeo-Salé, S., Eruteya, O. E., Cassola, T., Baniasad, A., Moscariello, A. (2020). A basin thermal modelling approach to mitigate geothermal energy exploration risks: The St. Gallen case study (eastern Switzerland). Geothermics, 87, 101876.

Omodeo-Salé, S., Hamidi, Y., Villagomez, D., Moscariello, A. (2021). Quantifying Multiple Erosion Events in the Distal Sector of the Northern Alpine Foreland Basin (North-Eastern Switzerland), by Combining Basin Thermal Modelling with Vitrinite Reflectance and Apatite Fission Tract. Geosciences, 11, 62. https://doi.org/10.3390/geosciences11020062.

Peters, K. E., Walters, C. C., Moldwan, J. M. (2005). The biomarker guide (2nd ed.). Cambridge, UK: Cambridge University Press.

Peters-Kottig, W., Strauss, H., Kerp, H. (2006). The land plant $\delta^{13}C$ record and plant evolution in the Late Palaeozoic. Palaeogeogr. Palaeoclimatol. Palaeoecol., 240, 237-252. doi:10.1016/j.palaeo.2006.03.051

Pickel, W., Kus, J., Flores, D., Kalaitzidis, S., Christanis, K., Cardott, B.J., Misz-Kennan, M., Rodrigues, S., Hentschel, A., Hamor-Vido, M., Crosdale, P., Wagner, N. ICCP (2017). Classifcation of liptinite– ICCP system (1994). Int J Coal Geol 169:40–61. https://doi.org/10.1016/j.coal.2016.11.004

Pullan, C. P., Berry, M. (2019). A Paleozoic-sourced oil play in the Jura of France and Switzerland. Geological Society, London, Special Publications, 471(1), 365-387. https://doi.org/10.1144/sp471 .2.

Radke, M. (1988). Application of aromatic compounds as maturity indicators in source rocks and crude oils. Mar Petrol Geo.

Radke, M., Schaefer, R.G., Leythaeuser, D., Teichmüller, M. (1980). Composition of soluble organic matter in coals: relation to rank and liptinite fuorescence. Geochim Cosmochim Acta 44:1787–1800.

Radke, M., Welte D.H., Willsch, H. (1986). Maturity parameters based on aromatic hydrocarbons: infuence of the organic matter type. Org Geochem 10:51–63.

Radke, M. Welte, D.H. (1983). The Methylphenanthrene Index (MPI): A maturity parameter based on aromatic hydrocarbons. In: Bjoroy, M. (ed.) Advances in Organic Geochemistry 1981. Wiley, Chichester, 504–512.

Sachsenhofer, R.F., Schulz, H.-M. (2006). Architecture of Lower Oligocene source rocks in the Alpine Foreland Basin: A model for syn- and postdepositional source rock features in the Paratethyan Realm. Petroleum Geoscience, 12, 363-377.

Sachsenhofer R.F., Leitner B., Linzer H.-G., Bechtel A., Ćorić S., Gratzer R., Reischenbacher D., Soliman A. (2010). Deposition, erosion and hydrocarbon source potential of the Oligocene Eggerding Formation (Molasse Basin, Austria). Austrian Journal Earth Sciences, 103, 76-99.

Schnyder, J., Stetten, E., Baudin, F., Pruski, A.-M., Martinez, P. (2017). Palynofacies reveal fresh terrestrial organic matter inputs in the terminal lobes of the Congo Deep-Sea fan. Deep-Sea Research II, 142, p. 91-108.

Schouten, S., Klein Breteler, W.C.M., Blokker, P., Schogt, N., Rijpstra, W.I.C., Grice, K., Baas, M., Sinninghe Damsté, J.S. (1998). Biosynthetic effects on the stable carbon isotopic compositions of algal lipids: implications for deciphering the carbon isotopic biomarker record. Geochimica et Cosmochimica Acta, 62, 1397-1406. https://doi.org/10.1016/S0016-7037(98)00076-3

Schulz H.-M., Sachsenhofer R. F., Bechtel A., Polesny H., Wagner L. (2002). The origin of hydrocarbon source rocks in the Austrian Molasse Basin (Eocene-Oligocene transition). Marine and Petroleum Geology 19, 683-709.

Sebag, D., Copard, Y., Di Giovanni, C., Durand, A., Laignel, B., Ogier, S. and Lallier-Verges, E. (2006). Palynofacies as useful tool to study origins and transfers of particulate organic matter in recent terrestrial environments: synopsis and prospects. Earth Sci. Rev., 79, 241-259.

Steffen, D., Gorin, G. (1993). Sedimentology of organic matter in Upper Tithonian-Berriasian deep-sea carbonates of southeast France: evidence of eustatic control. In: Katz, B., Pratt, L. (Eds.), Source rocks in a sequence stratigraphic framework: AAPG Studies in Geology, vol. 37, pp. 49–65.

Storme, J.-Y., Devleeschouwer, X., Schnyder, J., Cambier, G., Baceta, J.I., Pujalte, V., Di Matteo, A., Iacumin, P., Yans, J., 2012. The Palaeocene/Eocene boundary section at Zumaia (Basque-Cantabric Basin) revisited: new insights from high-resolution magnetic susceptibility and carbon isotope chemostratigraphy on organic matter (δ13Corg). Terra Nova 24, 310–317. https://doi.org/10.1111/j.1365-3121.2012.01 064.x.

Sykes, R., Snowdon, L.R. (2002). Guidelines for assessing the petroleum potential of coaly source rocks using Rock-Eva pyrolysis. In: Organic Geochemistry, 33, 1441-1445.

Taylor, G., Teichmüller, M., Davies, A., Diessel, D., Littke, R., Robert, P. (1998). Organic Petrology: A New Handbook Incorporation some Revised Parts of Stach's Textbook of Coal Petrology. Gebrüder Borntraeger, Berlin.

Thury, M., A. Gautschi, M. Mazurek, W. Müller, H. Naef, F. Pearson, S. Vomvoris, and W. Wilson, (1994). Geology and hydrogeology of the crystalline basement of Northern Switzerland: Nagra Tech. Ber. NTB 93-01, p. 93-01.

Tyson, R.V. (1995). Sedimentary Organic Matter. Organic Facies and Palynofacies.

Veron, J. (2005). The Alpine Molasse Basin – Review of Petroleum Geology and Remaining Potential. Bull. Angew. Geol., 10, 75-86.

Vollmayr, T., Wendt, A. (1987). Die Erdgasbohrung Entlebuch 1, ein Tiefenaufschluss am Alpennordrand. Bulletin der Vereinigung Schweiz. Petroleum-Geologen und -Ingenieure, 53, 67-79.

Wehner, H., Kuckelkorn, K. (1995). Zur Herkunft der Erdöle im nördlichen Alpen-Karpatenvorland. Erdöl, Erdgas, Kohle 111, 508e514.

Wolf, M., Hagemann. W. H., Haverkamp, S., Linnenberg, W. (1988). Kohlenpetrographie und - chemie. In: Matter, A. et al.: Sondierbohrung Weiach Geologic - Nagra Technischer Bericht NTB 86-01, pp. 231-256. Nagra, Baden.

Zdravkov, A., Bechtel, A., Sachsenhofer, R.F., Kortenski, J. (2017). Palaeoenvironmental implications of coal formation in Dobrudzha Basin, Bulgaria: Insights from organic petrological and geochemical properties. Int. J. Coal Geol., 180, 1-17.

Ziegler, P.A., Schumacher, M.E., Dezes, P., van Wees, J.D., Cloetingh, S. (2006). Post-Variscan evolution of the lithosphere in the area of the European Cenozoic Rift System. In: Gee, D.G., Stephenson, R.A. (eds): European lithospheric dynamics. Geological Society, London, Memoirs, 32, 97-112.

10 Publication III

The Toarcian Posidonia Shale at Salem (North Alpine Foreland Basin; South Germany): Hydrocarbon potential and paleogeography

Stephen Ajuaba[1, *], Reinhard F. Sachsenhofer[1], Francesca Galasso[2,3], Thorsten U. Garlichs[4], Doris Gross[1], Elke Schneebeli-Hermann[2], David Misch[1], Jonathan E. Oriabure[1]

[1] Lehrstuhl Erdölgeologie, Montanuniversitaet Leoben, Peter-Tunner-Strasse 5, 8700 Leoben, Austria

[2] Paläontologisches Institut und Museum, Universität Zürich, Karl-Schmid-Strasse 4, CH-8001 Zürich, Switzerland

[3] Senckenberg Forschungsinstitut und Naturmuseum Frankfurt, Senckenberganlage 25, 60325 Frankfurt am Main, Germany

[4] Wintershall Dea Norge AS, Jåttåflaten 27, 4020 Stavanger, PO Box 230 Sentrum, 4001 Stavanger, Norway

International Journal of Earth Sciences
Submitted

*corresponding author. E-mail address: stephen.ajuaba@unileoben.ac.at

Stephen Ajuaba (orcid.org/0000-0001-5748-7284)
Reinhard F. Sachsenhofer (orcid.org/0000-0002-6616-5583)
Francesca Galasso (orcid.org/0000-0001-5391-7902)
Thorsten U. Garlichs
Doris Gross (orcid.org/0000-0001-7442-5093)
Elke Schneebeli-Hermann (orcid.org/0000-0002-1552-4785)
David Misch (orcid.org/ 0000-0002-4656-7956)
Jonathan E. Oriabure

Abstract

The Posidonia Shale in the basement of the North Alpine Foreland Basin of southwestern Germany represents an important archive for environmental changes during the Toarcian oceanic anoxic event (T-OAE) and the associated carbon isotope excursion (T-CIE), and an important hydrocarbon source rock. In the Salem borehole, the Posidonia Shale is ~10 m thick. The lower 7.5 m (1763.5-1756.0 m) and the uppermost part of the underlying Amaltheenton Shale were cored and studied using a total of 62 samples. Rock–Eval, palynological, maceral, biomarker and carbon isotope data were determined to assess variations in environmental conditions and to quantify the source rock potential. In contrast to other Toarcian sections, TOC contents are high in sediments deposited during the T-CIE, but reach a peak in post-CIE sediments. Biomarker ratios suggest that this reflects strong oxygen-depletion during the T-CIE (*elegantulum* to lower *elegans* subzones), but also during the *falciferum* Subzone, which is also reflected by a prolonged dinoflagellate cyst blackout. While sediments of the *tenuicostatum* Zone to the *elegans* Subzone are thinner than in neighbouring sections (e.g., Dotternhausen), sediments of the *falciferum* Subzone are unusually thick, suggesting that increased subsidence might have contributed to anoxia. The T-CIE interval is comparibly very thin. $\delta^{13}C$ values of *n*-alkanes show that the maximum negative isotope shift predates the strongest basin restriction during the T-CIE and that the carbon isotope shift is recorded earlier for aquatic than for terrigenous organisms. In Salem, the Posidonia Shale is thermally mature and highly oil-prone. The residual source petroleum potential is about 0.8 tHC/m².

Keywords:
Biomarkers, stable carbon isotopes, palynology, Toarcian oceanic anoxic event, carbon isotope excursion, Lower Jurassic

Author contributions

SA, RFS and DG contributed to the study conception and design. SA performed the analysis and interpreted the data. Palynology analysis and interpretation was done by FG and ESH. RFS, FG, ESH, TUG, DG, DM and JO helped interpret the entire data. SA wrote the first draft of the manuscript and all authors commented on previous versions. All authors read and approved the final manuscript.

Acknowledgments

The authors thank Wintershall Dea for providing access to the core and for the permission to publish the data. The authors thank Boris Jammernegg for scanning the core.

Funding

Availability of data and materials

All data are published in the paper. Rock samples are stored at Montanuniversität Leoben and palynological slides are hosted at the Paläontologisches Institut und Museum, Universität Zürich.

Code availability Not applicable.

Declarations

Conflict of interest All authors declare that they have no conflict of interest.

Ethics approval Not applicable

Consent to participate Not applicable

Consent for publication Not applicable

Introduction

Oceanic anoxic events are important features of the Mesozoic Era (e.g., Schlanger and Jenkyns 1976; Jenkyns 2010). The Toarcian oceanic anoxic event (T-OAE; ~183 Ma) is the oldest of these Mesozoic events (Jenkyns 1985, 1988). It is characterized by global climate change (Ruebsam and Schwark 2021 and references therein), mass extinction of marine biota (e.g., Harries and Little 1999; Pálfy and Smith 2000; Dera et al. 2010; Caruthers et al. 2013), and a prominent negative carbon isotope shift (3-8‰) referred to as the Toarcian Carbon Isotope Excursion (T-CIE) (e.g., Hesselbo et al. 2000; 2007).

While records of the T-OAE are found globally (e.g., Jenkyns et al. 2001; Chen et al. 2023), the most organic-rich sediments related to the T-OAE occur in the epicontinental Central European Basin (CEB) of Britain, Germany, Switzerland, and France (Fig. 1a; e.g., Küspert 1982; Littke et al. 1991a,b; Baudin 1995; Jenkyns and Clayton 1997; Röhl et al. 2001). In Germany and Switzerland the Toarcian black shales are called Posidonia Shale.

In southern Germany and Switzerland, the Posidonia Shale has been described in detail in the Swabian and Franconian Alb (e.g., Riegraf et al. 1984; Riegraf 1985; Röhl et al. 2001; Röhl and Schmid-Röhl 2005; Hougård et al. 2021) and the Swiss Jura (Kuhn and Etter 1994; Montero-Serrano et al. 2015; Fantasia et al. 2019) (Fig. 1b). Here, the oil-prone Toarcian sediments are thermally immature or marginal mature (Littke et al. 1991b), which is favorable for applying organic parameters (e.g., biomarkers) to reconstruct the depositional environment.

The most comprehensive data in the area are available for the Dotternhausen and Dormettingen) sections (Fig. 1a, b). The latter being ca. 2 km NW of Dotternhausen have been studied in great detail using different sedimentological, paleontological, and geochemical techniques (e.g., Riegraf 1985; Schouten et al. 2000; Röhl et al. 2001; Frimmel et al. 2004; Schwark and Frimmel 2004; Röhl and Schmid-Röhl 2005, van de Schootbrugge et al. 2005; Bour et al. 2007; Mattioli et al. 2008; Suan et al. 2008, 2015; Wang et al. 2020, 2021; Galasso et al. 2021, 2022; Ajuaba et al. 2022; Reubsam et al. 2023).

The present study is based on core material from the “Salem a” borehole (in the following called Salem borehole), drilled in the German part of the North Alpine Foreland Basin about 65 km southeast of Dormettingen. In this borehole, Toarcian black shales have been noted between 1753 and 1763 m depth and are overlain by younger Jurassic and Cenozoic sediments. Based on the considerable depth, it is likely that the Posidonia Shale is thermally

mature (cf., Wehner and Kuckelkorn 1985). Moreover, its location close to Vindelician High (e.g., Riegraf 1985; Meyer and Schmidt-Kahler 1996) suggests deposition at shallower water depth than at Dormettingen.

Consequently, the examination of the Salem drill core presents an opportunity to explore variations in sedimentary facies between the proximal Salem location and the more distal Dormettingen/Dotternhausen sites. Additionally, it provides a means to investigate the impact of increasing thermal maturity on organic facies characteristics, a particularly pertinent aspect when utilizing biomarker data for establishing connections between oil and its source.

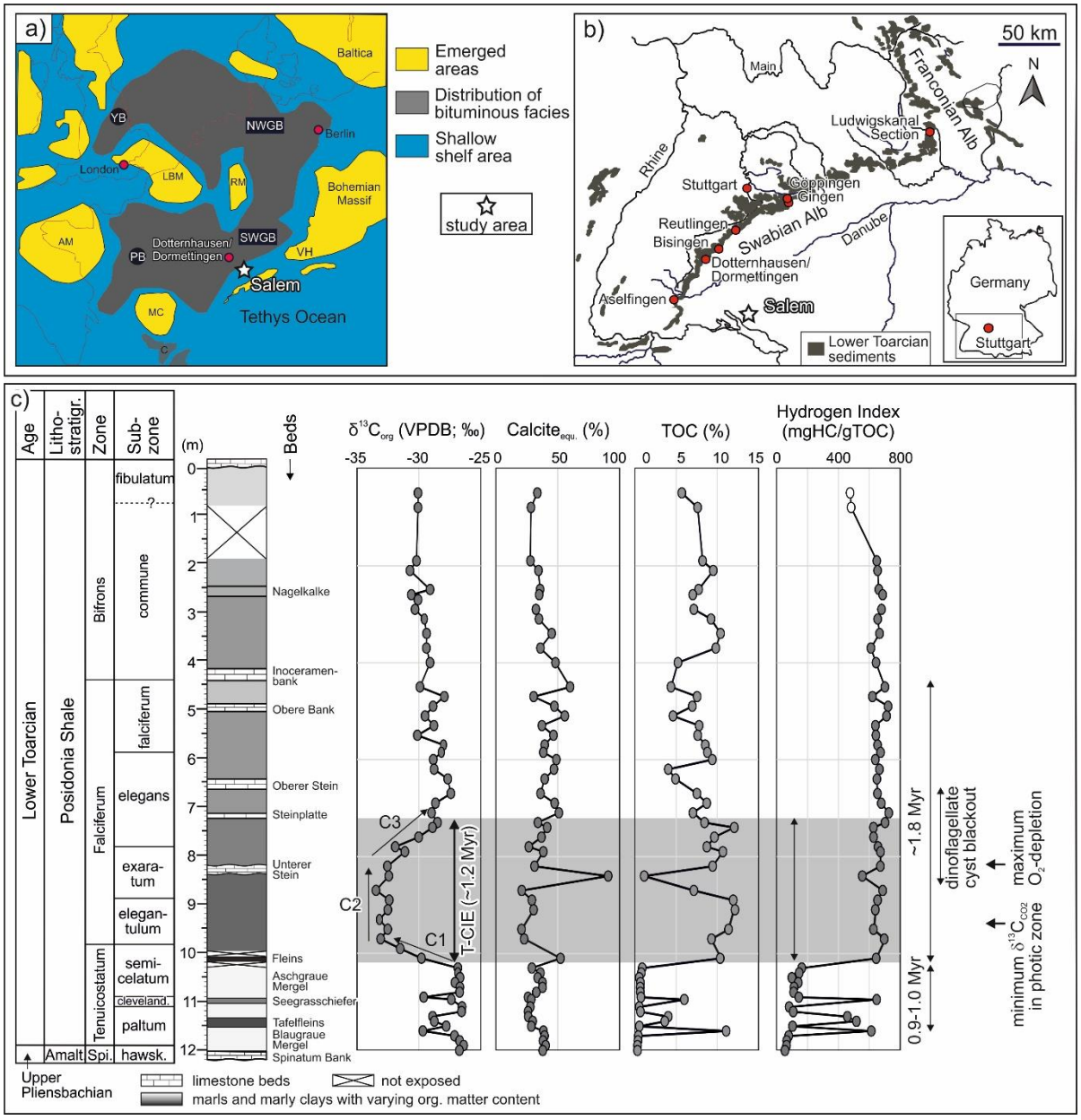

Fig. 1 a Early Toarcian paleogeography of the epicontinental Central European Basin with the distribution of bituminous black shale across various sub-basins (SWGB: SW German Basin, NWGB: NW German Basin, YB: Yorkshire Basin and PB: Paris Basin); **b** outcrops of the lower Toarcian sediments in southwestern Germany. The white star

indicates the study area (Salem). Maps are modified after Ziegler (1982), Röhl et al. (2001), and Galasso et al. (2021). **c** Stratigraphy, isotope data and bulk geochemical data of the Dormettingen section (after Galasso et al. 2021; 2022 and Ajuaba et al. 2022). The duration of the *tenuicostatum* and *falciferum* zones and of the T-CIE follows Ruebsam et al. (2023). HI values of weathered samples near the top of the succession are shown with open symbols

Geological Setting

Sediments with very high TOC contents were deposited during early Toarcian time in the epicontinental CEB (Fig. 1a; Ziegler 1982; 1988). Black shale deposition in the Yorkshire Basin (Hesselbo et al. 2000; Bowden et al. 2006; Kemp et al. 2011; French et al. 2014), the Northwest German Basin (e.g., Littke et al. 1991), the Southwest German Basin, and the Paris Basin (Hollander et al. 1991, Hermoso et al. 2009; 2014; Song et al. 2014) was controlled by strong oxygen-depletion due to climate change (T-OAE; Jenkyns 1985; 1988), water column stratification (e.g. Küspert 1982; Röhl et al. 2021; Schwark and Frimmel 2004, Hermoso et al. 2013; Song et al. 2015; 2017), and eustatic sea level variations (see Ruebsam and Schwark 2021 for a review).

The studied drill core is from the Southwest German Basin (SWGB). The Dotternhausen and Dormettingen quarries provide key sections for this part of the CEB. Some key parameters are displayed for the Dormettingen section in Fig. 1c. At Dormettingen, the lower Toarcian sediments overlie bioturbated marls assigned to the Pliensbachian Amaltheenton Formation (*Pleuroceras spinatum* Zone) intercalated with limestone bed ("Spinatum-Bank" or "Costaten-Kalk"), tens of cm thick. The Posidonia Shale Formation, about 12 m thick, follows above the Amaltheenton Formation without indication of a sedimentary gap (Galasso et al. 2021) and includes the *Dactylioceras tenuicostatum* zone, the *Harpoceras falciferum* and *Hildoceras bifrons* zones (Riegraf 1985; Röhl et al. 2001; Röhl and Schmid-Röhl 2005). Light-grey bioturbated marls and three several-cm-thick black shale layers (Tafelfleins, Seegrasschiefer, and Fleins) occur in the *tenuicostatum* Zone. The Fleins forms the base of massive black shales deposit representing the T-OAE (uppermost *tenuicostatum, falciferum* and *bifrons* zones; Fig. 1c). Prominent limestone beds are intercalated into the black shale succession and are labelled from base to top: Unterer Stein (20-30 cm thick; *exaratum* Subzone), Steinplatte (~ 10 cm thick; *elegans* Subzone), Oberer Stein (~ 20 cm thick; *elegans* Subzone), Obere Bank (~ 10 cm thick; *falciferum* Subzone) and Inoceramenbank (~ 10 cm thick; boundary between *falciferum and bifrons* zones). The Toarcian carbon isotope excursion (T-CIE; ~183 million years [Myr]) extends from the Fleins Bed to the Steinplatte

and spans an interval of 2.8 m at Dormettingen/Dotternhausen (Suan et al. 2008; Galasso et al. 2021; Ajuaba et al. 2022).

Using an astronomical timescale, Ruebsam et al. (2023) estimated the duration of the *tenuicostatum* and *falciferum* zones as 0.9-1.0 and 1.8 Myr, respectively (cf. Fig. 1c). The duration of the T-CIE (*elegantulum* to lower *elegans* Subzones of the *falciferum* Zone) has been estimated as 0.9 (Suan et al. 2008) or 1.2 Myr (Ruebsam et al. 2023). The sources of the carbon that caused the T-CIE are discussed controversially and may include CO_2 or methane emitted from the Karoo-Ferrar Large Igneous Province (e.g., Pálfy and Smith 2000; McElwain et al. 2005; Svensen et al. 2007) or methane emissions from marine gas hydrates (Hesselbo et al. 2000; Kemp et al. 2005), wetlands (Them et al. 2017) and permafrost areas (Ruebsam et al. 2019).

The Dotternhausen and Dormettingen sections occupied central positions within the SWGB (e.g., Riegraf et al. 1985). In contrast, the Salem drill site is located near the southeastern basin margin, where the SWGB was separated from the Tethys Ocean by a series of islands forming the continuation of the Vindelician High (Fig. 1a).

Samples and analytical methods

Samples

This present study is based on 62 samples collected from a nine-meter-long drill core from the Salem borehole drilled by Wintershall in the 1970s. The samples are from the Upper Pliensbachian Amaltheenton Formation (8 samples) and the Lower Toarcian Posidonia Shale (54 samples) (Fig. 2). Samples were collected in varying intervals ranging from 1 to 63 cm. In order to obtain a high resolution record of the T-CIE, the sampling interval was especially small in this interval.

Analytical methods

Geochemical and maceral analyses were performed at the laboratories of the Chair Petroleum Geology at Montanuniversitaet Leoben. Computed tomography (CT) scans were performed at the Chair Reservoir Engineering, Montanuniversitaet Leoben. Palynological investigations were done at the Paläontologisches Institut und Museum, Universität Zürich.

The upper 8 m of the drill core were scanned with Siemens Somatom Definition AS, a medical CT scanner at a resolution of 0.3×0.3 mm in the xy plane and 0.6 mm in the z direction, to image density contrast and to detect pyrite, shells, belemnites, etc.

All samples were powdered and analyzed for total carbon (TC; %), total sulfur (TS; %) and total organic carbon (TOC; %) using an Eltra Helios CS elemental analyzer. TOC contents were measured on samples pre-treated with concentrated phosphoric acid. Calcite equivalent percentages were derived using the equation $calcite_{equiv.}$ = 8.334 x (TC-TOC).

A "Rock-Eval 6" instrument was applied to determine S_1, S_2, [mgHC/g rock] and T_{max} [°C]. Hydrocarbons volatized at 300 °C form the S_1 peak, while hydrocarbons generated during gradual heating from 300 to 650 °C form the S_2 peak. T_{max} is the temperature of maximum hydrocarbon generation. Calculated parameters include hydrogen index (HI = 100×S_2/TOC), production index (PI = S_1/[S_1+S_2]) and genetic potential (GP = S_1+S_2) (Espitalié et al. 1977).

Different subsets of these samples were selected based on their TOC content and their stratigraphic position for maceral, palynology, biomarker and stable carbon isotope analysis.

Semi-quantitative maceral analysis was performed on polished blocks using white and fluorescence light, a 50× oil immersion objective, and a Leica DM 4P microscope. Close to 1500 points were counted per sample and the results are normalized to 100% organic matter. This analysis was in accordance to the ICCP system (ICCP 1998, 2001; Pickel et al. 2017). Measurements of mean random vitrinite reflectance (%Rr) (Taylor et al. 1998) was performed in non-polarized light with a wavelength of 546 nm. The microscope was calibrated with a synthetic reflectance standard (N-LASF46A; Rr: 1.311%).

Fourteen samples were selected to determine the origin and preservation state of particulate organic matter. About 15 g of dry sediment, was cleaned, crushed, and subsequently treated with concentrated HCl and HCF, followed by modified multi-step oxidation as described by Traverse (2007). After mineral dissolution and after oxidation, the residues were sieved over a 11-µm mesh screen. For palynofacies analysis, organic matter particles were counted in unoxidised kerogen slides until a minimum of 400 counts per sample was reached. Particle

counts include marine particles (i.e. acritarchs, prasinophytes, amorphous organic matter [AOM], foraminiferal test linings and dinoflagellate cysts) and terrestrial particles (i.e. translucent and opaque phytoclasts, cuticles, membranes, spores and bisaccate pollen grains) (Tyson 1995; Batten 1996). Subsequently, for a detailed palynological investigation, all samples were further treated (with a stepped process of oxidation) using concentrated HNO_3, and ultrasonic vibration. This treatment was done in order to increase the palynomorph concentration, remove the remaining inorganic residue (e.g. pyrite), and reduce the AOM density.

Thirty samples were selected for biomarker analysis. 5 to 10 g of the sample material was extracted for about 1 hour at 75 °C and 100 bar using dichloromethane as solvent and a Dionex ASE 350 Accelerated Solvent Extractor. The extract was concentrated to ~0.5 ml using a Zymark TurboVap 500 closed cell concentrator. Afterwards, asphalthenes were precipitated from a hexane:dichloromethane solution (80:1 according to volume) and separated by centrifugation. The hexane-soluble fractions were further separated into heterocompounds (NSO), saturated and aromatic hydrocarbons by medium-pressure liquid chromatography using a Köhnen-Willsch MPLC instrument (Radke et al. 1980). Proportionate amount of internal standards (*n*-tetracosane or squalene for aliphatics and 1,1´-binaphthyl for aromatics) were added to each sample prior to measurement.

The *n*-alkanes and isoprenoids in the saturated hydrocarbon fractions were analyzed using a gas chromatograph (Trace GC-Ultra) with a flame ionization detector (GC-FID). The GC was equipped with a 50 m HP-PONA capillary column (inner diameter [i.d] 0.2 mm, 0.50 µm film thickness). After splitless sample injection at 270 °C, the oven temperature was increased from 70 to 310 °C followed by 35 min isothermal period.

Specific biomarker molecules in the saturated and aromatic fractions were analyzed by gas chromatography-mass spectrometry (GC-MS) using a Thermo Scientific Trace GC-Ultra equipped with a 60 m TG/DB-5MS fused silica capillary column (i.d. 0.25 mm; 0.25 µm film thickness) coupled to ThermoFisher ISQ mass spectrometer. The GC oven temperature was initially programed from 40 °C/min, held for 2 minutes and ramped to 310°C with 4°C/min followed by an isothermal period of 40 min. Sample was injected in split mode with a split ratio of 20 at 260 °C using helium as carrier gas. The spectrometer was operated in the EI (electron ionization) mode with a mass-to-charge ratio (m/z) scan range from m/z 50 to m/z 650 (0.7 s total scan time). For the determination of methylsterane concentrations, further investigating aliphatic fractions of selected samples using a Trace^{TM} 1300 GC (ThermoFisher)

equipped with a 60 m TG-5MS fused silica capillary column (i.e. 0.25 mm; 0.25 µm film thickness)attached to a ThermoFisher TSQ9000 triple quadrupole GC-MS/MS. The oven was set to hold 40 °C for 2 minutes and then heated to 310 °C with 4 °C/min, followed by a constant temperature period of 40 min. The sample was injected splitless with an injector temperature of 310 °C. Methylsterane isomers were detected using selected reaction monitoring (SRM) through the application of different parent-to-daughter ion transitions (*m/z* 386–231, 400–231, 414–231, 414–98) to obtained C_{28} to C_{30} methylsteranes, methyldiasteranes, diamethylsteranes and dinosteranes.

The raw data were processed using Xcalibur and Chromeleon data systems. The respective retention time for each compound within the mass spectra or total ion current (TIC) were used for their identification in addition to comparing the mass spectra with published data. Correction factors were appropriately applied for mass chromatograms to correct for fragment ions while for TIC chromatograms, absolute concentrations were determined from the peak areas of the saturated and aromatic fractions in relation to their internal standards per sample.

A semi-quantitative calculation of the target compounds was conducted based on results of total ion current (TIC) chromatograms. Absolute concentrations were determined for the methylsteranes using their TIC chromatograms (also detectable using *m/z* 231) set in relation to an internal standard (5β(H)-Cholane) per sample.

For the bulk carbon isotope ($\delta^{13}C_{org}$) analysis, 58 powdered samples were pre-treated step-wise with 6 N HCl for almost 12 hours to remove all carbonates. Distilled water was used at each step to remove the added acid. The samples were later oven dried for 24 hours at 40 °C. 6-8 mg per sample was weighed into tin foil boats and measured by combustion in excess of oxygen at 1020 °C using an elemental analyzer (Flash EA 1112). The CO_2 by-product is separated by column chromatography and analysed online by the DELTA V ir-MS, mentioned above. The carbon isotopic ratio ($^{13}C/^{12}C$) of the sample CO_2 are compared with that of the CO_2 reference gas and calibrated against PDB. Analytical reproducibility is in the range of 0.1 - 0.3‰.

To analyse the stable carbon isotope of *n*-alkanes and isoprenoids, the *n*-alkanes were separated from the *iso*-alkanes within the saturated hydrocarbon fraction using an improved 5 Å molecular sieve method (Grice et al. 2008). Measurement of the stable carbon isotope ratio was performed using a Trace GC-Ultra gas chromatograph attached to the ThermoFisher Delta-V isotope ratio mass spectrometer (IRMS) via a combustion and high temperature reduction interface (GC Isolink, ThermoFisher). The GC column has been described above,

however the oven temperature was set to 70 °C for 2 min followed by a ramp from 4 °C/min to 300 °C and isothermal period of 15 min. A CO_2 reference gas was used for calibration and injected before and after each analysis. Isotope composition per sample was measured at least twice and their mean values reported in the δ notation in permil (‰) relative to the V-PDB standard. The analytical reproducibility per sample is below 0.3‰.

Results

According to well logs, the lower Toarcian Posidonia Shale was drilled at Salem between 1753 and 1763 m depth (below surface). The present study is based on a drill core representing the depth interval from 1756 to 1765 m. Hence, no analytical data are available for the uppermost 3 m of the Posidonia Shale (1753-1756 m).

Bulk organic carbon isotope data ($\delta^{13}C_{org}$)

Bulk organic carbon isotope ratios are an important correlation tool for Pliensbachian and Toarcian sediments. Hence, these ratios are presented first to provide a stratigraphic frame. $\delta^{13}C_{org}$ values in the studied interval vary between -25.7 and -33.1‰. Overall, they show a gradual upward decrease from ~ -26 to -29‰. Significantly lower ratios (-28.5 to -33.1‰) representing the T-CIE (*elegantulum* to lower *elegans* Subzones; Riegraf et al. 1984; Suan et al. 2008; 2015; Ruebsam and Al-Husseini 2020) are observed in a 0.75 m thick interval (1762.25-1761.50 m).

Lithology and Stratigraphy

Sediments below the T-CIE belong to the upper Pliensbachian Amaltheenton Formation and the lower part of the Toarcian Posidonia Shale. The uppermost part of the Amaltheenton Formation is composed of light- to dark-grey bioturbated marls and two limestone layers ("Spinatum Bank"). The "Spinatum Bank" is overlain by bioturbated marls with low organic matter contents ("Blaugraue Mergel") and two organic matter-rich intervals, which are also partly bioturbated (Tafelfleins, Seegrasschiefer). Organic-lean sediments with some shell remains ("Aschgraue Mergel") follow above the Seegrasschiefer. Bituminous sediments, about 20 cm thick, occur immediately below the T-CIE and are correlated with the "Fleins"

Bed at the base of the main black shale succession. Belemnite remains are present in the pre-CIE sediments, albeit in low quantities.

The Pliensbachian/Toarcian boundary (*spinatum/tenuicostatum subzones*) is located just above the Spinatum Bank and significantly below the first black shale layer (e.g., Riegraf 1985). For the Salem locality, we drew the boundary ~10 cm above the Spinatum Bank (1763.50 m).

Black Shales within the T-CIE (1762.25-1761.50 m) show a distinct lamination. A nodular limestone bed "Unterer Stein" is present in the middle part of the T-CIE (~1761.85 m). Black shales below the limestone marker contain a thin coaly layer and very low carbonate contents (average: 18 %). Carbonate contents above the limestone marker are higher (average 36 %). Some shells are present in the uppermost part of the T-CIE, but belemnite remains have not been observed (Fig. 2).

The sediments above the T-CIE are dominated by black shales with relatively high carbonate contents (average 44 wt.%). Two distinct limestone layers are present. The layer at 1761.83 represents the "Oberer Stein" (~1761.1 m), which is the best marker horizon in the SWGB (upper part of the *elegans* Subzone; Riegraf 1985). The layer at ~1756.9 m is the "Obere Bank", another wide-spread marker bed (upper part of the *falciferum* Subzone). Light bioturbation features are observed above the "Oberer Stein" (~1761.1 m), at about 1757.9 m and above the "Obere Bank" (~1756.5 m). In contrast, black shales with distinct lamination, locally containing pyrite veins and nodules, prevail in the middle part of the succession (1761.0-1757.9 m). Belemnite remains are largely missing below 1760.6 m, but highly abundant in the uppermost part of the section above the "Obere Bank" (1756.5-1756.0 m, Fig. 2). High amounts of belemnite in the uppermost *falciferum* Subzone above the "Obere Bank" have also been described at Dotternhausen (Röhl and Schimid-Röhl 2005; Schimd-Röhl 2019). In the Dotternhausen/Dormettingen sites, another limestone marker known as the "Inoceramen Bed" occurs roughly 60 cm above the "Oberer Stein." However, in the Salem core, this marker is absent and likely lies just above the core's sampled interval. This suggests that the uncored segment within the Posidonia Shale Formation, which is correlated with the *bifrons* Zone, is at least 3 meters thick.

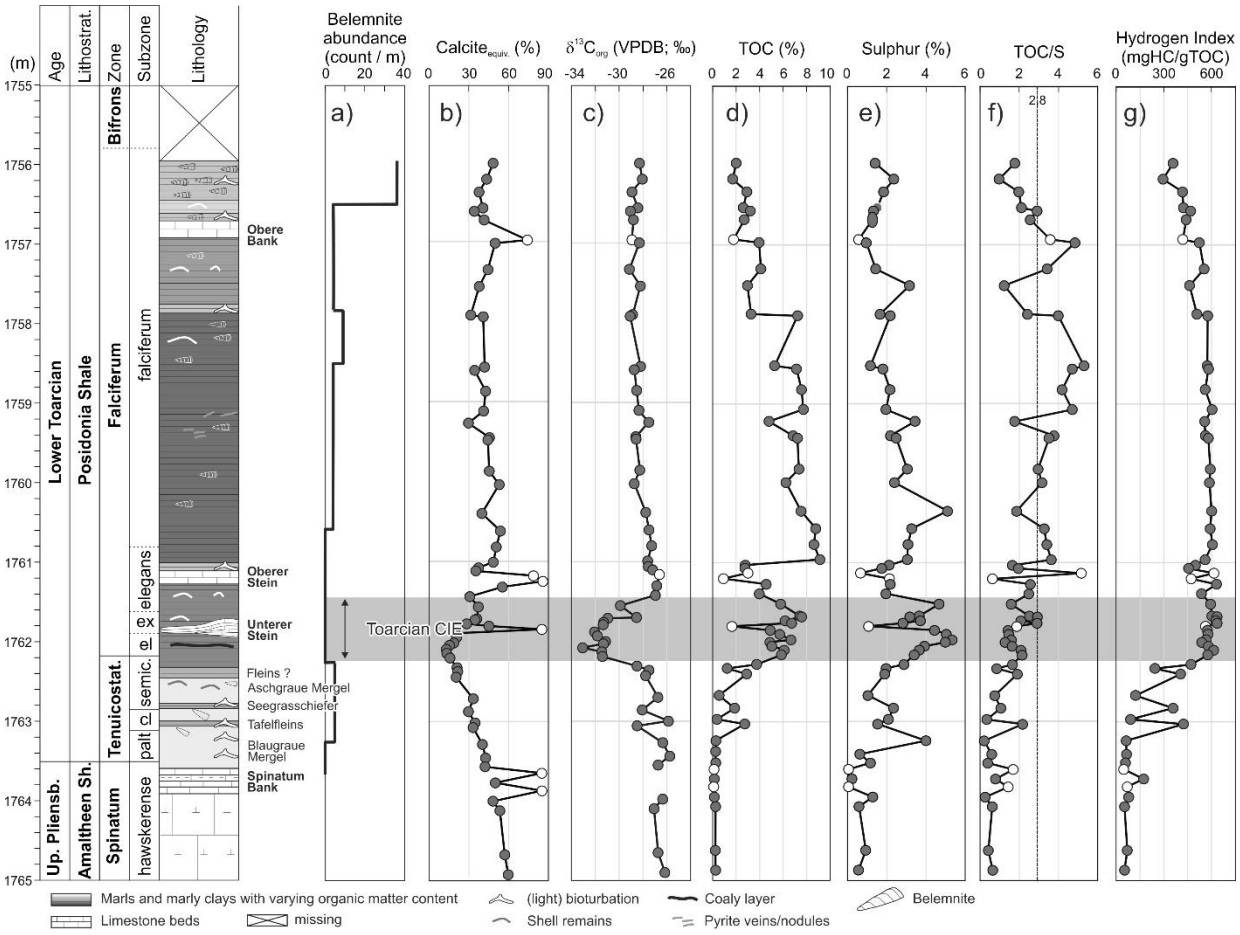

Fig. 2 Stratigraphic profile across the Salem drill core with ammonite zones; a) belemnite counts (obtained from CT scans; lowermost 1 m was not available for scanning), b) calcite equivalent percentage; c) bulk organic carbon isotope trend; d) total organic carbon (TOC); e) sulphur contents, f) TOC/S ratios, and g) hydrogen index. The subdivision of the Toarcian carbon isotope excursion (CIE) into phases C1–C3 follows Suan et al. (2008). Open symbols represent data points from limestone samples

Bulk geochemistry

TOC, sulphur and Rock-Eval data are reported in this section (Fig. 2; Table 1). The TOC contents within the Amaltheenton Formation are very low (< 0.3 %), while sulphur contents are moderate (0.08-1.12 %). HI values are generally low (average 73 mgHC/gTOC).

Below the T-CIE, organic matter richness (0.26-3.68 % TOC), sulphur content (0.56-3.39 wt.%) and HI (59-470 mgHC/gTOC) vary strongly in the Posidonia Shale. High values are observed in the “Tafelfleins”, the “Seegrasschiefer” and the black shale layer underlying the T-CIE.

As expected, the black shales within the T-CIE interval exhibit elevated TOC levels ranging from 4.78% to 7.44%, along with sulfur contents ranging from 2.41% to 4.50%. In contrast, the "Unterer Stein" limestone displays notably lower TOC and sulfur contents. The most substantial TOC concentrations, exceeding 7%, are found above the "Unterer Stein," while the highest sulfur contents, surpassing 4%, are observed below the "Unterer Stein".. HI values are high (538-634 mgHC/gTOC) in all samples.

The black shales above the T-CIE show varying TOC contents which allow a subdivision of the sediments into various units. The succession starts with an interval (unit I: 1761.50-1761.00 m) with moderate TOC contents (2.73-4.48 wt.%) and HI values varying from 455 to 630 mgHC/gTOC. Sulfur contents are relatively uniform (1.50-1.87 %). The overlying unit II (1761.99-1757.92 m) contains very high TOC contents (4.71-8.95 %) with a subtle upward decreasing trend, uniformly high HI values (557-660 mgHC/gTOC) and partly very high sulphur contents (1.02-4.31). TOC contents are only moderately high (2.92-4.04 %) in unit III (1757.9-1757.0 m), while HI (462-523 mgHC/gTOC) and sulphur contents (0.84-2.69 %) are also reduced. The uppermost interval (1756.96-1755.0 m; unit IV) is characterized by relatively low TOC contents (1.68-3.16 %), HI values (296-464 mgHC/gTOC) and sulphur contents ranging from 1.11 to 2.02 % and are lower than in unit III. The limestone marker beds in unit I (Oberer Stein) and at the base of unit IV (Obere Bank) contain low TOC and sulphur contents, but HI values are similar to those in adjacent black shales.

Across the entire study section, TOC/S ratios vary significantly, but show a general upward increase from the base of the Posidonia Shale (~1.0) to a depth of 1757.92 m (~4.5). Above a minimum (1.02) at 1757.54 m, TOC/S ratios decrease upwards between 1757.0 and 1756.0 m from ~4.7 to 1.0.

T_{max} values of samples with S_2 > 1.0 mgHC/grock vary from 431 to 439 °C (average 436 °C) (Table 1). The average PI for black shales (TOC >1.0 wt.%) and organic-lean sediments (TOC <1.0 wt.%) is 0.08 and 0.23, respectively.

Table 1. Bulk geochemical parameters for samples from the Salem drill core. GP-generation potential

Sample ID [m]	Calcite [wt%]	TOC [wt%]	Sulphur [wt%]	TOC/S [--]	S_1 [mg HC/g rock]	S_2 [mg HC/g rock]	HI [mg HC/ g TOC]	T_{max} [°C]	PI [--]	GP [mg HC/ g rock]	$\delta^{13}C_{org}$ [VPDB;‰]	
1756.00	49.74	1.98	1.22	1.62	0.44	7.10	358	435	0.06	7.54	-28.28	
1756.20	44.91	1.68	2.02	0.83	0.35	4.95	295	434	0.07	5.30	-28.05	
1756.36	39.09	2.88	1.58	1.82	0.74	12.01	417	435	0.06	12.75	-28.92	
1756.56	42.14	2.56	1.31	1.96	0.74	10.83	423	434	0.06	11.56	-28.42	
1756.60	35.59	3.16	1.15	2.74	0.72	14.76	468	438	0.05	15.48	-29.04	
1756.71	42.97	2.65	1.11	2.40	0.90	11.68	440	436	0.07	12.57	-28.79	
1756.96	75.58	1.76	0.52	3.41	0.75	7.38	419	432	0.09	8.12	-28.92	
1757.00	51.24	3.89	0.84	4.65	1.85	20.38	523	435	0.08	22.23	-28.30	
1757.33	45.84	4.04	1.24	3.25	1.44	22.32	553	436	0.06	23.76	-29.13	
1757.54	39.30	2.92	2.69	1.09	1.35	13.52	462	436	0.09	14.87	-28.21	
1757.90	32.91	3.22	1.43	2.26	1.23	16.39	508	434	0.07	17.62	-28.85	
1757.92	42.34	7.10	1.87	3.81	3.78	40.84	575	438	0.08	44.62	-29.06	
1758.55	43.34	5.18	1.02	5.10	4.00	29.68	573	438	0.12	33.68	-28.20	
1758.59	35.79	7.01	1.55	4.51	3.37	40.65	580	439	0.08	44.02	-28.72	
1758.85	44.12	7.42	1.85	4.00	3.93	41.57	660	437	0.09	45.50	-28.52	Post-CIE
1759.10	42.60	7.58	1.68	4.51	4.24	45.71	603	436	0.08	49.95	-28.34	
1759.25	31.16	4.71	2.93	1.61	2.53	26.23	557	437	0.09	28.76	-27.50	
1759.43	46.98	6.72	1.87	3.59	3.79	37.64	560	438	0.09	41.43	-28.59	
1759.46	45.81	7.09	2.12	3.34	3.75	41.08	579	438	0.08	44.83	-28.57	
1759.85	46.86	7.21	2.59	2.79	4.39	42.68	592	437	0.09	47.07	-28.26	
1760.02	54.34	6.12	2.05	2.99	4.02	35.90	586	437	0.10	39.92	-28.72	
1760.38	41.24	7.39	4.31	1.71	3.85	44.33	600	439	0.08	48.18	-27.76	
1760.60	55.25	8.61	2.78	3.10	5.50	50.88	591	437	0.10	56.38	-27.49	
1760.80	52.23	8.46	2.62	3.23	5.24	51.16	605	436	0.09	56.40	-27.26	
1760.99	49.86	8.95	2.59	3.45	5.22	50.01	559	438	0.09	55.23	-27.61	
1761.06	38.80	2.73	1.82	1.50	1.94	13.60	499	435	0.12	15.54	-27.55	
1761.10	36.76	2.70	1.50	1.80	1.90	12.28	455	438	0.13	14.18	-27.18	
1761.16	80.15	2.96	0.60	4.96	3.13	18.16	614	436	0.15	21.28	-26.61	
1761.23	87.25	0.91	1.83	0.50	0.76	4.29	471	433	0.15	5.05	*n.d*	
1761.30	56.76	4.48	1.87	2.40	3.91	28.26	630	437	0.12	32.17	-26.85	
1761.42	32.20	3.90	1.68	2.33	1.93	20.93	536	435	0.08	22.86	-26.96	
1761.55	38.57	5.68	3.95	1.44	2.99	33.74	594	436	0.08	36.73	-29.88	
1761.70	37.49	7.28	3.10	2.35	3.12	43.73	601	435	0.07	46.85	-28.54	
1761.71	36.19	7.44	2.70	2.75	3.13	47.19	634	437	0.06	50.32	-30.94	
1761.76	29.74	6.05	3.15	1.92	2.20	37.80	625	435	0.06	40.00	-31.29	
1761.79	46.54	6.59	2.41	2.74	3.23	41.84	634	435	0.07	45.07	-31.33	
1761.83	86.42	1.62	0.94	1.72	1.32	9.10	562	431	0.13	10.42	*n.d*	
1761.88	21.29	4.81	3.76	1.28	2.04	27.58	574	434	0.07	29.62	-32.05	T-CIE
1761.93	22.38	5.61	4.26	1.32	2.58	32.38	577	434	0.07	34.95	-31.82	
1762.00	20.10	6.53	4.50	1.45	2.60	36.94	565	436	0.07	39.53	-31.14	
1762.03	16.92	4.78	4.22	1.13	1.65	25.72	538	435	0.06	27.37	-31.30	
1762.08	14.46	4.95	3.33	1.49	1.74	28.64	579	435	0.06	30.37	-33.05	
1762.13	14.81	5.98	3.10	1.93	2.10	36.58	612	437	0.05	38.68	-31.45	
1762.19	17.28	5.74	2.89	1.99	2.02	33.02	575	433	0.06	35.03	-31.39	
1762.31	22.51	3.68	2.45	1.50	1.36	17.33	470	435	0.07	18.69	-28.49	
1762.36	23.07	1.21	1.69	0.72	0.46	2.95	244	436	0.13	3.41	-27.49	
1762.43	21.90	2.85	1.63	1.75	0.90	11.56	405	438	0.07	12.46	-27.78	
1762.70	34.87	0.55	0.91	0.61	0.12	0.68	123	434	0.15	0.80	-26.74	
1762.86	31.13	1.84	2.00	0.92	0.48	6.60	358	435	0.07	7.08	-28.06	
1763.00	36.10	0.37	1.79	0.21	0.07	0.34	92	431	0.17	0.41	-25.85	
1763.06	34.61	2.68	1.33	2.02	0.84	11.35	423	435	0.07	12.19	-28.48	
1763.27	41.68	0.28	3.39	0.08	0.03	0.18	64	430	0.14	0.21	-26.34	
1763.44	44.14	0.26	0.56	0.46	0.04	0.17	66	430	0.17	0.21	-25.74	Pre-CIE
1763.55	43.67	0.27	1.02	0.26	0.04	0.16	60	426	0.20	0.20	-26.73	
1763.63	86.44	0.12	0.08	1.54	0.06	0.06	49	426	0.50	0.12	*n.d*	
1763.75	51.00	0.15	0.23	0.65	0.11	0.26	173	428	0.28	0.37	*n.d*	
1763.83	87.25	0.09	0.08	1.13	0.01	0.03	33	424	0.25	0.04	*n.d*	
1763.85	86.51	0.11	0.08	1.29	0.06	0.08	71	426	0.44	0.14	*n.d*	
1763.98	49.67	0.15	1.12	0.13	0.03	0.12	80	428	0.20	0.15	-26.35	
1764.10	54.89	0.26	0.53	0.48	0.02	0.14	55	430	0.13	0.16	-27.07	
1764.65	58.58	0.24	0.82	0.30	0.06	0.17	70	428	0.26	0.23	-26.73	
1764.90	61.22	0.26	0.51	0.50	0.02	0.14	54	430	0.13	0.16	-26.16	

Palynofacies, Palynology and Organic Petrography

Palynofacies and palynological investigation have been performed on fourteen samples and semi-quantitative maceral analysis has been performed on eight sampls to obtain information on the origin of the organic matter.

Palynofacies

The particulate organic matter (POM) shows three phases (from base to top: A to C) with distinctive compositions (Fig. 3).

Phase A includes two organic-lean (1763.00; 1762.70) and one organic-rich sample (1762.43) from the Posidonia Shale below T-CIE (S09, S69, S08). The POM assemblage is marked by a conspicuous amount of opaque phytoclasts and a high occurrence of palynomorphs. Acritarchs, dinoflagellate cysts and amorphous organic matter (AOM) each contribute several percent to the POM (Table 2; Fig. 3).

Phase B is documented for samples from the T-CIE (1762.03; 1761.70) and the lower part of the post-CIE sediments (1761.10-1759.10 m). It is characterized by a strong increase in AOM. With the exception of the lowermost sample (1762.03), the terrestrial fraction is extremely reduced. However, opaque phytoclasts are recorded in similar relative abundances as in Phase A (~10%). Phase B marks the onset of a major marine turnover from a dinoflagellate-cyst- to prasinophytes-dominated assemblage.

Phase C occurs in the samples from the upper part of the core (1757.90-1756.20 m). Although a high percentage of AOM is still present (~ 65%), the terrestrial fraction rapidly rises again. While sporomorphs are fairly common and prasinophytes are frequent, dinoflagellate cysts are unrecovered.

As shown in Fig. 3, spore colour ranges from a TAI value of 3-/3 at the bottom of the borehole to values of 2+/3− at the top of the studied core falling within the mature stage of hydrocarbon generation (Taylor et al. 1998; Yule et al., 1998).

Table 2. Palynofacies percentages (in vol.%) for Toarcian sediments from the Salem drill core

Sample ID [m]	AOM	Acri-tarchs	Dinoflagellate cysts	Prasino-phytes	Foraminiferal test linings	Phytoclasts translucent	Phytoclasts opaque	Cuticles	Membranes	Bisaccate	Spore
			Marine			Terrigenous					
Post_CIE											
S62 1756.20	72.82	0.00	0.00	0.20	0.00	16.87	5.75	0.99	3.37	0.00	0.00
S63 1757.00	80.20	0.00	0.00	0.00	0.00	11.96	5.88	0.39	0.39	0.39	0.78
S02 1757.54	63.21	0.00	0.00	2.22	0.00	9.14	20.99	2.72	0.99	0.49	0.25
S64 1757.90	60.14	0.00	0.00	4.77	0.00	5.97	23.39	5.49	0.00	0.00	0.24
S65 1759.10	74.53	0.00	0.00	0.71	0.00	4.95	17.22	1.89	0.24	0.00	0.47
S04 1759.46	83.52	0.00	0.00	3.34	0.00	2.00	7.13	3.79	0.22	0.00	0.00
S66 1759.85	83.99	0.00	0.00	0.83	0.00	1.25	9.98	2.70	1.25	0.00	0.00
S67 1760.80	89.93	0.00	0.00	0.00	0.00	0.71	7.95	1.06	0.35	0.00	0.00
S061761.10	88.35	0.00	0.00	1.17	0.00	3.30	6.21	0.78	0.00	0.00	0.19
T-CIE											
S68 1761.70	88.06	0.00	0.00	0.29	0.00	1.29	8.35	1.73	0.14	0.14	0.00
S07 1762.03	78.31	0.00	0.00	0.00	0.20	10.64	5.42	2.01	0.60	0.80	2.01
Pre-CIE											
S08 1762.43	76.49	0.00	0.40	0.40	0.00	3.19	17.73	1.20	0.60	0.00	0.00
S69 1762.70	64.18	4.48	0.90	0.30	0.30	8.96	15.82	0.30	0.30	4.18	0.30
S09 1763.00	64.59	12.68	2.41	0.00	0.00	4.83	8.45	0.60	2.62	2.21	1.61

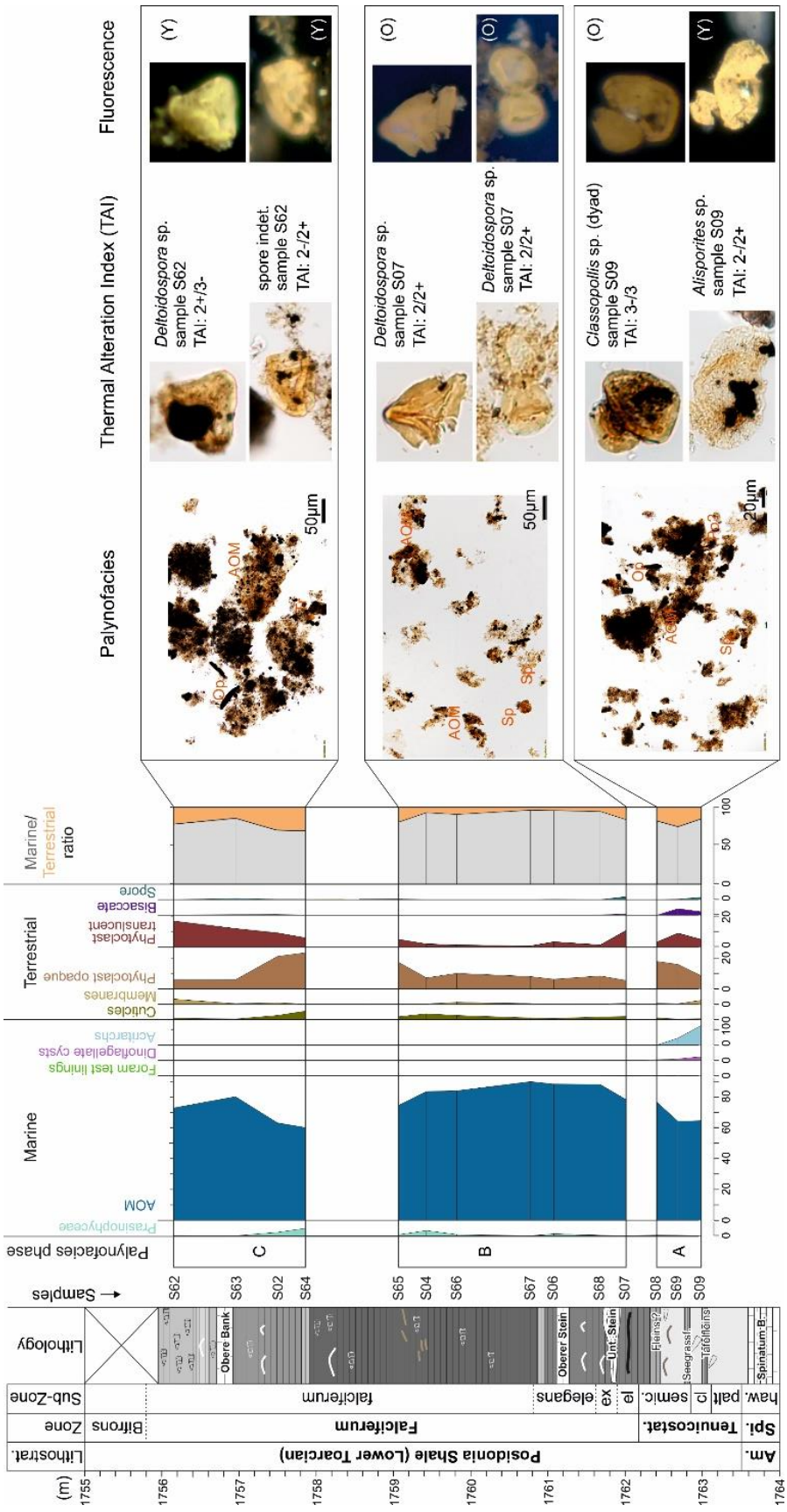

Fig. 3 Particulate organic matter and photomicrographs of the organic matter component, Thermal alteration index (TAI) and fluorescence colour. AOM - Amorphous Organic Matter, TR - translucent phytoclasts, Op - opaque phytoclasts, Sp - spore, Po pollen grain

Palynology

The Salem samples yielded few palynomorphs. The preservation is extremely variable, with palynomorphs reasonably well preserved in the lower part of the borehole, and poorly preserved in the rest of it. Thus, in some cases, sporomorphs were not assignable to any taxon. Consequently, the analysis of the relative abundances of palynomorphs and dinoflagellate cysts was impossible. The occurrence data are displayed in Fig. 4. Each dot represents a minimum of two occurrences for dinoflagellate cysts and sporomorphs.

In Phase A dinoflagellate cysts are highly common and diverse with *Luehndea spinosa, Nannoceratopsis* spp., *N. gracilis, N. senex,* and *Comparodinium punctatum*. The terrigenous fraction contains several pollen grains with *Classopollis* spp., *Alisporites* sp. and *Cerebropollenites* spp. The last occurrence datum (LOD) of *Luehndea spinosa* is recorded in sample S69 (1762.70 m) at the base of the thick black shale succession. A drastic reduction in dinoflagellate cysts taxonomic diversity occurs in sample S08, containing only a questionable *Mendicodinium spinosum perforatum* and *Mendicodinium* sp.

From sample S07 (1762.03 m; Phase B) onward, a major floral turnover was recorded, from a dinoflagellate-cyst-dominated assemblage to one with an elevated amount of prasinophytes (e.g., *Spheripollenites* spp. and *Tasmanaceae* spp.). Pollen grains and spores are reduced. Phase C samples do not show dinoflagellate cysts, but an elevated number of *Spheripollenites* sp. and prasinophytes are still documented.

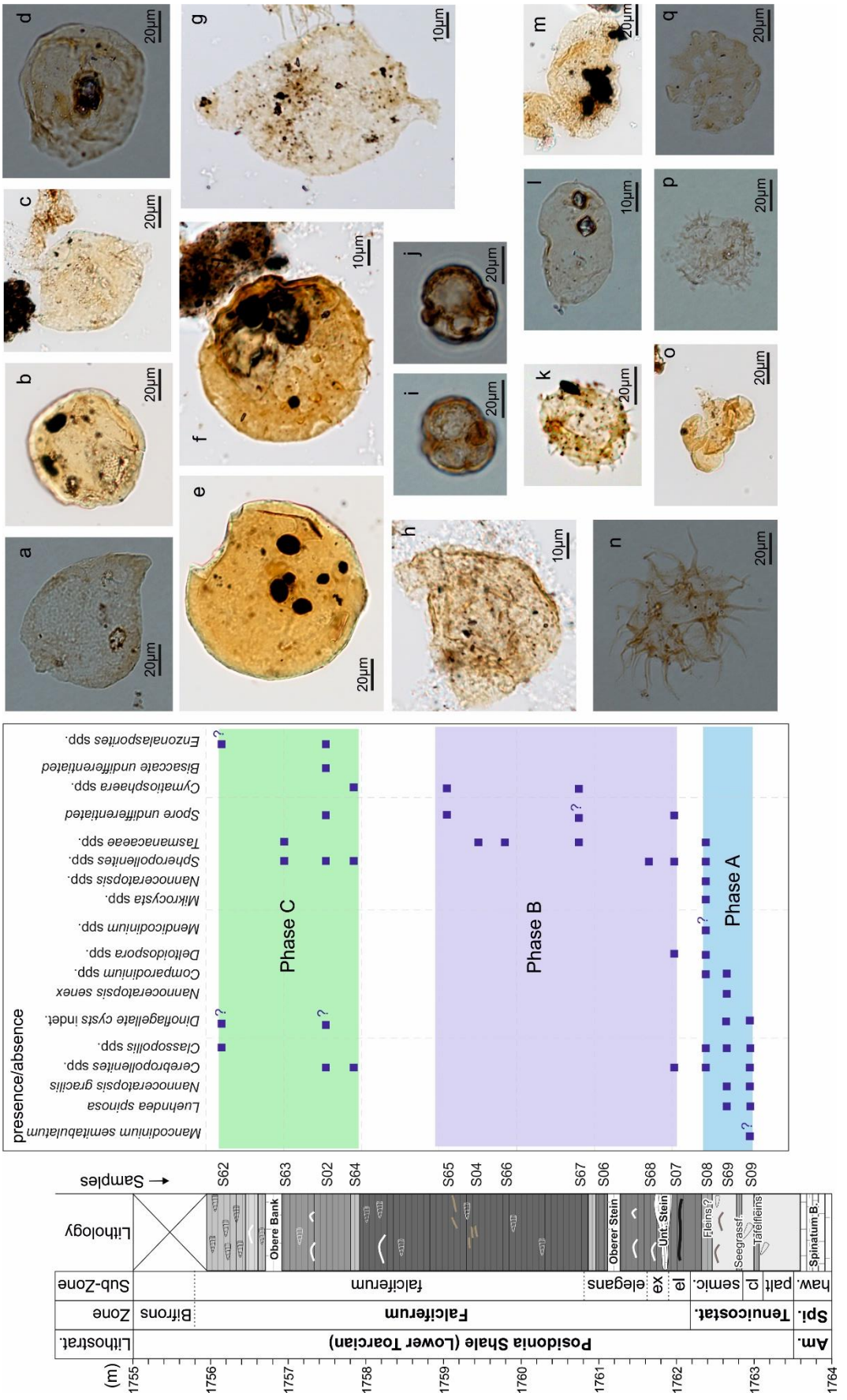

Fig. 4 Presence/absence data of terrestrial and marine palynomorphs. Each blue square represents a minimum of two occurrences of the respective dinoflagellate cyst and sporomorph

Characteristic assemblage from lower Toarcian strata of Salem core (SW Germany). The sample number is followed by the specification of the slide (**K**=kerogen **O**=oxidized), and England Finder coordinates. a) *Nannoceratopsis gracilis*, S09 **O**, O9. b) *Cymathiosphaera* sp., S65 **K**, U59. c) *Nannoceratopsis senex*, S09 **O**, O38/1. d) Dinoflagellate cyst indet., S09 **O**, X37/2. e) *Tasmanites* sp., S67 **K**, D63/4. f) *Pterosphaeridia* sp., S69 **K**, P67/1. g) *Nannoceratopsis senex,* S09 **K**, V47/2. h) *Mancodinium semitabulatum,* S69 **K**, S57/2. i) *Mikrocysta* sp., (high focus). S08 **O**, V44/3. j) *Mikrocysta* sp., (low focus). S08 **O**, V44/3. k) *Mendicodinium spinosum perforatum,* S08 **O**, Q67. l) *Comparodinium punctatum*, S069 **O**, O11/4. m) *Alisporites robustus,* S09 **K**, Q54/1. n) *Luehndea spinosa,* S09 **O**, R16/1. o) *Spheripollenites* sp., S07 **O**, Z51/4. p) *Mendicodinium* sp., S08 **O**, O47/4. q) *Mancodinium* sp., S09 **O**, S42/3.

Maceral Analysis

Liptinite is the dominating maceral group in most samples (>80 vol.%), while vitrinite and inertinite are typically much less abundant (Table 3). Exceptions are the low-TOC (0.26 %) sample at 1763.44 m and the lower sample from the T-CIE (1761.93 m), which contain very high amounts of inertinite and vitrinite, respectively. Lamalginite and telalginite are present in all samples. Typically lamalginte is significantly more abundant than telalginite (including tasmanite algae). Vitrinite reflectance was determined for the vitrinite-rich sample from the lower part of the T-CIE (1761.93 m) and yielded a value of 0.69±0.12 %Rr.

Table 3. Maceral percentages for Toarcian sediments from the drill core (Rr= Vitrinite reflectance, s=standard deviation, n = number of measurements)

Sample ID [m]	**Vitrinite** [Vol%]	**Inertinite** [Vol%]	**Sporinite** [Vol%]	**Telalginite** [Vol%]	**Lamalginite** [Vol%]	**Liptodetrinite** [Vol%]	**Rr / s / n**
Post-CIE							
1756.20	10	8	8	0	64	10	
1757.00	7	7	7	13	60	7	
1757.90	9	3	3	20	60	5	
1759.10	8	6	8	17	60	1	
1759.85	6	6	11	6	67	6	
1760.80	6	2	0	6	87	0	
1760.99	3	16	0	24	16	42	
T-CIE							
1761.70	4	7	0	14	75	0	
1761.93	36	2	0	19	27	17	0.69 / 0.12 / 29
Pre-CIE							
1762.70	5	8	0	31	55	0	
1763.44	14	71	0	0	14	0	

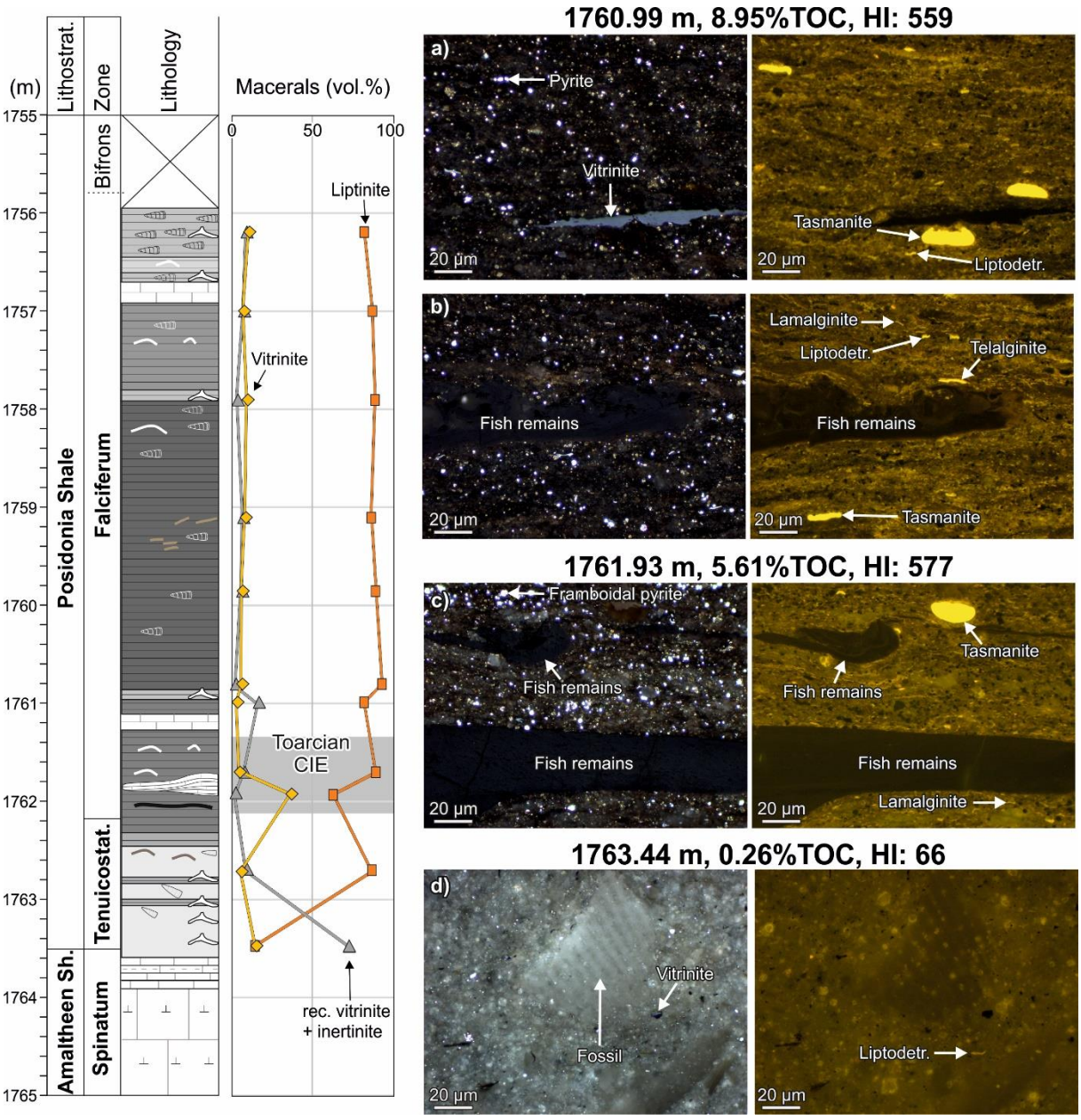

Fig. 5 Maceral composition of Salem samples with micro-photomicrographs of selected samples (left: white light; right: fuorescence mode)

Molecular composition of hydrocarbons

Representative GC-FID and GC-MS traces for the 31 samples investigated for biomarkers are displayed in Figs. 6 and 7. Concentrations and ratios of selected molecular compounds are presented in Table 4 and plotted versus depth in Fig. 8.

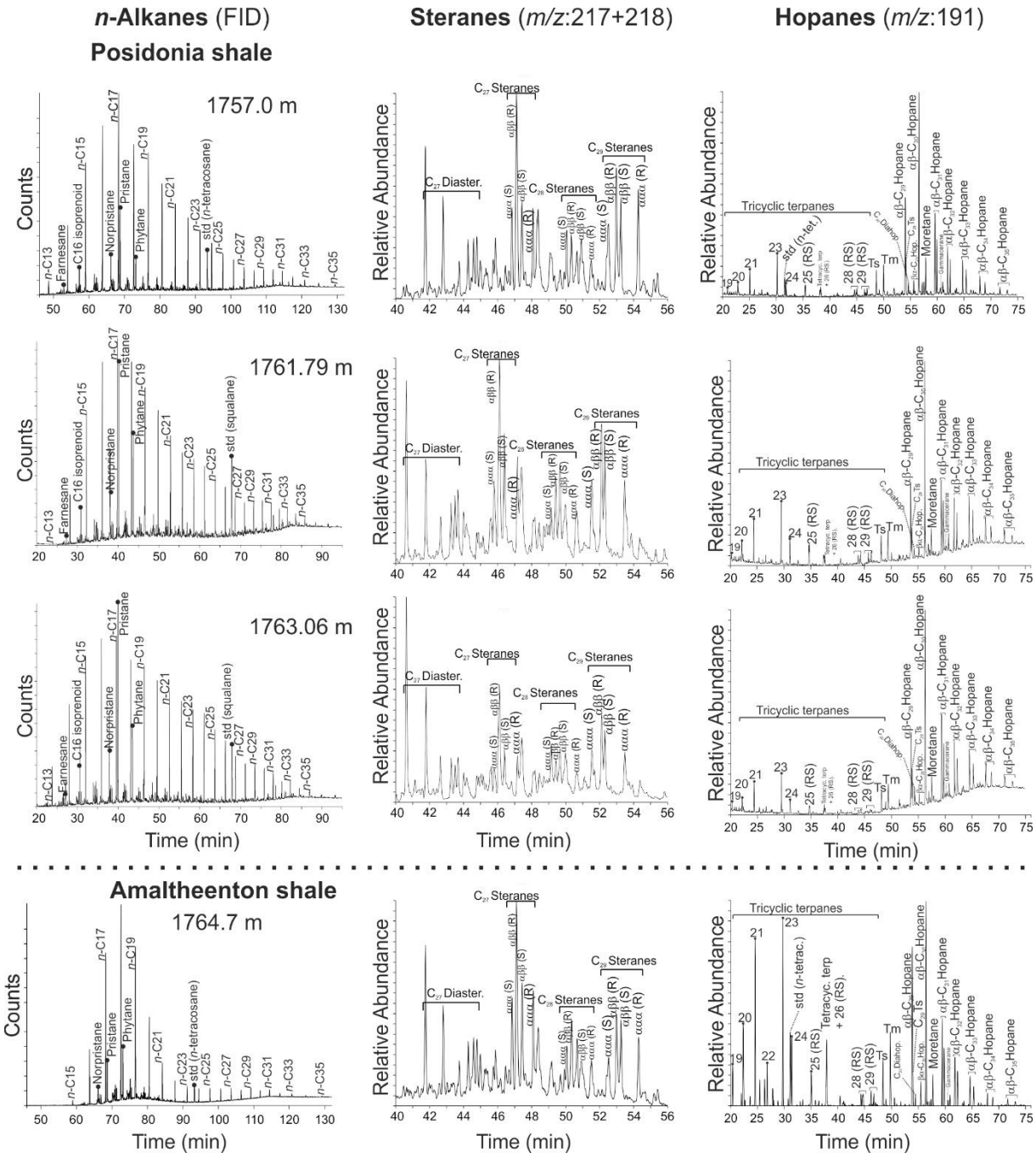

Fig. 6 FID (flame ionization detector) traces of the saturated hydrocarbon fraction and mass chromatogram representations of steranes and hopanes of samples from different stratigraphic positions within the Salem well

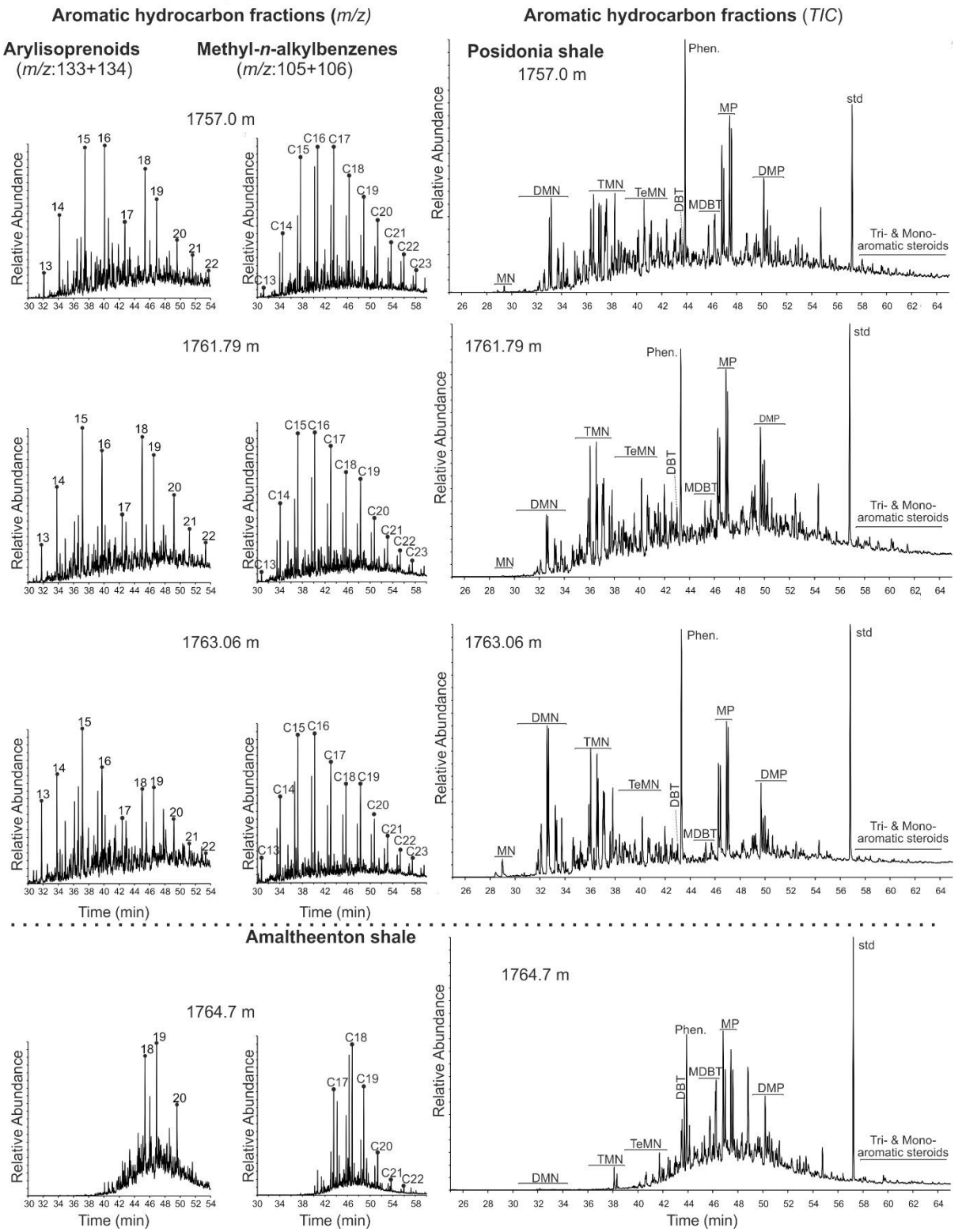

Fig. 7 Mass chromatogram representations of arylisoprenoids, methyl-*n*-alkybenzenes, naphthalenes, benzothiophenes, phenanthrenes and aromatic steroids of samples from different stratigraphic positions within the Salem well

Table 4. Concentrations and concentration ratios of compounds and compound groups within the hydrocarbon fractions of the Toarcian and Pliensbachian- samples of the Salem core

Sample ID [m]	*n*-C_{15-19}/ *n*-alkanes	*n*-C_{21-25}/ *n*-alkanes	*n*-C_{27-31}/ *n*-alkanes	CPI	Pr/Ph	(Pr+Ph)/ (*n*-C_{17+18})	Steranes [µg/g TOC]	C_{27}/ C_{27-29} steranes	C_{28}/ C_{27-29} steranes	C_{29}/ C_{27-29} steranes	20[S/(S+R)] C_{29} Steranes	αββ/(αββ+ααα) C_{29} Steranes	a	b	Methylsteranes C_{28} -dia [µg/g TOC]	Methylsteranes C_{28} [µg/g TOC]	Methylsteranes C_{29} -d [µg/g TOC]	Methylsteranes C_{29} -di [µg/g TOC]	Methylsteranes C_{30} [µg/g TOC]	Dino-steranes [µg/g TOC]
1756.20	0.50	0.26	0.08	1.09	2.32	0.57	11	0.42	0.21	0.37	0.50	0.50	0.36	0.22	0.22	0.24	0.17	0.11	0.28	0.00
1756.60	0.38	0.24	0.16	1.06	2.20	0.70	43	0.39	0.18	0.43	0.46	0.55	0.53	0.32	0.51	0.67	0.46	0.25	0.61	0.01
1757.00	0.57	0.20	0.06	1.02	2.50	0.41	18	0.38	0.23	0.39	0.50	0.50	0.32	0.19	0.23	0.31	0.20	0.11	0.28	0.00
1757.54	0.59	0.22	0.07	1.09	2.54	0.35	34	0.40	0.19	0.41	0.40	0.55	0.51	0.31	0.38	0.52	0.31	0.23	0.49	0.00
1757.90	0.45	0.24	0.11	1.03	2.17	0.62	27	0.39	0.24	0.37	0.52	0.55	0.33	0.20	0.69	0.94	0.59	0.46	0.80	0.01
1758.55	0.42	0.23	0.15	1.05	2.04	0.77	108	0.39	0.20	0.41	0.44	0.58	0.49	0.30	0.57	0.84	0.45	0.32	0.65	0.00
1759.10	0.50	0.20	0.08	1.00	2.01	0.76	27	0.41	0.25	0.34	0.52	0.57	0.39	0.23	1.10	1.55	1.04	0.63	1.25	0.01
1759.46	0.49	0.21	0.13	1.03	1.91	0.81	111	0.40	0.20	0.40	0.43	0.59	0.48	0.29	0.49	0.73	0.43	0.30	0.58	0.00
1759.85	0.49	0.22	0.09	1.00	1.95	0.82	20	0.42	0.24	0.34	0.53	0.57	0.37	0.22	0.79	1.13	0.70	0.48	0.86	0.01
1760.38	0.49	0.22	0.13	1.05	1.97	0.85	90	0.40	0.20	0.40	0.45	0.58	0.47	0.28	0.53	0.77	0.44	0.32	0.59	0.01
1760.80	0.51	0.19	0.08	1.02	1.96	0.76	30	0.40	0.25	0.35	0.51	0.56	0.35	0.21	1.12	1.67	0.95	0.69	1.29	0.02
1761.10	0.43	0.25	0.14	1.03	1.96	0.81	90	0.42	0.21	0.37	0.49	0.58	0.50	0.30	0.50	0.79	0.41	0.30	0.53	0.01
1761.30	0.47	0.25	0.09	1.03	2.00	0.63	153	0.39	0.21	0.40	0.55	0.54	0.41	0.24	*n.d*	*n.d*	*n.d*	*n.d*	*n.d*	*n.d*
1761.42	0.43	0.22	0.14	1.06	1.67	1.21	115	0.37	0.17	0.46	0.49	0.63	0.61	0.36	*n.d*	*n.d*	*n.d*	*n.d*	*n.d*	*n.d*
1761.70	0.60	0.15	0.05	1.04	1.82	0.88	28	0.38	0.24	0.37	0.57	0.56	0.34	0.20	0.91	1.57	0.70	0.60	1.15	0.02
1761.79	0.47	0.24	0.11	1.05	1.68	1.17	71	0.42	0.20	0.38	0.56	0.57	0.45	0.28	*n.d*	*n.d*	*n.d*	*n.d*	*n.d*	*n.d*
1761.93	0.58	0.18	0.08	1.02	1.59	0.90	81	0.41	0.20	0.39	0.57	0.57	0.44	0.27	*n.d*	*n.d*	*n.d*	*n.d*	*n.d*	*n.d*
1762.00	0.59	0.17	0.07	1.07	1.67	0.94	66	0.42	0.19	0.39	0.55	0.57	0.57	0.35	*n.d*	*n.d*	*n.d*	*n.d*	*n.d*	*n.d*
1762.03	0.58	0.18	0.10	1.04	1.76	1.00	44	0.41	0.20	0.38	0.46	0.57	0.53	0.32	0.31	0.45	0.26	0.16	0.34	0.00
1762.08	0.57	0.18	0.08	1.08	1.62	1.00	99	0.39	0.21	0.39	0.53	0.55	0.50	0.30	*n.d*	*n.d*	*n.d*	*n.d*	*n.d*	*n.d*
1762.13	0.54	0.21	0.09	1.05	1.54	1.13	72	0.39	0.21	0.40	0.58	0.57	0.49	0.29	*n.d*	*n.d*	*n.d*	*n.d*	*n.d*	*n.d*
1762.31	0.41	0.29	0.12	1.09	2.18	0.79	51	0.35	0.23	0.42	0.61	0.61	0.82	0.49	*n.d*	*n.d*	*n.d*	*n.d*	*n.d*	*n.d*
1762.70	0.47	0.27	0.10	1.15	1.33	0.42	12	0.45	0.21	0.33	0.52	0.53	0.34	0.38	0.14	0.17	0.09	0.07	0.15	0.00
1762.86	0.46	0.25	0.11	1.09	2.29	1.13	43	0.34	0.19	0.47	0.49	0.56	0.42	0.21	*n.d*	*n.d*	*n.d*	*n.d*	*n.d*	*n.d*
1763.00	0.50	0.23	0.11	1.29	1.64	0.59	11	0.45	0.18	0.37	0.33	0.43	0.46	0.42	0.06	0.07	0.04	0.03	0.07	0.00
1763.06	0.40	0.27	0.11	1.07	2.69	0.70	39	0.36	0.21	0.43	0.59	0.55	0.48	0.30	*n.d*	*n.d*	*n.d*	*n.d*	*n.d*	*n.d*
1763.27	0.51	0.21	0.11	1.46	0.99	0.40	18	0.36	0.33	0.32	0.15	0.35	0.22	0.48	0.02	0.03	0.01	0.02	0.03	0.00
1763.55	0.56	0.19	0.09	1.33	0.72	0.34	6	0.48	0.26	0.26	0.36	0.51	0.36	0.16	0.17	0.28	0.13	0.12	0.21	0.00
1764.10	0.58	0.19	0.12	2.33	1.03	0.53	90	0.21	0.53	0.25	0.03	0.18	0.03	0.22	0.01	0.02	0.00	0.01	0.02	0.00
1764.65	0.69	0.12	0.06	1.17	0.75	0.35	7	0.43	0.27	0.30	0.49	0.58	0.27	0.03	0.07	0.10	0.06	0.04	0.08	0.00
1764.90	0.70	0.12	0.06	1.47	1.11	0.40	70	0.25	0.53	0.22	0.03	0.24	0.03	0.16	0.04	0.21	0.03	0.22	0.22	0.01

TOC - Total organic carbon; CPI – Carbon preference index (Bray and Evans 1961); Pr – pristane; Ph – phytane; dia – methyl diasteranes; di – dimethylsterane; a - C_{27} [diasteranes/sterane]; b - C_{27} [diasterane/diasterane+sterane].

Table 4 continued

Sample ID [m]	Hopanes [µg/g TOC]	Steranes/ Hopanes	22[S/(S+R)] C_{31} Hopanes	Moretane / Hopane	Ts/ (Ts+Tm)	Gamm./ (Gamm.+C_{30} Hop.)	C_{35} / C_{31-35} Hopanes	Tricyclic terpanes Σ [µg/g TOC]	C_{19}/C_{23}	C_{20}/C_{23}
1756.20	21	0.51	0.59	0.21	0.31	0.05	0.04	4	0.26	0.28
1756.60	76	0.56	0.59	0.20	0.37	*n.d*	0.07	16	0.12	0.25
1757.00	29	0.62	0.60	0.18	0.46	0.06	0.06	6	0.11	0.21
1757.54	51	0.67	0.60	0.17	0.34	*n.d*	0.07	13	0.13	0.31
1757.90	33	0.83	0.60	0.19	0.53	0.07	0.07	10	0.10	0.17
1758.55	119	0.91	0.61	0.17	0.41	*n.d*	0.08	32	0.05	0.19
1759.10	29	0.93	0.61	0.18	0.52	0.12	0.08	11	0.08	0.15
1759.46	117	0.95	0.60	0.18	0.40	*n.d*	0.09	33	0.05	0.20
1759.85	17	1.16	0.61	0.17	0.52	0.10	0.08	6	0.08	0.17
1760.38	95	0.94	0.60	0.16	0.43	*n.d*	0.09	24	0.05	0.20
1760.80	33	0.91	0.59	0.17	0.52	0.09	0.09	10	0.11	0.17
1761.10	87	1.03	0.60	0.18	0.33	*n.d*	0.06	25	0.09	0.26
1761.30	224	0.68	0.61	0.14	0.38	0.02	0.09	48	0.12	0.25
1761.42	175	0.66	0.60	0.15	0.46	0.02	0.07	44	0.07	0.25
1761.70	43	0.65	0.60	0.16	0.55	0.08	0.08	12	0.07	0.19
1761.79	103	0.68	0.60	0.15	0.45	0.02	0.07	31	0.06	0.28
1761.93	175	0.46	0.61	0.15	0.45	0.02	0.09	38	0.08	0.30
1762.00	209	0.32	0.60	0.20	0.47	0.02	0.09	40	0.08	0.30
1762.03	103	0.43	0.60	0.15	0.45	*n.d*	0.10	21	0.06	0.28
1762.08	290	0.34	0.59	0.16	0.45	0.02	0.10	52	0.08	0.27
1762.13	235	0.31	0.60	0.16	0.47	0.02	0.09	41	0.07	0.27
1762.31	132	0.39	0.60	0.15	0.40	0.02	0.07	41	0.09	0.29
1762.70	19	0.63	0.59	0.20	0.35	0.07	0.05	5	0.30	0.29
1762.86	204	0.21	0.59	0.16	0.40	0.07	0.59	25	0.20	0.38
1763.00	25	0.44	0.58	0.24	0.26	*n.d*	0.06	8	0.46	0.74
1763.06	176	0.22	0.60	0.15	0.42	0.02	0.06	30	0.13	0.30
1763.27	18	1.04	0.54	0.27	0.23	*n.d*	0.04	6	0.44	0.77
1763.55	14	0.39	0.60	0.20	0.35	*n.d*	*n.d*	6	0.23	0.37
1764.10	24	3.68	0.54	0.28	0.45	*n.d*	0.08	9	0.41	1.56
1764.65	10	0.69	0.60	0.18	0.36	0.06	0.04	9	0.25	0.41
1764.90	15	4.53	0.51	0.38	0.50	*n.d*	0.07	8	0.67	1.94

Table 4 continued

Sample ID [m]	MP	DMP	MPI-1	Rc	MDBT	MDR	Rc´ (%) Type-I/II	DBT/Phen	Methylated Alkylbenzenes	Aryl-Isoprenoids
	[µg/g TOC]		[--]	[%]	[µg/g TOC]				[µg/g TOC]	[µg/g TOC]
1756.20	31	52	0.53	0.72	3	1.63	0.75	0.06	72	7
1756.60	83	88	0.38	0.63	8	1.54	0.75	0.08	105	26
1757.00	88	130	0.43	0.66	14	1.29	0.74	0.13	353	49
1757.54	85	105	0.46	0.68	5	1.56	0.75	0.06	207	50
1757.90	90	135	0.45	0.67	10	1.49	0.75	0.09	374	65
1758.55	68	114	0.46	0.67	13	1.44	0.74	0.14	314	84
1759.10	82	135	0.45	0.67	14	1.48	0.75	0.13	488	83
1759.46	62	94	0.46	0.68	12	1.47	0.75	0.14	189	52
1759.85	55	91	0.46	0.68	11	1.34	0.74	0.14	322	53
1760.38	69	118	0.45	0.67	15	1.30	0.74	0.16	192	53
1760.80	86	142	0.44	0.66	17	1.45	0.74	0.14	548	92
1761.10	70	126	0.50	0.70	6	2.06	0.76	0.06	271	61
1761.30	139	306	0.44	0.66	33	1.17	0.74	0.16	558	121
1761.42	133	276	0.48	0.69	19	1.51	0.75	0.09	262	63
1761.70	103	163	0.47	0.68	15	1.57	0.75	0.11	310	60
1761.79	115	262	0.48	0.69	30	1.30	0.74	0.17	213	53
1761.93	114	234	0.46	0.68	13	1.75	0.75	0.07	168	41
1762.00	125	247	0.47	0.68	14	1.67	0.75	0.07	160	40
1762.03	81	125	0.47	0.68	8	1.69	0.75	0.07	123	32
1762.08	143	284	0.44	0.66	23	1.46	0.75	0.10	168	43
1762.13	108	228	0.45	0.67	22	1.33	0.74	0.12	110	28
1762.31	99	199	0.47	0.68	13	1.54	0.75	0.09	136	0
1762.70	117	192	0.53	0.72	13	1.89	0.75	0.08	151	16
1762.86	298	295	0.47	0.68	22	1.79	0.75	0.06	196	28
1763.00	148	203	0.50	0.70	12	1.74	0.75	0.06	131	16
1763.06	113	152	0.40	0.64	15	1.30	0.74	0.09	142	25
1763.27	96	119	0.52	0.71	12	1.72	0.75	0.06	51	7
1763.55	49	75	0.64	0.78	6	1.69	0.75	0.06	115	10
1764.10	156	182	0.51	0.71	21	1.96	0.76	0.09	151	26
1764.65	37	51	0.65	0.79	4	2.19	0.76	0.07	159	15
1764.90	137	196	0.49	0.70	15	1.71	0.75	0.07	110	15

MP – Methylphenathrene; DMP – Dimethylphenanthrene; MPI – Methylphenathrene Index (Radke et al. 1986); MDBT – Methyldibenzothiophene; MDR - Methyldibenzothiophene ratio (Radke et al. 1986); Rc – calculated vitrinite reflectance; DBT – Dibenzothiophene; Phen – phenanthrene; AIR - aryl isoprenoid ratio (Schwark and Frimmel 2004)

n-Alkanes and isoprenoids

The *n*-alkane patterns are characterised by a unimodal distribution with chain lengths ranging from *n*-C_{15} to *n*-C_{35}. A clear distinction can be made between the distribution patterns of the Amaltheenton Shale and that of the Posidonia Shale (Fig. 6).

The *n*-alkanes concentrations vary between 716-7435 µg/g TOC. Their concentration ratios are dominated by short-chain *n*-alkanes (*n*-$C_{15\text{-}19}$/∑*n*-alkanes: 0.38-0.70) followed by mid- (*n*-$C_{21\text{-}25}$/∑n-alkanes: 0.12-0.29) and long-chain *n*-alkanes (*n*-$C_{27\text{-}31}$/∑*n*-alkanes: 0.05-0.15) (Fig. 8a). The highest amounts of short-chain *n*-alkanes occur in the Amaltheenton Shale with concentration ratios that decrease upward. The carbon preference index (CPI) values (according to Bray and Evans 1961) are close to unity within and above the T-CIE, whereas below this interval, the value varies from 1.15 to 2.33. The highest CPI occurs within the underlying Amaltheenton Shale (Fig. 8b).

Isoprenoid concentrations vary from 167- 1579 µg/g TOC. The pristane/phytane (Pr/Ph) ratio (Didyk et al. 1978) ranges from 0.72 to 2.54. It increases from the upwards from the Amaltheenton Shale (0.75-1.11) to the top of the Posidonia Shale below the T-CIE (2.31). Relatively low values (1.54-1.82) occur within the T-CIE, while values around 2.0 prevail in the sediments above the T-CIE. Even higher values (2.17-2.54) occur above 1758 m depth (Fig. 8c).

The (pristane+phytane)/(*n*-C_{17}+*n*-C_{18}) ratio is a useful redox parameter for the Posidonia Shale (e.g., Frimmel and Schwark 2004). It increases upwards from the Amaltheenton Shale (0.35-0.53) to the base of the T-CIE (~0.8) and shows high ratios (0.88-1.17) within the T-CIE interval. Above this interval the ratio decreases to 0.77 at 1758.55 m and is relatively low (0.35-0.77) in the interval above 1758 m depth (Fig. 8e; Table 4). For organic matter-rich samples (TOC >1.0 wt.%) there is a strong negative correlation between the Pr/Ph and (pristane+phytane)/(*n*-C_{17}+*n*-C_{18}) ratios (r^2=0.79).

Steroids

Sterane concentrations are typically low (7-153 µg/g TOC). Very low concentrations occur in the Amaltheenton, as well as in the lower- and uppermost parts of the Posidonia Shale (Table 4). Within the Posidonia Shale section, C_{27} steranes are typically slightly more abundant than C_{29} steranes, while C_{28} steranes occur in low amounts. High concentrations of C_{28} steranes have been determined only for two low-TOC samples from the Amaltheenton (1764.1 and 1764.9 m) and might be artefacts (Fig. 8f; Table 4).

The C_{29} sterane 20S/(20S+20R) ratio and the C_{29} sterane αββ/(αββ+ααα) ratios are maturity parameters (Seifert and Moldowan 1986). In organic matter-rich samples, C_{29} sterane 20S/(20S+20R) ratios vary between 0.40 and 0.61 (0.51 in average) and the C_{29} sterane αββ/(αββ+ααα) ratios vary between 0.50 and 0.63 (0.57 in average). Both ratios show a subtle upward decrease. In contrast, organic-lean sediments from the Amaltheenton Shale section and from the base of the Posidonia Shale, partly show significantly lower ratios (0.03-0.52 and 0.18-0.58) (Table 4).

The following 4-methylsteranes were identified in most of the samples: C_{28}: 4α-methyl-5α-cholestane, C_{29}: 4α, 24-dimethyl-5α-cholestane, C_{30}: 4α-methyl-24-ethyl-5α-cholestane, and dinosterane (4α, 23S, 24R-trimethyl-5α-cholestane) isomers (Figs. 8h,i.j, 9). Their highest concentrations are observed within the Posidonia Shale Formation above the "Unterer Stein," after which they begin to gradually decrease upwards. Below the "Unterer Stein," these concentrations are notably lower (Fig. 8h,i,j).

Hopanoids and related compounds

Hopanes dominate the non-aromatic cyclic triterpenoids with concentration ranging from 10 to 290 µg/gTOC. The highest concentration occurs in the lower part of the T-CIE (Table 4).

The steranes/hopanes ratio varies strongly in organic-lean sediments (0.39-4.53). In the organic matter-rich part of the Posidonia Shale, the ratio increases upward from the base of the T-CIE (0.31), reaches a maximum of 1.16 within the sediments above the T-CIE at a depth of 1759.85 m and decreases again above this level (Fig. 8k).

There is a constant decrease in concentration from carbon number C_{31} to C_{35} 17α,21β(H)-homohopanes (Fig. 6). The C_{31} hopane isomerization ratios of 22S/(22S+22R) are at equilibrium (~0.60; Mackenzie and Maxwell, 1981), but lower values occur in some samples with very low TOC (Table 3).

The moretane/hopane ratios are between 0.18 and 0.38 in low-TOC samples and vary between 0.14 and 0.21 in the black shale part. A subtle increase can be observed above the T-CIE (Table 4). The Ts/(Ts+Tm) ratios varies between 0.23 and 0.53 (Fig. 8m). The Gammacerane Index (GI=gammacerane/(gammacerane+C_{30} hopane); Sinninghe Damsté et al. 1995) ranges from 0.02 to 0.12 with maximum value occurring at 1759.1 m depth. Remarkably, GI is low (~0.02) within the T-CIE interval (Table 3).

Tricyclic terpanes (TT) concentrations are significant and range from 4 to 52 µg/g TOC. There is a very strong positive correlation between TTs and hopanes (r~=0.90). Similar to

hopanes, the highest TT concentrations occur within the T-CIE interval (Fig. 8o; Table 3). The TTs occur within their C_{19} to C_{29} chain length. C_{23} TT is the most prominent one, followed by C_{19}, C_{20}, and C_{21}, while C_{27} is absent (Fig. 6). Depth plots of C_{19}/C_{23} TT, C_{20}/C_{23} TT show that the low-TOC samples below the T-CIE have higher C_{19}/C_{23} TT, C_{20}/C_{23} TT ratios than the black shales (Fig. 8n; Table 4). Amongst the latter, relatively high ratios occur in the uppermost part of the studied section (1758-1756 m).

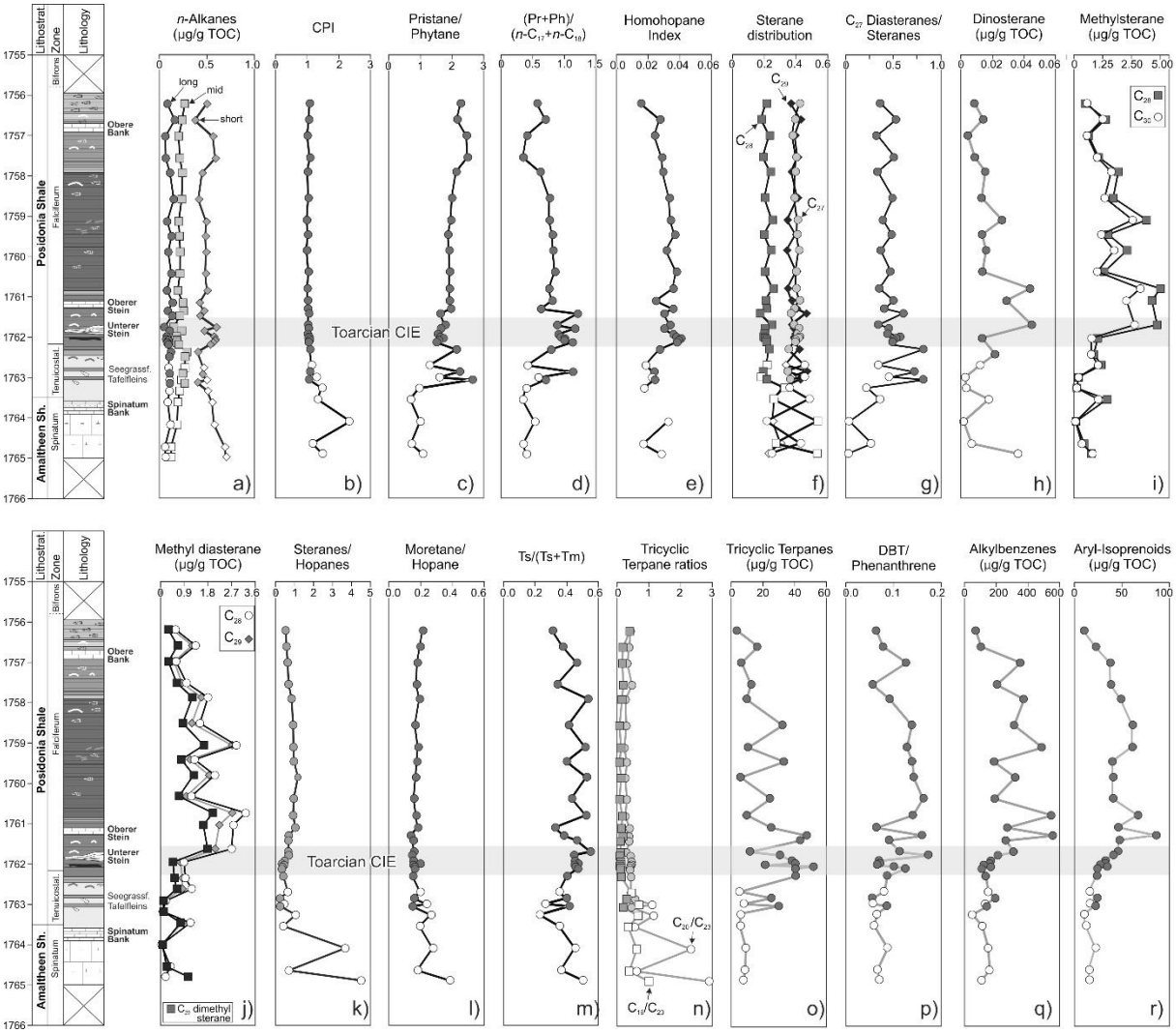

Fig. 8 Concentrations and ratios of selected organic compounds at Salem well showing position of the negative carbon isotope excursion (CIE). Short-chain *n*-alkanes: *n*-$C_{15\text{-}19}/\Sigma$ *n*-alkanes; mid-chain *n*-alkanes: *n*-$C_{21\text{-}25}/\Sigma$ *n*-alkanes; long-chain *n*-alkanes: *n*-$C_{27\text{-}31}/\Sigma$ *n*-alkanes; CPI: Carbon Preference Index (Bray and Evans 1961), sterane distribution: $C_{27}/C_{27\text{-}29}$ steranes, $C_{28}/C_{27\text{-}29}$ steranes, $C_{29}/C_{27\text{-}29}$ steranes; DBT: dibenzothiophene. Low TOC samples below the T-CIE are marked by open symbols.

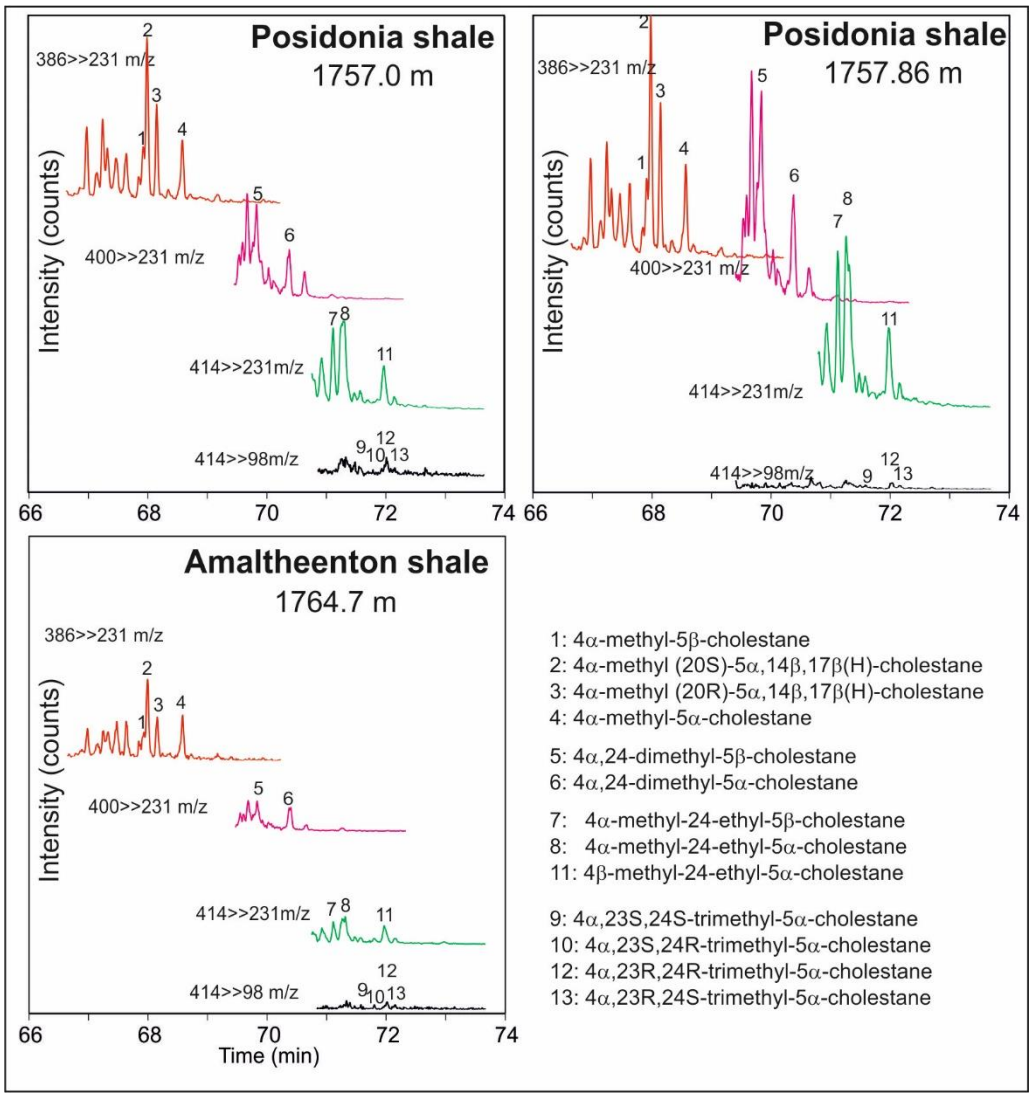

Fig. 9 4-Methylsterane distributions of three samples. Data were acquired by GC-MSMS. Identification of 4α-methylsteranes, 4β-methylsteranes is based on Goodwin et al. (1988) and Schouten et al. (2000).

Aromatic hydrocarbons

The aromatic fraction of the Posidonia and Amaltheenton shales contain low to significant amount of benzenes, napthalenes, phenanthrenes, dibenzothiophenes, and their alkylated analogues (Table 3; Fig. 7). Relevant alkylphenanthrenes present include methylphenanthrene (MP), and dimethylphenanthrene (DMP) with concentrations varying from 31-156 and 51-306 µg/g TOC, respectively. The methylphenanthrene index (MPI-1; Radke et al. 1986; Radke 1988) in black shales varies from 0.38 to 0.53 (0.46 in average), while it is slightly higher in organic-lean sediments (0.49-0.65; 0.55 in average). The average equivalent vitrinite reflectance derived from the MPI-1 is 0.68 %Rr for black shales and 0.73 %Rr for organic-lean deposits (Table 4). Concentrations of methyldibenzothiophenes (MDBT) are low (3-33 µg/g TOC). The methydibenzothiophene ratio (MDR; Radke et al. 1986) ranges from 1.17-2.19. The dibenzothiophene/phenathrene (DBT/Phen) ratios are generally low (0.06-0.17) and show the highest value in the upper part of the T-CIE (Fig. 8p). Mono- (0.2-7.4 µg/g TOC) and tri-(0.4-18 µg/g TOC) aromatic steroids are present in low concentrations. Significant concentration of methyl-*n*-alkylbenzenes are present in the aromatic fraction (Table 4) (e.g., Zhang et al. 2014) ranging from 51 to 558 µg/g TOC and reaching the maximum just above the T-CIE (Fig. 8q).

Aryl isoprenoids with C_{13} to C_{23} chain distribution are present with low to moderate concentrations (7-121 µg/g TOC). Their concentrations are low below the T-CIE, increase upwards within the T-CIE, reach a maximum immediately above the T-CIE and decrease gradually in the upper part of the section (Fig. 8r). The arylisoprenoid ratio (AIR= $C_{13\text{-}17}/C_{18\text{-}22}$ aryl isoprenoids; Schwark and Frimmel 2004) ranges from 0.09 to 1.92. Within the Posidonia Shale, AIR increases upwards, but is relatively low in the uppermost samples (Fig. 8r).

Stable carbon isotope composition of selected organic molecules

Compound-specific carbon isotope ratios were determined for a sub-set of the samples. Carbon isotope ratios are presented for *n*-alkanes with 15 to 29 carbon atoms and for selected isoprenoids (norpristane, pristane, and phytane) in Table 5. All studied *n*-alkanes show a negative shift of $\delta^{13}C$ ratios in the T-CIE interval (Fig. 10) with the most negative values in the interval below the Unterer Stein. The negative shift of $\delta^{13}C$ ratios is slightly higher for mid- and long-chain *n*-alkanes (3.5-4.0‰) than for short-chain n-alkanes (~3‰). The strongest negative shift in $\delta^{13}C$ for all *n*-alkanes is recorded for the sample at 1762.13 m.

$\delta^{13}C$ ratios of pristane are slightly more negative than those of phytane, but both compounds show only a moderate negative shift in the T-CIE (~2‰; Fig. 10) and are in the range of $\delta^{13}C$ ratios of those from the Seegrasschiefer and the Tafelfleins. In contrast to *n*-alkanes, $\delta^{13}C$ ratios of pristane and phytane are uniform within the T-CIE and return to background values only at 1761.30 m depth.

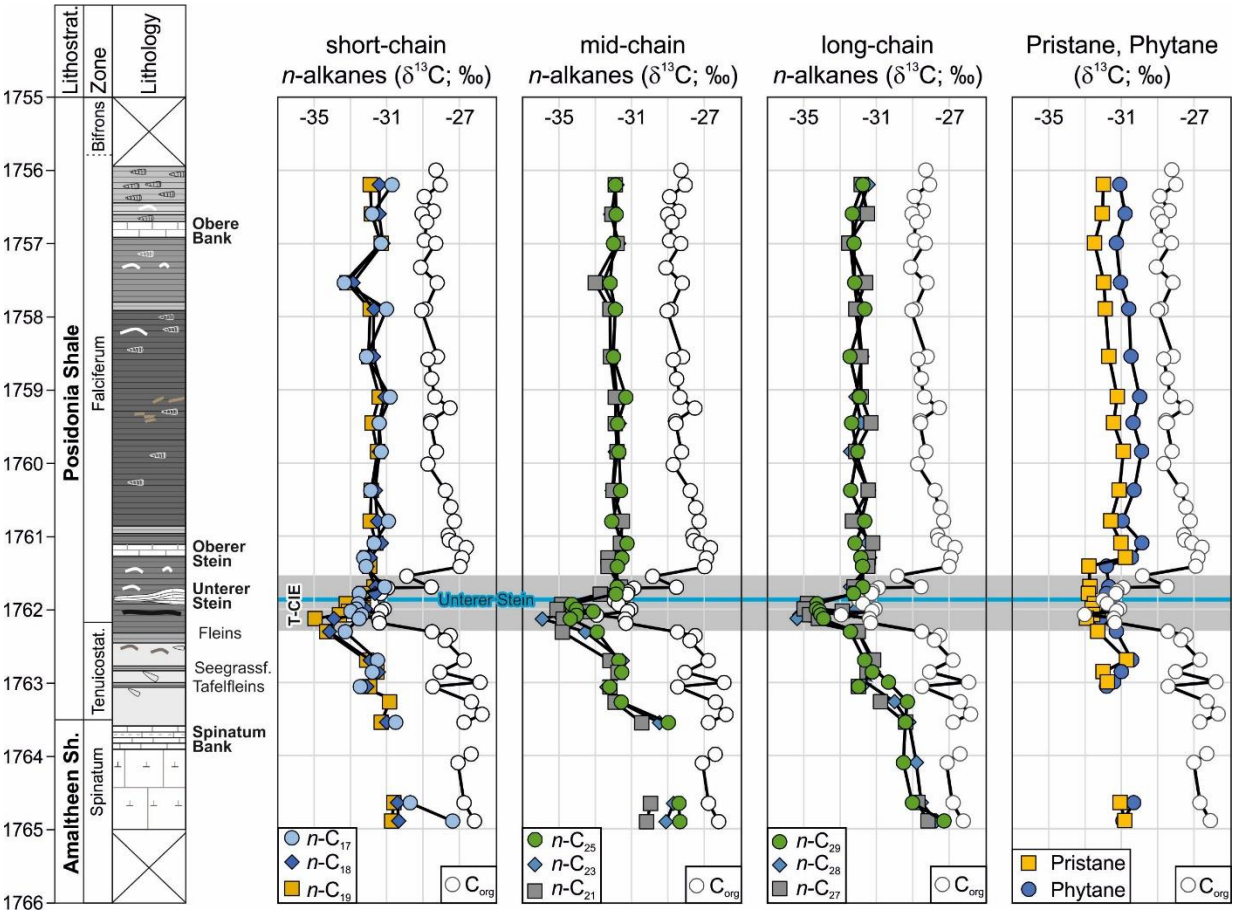

Fig. 10 Depth plot representation of variation in $\delta^{13}C$ of *n*-alkanes, pristane and phytane. Vertical variation of bulk carbon isotope values ($\delta^{13}C_{org}$) is shown for comparison. The position of the Unterer Stein marker bed (blue line) and the T-CIE (grey rectangle) are highlighted.

The variation of $\delta^{13}C$ values as a function of chain length of *n*-alkanes is shown in Fig.11 together with $\delta^{13}C$ values of norpristane, pristane and phytane. The samples are grouped according to their stratigraphic position.

- Low-TOC samples from the Amaltheenton Shale (*Spinatum* Zone) (1764.90-1763.55) are characterized by high $\delta^{13}C$ ratios and an increase in $\delta^{13}C$ with increasing chain length. Pristane and phytane show similar $\delta^{13}C$ values than short-chain *n*-alkanes. Low- and high-TOC samples from the *tenuicostatum* Zone below the T-CIE (1763.06-1762.31 m) are isotopically lighter and *n*-alkanes with different chain lengths show fairly uniform $\delta^{13}C$ values, but short-chain *n*-alkanes from the organic matter-rich "Fleins" (1762.31 m) are characterized by low $\delta^{13}C$ values. $\delta^{13}C$ values of isoprenoids are in the range of those for *n*-alkanes.
- Samples from the lower part of the T-CIE interval (1762.13-1761.93 m) are isotopically lighter than the rest of the samples. They show decreasing $\delta^{13}C$ values with increasing chain length for short- and mid-chain length *n*-alkanes and constant values for long-chain *n*-alkanes. $\delta^{13}C$ values of isoprenoids from these samples are higher than for *n*-alkanes. In contrast, samples from the uppermost part of the T-CIE (1761.79 and 1761.70 m) are isotopically slightly heavier and show uniform $\delta^{13}C$ values for *n*-alkanes with varying carbon numbers. $\delta^{13}C$ values of pristane and phytane from these shallow samples are similar to those of the *n*-alkanes.
- CSI data from samples above the T-CIE are rather uniform. *n*-C_{15} and *n*-C_{16} in all samples are isotopically relatively heavy, while *n*-alkanes with longer chain length show similar $\delta^{13}C$ values between -31 and -33‰. $\delta^{13}C$ values of pristane and phytane are similar to those of *n*-alkanes.

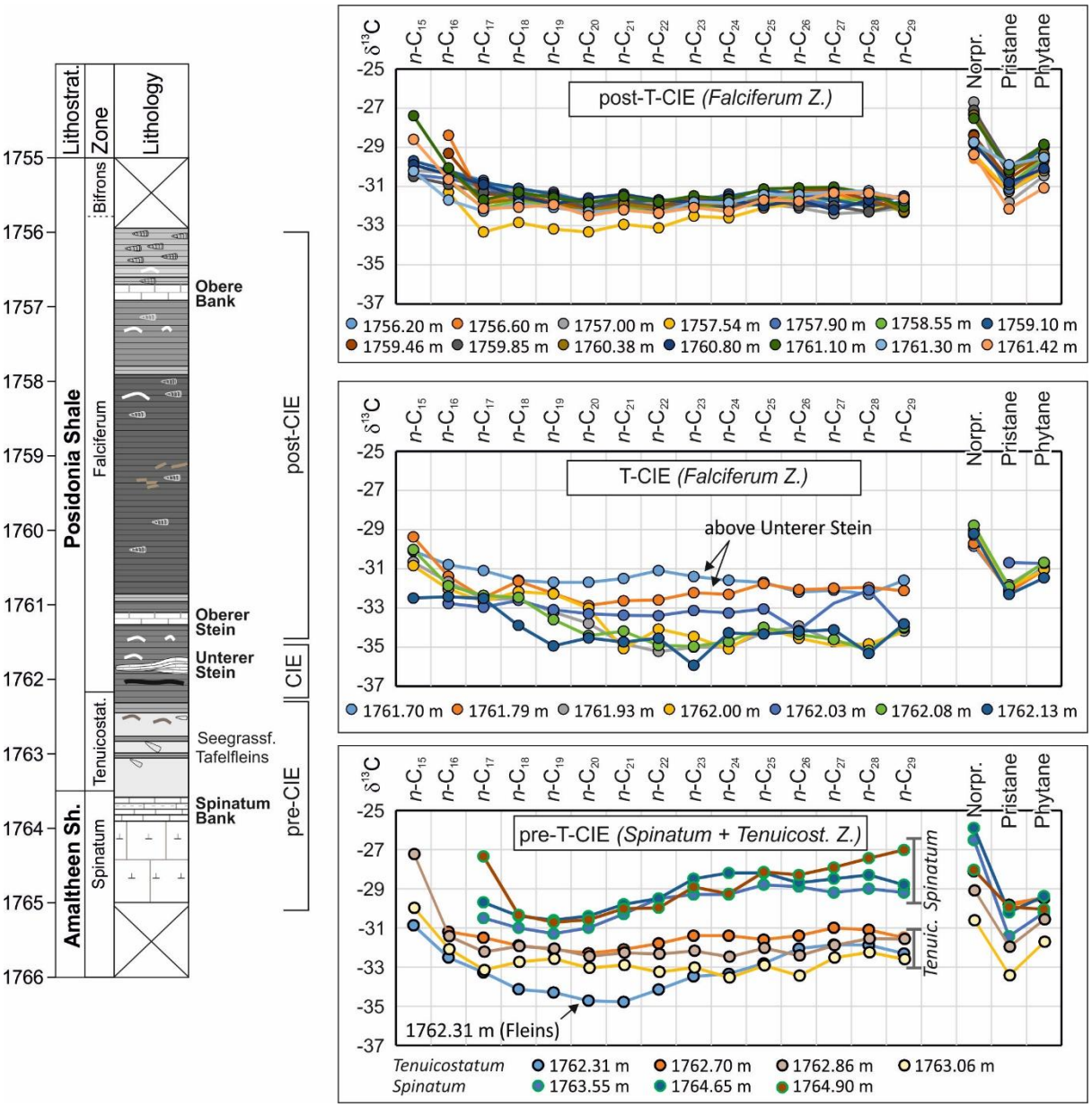

Fig. 11 Carbon isotope composition of individual *n*-alkanes and isoprenoids for samples from different stratigraphic intervals in the Salem section.

Table 5. Compound specific carbon isotope ratios ($\delta^{13}C$; ‰) of Upper Pliensbachian and Lower Toarcian sediments from the Salem drill core.

Sample ID[m]	*n*-C_{15}	*n*-C_{16}	*n*-C_{17}	*n*-C_{18}	*n*-C_{19}	*n*-C_{20}	*n*-C_{21}	*n*-C_{22}	*n*-C_{23}	*n*-C_{24}	*n*-C_{25}	*n*-C_{26}	*n*-C_{27}	*n*-C_{28}	*n*-C_{29}	Nor-pristane	Pristane	Phytane
Post-CIE																		
1756.20	*n.d*	-30.20	-30.70	-31.40	-31.90	-32.00	-31.80	-31.80	-31.70	-31.90	-31.80	-31.90	-31.70	-31.30	-31.60	*n.d*	-31.26	-30.25
1756.60	*n.d*	-28.39	-31.79	-31.41	-31.83	-32.07	-31.99	-32.21	-32.06	-32.00	-31.75	-31.47	-31.34	-31.86	-32.20	-29.60	-31.33	-29.91
1757.00	-30.20	-30.30	-31.30	-31.20	-31.30	-31.80	-31.70	-31.90	-31.60	-31.50	-31.90	-32.10	-32.40	-32.30	-32.10	-26.69	-31.82	-30.46
1757.54	*n.d*	-31.30	-33.33	-32.85	-33.18	-33.33	-32.94	-33.12	-32.52	-32.61	-32.10	-31.86	-31.46	-32.08	-32.06	-29.35	-31.24	-30.20
1757.90	-30.40	-30.60	-31.00	-31.70	-31.90	-32.20	-32.10	-32.30	-31.80	-31.40	-31.80	-31.60	-32.00	-31.90	-31.50	-28.36	-31.15	-29.68
1758.55	-27.85	-30.75	-32.10	-31.73	-32.00	-32.18	-32.07	-32.38	-31.94	-32.08	-31.91	-31.46	-31.72	-31.66	-32.33	-28.71	-30.92	-29.55
1759.10	-29.70	-30.20	-30.80	-31.10	-31.40	-31.80	-31.80	-31.70	-31.70	-31.50	-31.20	-31.40	-31.70	-32.00	-31.80	-27.26	-30.40	-29.01
1759.46	*n.d*	-29.31	-31.40	-31.42	-31.80	-32.11	-31.79	-32.04	-31.57	-31.63	-31.67	-31.16	-31.16	-31.70	-32.23	-28.42	-30.63	-29.41
1759.85	-30.50	-30.90	-31.30	-31.40	-31.50	-32.10	-31.70	-32.10	-31.80	-32.10	-31.60	-32.00	-32.00	-32.30	-31.90	-27.11	-30.02	-28.89
1760.38	-25.14	-30.09	-31.88	-31.62	-31.84	-32.30	-31.92	-32.12	-31.97	-31.83	-31.50	-31.36	-31.31	-31.28	-32.29	-27.36	-30.27	-29.35
1760.80	-29.90	-30.40	-30.90	-31.50	-31.90	-31.60	-31.40	-31.70	-31.80	-31.70	-32.00	-31.70	-32.20	-31.70	-31.50	-28.82	-30.81	-30.09
1761.10	-27.39	-30.06	-31.69	-31.29	-31.59	-31.84	-31.50	-31.79	-31.49	-31.67	-31.13	-31.08	-31.04	-31.35	-32.05	-27.53	-30.17	-28.86
1761.30	-30.22	-31.70	-32.26	-31.90	-32.08	-32.31	-32.20	-32.37	-31.80	-31.84	-31.43	-31.42	-31.29	-31.22	-31.72	-28.74	-29.90	-29.52
1761.42	-28.60	-30.64	-32.13	-32.07	-31.94	-32.50	-32.20	-32.36	-32.08	-32.28	-31.69	-31.76	-31.33	-31.34	-31.62	-29.37	-32.16	-31.08
T-CIE																		
1761.70	-30.10	-30.80	-31.10	-31.60	-31.70	-31.70	-31.50	-31.10	-31.40	-31.60	-31.70	-32.20	-32.10	-32.30	-31.60	-29.86	-32.11	-30.92
1761.79	-29.38	-31.39	-32.50	-31.64	-32.27	-32.88	-32.64	-32.60	-32.23	-32.31	-31.77	-32.08	-32.00	-31.96	-32.13	-29.72	-32.20	-31.07
1761.93	-30.66	-31.67	-32.55	-32.55	-33.22	-33.79	-34.83	-35.23	-35.01	-35.00	-34.27	-33.94	-34.73	-34.92	-34.19	-29.29	-31.82	-30.70
1762.00	-30.85	-32.04	-32.67	-32.17	-32.29	-33.02	-35.09	-34.08	-34.47	-35.10	-34.01	-34.55	-34.92	-34.84	-34.23	-29.04	-31.97	-31.04
1762.03	*n.d*	-32.78	-32.97	-32.62	-33.10	-33.30	-33.38	-33.40	-33.14	-33.26	-33.06	-34.16	-32.77	-32.10	-34.04	*n.d*	-30.69	-30.73
1762.08	-30.03	-31.87	-32.37	-32.47	-33.60	-34.42	-34.19	-34.92	-34.97	-34.73	-34.00	-34.36	-34.62	-35.17	-33.98	-28.79	-31.92	-30.68
1762.13	-32.50	-32.43	-32.52	-33.90	-34.94	-34.54	-34.75	-34.55	-35.93	-34.28	-34.34	-34.20	-34.12	-35.32	-33.82	-29.22	-32.32	-31.47
Pre-CIE																		
1762.31	-30.87	-32.52	-33.27	-34.14	-34.30	-34.72	-34.78	-34.15	-33.48	-33.35	-32.82	-32.06	-31.86	-31.88	-32.31	-28.12	-31.62	-30.46
1762.70	*n.d*	-31.20	-31.50	-31.90	-32.10	-32.30	-32.10	-31.80	-31.40	-31.40	-31.60	-31.40	-31.00	-31.10	-31.50	*n.d*	-29.82	-29.50
1762.86	-27.41	-30.91	-31.57	-31.33	-31.43	-31.76	-31.61	-31.66	-31.53	-31.78	-31.41	-31.73	-31.29	-31.01	-31.03	-28.96	-31.35	-30.19
1763.06	-29.70	-31.46	-32.34	-32.00	-31.87	-32.26	-32.13	-32.43	-32.24	-32.67	-32.15	-32.59	-31.82	-31.59	-31.89	-30.23	-32.57	-31.14
1763.27	*n.d*	*n.d*	*n.d*	*n.d*	-30.84	-31.22	-31.81	-31.70	-31.54	-31.55	-31.46	-30.92	-30.60	-29.81	-29.09	*n.d*	*n.d*	*n.d*
1763.55	*n.d*	*n.d*	-30.50	-31.00	-31.30	-31.00	-30.30	-29.50	-29.30	-29.30	-28.80	-28.90	-29.20	-29.00	-29.20	-26.52	-31.43	-30.22
1764.65	*n.d*	*n.d*	-29.70	-30.40	-30.60	-30.40	-29.80	-29.50	-28.50	-28.20	-28.20	-28.70	-28.50	-28.30	-28.80	-25.90	-30.21	-29.38
1764.90	*n.d*	*n.d*	-27.36	-30.34	-30.72	-30.59	-30.02	-29.98	-28.92	-29.26	-28.15	-28.30	-27.92	-27.45	-27.02	-28.04	-29.93	-30.05

Discussion

Thermal maturity

Thermal maturity parameters such as vitrinite reflectance (0.69±0.12 %Rr), T_{max} (436 °C in average) and TAI (2-3) suggest that the Posidonia Shale at Salem has reached early to peak oil window maturity. The average equivalent vitrinite reflectance derived from the MPI-1 is 0.68 %Rr for black shales and 0.73 %Rr for organic-lean deposits. Oil window maturity is also supported by 20S/(20S+20R) and αββ/(αββ+ααα) C_{29} sterane isomerisation ratios (0.51 and 0.57 in average, respectively; Fig. 12) and by the 22S/(22S+22R) C_{31} hopane ratio (0.60 in average; Mackenzie and Maxwell, 1981).

Maturity parameters from immature to early oil window mature Dormettingen samples (0.40-0.54 %Rr; Ajuaba et al. 2022) are plotted in Figure 12a for comparison. PI of black shales at Salem is higher than at Dormettingen (0.08 and 0.04 in average, respectively), but still below the value of 0.10, which is often taken as the threshold value for the onset of the oil window (e.g., Peters, 1986; Fig. 12b). In any case, the value indicates that some hydrocarbons have already been generated. This fact must be taken into account when discussing the (remaining) hydrocarbon potential and evaluating environmental proxies based on organic geochemical data.

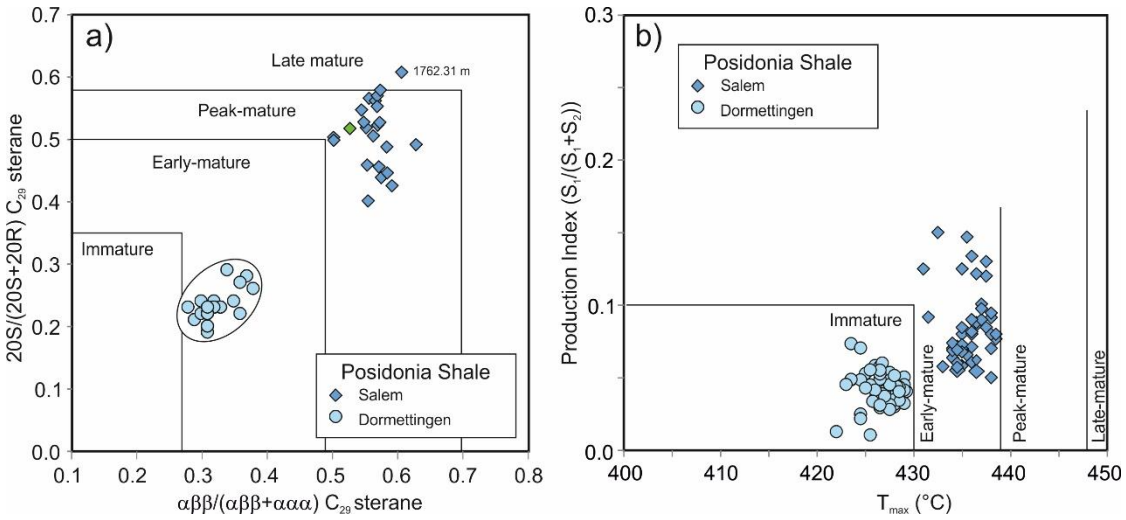

Fig. 12 Cross plots of (a) 20S/(20S+20R) isomer ratios of ααα C_{29} steranes versus αββ/(αββ+ααα) C_{29} steranes (boundaries between maturity fields after Peters et al. 2005) and (b) Production Index versus T_{max} for Posidonia Shale at Salem and Dormettingen (boundaries between T_{max}-based maturity fields for Posidonia Shale according to Song et al. 2015)

Source rock potential

High TOC contents (average 4.9 %) and high HI values (~530 mgHC/gTOC) show that the Posidonia Shale at Salem has an excellent potential to generate oil. The high source rock potential of the Posidonia Shale in the SWGB has been shown previously by Littke et al. (1991b). Indeed, the Posidonia Shale has been assumed by many authors (e.g., Wehner and Kuckelkorn 1995; Veron 2005; Misch et al. 2017) to be one of the main source rocks in the North Alpine Foreland Basin, although Bechtel et al. (2019) showed that it contributed only to oil deposits west of Munich.

Interestingly, the average HI at Salem is significantly lower than at Dormettingen (~650 mgHC/gTOC; Ajuaba et al. 2022). Although a facies effect on HI cannot be excluded, this difference may suggest that 15 to 20 % of the original hydrocarbon potential has already been generated at Salem. This percentage is even higher, if the possible presence of retained bitumen (e.g., Ziegs 2017) is assumed.

The Source Potential Index (SPI [tHC/m²] = (S_1+S_2 [mgHC/g rock])*thickness [m]*rock density [g/cm^3]/1000) of Demaison and Huizinga (1994), which gives the amount of hydrocarbon generated beneath one square meter of surface area, is used to quantify the remaining source rock potential of the Posidonia Shale at Salem.

For the calculation, an average density of 2.55 (cf. Stock and Littke 2018) has been considered. Following the guidelines of Demaison and Huizinga (1994), low-TOC layers have been neglected for the calculation of the average genetic potential (S_1+S_2: 31.5 mgHC/g rock) and the net source rock thickness (6.14 m). On that assumption, the SPI for the cored interval is calculated as 0.49 tHC/m². For comparison, the SPI has been calculated for the same stratigraphic interval (Posidonia Shale below the Inoceramen Bed) using data from the Dormettingen section (Ajuaba et al. 2022). The comparison shows a slightly higher SPI for Dormettingen (0.59 tHC/m²). The difference is mainly due to the significantly higher genetic potential at Dormettingen (52.10 mgHC/g rock), which overcompensates for the lower thickness.

The SPI of the upper part of the Posidonia Shale at Dormettingen (*bifrons* Zone) is 0.53 tHC/m². No data are available from that interval from Salem. However, considering its lower thickness (3 vs. 4 m) and a lower genetic potential, the SPI might be in the order of 0.30 tHC/m² suggesting a total SPI of 0.80 tHC/m². This value is slightly lower than the SPI for the entire Lower Oligocene in the Austrian part of the North Alpine Foreland Basin (1.09

tHC/m²), but higher than that of the main source rock interval (Schöneck Formation) alone (0.35 tHC/m²; Sachsenhofer et al. 2010).

Table 6. Thickness, genetic potential (S_1+S_2), density, and Source Potential Index (SPI) of different stratigraphic units at Salem and Dormettingen

	Net thickness (m)	Average S_1+S_2 (mgHC/g rock)	SPI (tHC/m²)
Salem			
Bifrons Z.	3.0	?	0.30??
Falciferum Z.	6.43	28.94	0.49
Dormettingen			
Bifrons Z.	4.0	50.21	0.53
Falciferum Z.	4.2	52.10	0.58

Depositional environment

Geochemical and palynological proxies are employed in this section to reconstruct the depositional environment of the Posidonia Shale at Salem. In doing so, extensive published information on the Posidonia Shale in SW Germany, especially on the Dotternhausen/ Dormettingen sections, is taking into account (Röhl et al. 2001; Schmid-Röhl et al 2002; Frimmel et al. 2004; Schwark and Frimmel 2004; Röhl and Schmid-Röhl 2005; van den Schootbrugge et al. 2005; Bour et al. 2007; van Acken et al. 2019; Wang et al. 2020, 2021; Galasso et al. 2021; 2022; Ajuaba et al. 2022).

Before the depositional environment is described for different stratigraphic units, some peculiarities of isoprenoid-based redox parameters are discussed first. It is widely accepted that Pr/Ph ratios < 1 indicate anoxic conditions (e.g., Didyk et al. 1978). Although the Pr/Ph ratio is a reliable redox parameter for the Posidonia Shale, absolute values are skewed towards higher ratios (e.g., Schouten et al. 2000; Frimmel et al. 2004; Ajuaba et al. 2022). For example, Frimmel et al. (2004) showed that the limit for anoxic conditions in the case of Posidonia Shale is as high as 1.6. These authors also showed that the (Pr+Ph)/(*n*-C_{17}+*n*-C_{18}) ratio is an additional useful redox parameter with ratios >1.75 corresponding to strictly anoxic conditions. On average, Pr/Ph ratios at Salem are slightly higher (1.5-2.6) than at Dormettingen (1.0-2.6), but the (Pr+Ph)/(*n*-C_{17}+*n*-C_{18}) ratios are significantly lower (0.3-1.2 versus 0.6-2.5). The low (Pr+Ph)/(*n*-C_{17}+*n*-C_{18}) ratios at Salem are clearly a consequence of hydrocarbon generation, which produces *n*-alkanes, but not isoprenoids. Moreover, preferential thermal cracking of isoprenoids compared to *n*-alkanes may also contribute to the decreased values (McNeil and Bement 1996; Zheng et al. 2023). Hydrous pyrolysis experiments showed that thermal stress can also lead to a significant increase in Pr/Ph ratios

(Zheng et al. 2023). Therefore, vertical trends of the Pr/Ph and (Pr+Ph)/(*n*-C_{17}+*n*-C_{18}) ratios are used for interpretation, but not their absolute values.

Pre-CIE (*spinatum* and *tenuicostatum* zones: 1764.90-1762.31 m)

The lower part of the core (below the T-CIE) is formed by predominating marly sediments with strong bioturbation indicating oxic conditions. Thin limestone layers (Spinatum- or Costatenklalk) and two organic-rich layers (Tafelfleins: 1763.07 m; Seegrasschiefer: 1762.86 m) are intercalated in the background sediments. Organic matter contents are also high in the upper part of this succession (Fleins; 1762.43-1762.31 m), which is considered the basal part of the thick black shale succession. The prevailing oxic conditions resulted in low TOC contents in the background marls.

The HI of low-TOC sediments (<0.6 wt.%) ranges from 33 to 173 mgHC/gTOC suggesting the presence of terrigenous or strongly degraded marine organic matter. Relatively high contributions of landplants are also indicated by the lowermost two palynofacies samples (S09 [1763.00 m], S69 [1762.70 m]), macerals data, and geochemical parameters (elevated CPI [Fig. 6b]; high C_{20}/C_{23} and C_{19}/C_{23} tricyclic terpane ratios [Fig. 6n]). Low (Pr+Ph)/(*n*-C_{17}+*n*-C_{18}) ratios of the bioturbated sediments agree with an oxygenated environment. In contrast, low Pr/Ph ratios (<0.6) pretending strictly anoxic conditions clearly must not be considered for interpretation. A change in CSI patterns (Fig. 11) between Pliensbachian (1764.90-1763.55 m) and Toarcian pre-CIE samples (1763.55-1762.31 m) may be related to a change in organic matter input.

Both, the organic matter-rich Tafelfleins and the Seegrassschiefer are bioturbated. Nevertheless, TOC (2.68 and 1.84 wt.%, respectively) and HI (423 and 358 mgHC/gTOC) are high. This suggests a high amount of aquatic organic matter and relatively good organic matter preservation despite of later bioturbation. The higher HI values, as well as CPI values and C_{20}/C_{23} and C_{19}/C_{23} tricyclic terpane ratios, which are lower than in the adjacent organic-poor sediments indicate the higher amount of aquatic organic matter. Similar to the low-TOC samples, the redox parameters yield contradicting results. However, it is obvious that oxygen-depleted conditions occurred during deposition, but later bioturbation helped to transport oxygen into the freshly deposited sediment.

In the upper part of the *tenuicostatum* Zone (*semicelatum* Subzone), TOC contents increase gradually and reach 3.68 wt.% at 1762.31 m (Fleins). Pr/Ph and (Pr+Ph)/(*n*-C_{17}+*n*-C_{18}) ratios

as well as the homohopane index (HHI) suggest oxygen-depleted, but not yet strictly anoxic conditions, which were established only during the T-CIE. Sample S08 (1762.43 m) from this interval records a drastic reduction in dinoflagellate diversity. Striking is the questionable *Mendicodinium* sp. at 1762.43 m depth (sample S08; Phase A), before the complete dinoflagellate cysts demise. In the Posidonia Shale (SW Germany) before the inception of the fully anoxic conditions, *Mendicodinium spinosum perforatum* was recorded in the lowermost *falciferum* Zone described as the last taxon able to survive and stand the initial severe environmental condition as a consequence of the T-OAE (Galasso et al. 2022).

T-CIE (uppermost *tenuicostatum* and lower *falciferum* zones: 1762.25-1761.50 m)

The T-CIE interval the Salem is very thin (~ 0.75 m). Strongly oxygen-depleted conditions during the T-CIE are evidenced by the presence of laminated black shales and the absence of benthic faunas (Röhl and Schmid-Röhl 2005). Anoxic conditions are also evidenced by relatively low Pr/Ph ratios (1.54-1.82; Fig. 8c), relatively high (Pr+Ph)/(*n*-C_{17}+*n*-C_{18}) (0.88-1.17; Fig. 8d) and high C_{35} HHI (0.03-0.04; Fig. 8c). The presence of aryl-isoprenoids, which have been used as proxies for photosynthetic sulphide-oxidizing bacteria (Summons and Powell 1987), indicates photic zone anoxia (Schouten et al. 2000; Frimmel et al. 2004; Schwark and Frimmel 2004). At Salem, the concentration of aryl-isoprenoids increases upwards within the T-CIE (Fig. 8r). The concentrations of methyl-alkylbenzenes and aryl-isoprenoids are strongly correlated (r^2=0.81) and show similar depth trends within the T-CIE (Fig. 8q). Probably, both compound groups formed by the degradation of carotenoids (e.g., isorenieratene). Alternative formation mechanisms include direct cyclization and aromatization of straight chain fatty acids (Derenne et al. 1990; Chairi et al. 2010). The maximum methyl-alkylbenzenes concentration in Salem (548 µg/g TOC; 1760.80 m) is 10 times higher than for Dormettingen (51 µg/g TOC). This suggests a maturity effect on the degradation of aromatic carotenoids or the cyclization and aromatization. As elevated amounts of alkylbenzenes have been recorded in sediments deposited during periods of enhanced salinity (Sinninghe-Damsté et al. 1993; Chairi et al. 2010), it is possible that their elevated amounts within (and above) the T-CIE in the Salem section were triggered by salinity stratification and water column anoxia. However, the gammacerane index is typically low (Table 4) suggesting only weak salinity stratification. In contrast, the DBT/Phen ratio, a proxy for free H_2S in the water column or the pore water (Hughes et al. 1995), varies strongly in the T-CIE, but is generally high (Fig. 8p).

Strictly anoxic conditions resulted in high TOC contents (4.78-7.44 %), which are below 2 wt.% only in the Unterer Stein marker bed (1.62 wt.%; 1761.83 m). High HI values (538-634 mgHC/gTOC; Fig. 3b) reflect the dominance of aquatic organic matter and the excellent preservation conditions. The observed upward increase in the concentration of aryl-isoprenoids (and methyl-alkylbenzenes) together with slightly lower HHI values may indicate an even higher degree of oxygen-depletion above the Unterer Stein. Probably, increased oxygen-depletion caused slightly higher HI values above the Unterer Stein (average 618 mgHC/gTOC) compared to the interval below this marker (574 mgHC/gTOC). Alternatively, the slightly lower HI below the Unterer Stein may indicate a stronger terrigenous organic matter input during the early T-CIE, as indicated macroscopically by a thin coaly layer and microscopically by relatively high amounts of translucent phytoclasts in the sample at 1762.03 m depth (Table 2) and vitrinite in the sample at 1761.93 m depth (Table 3). In contrast, terrigenous phytoclasts or macerals are very rare in samples above the Unterer Stein. Similar to Dormettingen (Galasso et al. 2021), dinoflagellate cysts were not recorded in the T-CIE (lower part of palynofacies B; Fig. 5).

TOC contents in the T-CIE at Salem reach 7.44 %. This value is high, but lower than in the same interval at Dormettingen (~10 wt.%; Fig. 1c) and in post-CIE sediments in the Salem core (max. 8.95 wt.%; see below). As the low thickness of the T-CIE contradicts a dilution of organic matter by high clastic input and the similar high HI values in the T-CIE and post-CIE sediments contradict variations in organic matter preservation, it is likely that the relatively low TOC content in the T-CIE is due to limited organic productivity (see also Littke et al. 1991b). Sterane/hopane ratios have been used to estimate paleo-productivity of phytoplankton (Schulz et al. 2002). Thus, the observed low ratios in the T-CIE interval (Fig. 8k) support this interpretation. In this connection, it should be noted that only stratigraphic trends of the sterane/hopane ratio, but not absolute values are considered, because the sterane/hopane ratio decreases significantly with maturity (Zheng et al. 2023). Thus it is not surprising that the sterane/hopane ratio is significantly lower in Salem (0.21-1.16) than in Dormettingen (1.01-6.32; Ajuaba et al. 2022).

The concentrations of 4-methylsteranes including dinosteranes and 4-methyl-diasteranes have been determined only for a limited sample set. These compounds are generally ascribed to dinoflagellates (Withers 1987; Moldowan and Talyzina 1998; Volkman et al. 1990) and show similar depth trends (Fig. 8 h,i,j) with maxima in the upper part of the T-CIE. . Consequently,

despite the generally low phytoplankton productivity, it is likely that the productivity of non-cyst-forming dinoflagellates was relatively high in the upper part of the T-CIE.

Post-CIE (upper *falciferum* Zone: 1761.50-1756.00 m)

Based on TOC trends, the post-CIE sediments are subdivided into four units. Environmental proxies are discussed separately for each of them starting with the lower unit I.

Unit I (1761.5-1761.0 m) includes the Oberer Stein marker and is slightly bioturbated in its upper part. An increase in oxygen availability between 1761.42 and 1761.30 m is also indicated by isoprenoid-based redox parameters (Pr/Ph; (Pr+Ph)/(*n*-C_{17}+*n*-C_{18})), while HHI and the concentration of aryl-isoprenoids suggest an increase in oxygen availability between 1761.30 and 1761.10 m. HI values in unit I vary considerably (455-630 mgHC/gTOC). The sample with the minimum HI (S06; 1761.1 m) contains a very low amount of terrigenous organic matter (Fig. 3). This shows that varying HI values reflect varying oxygen availability rather than changes in organic matter input. Similar to the sediments deposited during the T-CIE, dinoflagellate cysts are missing (palynofacies phase B sensu Galasso et al. 2021). $\delta^{13}C$ values of bulk organic matter in this interval are relatively high. The same interval at the Dormettingen section (e.g., Fig. 1c) has been dated into the *elegans* Subzone within the *falciferum* Zone.

Unit II (1761.99-1757.92 m) is an approximately 3 m thick interval that includes the highest TOC contents (4.71-8.95 %) in the studied profile (Fig. 2). Overall there is a slight upward decrease in TOC (from ~9 to ~6 %). Sterane/hopane ratios reach a maximum at 1759.85 m depth and decrease upwards (Fig. 8k). This suggests that high TOC contents are due to enhanced phytoplankton productivity. HI values are uniformly high (557-660 mgHC/gTOC). The highest amount of marine POM is recorded at 1760.80 m depth. . Beyond this point, the input of terrigenous POM experiences only a minor increase (Fig. 3). Consequently, the marine/terrestrial ratio remains high in all samples from unit II. Tasmanaceae algae are present in both POM and maceral assemblages, while dinoflagellate cysts are absent. Belemnite remains, which are absent in the T-CIE and in unit I, reappear in small number and shows an upward increasing trend in unit II.

The redox parameters (Pr/Ph; (Pr+Ph)/(*n*-C_{17}+*n*-C_{18}); HHI) suggest strongly reduced oxygen availability, with a subtle trend towards less strictly anoxic conditions in the upper part of the succession. This agrees with the observed increase in belemnite remains and the presence of

some shell layers. Concentrations of aryl-isoprenoids are generally high and even more so in the upper part of Unit II. Overall, redox parameters and high TOC contents suggest that the degree of oxygen-depletion during deposition of unit II was in a similar range compared to the T-CIE. This differs from the condition observed in the Dotternhausen (Schwark and Frimmel 2004) and Dormettingen (Ajuaba et al. 2022) sections, where the maximum oxygen depletion occurred during the T-CIE just above the Unterer Stein, at the onset on the carbon isotope recovery phase (C3 after Suan et al. 2008; cf. Fig. 1c). The availability of free H_2S is evidenced by high DBT/Phen ratios. The high sulphur contents (max. 4.31 % at 1760.38 m) agree with this interpretation. Despite of anoxic marine conditions, TOC/S ratios are high in the upper 1.2 m of unit II (3.8-5.1). This may indicate an increase in freshwater runoff.

Unit III (1757.9-1757.0 m) starts with a bioturbated layer and includes some shells. TOC contents are significantly lower (2.92-4.04 %) than in unit II and HI values are slightly reduced (462-523 mgHC/gTOC). Bioturbation and the stratigraphic trends of biomarker proxies (Fig. 8c, d, e, r) show an increase in oxygen availability during deposition of unit III.

Unit IV (1756.96-1755.0 m) follows above the Obere Bank limestone marker. The presence of several bioturbated horizons and the high number of belemnites show a well oxygenated environment. Consequently, TOC (1.68-3.16 % and HI (296-464 mgHC/gTOC) are even lower than in unit III. The organic matter input during deposition of units III and IV is characterized by an increasing fraction of terrigenous organic material. A subtle increase in C_{19}/C_{23} and C_{20}/C_{23} TT ratios (Fig. 8n) is probably another consequence of the increased contribution of terrigenous organic matter. Sterane/hopane ratios (Fig. 8k) are also decreased in units III and IV suggesting reduced phytoplankton productivity. *Spheropollenites* sp. and prasinophytes are common (palynofacies C sensu Galasso et al. 2021; Fig. 3), but dinoflagellate cysts are still absent.

Comparison with other Toarcian sections in the SWGB

The position of marker beds and the T-CIE in the Salem core enable detailed correlation with other Toarcian sections in the SWGB. In addition to examining variations in lateral thickness, this section delves into an investigation of both similarities and differences among depositional environments.

It is noticeable that the lower part of the Posidonia Shale at Salem is very thin. For example, the sediment succession between the top of the Spinatum Bank and the Oberer Stein is only

2.4 m thick. In contrast, this same interval in the Dotternhausen/Dormettingen area, located about 65 km NW of Salem, is more than twice as thick (~ 5.5 m; Fig. 13). The transition of the Amaltheenton Formation to the Posidonia Shale is gradual and there is no sign of an erosional unconformity at the base of the Posidonia Shale, as recently described by Arp et al. (2021) in the Franconian Alb (Ludwigskanal section; Fig. 1a). The only stratigraphic layer, which is absent in the lower Posidonia Shale at Salem is the "Steinplatte" near the top of the T-CIE (e.g. Ajuaba et al. 2022; Fig. 1c). The latter marker bed, however, is not as continuous as the Oberer Stein and is absent, for example, in the German-Swiss border area (e.g., Aselfingen; Riegraf 1985; Fernandez et al. 2021) and east of Reutlingen (Stuttgart; Riegraf 1985). Moreover, each stratigraphic unit (including the T-CIE is thinner at Salem compared to Dormettingen (Fig. 13). Thus, the low thickness of the lower part of the Posidonia Shale is clearly is not due to non-deposition or erosion of specific layers. Thickness variations were also observed by Riegraf (1985), who interpreted these as consequences of deposition in paleo-basins and paleo-swells. Based on this interpretation, it's evident that the Salem section was likely deposited within an early Toarcian paleo-swell, and a potential connection to the Vindelician High is plausible.

While the thickness of the Lower Posidonia Shale at Salem is reduced, the thickness of the middle part of the Posidonia Shale (i.e., interval between Oberer Stein and Obere Bank; ~ 4.2 m) is higher than in the Dotternhausen/Dormettingen area (~ 1.5 m; Fig. 13). Although the Inoceramen Bed at the *falciferum/bifrons* boundary was not cored, it is likely present immediately above the core (see section "lithology and stratigraphy"). Thus the total thickness of the *falciferum* Zone probably slightly exceeds 5 m. This exceeds the thickness observed in most sections in the SWGB and indicates increased subsidence during deposition of the upper part of the *falciferum* Zone (units II-IV of the post-CIE sediments).

The *bifrons* Zone in the Salem borehole is about 3 m thick, but was not cored. This is less than the thickness measured at Dormettingen, where where it spans about 4.4 m (Galasso et al. 2021, 2022). However, it's important to note that, the thickness of the *bifrons* Zone in the SWGB varies considerably due to late Toarcian erosion, In some areas, such as the northeast Swabian Alb (locations like Gingen/Fils and Göppingen; Fig. 1b), this erosion has led to the complete removal of the entire *bifrons* Zone and has even cut down to the Oberer Stein horizon (within the *elegans* Subzone; (e.g. Riegraf 1985). Since the *bifrons* Zone and the boundary with the overlying upper Toarcian sediments were not cored in the Salem borehole,

it is impossible to determine whether the upper part of the Posidonia Shale was affected by erosion in this specific location.

The changes in depositional environment are largely synchronous in the Salem and in the Dormettingen/Dotternhausen areas, which is also reflected by similar TOC trends (Fig. 13). In both areas, a peak in oxygen depletion is observed during the T-CIE shortly after deposition of the Unterer Stein. However, at Salem, following a short period with deposition of bioturbated sediments, anoxia continued during the early *falciferum* Subzone (unit II of the post-CIE sediments) and caused TOC contents, which are even higher than in the T-CIE. In addition, the dinoflagellate cyst blackout (Prauss and Riegel 1989; 1996; Prauss et al. 1991), which is restricted to upper *exaratum* and lower *elegans* subzones at Dormettingen (Galasso et al. 2022; Fig. 1c), continued in the *falciferum* Subzone at Salem. Similarly, Prauss et al. (1991) noted that the entire bituminous facies within the *falciferum* and *bifrons* zones in borehole Bisingen/Zimmern #1002, situated approximately 20 kilometers northeast of Dormettingen (Fig. 1b), showed virtually no presence of dinocysts. The extended absence of dinoflagellate at Salem may be a result of continuing anoxia during the *falciferum* Subzone or its proximal setting resulting in increased turbidity and low salinity.

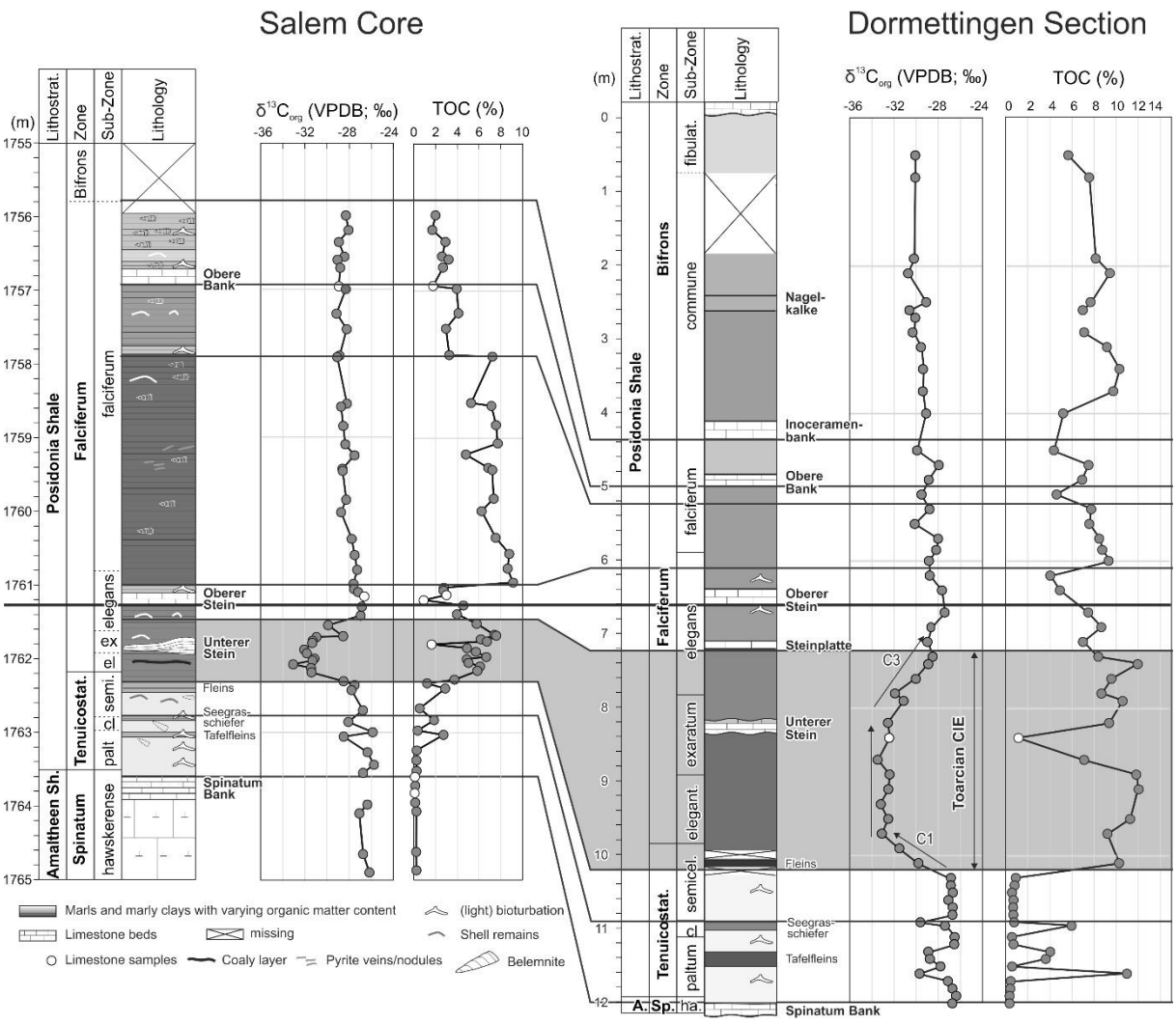

Fig. 13 Correlation of the Salem drill core with the Dormettingen section. Datum is the base of the Oberer Stein marker bed. Note the lower thickness of the lower part of the Posidonia Shale and the higher thickness of the upper part (*falciferum* Subzone) in the Salem core. Data from the Dormettingen section are from Galasso et al. (2021) and Ajuaba et al. (2022)

Bulk and compound-specific carbon isotope data

Bulk organic carbon isotope ratios

Bulk organic carbon isotope ratios ($\delta^{13}C_{org}$) in the Salem section (-25.7 to -33.1‰) are similar to those at Dormettingen (Fig. 13). The lowermost part of the black shale interval (1762.43-1762.31 m) shows $\delta^{13}C_{org}$ values (-27.49 to -28.49‰) similar to those of the underlying Tafelfleins and the Seegrasschiefer (-28.06 to -28.48‰). The largest drop in $\delta^{13}C_{org}$ occurs between 1762.31 (Fleins) and 1762.19 m (-31.39‰). A depth of ~1762.25 m, therefore, has been accepted as the base of the T-CIE, while the top of the T-CIE is at ~1761.50 m. Although the T-CIE at Salem is much thinner (0.75 m) than at Dormettingen (~2.8 m), its amplitude falls within a similar range (5-6‰). A similar strong negative CIE has been determined in the Cleveland Basin (5-7‰), while the CIE is smaller in the Paris (3.7‰), Iberian (~3‰) and Sichuan basins (~ 4‰) (see Ajuaba et al. 2022 and references therein).

Stable carbon isotope ratios of *n*-alkanes

As expected, $\delta^{13}C$ ratios of *n*-alkanes also show a shift in the T-CIE, but the negative shift (3-4‰) is lower compared to that observed for $\delta^{13}C_{org}$. Moreover, there are some interesting differences between trends of $\delta^{13}C_{org}$ and $\delta^{13}C$ of different *n*-alkanes.

As stated above, the base of the T-CIE is located above the Fleins (1762.31 m) based on $\delta^{13}C_{org}$. This interpretation is also valid for long-chain *n*-alkanes (Fig. 10). However, it appears that the CIE begins slightly earlier (during deposition of the Fleins) for short-chain *n*-alkanes (up to *n*-$C_{21/22}$) (Figs. 10, 11). While long-chain *n*-alkanes may be derived from landplants, short-chain n-alkanes are typically derived from algae and other aquatic organisms (Eglinton and Hamilton 1967). Hence, this result suggests that isotopically light CO_2 was first recorded in the aquatic environment.

The $\delta^{13}C$ values of *n*-alkanes in the upper part of the T-CIE (above the Unterer Stein; 1761.79 and 1761.70 m) are significantly less negative than those in the lower part (below the Unterer Stein; 1762.13-1761.93 m) and similar to post-CIE background values (Figs. 10, 11). Similar to Dormettingen, redox-sensitive parameters suggest a higher degree of oxygen-depletion above the Unterer Stein. This supports the temporal decoupling of the maximum isotope excursion and the strongest basin restriction as postulated based on isotope ratios of pristane and phytane in the Dormettingen section (Ajuaba et al. 2022; Fig. 1c).

No systematic variation between $\delta^{13}C$ ratios of *n*-alkanes in the mature Salem core and the immature Dormettingen section can be observed. For example, $\delta^{13}C$ ratios of *n*-alkanes from the *teniucostatum* Zone are slightly more negative than those at Dormettingen, while those from the falciferum Zone (including the T-CIE) are slightly less negative. This suggests that maturity has a no significant effect on $\delta^{13}C_{alkanes}$ (see also Pedentchouk and Turich 2017).

Stable carbon isotope ratios of pristane and phytane

At Dormettingen, the amplitude of the CIE of pristane and phytane is about 4.5‰ and $\delta^{13}C_{isoprenoid}$ values increase continuously upwards within the T-CIE. A similar trend was expected for Salem, but the amplitude of the CIE is only 2‰ and no clear depth trend is observable (Fig. 10). Indeed, the most negative $\delta^{13}C_{pristane}$ value is recorded for the Tafelfleins (1763.06 m) in the pre-CIE interval and not for the T-CIE.

No correlation between $\delta^{13}C$ of isoprenoids and *n*-alkanes could be established. This might indicate that pristane and phytane are not derived from the phytol side chain of chlorophyll of aquatic or terrestrial plants. Frimmel et al. (2004) suggested that the surprisingly high Pr/Ph ratios in Posidonia Shale may be due to secondary input of pristane from tocopherol or chromanes. However, as tocopherol- and chromane derived pristane has the same $\delta^{13}C$ as the phytol side chain (Hughes et al. 1995; Grice et al. 1998; Peters et al. 2005; Zhang et al. 2012), it is expected to have a minor influence on isotope data. This is also supported by the excellent correlation exists between $\delta^{13}C_{pristane}$ and $\delta^{13}C_{phytane}$ at Dormettingen (Ajuaba et al. 2022) and Salem. It should be added that an effect of hydrocarbon migration on $\delta^{13}C$ of pristane and phytane can be excluded, as isoprenoids are less mobile than *n*-alkanes (e.g., Leythaeuser et al. 1982; Zhang et al. 2021; Zheng et al. 2023). Hence, additional investigations are necessary to determine the factors controlling $\delta^{13}C$ values of pristane and phytane at Salem.

Conclusion

A total of 62 core samples were collected from the Salem borehole in southwestern Germany to assess the depositional environment and petroleum potential of the lower Toarcian Posidonia Shale beneath the North Alpine Foreland Basin. The most important results of the comprehensive geochemical and petrographic investigation are summarized below.

The Salem core spans the *tenuicostatum* and *falciferum* ammonite zones of the Posidonia Shale and the uppermost 1.5 m of the underlying Pliensbachian Amaltheen Shale. The upper part of the Posidonia Shale (*bifrons* Zone), which is about 3 m thick was not cored.

Compared to the Dormettingen section, located about 65 km NW of Salem, the thickness of the lower part of the Posidonia Shale (*tenuicostatum* Zone to *elegans* Subzone of the *falciferum* Zone) is sigificantly thinner, while the thickness of the *falciferum* Subzone is increased. This suggests significant changes in basin geometry at the *elegans/falciferum* boundary.

As observed in many Toarcian sections, the strongest oxygen depletion occurred during deposition of the upper part of the T-CIE (above Unterer Stein). However, strong anoxia also occurred during deposition of the post-CIE sediments. This together with higher productivity resulted in peak TOC values in the uppermost *elegans* and lower *falciferum* subzones. The dinoflagellate cyst blackout lasted throughout the entire *falciferum* Zone, likely as another consequence of significant oxygen-depletion.

The T-CIE interval at Salem is very thin (0.75 m), but the amplitude of the CIE ($\delta^{13}C_{Corg}$) is similar to other section in the SWGB (~5-6‰). The T-CIE is less pronounced for *n*-alkanes (3-4 ‰).

Similar to Dormettingen, an obvious time shift exists between the isotopic minimum ($\delta^{13}C_{alkanes}$) and peak anoxic conditions. This supports the assumption that isotopically light inorganic carbon from deeper water levels of the stratified water body is probably not the only source for isotopically light carbon. Despite this, differences in $\delta^{13}C$ of *n*-alkanes derived from aquatic and terrigenous organisms, suggest that isotopically light carbon influenced the marine before the atmospheric CO_2 pool.

Pristane and phytane show only a small negative isotope excursion (2‰) without depth trend in the T-CIE. As $\delta^{13}C$ of isoprenoids and *n*-alkanes or bulk organic matter are not correlated, it is likely that they reflect a different, yet unidentified CO_2 reservoir.

The Posidonia Shale at Salem is thermally mature and highly oil-prone. PI values are higher and HI values are lower than those in the immature to marginal mature Dormettingen section. The residual source petroleum potential of the cored section is about 0.5 tHC/m² and may be 0.8 tHC/m² for the entire Posidonia Shale.

References

Ajuaba S, Sachsenhofer RF, Galasso F, Bechtel A, Gross D, Misch D, Schneebeli-Hermann E (2022) Biomarker and compound-specific isotope records across the Toarcian CIE at the Dormettingen section in SW Germany. Int. J. Earth Sciences, 111: 1631–1661. https://doi.org/10.1007/s00531-022-02196-z

Arp G, Gropengießer S, Schulbert C, Jung D, Reimer A (2021) Biostratigraphy and sequence stratigraphy of the Toarcian Ludwigskanal section (Franconian Alb, Southern Germany). Zitteliana 95: 57-94. https://doi.org/10.3897/zitteliana.95.56222

Batten DJ (1996) Palynofacies. In J. Jansonius and D.C. McGregor (Eds), Palynology: Principles and applications (Vol. 3, pp. 1011–1064). Park Ridge; American Association of Stratigraphy Palynologists Foundation

Baudin F (1995) Depositional controls on Mesozoic source rocks in the Tethys. In: Huc, A-Y (ed.), Paleogeography, Paleoclimate, and Source Rock. American Association of Petroleum Geologists Studies in Geology 40: 191–211 Houston

Bechtel A, Berling M, David P, Dax F, Garlichs TU, Gratzer R, Groß, D, Köhler V, Oriabure JE, Sachsenhofer RF (2019) Oil-source correlation in the German Molasse basin. 29th Int. Meeting Org. Geochem. https://doi.org/10.3997/ 2214-4609.201902720 (IMOG 2019)

Bour I, Mattioli E, Pittet B (2007) Nannofacies analysis as a tool to reconstruct paleoenvironmental changes during the Early Toarcian anoxic event. Palaeogeography, Palaeoclimatology, Palaeoecology 249: 58–79

Bowden SA, Farrimond P, Snape CE, Love GD (2006) Compositional differences in biomarker constituents of the hydrocarbon, resin, asphaltene and kerogen fractions: An example from the Jet Rock (Yorkshire, UK). Organic Geochemistry 37: 369-383

Bray EE, Evans ED (1961) Distribution of n-parafins as a clue to recognition of source beds. Geochimica et Cosmochimica Acta 22: 2-15

Caruthers AH, Smith PL, Gröcke DR (2013) The Pliensbachian–Toarcian (Early Jurassic) extinction, a global multi-phased event. Palaeogeography, Palaeoclimatology, Palaeoecology 386: 104–118. https://doi.org/10.1016/j.palaeo.2013.05.010

Chairi R, Derenne S, Largeau C (2010) Alkylbenzene origin in recent sediments from the hypersaline environment of Moknine Sebkha, Tunisi. Rapp Comm int Mer Médit 39: 233

Chen W, Kemp DB, He T, Newton RJ, Xiong Y, Jenkyns HC, Izumi K, Cho T, Huang C, Poulton SW (2023) Shallow-and deep-ocean Fe cycling and redox evolution across the Pliensbachian–Toarcian boundary and Toarcian Oceanic Anoxic Event in Panthalassa. Earth and Planetary Science Letters 602: 117959. https://doi.org/10.1016/j.epsl.2022.117959

Demaison G, Huizinga BJ (1994) Genetic classification of petroleum systems using three factors: charge, migration and entrapment. In: Magoon, L.B., Dow, W.G. (Eds.), The Petroleum System, from Source to Trap., AAPG Memoir 60: 73–89

Dera G, Neige P, Dommergues J-L, Fara E, Laffont R, Pellenard P (2010) High resolution dynamics of Early Jurassic marine extinctions: the case of Pliensbachian-Toarcian ammonites (Cephalopoda). Journal of the Geological Society of London 167: 21–33. https://doi.org/10.1144/0016-76492009-068

Derenne S, Largeau C, Casadevall E, Sinninghe-Damsté JS, Tegelaar EW, de Leeuw JW (1990) Characterisation of Estonian Kukeriste by spectroscopy and pyrolysis: Evidence for abundant alkyl phenolic moieties in an Ordovician, marine, Type II/I kerogen. Org Geochem 16:873–888

Didyk B, Simoneit B, Brassell S, Eglinton G (1978) Organic geochemical indicators of palaeoenvironmental conditions of sedimentation. Nature 272: 216–222

Eglinton G, Hamilton R (1967) Leaf epicutular waxes. Science 156: 1322–1335

Espitalié J, Laporte JL, Madec M, Marquis F, Leplat P, Paulet J, Boutefeu A (1977) Méthode rapide de caractérisation des roches mètres, de leur potentiel pétrolier et de leur degré d´éevolution. Rev. l'Institut Français du Pétrole 32: 23-42. https://doi.org/10.2516/ogst:1977002

Fantasia, A., Adatte, T, Spangenberg, J E., Font, E, Duarte, LV, & Follmi, KB (2019a) Global versus local processes during the Pliensbachian-Toarcian transition at the Peniche GSSP, Portugal: A multi-proxy record. Earth-Science Reviews, 198 https://doi.org/10.1016/j.earscirev.2019.102932

Fernandez A, Korte C, Ullmann CV, Looser N, Wohlwend S, Bernasconi SM (2021) Reconstructing the magnitude of Early Toarcian (Jurassic) warming using the reordered clumped isotope compositions of belemnites. Geochimica et Cosmochimica Acta 293: 308-327. https://doi.org/10.1016/j.gca.2020.10.005

French K.L, Sepulveda J, Trabucho-Alexandre J, Gröcke DR, Summons RE (2014) Organic geochemistry of the early Toarcian oceanic anoxic event in Hawsker Bottoms, Yorkshire, England. Earth and Planetary Science Letters 390: 116-127. https://doi.org/10.1016/j.epsl.2013.12.033

Frimmel A, Oschmann W, Schwark L (2004) Chemostratigraphy of the Posidonia Black Shale, SW Germany I. Influence of sea-level variation on organic facies evolution, Chemical Geology 206: 199-230

Galasso F, Schmid-Röhl A, Fesit-Burkhardt S, Bernasconi SM, Schneebeli-Hermann E (2021) Changes in organic matter composition during the Toarcian Oceanic Anoxic Event (T-OAE) in the Posidonia Shale Formation from Dormettingen (SW-Germany). Palaeogeography, Palaeoclimatology, Palaeoecology 569: 110327. https://doi.org/10.1016/j.palaeo.2021.110327

Galasso F, Feist-Burkhardt S, Schneebeli-Hermann E (2022) The palynology of the Toarcian Oceanic Anoxic Event at Dormettingen, southwest Germany, with emphasis on changes in vegetational dynamics. Review of Palaeobotany and Palynology 304: 104701. https://doi.org/10.1016/j.revpalbo.2022.104701

Goodwin NS, Mann AL, Patience RL (1988) Structure and significance of C30 4-methylsteranes in lacustrine shales and oils. Organic Geochemistry 12: 495-506

Grice K, de Mesmay R, Glucina A, Wang S (2008) An improved and rapid 5A molecular sieve method for gas chromatography isotope ratio mass spectrometry of n-alkanes (C8-C30+). Organic Geochemistry 39: 284–288. https://doi.org/10.1016/j.orggeochem.2007.12.009

Grice K, Schouten S, Peters KE, Sinninghe Damsté JS (1998) Molecular isotopic characterisation of hydrocarbon biomarkers in Palaeocene-Eocene evaporitic, lacustrine source rocks from the Jianghan Basin, China. Organic Geochemistry 29: 1745–1764Grice K, de Mesmay R, Glucina A, Wang S (2008) An improved and rapid 5A molecular sieve method for gas chromatography isotope ratio mass spectrometry of n-alkanes (C8-C30+). Organic Geochemistry 39: 284–288. https://doi.org/10.1016/j.orggeochem.2007.12.009

Harries PJ and Little CTS (1999) The early Toarcian (Early Jurassic) and Cenomanian–Turonian (Late Cretaceous) mass extinctions: similarities and contrasts. Palaeogeography, Palaeoclimatology, Palaeoecology 154: 39–66. https://doi.org/10.1016/S0031-0182(99)00086-3

Hermoso M, Delsate D, Baudin F, Le Callonnec L, Minoletti F, Renard M, Faber A (2014) Record of Early Toarcian carbon cycle perturbations in a nearshore environment: the Bascharage section (easternmost Paris Basin). Solid Earth 5: 793–804. https://doi:10.5194/se-5-793-2014

Hermoso M, Minoletti F, Pellenard P (2013) Black shale deposition during Toarcian super-greenhouse driven by sea level. Climate of the Past 9: 2703.2712

Hermoso M, Minoletti F, Le Callonnec L, Jenkyns HC, Hesselbo SP, Rickaby REM, Renard M, de Rafélis M, Emmanuel L (2009) Global and local forcing of Early Toarcian seawater chemistry: A comparative study of different paleoceanographic settings (Paris and Lusitanian basins), Paleoceanography 24: 1-15. https://doi:10.1029/2009PA001764

Hesselbo SP, Gröcke DR, Jenkyns HC, Bjerrum CJ, Farrimond P, Morgans Bell HS, Green OR (2000) Massive dissociation of gas hydrate during a Jurassic oceanic anoxic event. Nature 406: 392–395. https://doi.org/10.1038/35019044

Hesselbo SP, Jenkyns HC, Duarte LV, Oliveira LCV (2007) Carbon-isotope record of the Early Jurassic (Toarcian) Oceanic Anoxic Event from fossil wood and marine carbonate (Lusitanian Basin, Portugal). Earth Planet Sci Lett 253: 455–470

Hollander DJ, Bessereau G, Belin S, Huc AY, Houzay JP (1991) Organic matter in the early Toarcian shales, Paris Basin, France: a response to environmental changes. Reve De L´institut Francais Du Petrole 46: 543–562

Hougård IW, Bojese-Koefoed JA, Vickers ML, Ullmann CV, Bjerrum CJ, Rizzi M, Korte C (2021) Redox element record shows that environmental perturbations associated with the T-OAE were of longer duration than the carbon isotope record suggests – the Aubach section, SW Germany. Newsletters on Stratigraphy 54: 229-246

Hughes WB, Holba AG, Dzou LIP (1995) The ratios of dibenzothiophene to phenanthrene and pristane to phytane as indicators of depositional environment and lithology of petroleum source rocks. Geochimica et Cosmochimica Acta 59: 3581–3598. https://doi.org/10.1016/0016-7037(95)00225-O

ICCP (1998) The new vitrinite classification (ICCP System 1994). Fuel 77: 349-358. https://doi.org/10.1016/S0016-2361(98)80024-0

ICCP (2001) The new inertinite classification (ICCP System 1994). Fuel 80: 459-471. https://dx.doi.org/10.1016/S0016-2361(00)00102-2

Jenkyns HC (1985) The early Toarcian and Cenomanian-Turonian Anoxic Events in Europe: comparisons and contrasts. Geol Rundsch 74: 505–518

Jenkyns HC (1988) The early Toarcian (Jurassic) anoxic event: stratigraphic, sedimentary, and geochemical evidence. Am J Sci 288: 101–151

Jenkyns HC (2010) Geochemistry of oceanic anoxic events. Geochem. Geophys. Geosyst 11: 1–30. https://doi.org/10.1029/2009GC002788

Jenkyns HC, Clayton CJ (1997) Lower Jurassic epicontinental carbonates and mudstones from England and Wales: Chemostratigraphic signals and the early Toarcian anoxic event, Sedimentology 44: 687–706, doi:10.1046/j.1365-3091.1997.d01-43.x

Jenkyns HC, Gröcke DR, Hesselbo SP (2001) Nitrogen isotope evidence for water mass denitrification during the early Toarcian (Jurassic) oceanic anoxic event. Paleoceanography 16: 593-603

Kemp DB, Coe AL, Cohen AS, Schwark L (2005) Astronomical pacing of methane release in the Early Jurassic period. Nature 437: 396-399. https://doi:10.1038/nature04037

Kemp DB, Coe AL, Cohen AS, Weedon GP (2011) Astronomical forcing and chronology of the early Toarcian (Early Jurassic) oceanic anoxic event in Yorkshire, UK. Palaeogeogr. Palaeoclimatol. Palaeoecol 530: 90-102.

Kuhn O, Etter W (1994) Der Posidonienschiefer der Nordschweiz: Lithostratigraphie, Biostratigraphie, Fazies. Eclogae geol. Helv. 87/1: 113-138.

Küspert W (1982) Environmental change during oil shale deposition as deduced from stable isotope ratios. In: Einsele S, Seilacher A (eds) Cyclic and event stratification. Springer, New York, pp 482-501

Leythaeuser D, Schaefer RG, Yukler A (1982) Role of diffusion in primary migration of hydrocarbons. AAPG Bull. 66: 408–429.

Littke R, Baker DR, Leythaeuser D, Rullkotter J (1991a) Keys to the depositional history of the Posidonia Shale (Toarcian) in the Hils Syncline, northern Germany. In: Tyson RV, Pearson TH (eds) Modern and Ancient Continental Shelf Anoxia, Special Publications, vol 58. Geological Society, London, pp 311a, Spehttps://doi.org/10.1144/GSL.SP.1991.058.01.20

Littke R, Rotzal H, Leythaeuser D, Baker DR (1991b) Lower Toarcian Posidonia Shale in Southern Germany (Schwaebische Alb). Organic Facies, Depositional Environment and maturity. Erdöl Kohle Erdgas Petrochemie Hydrocarbon Technol., 44: 407-414

Mackenzie AS, Maxwell JR (1981) Assessment of thermal maturation in sedimentary rocks by molecular measurements. In: Brooks, J. (Ed.), Organic Maturation Studies and Fossil Fuel Exploration. Academic Press, London, pp. 239-254

Mattioli E, Pittet B, Suan G, Mailliot S (2008) Calcareous nannoplankton changes across the early Toarcian oceanic anoxic event in the Western Tethys. Paleoceanography 23: PA3208. https:// doi. org/10. 1029/ 2007P A0014 35

McElwain JC, Wade-Murphy J, Hesselbo SP (2005) Changes in carbon dioxide during an oceanic anoxic event linked to intrusion into Gondwana coals. Nature 435 (7041), 479–482. McNeil, RI, BeMent, WO (1996) Thermal stability of hydrocarbons: Laboratory criteria and field examples. Energy Fuel 10: 6067

Meyer RKF, Schmidt-Kaler H (1996) Jura. In Freudenberger W, Schwerd K, (eds.) Erläuterungen zur Geologischen Karte von Bayern 1 : 500 000. Bayrisches Geologisches Landesamt. 4th ed., München 90-111

Misch D, Leu W, Sachsenhofer RF, Gratzer R, Rupprecht B, Bechtel A (2017) Shallow hydrocarbon indications along the Alpine thrust belt and adjacent foreland basin: distribution and implications for petroleum exploration. J. Petrol. Geol. 40: 341–362

Moldowan JM, Talyzina NM (1998) Biogeochemical evidence for dinoflagellate ancestors in the Early Cambrian. Science 281: 1168-70

Montero-Serrano J-C, Föllmi KB, Adatte T, Spangenberg JE, Tribovillard N, Fantasia A, Suan G (2015) Continental weathering and redox conditions during the early Toarcian Oceanic Anoxic Event in the northwestern Tethys: Insight from the Posidonia Shale section in the Swiss Jura Mountains. Palaeogeography, Palaeoclimatology, Palaeoecology 429: 83-99. http://dx.doi.org/10.1016/j.palaeo.2015.03.043

Pálfy J, Smith PL (2000) Synchrony between Early Jurassic extinction, oceanic anoxic event, and the Karoo-Ferrar flood basalt volcanism. Geology 28: 747-750. https://doi.org/10.1130/0091-7613(2000)028<0747:SBEJEO>2.3.CO;2

Pedentchouk N, Turich C (2017) Carbon and hydrogen isotopic compositions of n-alkanes as a tool in petroleum exploration. In: Hydrocarbon Systems, Geological Society, London, Special Publications 468: 105-125. https://doi.org/10.1144/SP468.1

Peters KE (1986) Guidelines for Evaluating Petroleum Source Rock Using Programmed Pyrolysis. Aapg Bulletin-American Association of Petroleum Geologists, 70(3), 318 - 329. https://doi.org/10.1306/94885688-1704-11D7-8645000102C1865D

Peters KE, Walters CC, Moldowan JM (2005) The Biomarker Guide: Biomarkers and Isotopes In Petroleum Systems and Earth History, 2nd ed. Cambridge University Press

Pickel W, Kus J, Flores D, Kalaitzidis S, Christanis K, Cardott BJ, Misz-Kennan M, Rodrigues S, Hentschel A, Hamor-Vido M, Crosdale P, Wagner N, ICCP (2017) Classification of liptinite–ICCP System (1994) Int. J. Coal Geol 169: 40-61. https://doi.org/10.1016/j.coal.2016.11.004

Prauss, M. (1996) The Lower Toarcian Posidonia Shale of Grimmen, Northeast Germany. Implications from the palynological analysis of a near-shore section. Neues Jahrbuch für Geologie und Paläontologie-Abhandlungen 200: 107-132

Prauss M, Riegel W (1989) Evidence from phytoplankton associations for causes of black shale formation in epicontinental seas. Neues Jahrbuch für Geologie und Paläontologie Monatshefte 11: 671–682

Prauss M, Ligouis B, Luterbacher H (1991) Organic matter and palynomorphs in the 'Posidonienschiefer' (Toarcian, lower Jurassic) of southern Germany. Geol Soc Lond Spec Publ 58: 335–351

Radke M (1988) Application of aromatic compounds as maturity indicators in source rocks and crude oils. Mar Petrol Geol 5: 224–236

Radke M, Willsch H, Welte DH (1980) Preparative hydrocarbon group type determination by automated medium pressure liquid chromatography. Analytical Chemistry 52: 406–411

Radke M, Welte DH, Willsch H (1986) Maturity parameters based on aromatic hydrocarbons: Influence of the organic matter type. Organic Geochemistry 10: 51-63

Riegraf W, Werner G, Lörcher F (1984) Der Posidonienschiefer – Biostratigraphie, Fauna und Fazies des südwestdeutschen Untertoarciums (Lias ε). Enke, Stuttgart, 195 pp

Riegraf W (1985) Mikrofauna, Biostratigraphie und Fazies im Unteren Toarcium Sudwestdeutschlands und Vergleiche mit benachbarten Gebieten. Tubinger Mikropalaontologische Mitteilungen 3: 232 pp.

Röhl H-J, Schmid-Röhl A (2005) Lower Toarcian (Upper Liassic) black shales of the Central European Epicontinental Basin: A sequence stratigraphic case study from the SW German Posidonia Shale. In: The Deposition of Organic-Carbon-Rich Sediments: Models, Mechanisms, and Consequences, SEPM (Society for Sedimentary Geology) Spec. Publ 82: 165-189. ISBN 1-56576-110-3

Rohl H-J, Schmid-Rohl A, Oschmann W, Frimmel A, Schwark L (2001) Erratum to "The Posidonia Shale (Lower Toarcian) of SW-Germany: an oxygen-depleted ecosystem controlled by sea level and palaeoclimate." Palaeogeogr Palaeoclimatol Palaeoecol 169:273–299

Röhl H-J, Schmid-Röhl A, Oschmann W, Frimmel A, Schwark L (2001) Erratum to "The Posidonia Shale (Lower Toarcian) of SW-Germany: an oxygen-depleted ecosystem controlled by sea level and palaeoclimate". Palaeogeogr. Palaeoclimatol. Palaeoecol. 169: 273–299

Ruebsam W, Mayer B, Schwark L (2019) Cryosphere carbon dynamics control early Toarcian global warming and sea level evolution. Global and Planetary Change 172: 440–453. https://doi.org/10.1016/j.gloplacha.2018.11.003

Ruebsam W, Al-Husseini M (2020) Calibrating the Early Toarcian (Early Jurassic) with stratigraphic black holes (SBH). Gondwana Res 82:317–336. https:// doi. org/ 10. 1016/j. gr. 2020. 01. 011

Ruebsam W, Schwark L (2021) Impact of a northern-hemispherical cryosphere on late Pliensbachian–early Toarcian climate and environment evolution. Geological Society, London, Special Publications 514: 359-385. https://doi.org/10.1144/SP514-2021-11

Ruebsam W, Schmid-Röhl A, Al-Husseini M (2023) Astronomical timescale for the early Toarcian (Early Jurassic) Posidonia Shale and global environmental changes. Palaeogeography, Palaeoclimatology, Palaeoecology 623 (2023) 111619

Sachsenhofer RF, Leitner B, Linzer H-G, Bechtel A, Ćorić S, Gratzer R, Reischenbacher D, Soliman A (2010) Deposition, Erosion and Hydrocarbon Source Potential of the Oligocene Eggerding Formation (Molasse Basin, Austria). Austrian Journal Earth Sciences 103: 76-99

Schmid-Röhl A (2019) Ölschiefer – mehr als ein Rohstoff. Holcim (Süddeutschland) GmbH, Dotternhausen, 214 p

Schlanger SO, Jenkyns HC (1976) Cretaceous oceanic anoxic events: causes and consequences. Geologieenmijnbouw 55(3-4): 179–184

Schmid-Röhl A, Röhl H-J, Oschmann W, Frimmel A, Schwark L (2002) Palaeoenvironmental reconstruction of Lower Toarcian epicontinental black shales (Posidonia Shale, SW Germany): global versus regional control. Geobios 35: 13-20

Schouten S, van Kaam-Peters HME, Rijpstra WIC, Schoell M, Sinninghe Damste JS (2000) Effects of an oceanic anoxic event on the stable carbon isotopic composition of early Toarcian carbon. American Journal of Science 300: 1-22

Schulz H-M, Sachsenhofer RF, Bechtel A, Polesny H, Wagner L (2002) The origin of hydrocarbon source rocks in the Austrian Molasse Basin (Eocene-Oligocene transition). Marine and Petroleum Geology 19: 683-709.

Schwark L, Frimmel A (2004) Chemostratigraphy of the Posidonia Black Shale, SW Germany II. Assessment of extent and persistence of photic-zone anoxia using aryl isoprenoid distribution. Chemical Geology 206: 231– 248

Seifert WK, Moldowan JM (1986) Use of biological markers in petroleum exploration. In: Methods in Geochemistry and Geophysics Vol 24 (R. B. Johns, ed.), Elsevier, Amsterdam, pp. 261–90

Sinninghe Damsté J, Kenig F, Koopmans M, Köster J, Schouten S, Hayes J, de Leeuw J (1995) Evidence for gammacerane as an indicator of water column stratification. Geochim. Cosmochim. Acta 59: 1895–1900

Sinninghe-Damsté JS, Keely BJ, Betts SE, Baas M, Maxwell JR, de Leeuw JW (1993) Variations in abundances and distributions of isoprenoid chromans and longchain aikylbenzenes in sediments of the Mulhouse Basin: a molecular sedimentary record of palaeosalinity. Org Geochem 20: 1201–1215

Song J, Littke R, Maquil R, Weniger P (2014) Organic facies variability in the Posidonia Black Shale from Luxembourg: implications for thermal maturation and depositional environment. Palaeogeography, Palaeoclimatology, Palaeoecology 410: 316–336

Song J, Littke R, Weniger P, Ostertag-Henning C, Nelskamp S (2015) Shale oil potential and thermal maturity of the Lower Toarcian Posidonia Shale in NW Europe. Int. J. Coal Geol. 150-151, 127-153

Song J, Littke R, Weniger P (2017) Organic geochemistry of the Lower Toarcian Posidonia Shale in NW Europe. Organic Geochemistry 106 (2017): 76–92.

Stock AT, Littke R (2018) The Posidonia Shale of northern Germany: unconventional oil and gas potential from high-resolution 3D numerical basin modelling of the cross-junction between the eastern Lower Saxony Basin, Pompeckj Block and Gifhorn Trough. In: Kilhams B, Kukla PA, Mazur S, McKie T, Mijnlieff HF, Van Ojik K (eds Mesozoic Resource Potential in the Southern Permian Basin. Geological Society, London, Special Publications 469: 399–421.

Suan G, Pittet B, Bour I, Mattioli E, Duarte LV, Mailliot S (2008) Duration of the Early Toarcian carbon isotope excursion deduced from spectral analysis: Consequence for its possible causes. Earth and Planetary Science Letters 267: 666–679.

Suan G, van de Schootbrugge B, Adatte T, Fiebig J, Oschmann W (2015) Calibrating the magnitude of the Toarcian carbon cycle perturbation. Paleoceanography 30: 495-509, https://doi:10.1002/2014PA002758

Summons RE, Powell TG (1987) Identification of aryl isoprenoids in source rocks and crude oils: Biological markers for the green sulphur bacteria. Geochimica et Cosmochimica Acta 51: 557-566.

Svensen H, Planke S, Chevallier L, Malthe-Sørenssen A, Corfu F, Jamtveit B (2007) Hydrothermal venting of greenhouse gases triggering Early Jurassic global warming. Earth Planet. Sci. Letters 256: 554–566.

Taylor G, Teichmüller M, Davies A, Diessel D, Littke R, Robert P (1998) Organic Petrology: A New Handbook Incorporation some Revised Parts of Stach's Textbook of Coal Petrology. Gebrüder Borntraeger, Berlin.

Them TR II, Gill BC, Caruthers AH, Gröcke DR, Tulsky ET, Martindale RC, Poulton TP, Smith PL (2017) High-resolution carbon isotope records of the Toarcian Oceanic Anoxic Event (Early Jurassic) from North America and implications for the global drivers of the Toarcian carbon cycle. Earth and Planetary Science Letters 459: 118–126, https://doi.org/10.1016/j.epsl.2016.11.021

Traverse A (2007) Paleopalynology. In: Topics in geobiology (Vol. 28). Dordrecht: Springer

Tyson RV (1995) Sedimentary organic matter- Organic facies and palynofacies. London: Chapman and Hall

van Acken D, Tütken T, Daly JS, Schmid-Röhl A, Orr PJ (2019) Rhenium-osmium geochronology of the Toarcian Posidonia Shale, SW Germany. Palaeogeography, Palaeoclimatology, Palaeoecology 534: 109294

Van de Schootbrugge B, McArthur JM, Bailey TR, Rosenthal Y, Wright JD, Miller KG (2005) Toarcian oceanic anoxic event: An assessment of global causes using belemnite C isotope records. Paleoceanography 20: 1-10 PA3008. https://doi:10.1029/2004PA001102

Veron J (2005) The Alpine Molasse basin – review of petroleum Geology and remaining potential. Bull. Angew Geol. 10: 75–86.

Volkman JK, Kearney P, Jeffrey SW (1990) A new source of 4-methyl and 5α(H)-stanols in sediments: prymnesiophyte microalgae of the genus *Pavlova*. Organic Geochemistry 15: 489-497.

Wang Y, Ossa Ossa F, Spangenberg JE, Wille M, Schoenberg R (2021) Restricted oxygen-deficient basins on the Northern European epicontinental shelf across the Toarcian carbon isotope excursion interval. Paleoceanography and Paleoclimatology 36: e2020PA004207. https://doi.org/10.1029/2020PA004207

Wang Y, Ossa Ossa F, Wille M, Schurr S, Saussele M, Schmid-Röhl A, Schoenberg R (2020) Evidence for local carbon-cycle perturbations superimposed on the Toarcian carbon isotope excursion. Geobiology 18: 682-709. https://doi.org/10.1111/gbi.12410

Wehner H, Kuckelkorn K (1995) Zur Herkunft der Erdöle im nördlichen Alpen-/Karpatenvorland. Erdöl Erdgas Kohle 111: 508-514.

Wehner H, Kuckelkorn K (1995) Zur Herkunft der Erdöle im nördlichen Alpen-/Karpatenvorland. Erdöl Erdgas Kohle 111: 508-514.

Withers N (1987) Dinoflagellate sterols. In: Taylor, FJR (Ed.) The Biology of Dinoflagelltes. Blackwell Scientific Oxford pp. 316–359.

Yule B, Roberts S, Marshall JEA, Milton JA (1998) Quantitative spore colour measurement using colour image analysis. Organic Geochemistry 28: 139-149

Zhang S, Huang H, Su J, Liu M, Zhang H (2014) Geochemistry of alkylbenzenes in the Paleozoic oils from the Tarim Basin, NW China. Organic Geochemistry 77: 126-139.

Zhang YD, Jiang AZ, Sun YG, Xie LJ, Chai PX (2012) Stable carbon isotope compositions of isoprenoid chromans in cenozoic saline lacustrine source rocks from the Western Qaidam Basin, NW China: Source implications. Chinese Science Bulletin 57: 560–570.

Zheng T, Grohmann S, Arysanto A, Baniasad A, Zhang Q, Littke R (2023) Petrographical and geochemical investigations on maturation and primary migration in intact source rock micro-plugs: Insight from hydrous pyrolysis on Woodford Shale. Int J Coal Geol 266, 104170.

Ziegler PA (1982) Geological Atlas of Central and Western Europe. Shell International Petroleum Maatschappij BV, Amsterdam 130 pp.

Ziegler PA (1988) Evolution of the Arctic–North Atlantic and the Western Tethys. American Association of Petroleum Geologists, Memoirs 43: 197 pp.

Ziegs V, Horsfield B, Skeie JE, Rinna J (2017) Petroleum retention in the Mandal Formation, Central Graben, Norway. Mar. Pet. Geol. 83: 195–214.

11 Appendix list

Publication III (section 10) describes the depositional environment of the Amaltheenton and Posidonia Shale in Salem borehole. Core photographs and SEM pictures have been taken from this core and CT scans were made. Because of limitations on the length of scientific papers, these aspects could not be included in the published article in the desired detail. Therefore, core photographs, SEM pictures and CT scans are included in Appendix I to III.

Appendix I: Core photographs of the Salem core

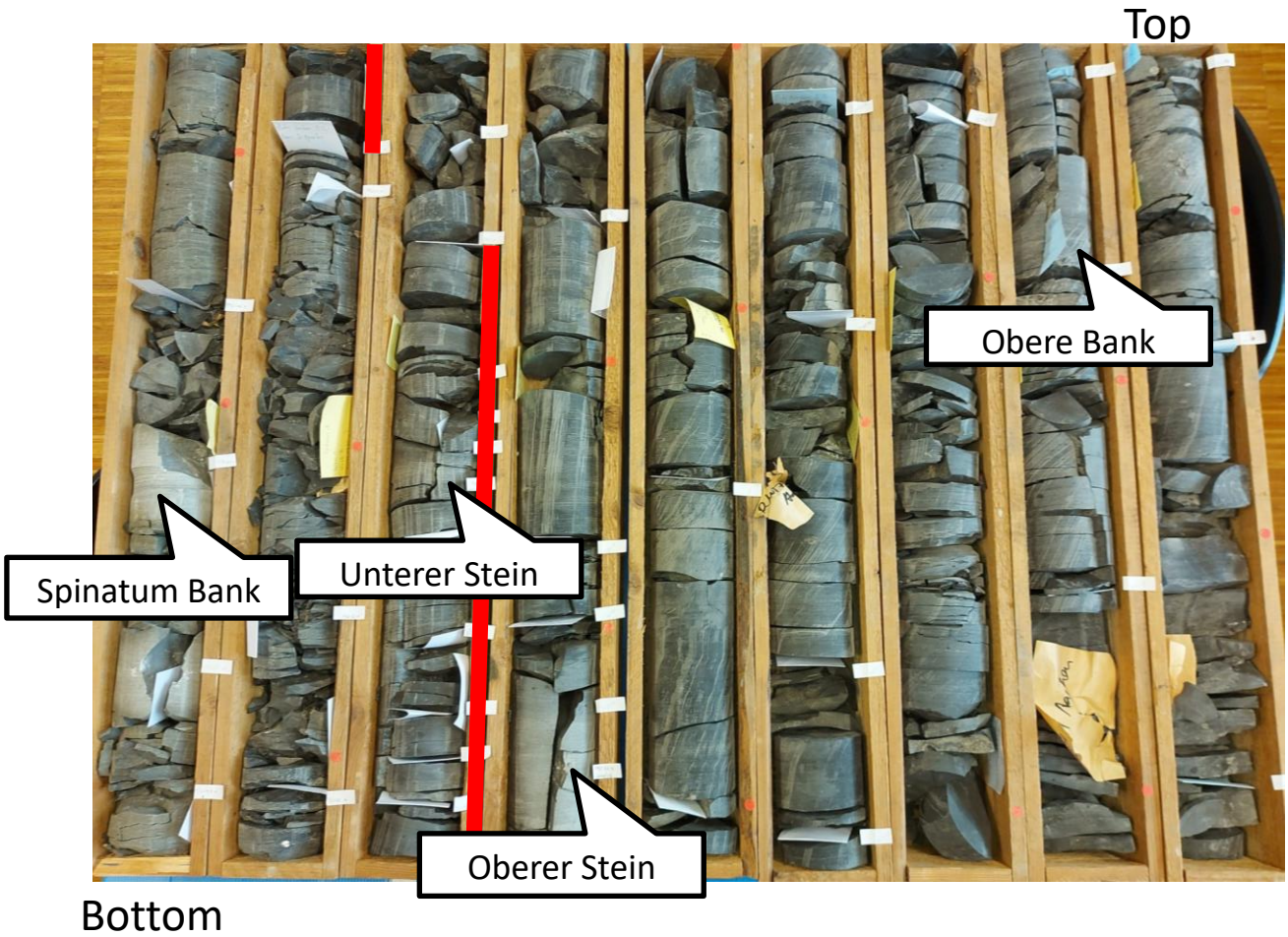

Fig. A1. Overview of the Salem drill core. The lowermost 1-m of the core is not shown. Limestone marker beds intercalating the black shales are labelled.

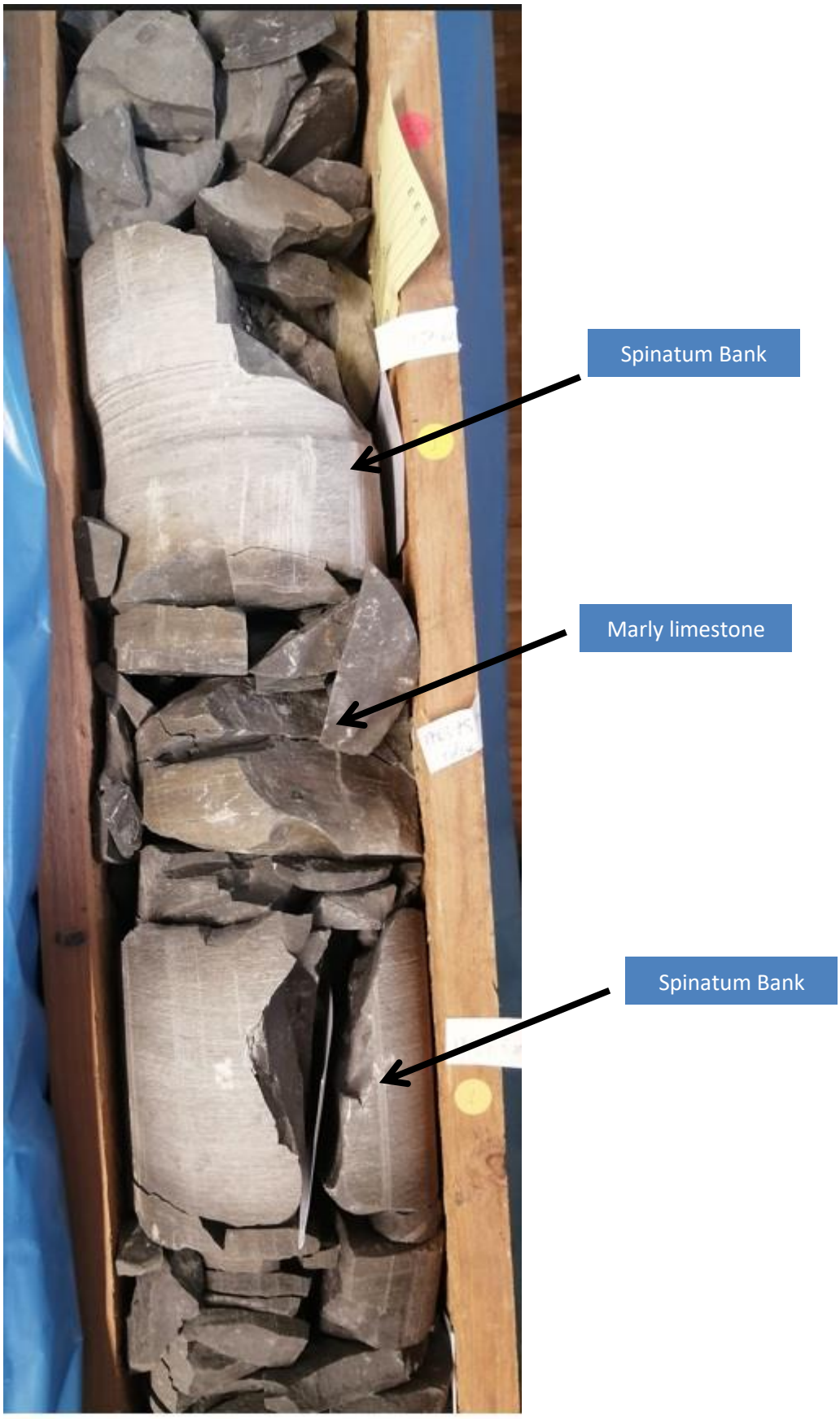

Fig. A2. Drill core section showing the bipartite Spinatum bank near the top of the Amaltheenton Shale.

Fig. A3. Drill core section showing a bioturbated black shale layer (Seegrassschiefer) and a loose belemnite rostrum in the *Tenuicostatum* Zone.

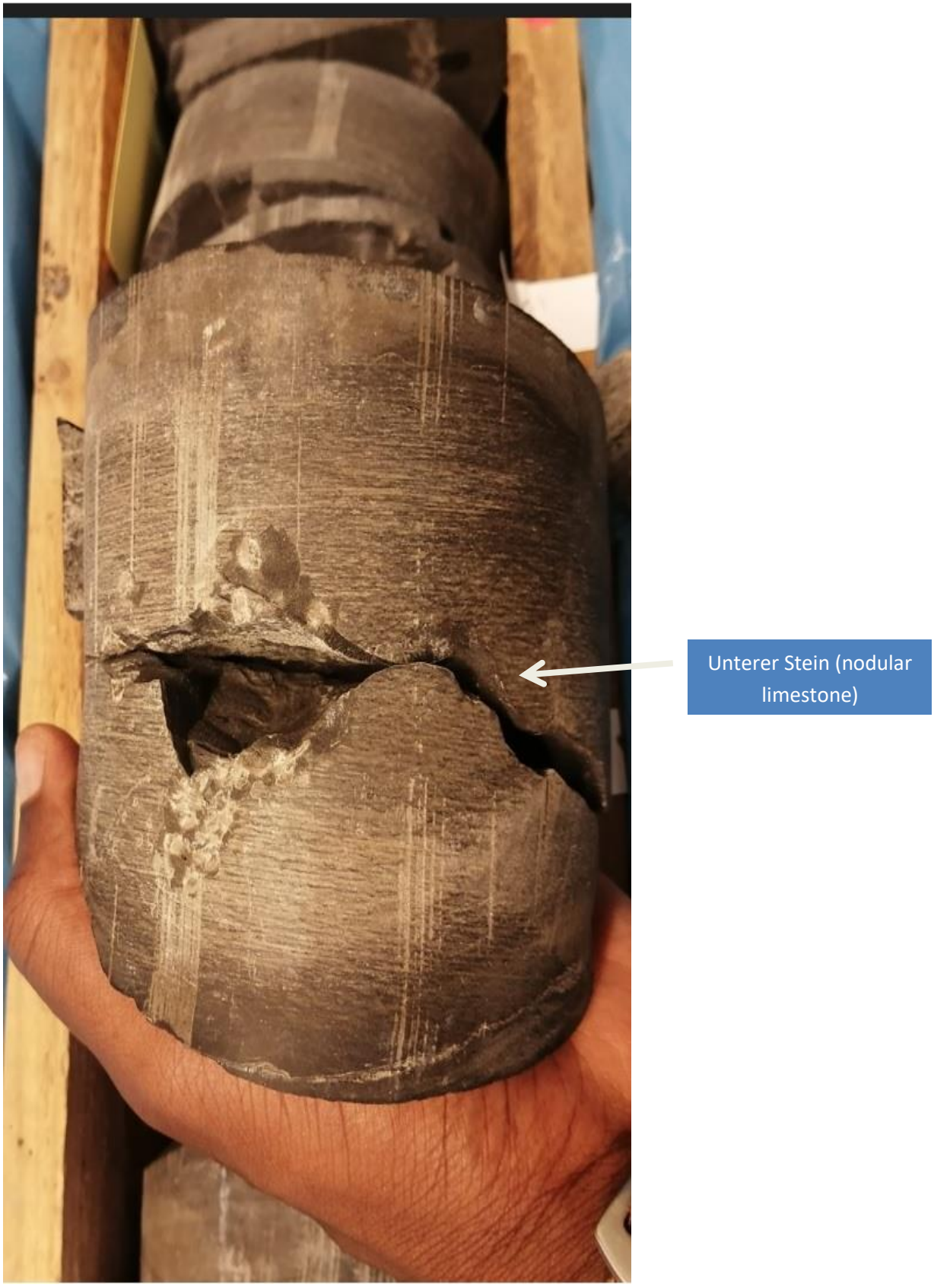

Fig. A4. Drill core section showing the nodular Unterer Stein limestone layer within the *Exaratum* sub-zone.

Fig. A5. Drill core section showing the Oberer Stein limestone layer within the *Elegans* sub-zone

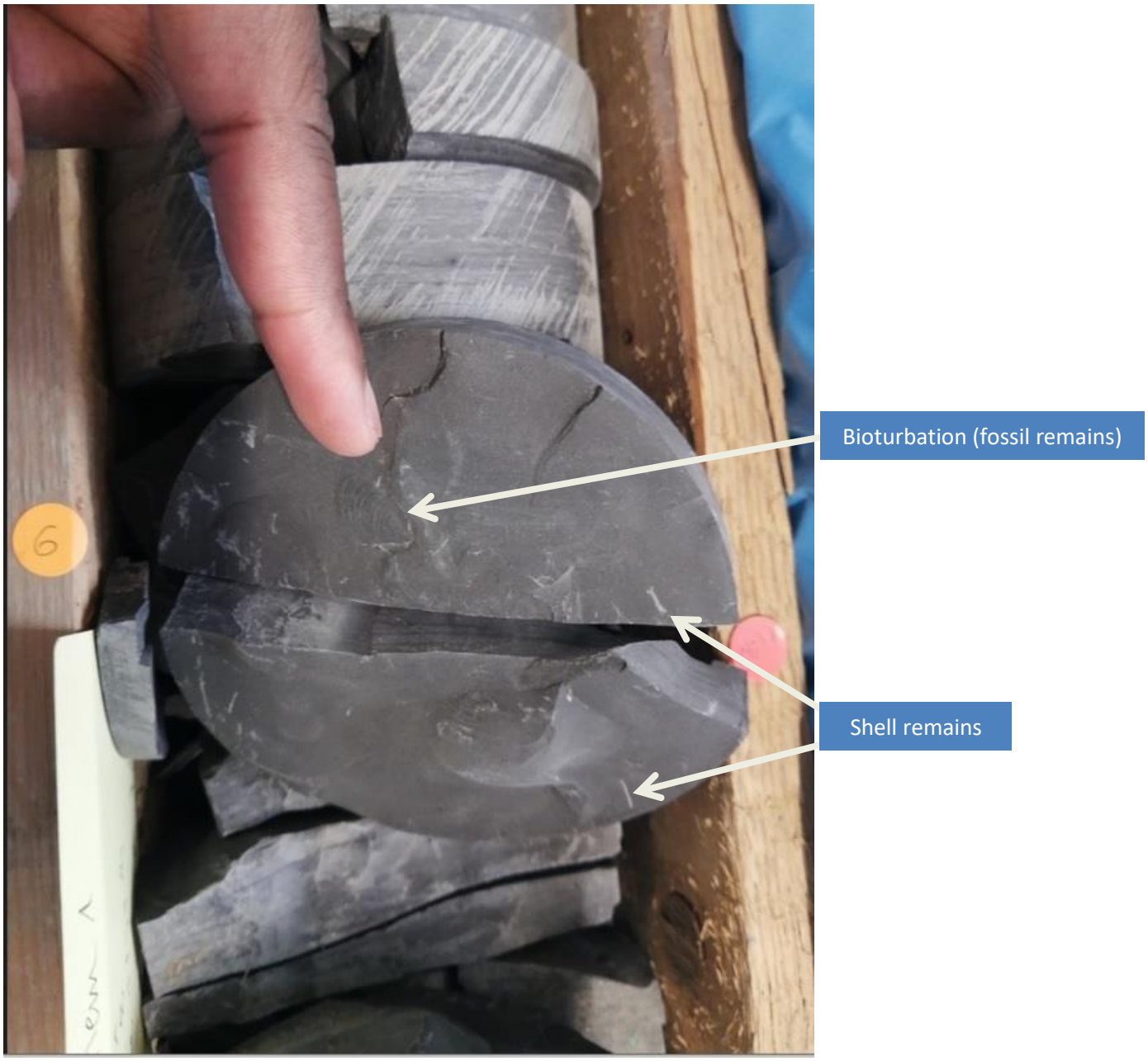

Fig. A6. Drill core section showing light biotubation and shell remains within the upper *Falciferum* sub-zone.

Fig. A7. Drill core section showing the Obere Bank limestone layer within the upper *Falciferum* sub-zone.

Fig. A8. Drill core section showing increased amounts of belemnite fossils and bioturbation structures in the uppermost *Falciferum* sub-zone.

Appendix II: SEM photographs of the Salem core

For scanning electron microscope analysis, a Tescan Clara field emmssion (FE)-SEM at the Chair of Physical Metallurgy and Metallic Materials, Montanuniversitaet Leoben (Austria) was employed on freshly broken limestone surfaces coated with few nm Au to prevent electron charging during high resolution imaging at 5 – 10 kV. The microscope was adapted with backscattered (BSE) and secondary electron detectors including an energy-dispersed X-ray (EDX) detector (Oxford Instrument). The objective was to determine evidence of diagenetic alteration of limestone layers and to identify microfossils.

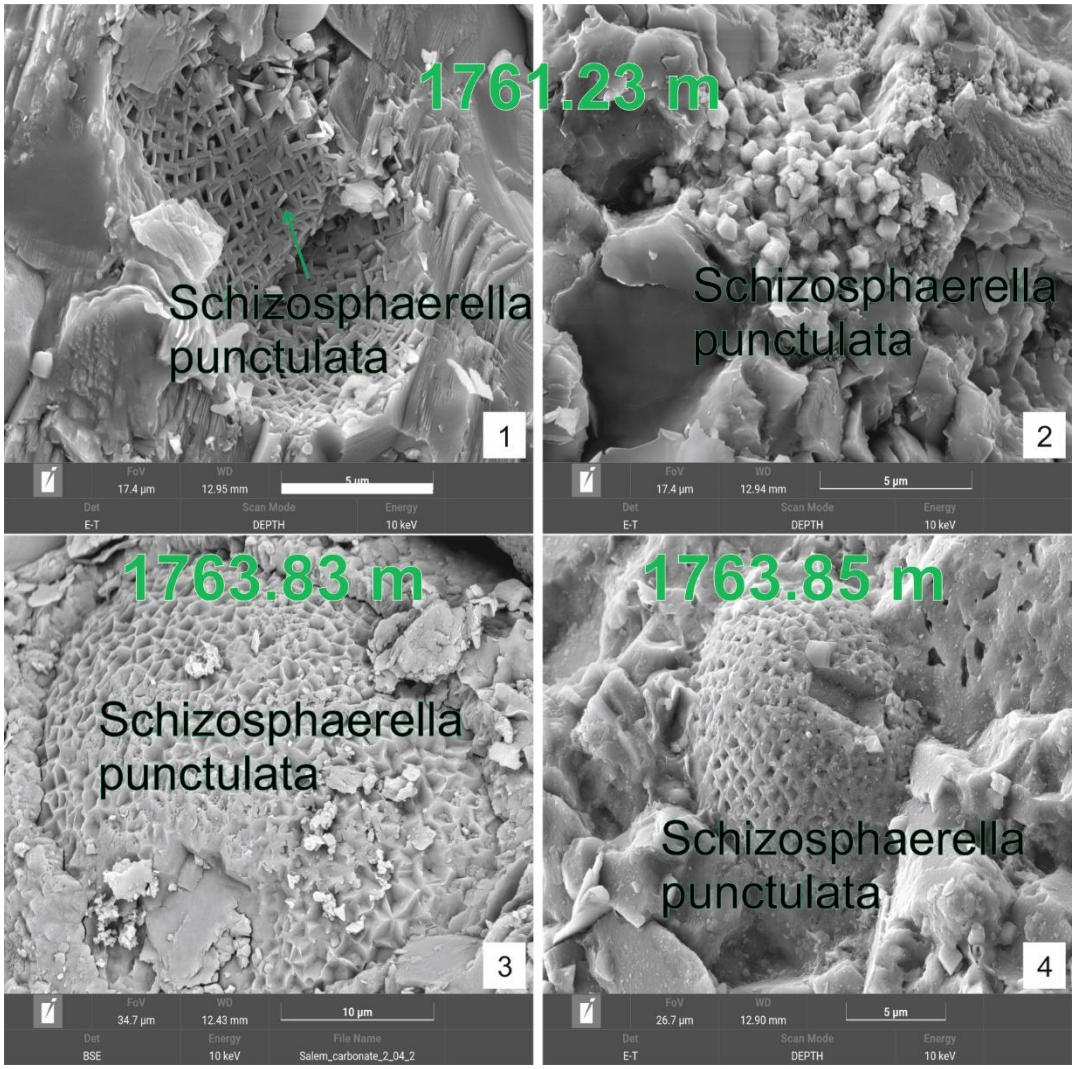

Fig. A9. SEM mircrographs of limestone surfaces showing Schizosphaerella punctulata; 1) test morphology, wall structure, and its modification with progressive diagenetic overgrowth; 2) Diagenetically strongly altered valve surface with complete obliteration of the primary surface morphology and the development of a random crystal mosaic are the consequence of a continued growth of cement, beyond the bounds of the original skeletal frame; 3) Surface aspect of diagenetically altered valves; 4) largely smoothed surface topography due to precipitation of syntaxial overgrowth cement with characteristic square-reticulate partition still in place. Identification is based on Kälin and Bernoulli (1984).

Appendix III: CT scans of the Salem core

CT scans of Amaltheenton and Posidonia Shale showing belemnites and shell remains. ImageJ software was used to enhance the contrast between fossils and background sediment.

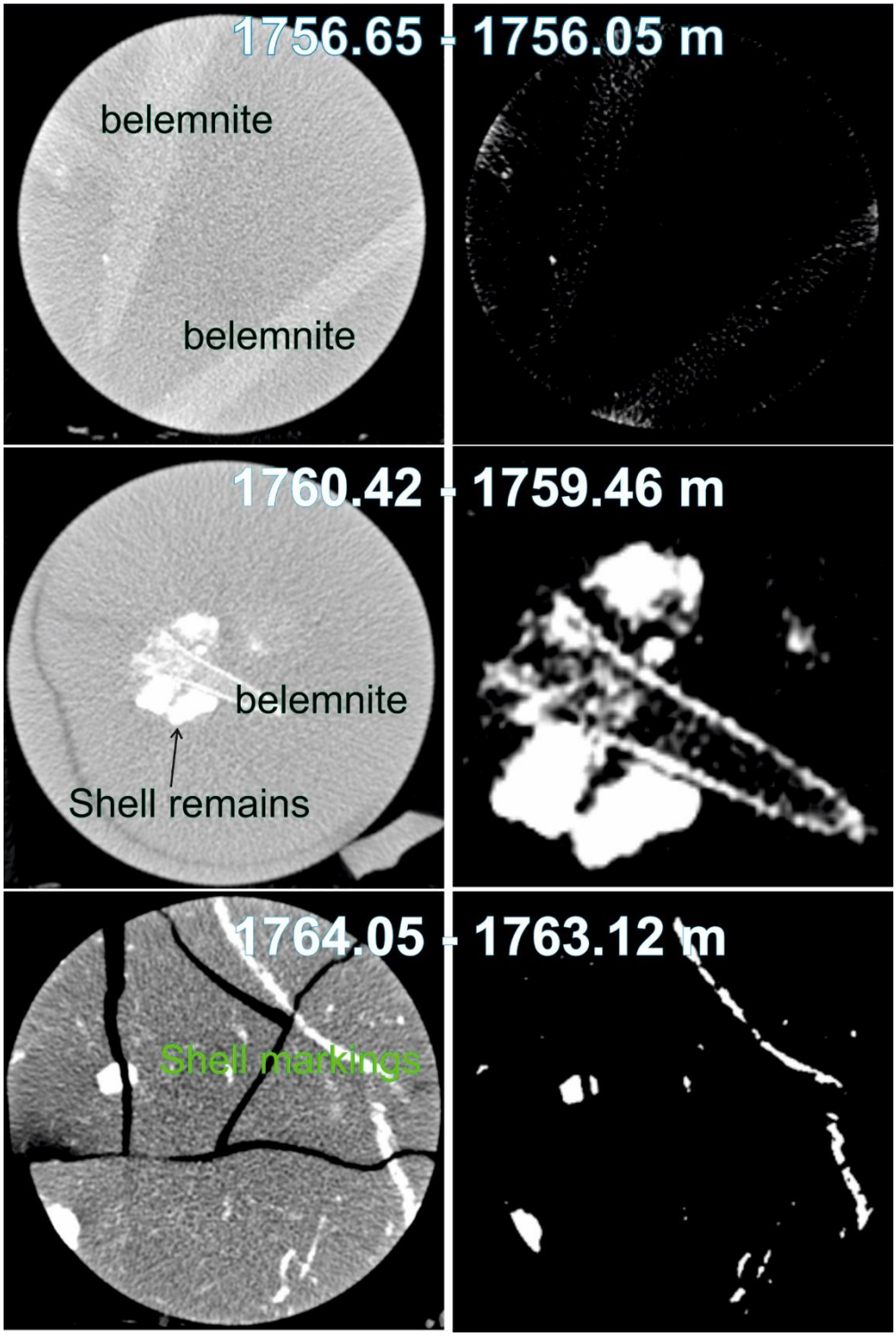

Fig. A9. CT scan slide images after enhancing density contrast using the imageJ software enabling the identification of shell remains and belemnites.